Measurement of Bearing Load in Unicompartmental Knee Arthroplasty Using an Instrumented Knee Bearing

Michael Johannes Antonius Mentink

St Hugh's College

A thesis submitted for the degree of

Doctor of Philosophy

Michaelmas Term 2013/2014

Abstract

Measurement of Bearing Load in Unicompartmental Knee Arthroplasty using an Instrumented Knee Bearing

Michael Johannes Antonius Mentink, St Hugh's College
For the title of Doctor of Philosophy, Michaelmas term 2013

The aim of this thesis was to investigate how to construct a system to measure load in a mobile unicompartmental knee replacement (UKR) bearing. *In vivo* loads have been measured in a total knee replacement (TKR), but with TKR the kinematics are different from those of the normal knee, whereas they are close to normal in a mobile UKR, so the loads measured by an instrumented UKR would be more representative of the normal knee.

On the principle of measuring compression of an object under load, the load may be estimated. Compression measurement using a capacitive sensor was the optimal solution to measure load, based on life expectancy of the sensor and bearing integrity.

A capacitive sensor within a polyethylene (UHMWPE) bearing has not been used before. The visco-elastic and temperature dependent properties of UHMWPE were determined with experiments. UHMWPE had an approximately linear response after ten minutes of applying a constant load. A temperature sensor should be used *in vivo* to compensate for temperature effects acting on the elastic modulus of UHMWPE.

Finite element modelling demonstrated that positioning the sensor under the centre of the bearing concavity resulted in the largest capacitive change. The influence of various dimensional parameters on sensor output was simulated, and the conclusion was that the sensor only needs to be calibrated once. An electronic module inserted into a bearing had less than 5 % influence on bearing compression.

Capacitive sensors were made from polyimide, using standard production methods, and embedded within a UKR bearing using the standard compression moulding process. The embedded sensor had a second order low pass frequency response, with a corner frequency of 9 Hz, twice the frequency required for typical functional loading such as gait. Physiological load signals, gait and step up/down, were applied to the bearing. The capacitance to load response was approximately linear. Load was estimated using a linear method and a dynamic method. The linear method performed best, with an accuracy of force estimation better than 90 %.

In vitro tests were performed using a commercially available transceiver, two standard antennas and a custom antenna, designed to be incorporated in the bearing. Wireless communication between an implanted custom antenna and an external antenna was shown to be feasible. Experiments were also performed that demonstrate that inductive powering of the bearing was feasible.

In addition to load measurement, a proposal for dynamic measurement of the orientation angles of both the tibia and the femur was made. Power and volume calculations showed that it is possible to place an electronic module within the bearing.

This thesis has not only demonstrated that it is feasible to make an instrumented bearing for UKR but has also provided a basic design for manufacturing.

To my parents.

Acknowledgements

I would like to thank the following people for helping me in my work, and without whom this work would not have been possible: Professor David Murray, Professor Richie Gill, Professor Andrew Price, Barbara Marks, Jo Brown, Ben van Duren, Elise Pegg, Alex Liddle and Stephen Mellon.

I would like to thank Juan Guan and Ray Tanuhardja for helping me to gather data for Chapter 3 and 6 respectively.

I would like to thank SJ Electronics (SJ Electronics Ltd, Kettering, UK) for lending me an oscilloscope and accompanying active probe which were used for calibration measurements in Chapter 6.

I would like to thank Biomet UK Ltd, Swindon, UK, especially Mark Butcher and Russell Lloyd, for helping me to manufacture instrumented bearings.

I would like to thank my examiners, Professor Peter Kyberd, and Dr Julie Stebbins.

I would like to thank my girlfriend Helen Davies (BSc(Econ) MSc(Env) AIEMA ACIEEM) for being there for me.

Finally, I would like to thank St Hugh's college. For having me as a student and providing me with a home.

Contents

List of Figures

List of Tables

Commonly used terms and Abbreviations

ACL	Anterior Cruciate Ligament
ADC	Analog to Digital Converter
BW	Body Weight
BTR	Body Temperature Range
COP	Centre of Pressure
C2D	Capacitance to Digital Converter
in vitro	in a test setup using body parts that have been removed from the body
in vivo	within the human body
PI	PolyImide
RSSI	Received Signal Strength Indicator
SPA	SPectral Analysis
TKR	Total Knee Replacement
Transceiver	Transmitter and Receiver
UHMWPE	Ultra High Molecular Weight Polyethylene
UKR	Unicompartmental Knee Replacement

1 Introduction

Accurate measurement of knee load data is important to gain a better understanding of the mechanical functioning of the knee and the data can be used to develop and improve musculoskeletal models, orthopaedic implants, and implant models. The aim of this thesis was to investigate how to construct a system to measure load in a mobile unicompartmental knee replacement (UKR) bearing.

Attempts have been made to estimate the mechanical force and moment from external gait measurements, *in vitro* assessment [1], finite element modelling computer simulations [2] and telemetered implants. However, all these methods have shortcomings. Force estimates from external gait measurements or electromyogram measurements are subject to a large number of assumptions, (i.e. geometry, location of muscle inserts, muscle forces, motion analyses), and can be inaccurate [3]. The accuracy of simulations is dependent on the assumptions made and the input data [4]. Forces that have been measured *in vivo* are reported to be lower than those calculated by models [5]. Because of these issues with force estimation from indirect methods, the ideal way to measure forces is direct measurement *in vivo*.

Instrumented total knee replacements (TKR) have been developed that measure forces *in vivo* [5–11]. However, the design and functioning of the total knee replacement, in particular the massive instrumented total knee replacement that are used to measure force, results in some shortcomings that make it sub-optimal to measure forces within the knee. During the total knee replacement operation, a large number of natural structures are removed, resulting in changed kinematics and abnormal loading compared to the normal knee.

Additional to the total knee replacement where the two condyles of the knee (see Section 1.2) are replaced, there is also a type of knee replacement where only one condyle is replaced; this is termed unicompartmental knee replacement (UKR). One of the advantages of instrumenting a unicompartmental knee replacement is that, compared to the total knee replacement, more natural structures of the knee can be retained, particularly the cruciate mechanism, resulting in more normal kinematics and improved mechanosensory feedback for the patient (this will be discussed in more detail in the next few sections). Therefore, the unicompartmental knee replacement knee is more representative of a normal knee, compared to a total knee replacement knee. The survival rate of the UKR is 94-100% at 10 years, 95% at 14 years [12–15], and 90% at 15 years [16]. These failures may be loading-related; for instance, one cause of failure is failure of fixation [12]. If more accurate information were available about the loads acting on the knee replacement *in vivo*, future generations of knee replacements may be improved.

This is the first time that a unicompartmental knee replacement has been instrumented. In this thesis, all the relevant aspects of instrumenting a unicompartmental knee replacement are analysed. A novel type of load sensor was developed, and mechanical tests with several prototypes have shown that the concept of measuring load within a unicompartmental knee replacement bearing works. Where necessary, other tests were performed to provide crucial information that was formerly not available, and finally a design is proposed for an instrumented unicompartmental knee replacement bearing for continuous *in vivo* use.

1.1 Aims

The following aims have been set for this chapter:

1 Provide background information about anatomical characteristics of the knee.

2 Provide background information about osteoarthritis.

3 Provide information about the existing knee replacement types.

4 Analyse and establish the shortcomings of current instrumented knee implants.

5 Establish the loading conditions acting on a knee.

6 Establish the specifications an instrumented knee replacement must fulfill.

1.2 Normal Knee Anatomy

The knee is one of the largest and most complex joints of the human body. It is a joint formed between three bones; the femur, the tibia, and the patella. There is a large contact area between the femur and tibia with the menisci in place. The movements of the knee incorporate translation, flexion, and rotation (Figure 1.1).

The knee joint is a complex arrangement of bone and soft tissues. In this chapter, the focus will lie on the most important soft and hard tissues that are involved in the kinematics of the knee; the hard tissue being the tibia, femur, and patella; the soft tissue being the cartilage, capsular structures, ligaments, and the menisci. The menisci are deformable soft tissue structures, located between the round distal end of the femur and the flat tibial plateau, that help to create a large surface area between

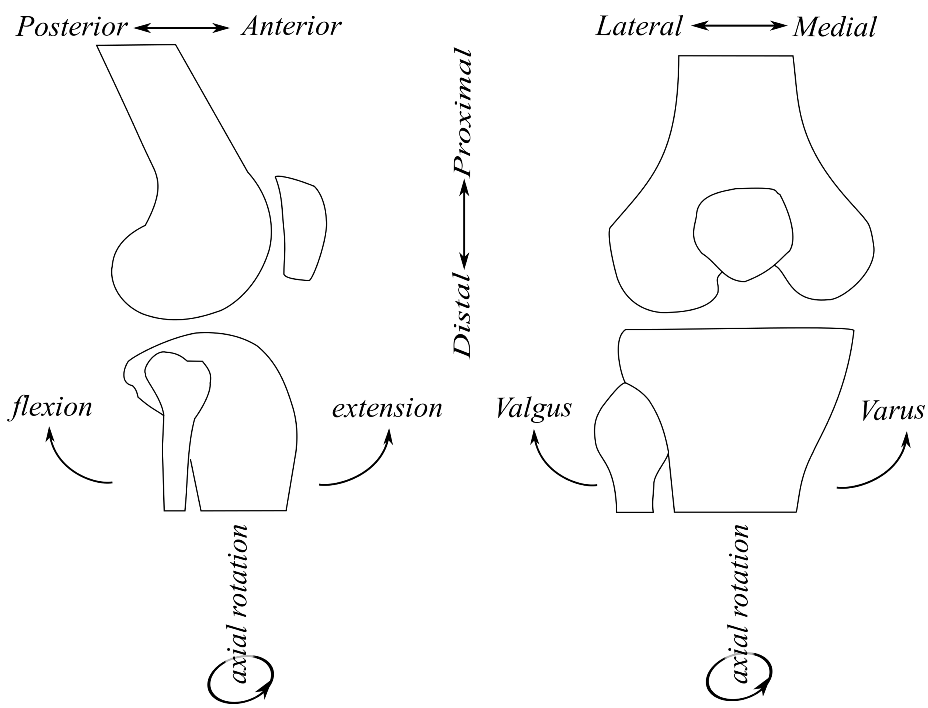

Figure 1.1: *The axes of rotation and planes of rotation of the knee joint, superimposed over the outline of the bones of a right knee from the side (left image) and the front (right image). Anterior-posterior (front-back), medial/lateral (inside/outside of the knee), proximal/distal (closer/further away from the torso), and the rotational movements: varus/valgus (tibia rotating medially/laterally in the medial/lateral plane), flexion/extension (bending/extending the knee), rotation around the proximal-distal axis.*

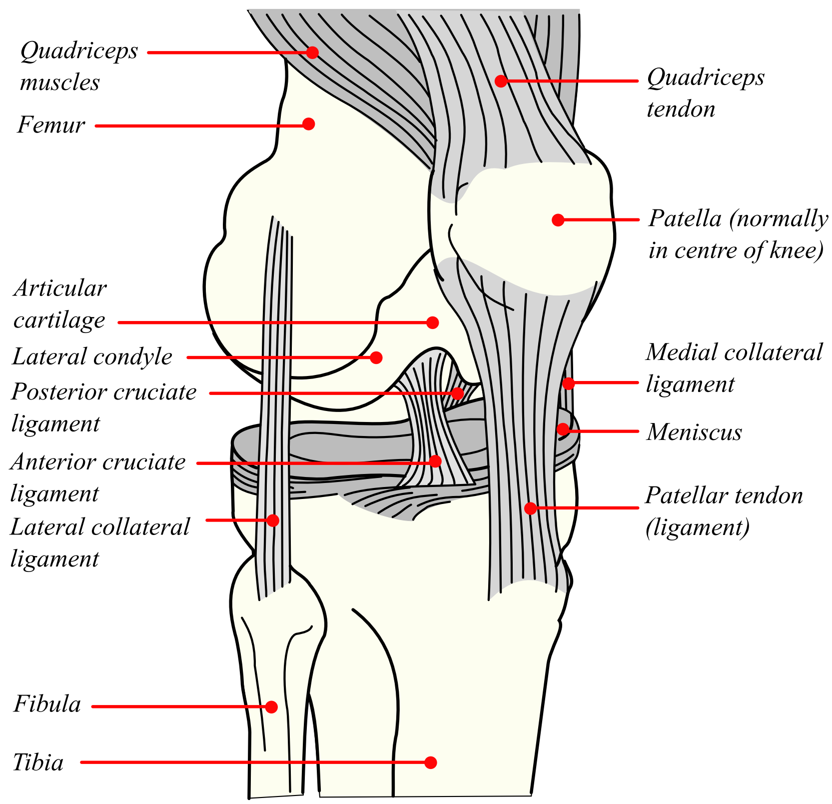

(a)

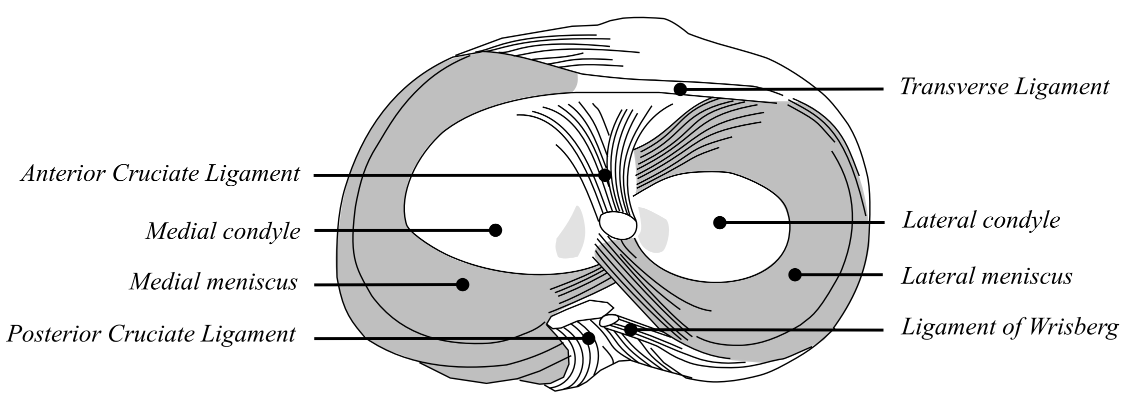

(b)

Figure 1.2: *(a) A schematic view of a normal knee. The knee is shown distracted, for illustrative purposes, adapted from [17] and (b) a schematic view of the proximal part of the tibia, showing menisci and attachments of ligaments, adapted from [18].*

the femur and tibial plateau, to reduce contact stresses on the articular cartilage, to promote circulation of the synovial fluid, and to maintain joint stability. Tendons insert at various points around the knee to provide a connection to the muscles that give rise to active movements of the knee. The ligaments constrain the knee movement; the anterior and posterior cruciate ligaments (ACL/PCL) mainly constrain anterior-posterior translation and rotation of the femur in respect to the tibia [19], whilst the medial and lateral collateral ligaments provide mainly medial-lateral stability (Figure 1.2a). The femur has two condyles, the medial condyle and the lateral condyle. The condyles articulate with the two tibial plateaux. In full extension, the knee has a "screw-home" or "locking" mechanism in which the femur rotates internally, partly due to the shape of the tibial plateau [20], asymmetry between the lateral and medial condyles, aided by the location where the cruciates insert into the bone, guiding the rotation and centring the femur and tibia, providing stability [21].

1.3 Osteoarthritis

The most common disorder of the knee joint is osteoarthritis (OA). OA is a clinical syndrome where joint damage is associated with pain and loss of function. The joint structure becomes irreversibly and increasingly damaged, bony growths *(osteophytes)* develop around the joint, and the soft tissue of the knee becomes inflamed. The aetiology of OA is multi-factorial and mechanical loads are considered to play a major role [22]. Other predisposing factors are obesity, occupation and trauma [23]. As OA develops many structures of the knee may be affected, such as soft tissues and bone, and the patient may experience pain. End stage OA is a very severe disease in which bone rubs on bone. Currently, joint replacement is considered to be the treatment of choice for end stage OA, in the knee. This may either be a total knee replacement (TKR), or if the disease is confined to one compartment of the knee, a unicompartmental knee replacement (UKR).

1.4 Total Knee Replacement

In a TKR, the distal part of the femur is replaced by a metallic component and the proximal part of the tibia is replaced by a tibial plate with a mobile or fixed polyethylene bearing. In order to insert these components into the knee, the meniscus is removed, as well as the anterior cruciate ligament [7]. In some designs the posterior cruciate ligament is also removed [10]. The combination of removing the tibial plateau, the meniscus and one or both of the cruciate ligaments significantly changes the kinematics of the TKR knee compared to those of the normal knee [24, 25]. Specifically, following TKR a gross anterior subluxation of the tibia relative to the femur occurs during extension, which is prevented by the ACL in the normal knee. This is believed to be the result of the patella tendon force [25]. Paradoxically, during flexion the tibia subluxes posteriorly. This is partly due to the patella tendon force. In TKR, the PCL is defunctioned in part due to the ACL deficiency and partly because of damage during surgery, reducing its constraining function (Figure 1.3) [19]. Because the constraint of the ACL is lost, more constraint is built into the implant, such as a tibial implant that has a concavity, or a peg that constrains posterior translation.

A disadvantage of using an instrumented TKR is that additional bone has to be resectioned using custom instrumentation to accommodate the larger tray and stem with sensors, electric measurement components, and the antenna [26] (Figure 1.4 and 1.5 for an illustration).

1.5 Unicompartmental Knee Replacement

In a UKR, only the compartment that is affected by OA is replaced by artificial components, predominantly the medial compartment. In a medial UKR, the lateral side, including the lateral meniscus, and the cruciate mechanism is kept intact. Bone is removed from the femoral condyle, and the tibial plateau and is replaced by a tibial tray and a femoral component (Figure 1.6). There are mobile and fixed bearing ver-

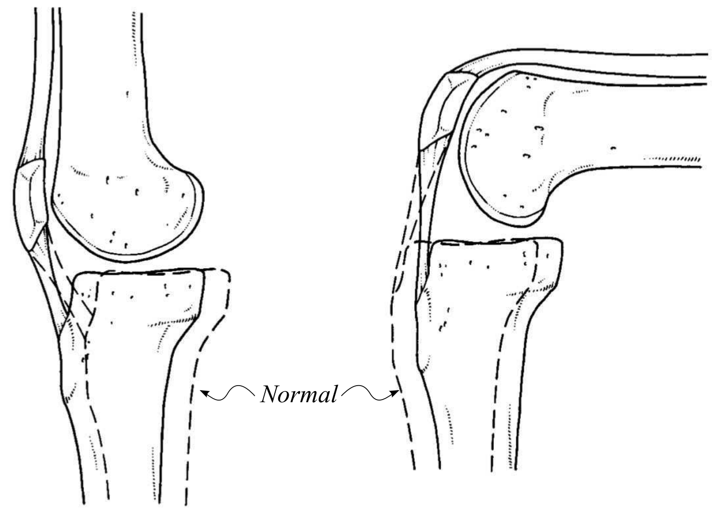

Figure 1.3: *Subluxation of the femur in respect to the tibia. The discontinuous line represents the normal knee. In ACL and PCL deficient and ACL deficient TKA (solid line), the tibia subluxes forward during extension. In flexion with the PCL retaining TKA the tibia subluxes posteriorly [19].*

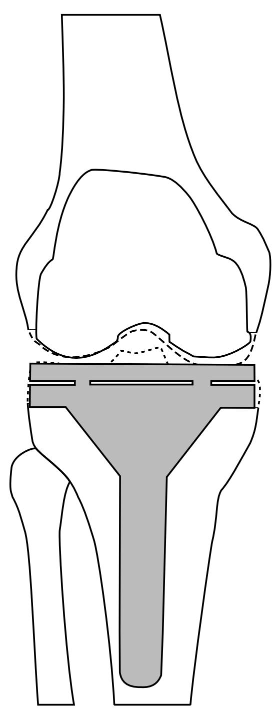

Figure 1.4: *Schematic representation of an instrumented TKR (solid line), adapted from [26], and an approximation of a normal knee (intermittent line).*

(a)

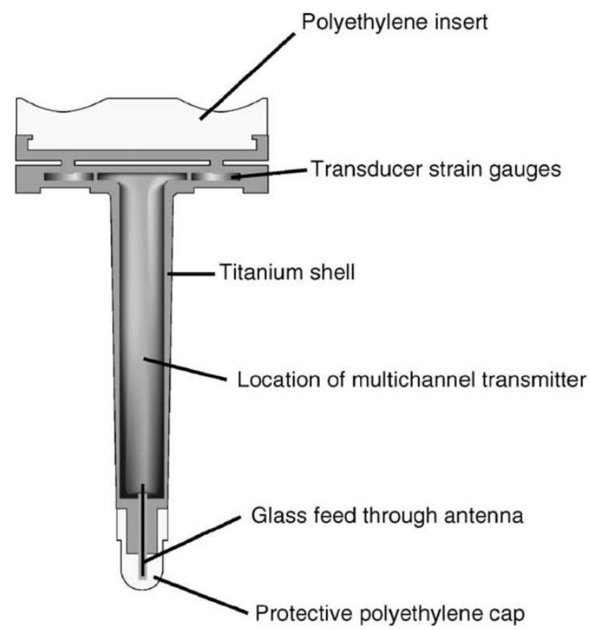

(b)

Figure 1.5: *Two types of TKR with strain gauges; (a) located in the stem [10], and (b) underneath the tibial plateau [26].*

sions of the UKR. Because the normal constraint provided by the ACL is retained, the tibiofemoral articulation can be completely unconstrained. In a mobile bearing UKR, such as the Oxford UKR (Biomet, Swindon, UK), a free moving mobile bearing is placed between the femoral component and the tibial tray. Because of a flat tibial tray, congruent bearing concavity, and unconstrained bearing, the majority of the knee load is perpendicular to the tibial tray, but there will be some small anterior-posterior forces, because of friction, that result in shear of the bearing; however, these forces are small compared to the normal load. In the UKR, both cruciates are retained, so the kinematics are similar to normal [24, 25, 27–33]. An instrumented Oxford UKR would, therefore, measure forces that are very similar to those occurring within a normal human knee and are expected to be different to those measured with instrumented TKR.

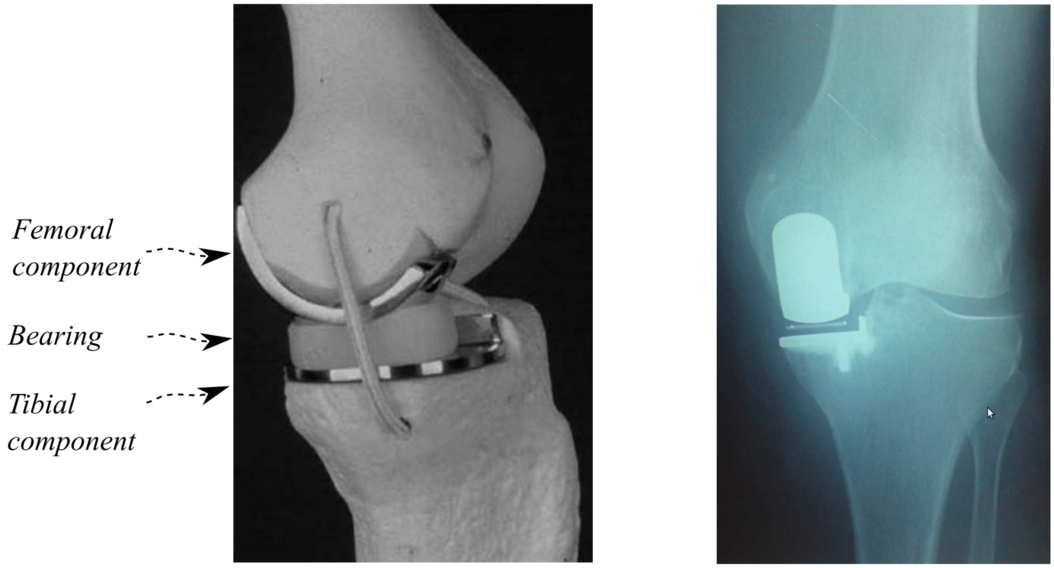

(a) (b)

Figure 1.6: *Photograph of the phase 3 Oxford UKR [37], and (b) Radiograph of implanted Oxford UKR on the medial side of the knee [38].*

There are other advantages of the UKR: the *in vivo* mean wear rate of the Oxford UKR is much lower (0.02 mm/yr, maximum: 0.03 mm/yr) [34] than that of TKR (0.1 to 0.13 mm/yr) [35, 36]. Additionally, the UKR allows for minimal incision surgery, and fewer normal knee structures are removed; in case of failure of the UKR, often a TKR operation can be performed.

To the author's knowledge, there have been no previous reports of an instrumented UKR.

1.6 Location of the Load Sensor

In a knee replacement, there are three structures that bear load; the femoral component, the tibial component and the bearing, and in order to measure loads, a load sensor has to be inserted in or between one or more of them. The patella is disregarded for instrumentation purposes, because it does not directly bear the load of the knee during standing. The femoral component also is not suitable for instrumenting to measure load, because of the movement in three axes (Figure 1.1) during use in respect to the tibia, 1) the distal end of the femur rolls over the tibial plateau, 2) there is translation anteriorly and posteriorly, and 3) there is rotational movement of the femur over the medial-lateral axis of the tibia. Especially 1) poses a challenge; in order to measure knee force with an instrumented femoral component, the aggregate data of multiple load sensors distributed along the curvature of the femoral component would have to be measured and mathematically integrated into one force measurement, which is more difficult than measuring loads acting on a flat surface.

Instrumenting the tibial component simplifies load measurement considerably; the sensor is not mounted on a rolling contact surface, and therefore load can be measured by placing sensors at the corner points of the tibial plateau. In the instrumented TKR, multiple sensors have been used to instrument the tibial component [26], because in a TKR, the femoral component translates anterior-posteriorly over the bearing and tibial component, resulting in a moving force vector. A moving force sensor results in loads perpendicular to the tibial plateau, and shear forces perpendicular to- and rotational around that axis.

In addition, to accommodate these sensors, extra bone needs to be removed. One of the advantages of instrumenting a UKR is that less knee structures have to be removed, compared to the TKR.

In case of an instrumented tibial component, movement 1) is no longer an issue, but movements 2) and 3) still mean that multiple sensors would have to be used, making the problem more complex than necessary, and resulting in a need to remove additional knee structures.

In a mobile UKR bearing, the bearing moves with the femoral component, which rolls in the bearing concavity, so that movements 1), 2) and 3) are all eliminated with respect to the bearing. Therefore, the load vector is perpendicular to the tibial plateau.

Additionally, the advantage of measuring forces within a UKR bearing is that no additional knee structures have to be removed, on the condition that changing the bearing geometry to house the load measurement components does not require too much additional space. The load measurement components therefore need to use the smallest amount of space possible - in addition to the goals that are set at the end of this chapter.

1.7 Loading Data

In 2011, data from the National Joint Registry showed that the average knee replacement patient from England and Wales undergoing a UKR was 64.4±1.0 ($\mu \pm \sigma$) years old, with a BMI of 30.1±5.1 ($\mu \pm \sigma$) [39]. An average UK person of age 64 had a body weight (BW) of 80.0±0.6 (μ±SE) kg, and a BMI of 28.3±0.17 (μ±SE) [40]. One BW is therefore equal to 80.0 [kg] $\times$ 9.81 [m/s^2] = 785 [N]. The average daily number of steps for a British person aged 64 years old is 3,221 per limb [41]. Assuming a 30 year lifespan of a bearing, with 12×10^6 cycles per year, the sensor will have to survive 36×10^7 cycles.

Measurements with an instrumented TKR (Orthoload.com, accessed 27th June 2012, file name: k1l110108_1_80p_gait.akf [42]) show that the normal forces acting on the medial condyle during gait can range from 171 to 2,871 N (approximately 3.5×BW) (Figure 1.7a). To establish what the maximum frequency is that the instrumented UKR needs to measure, the spectral density was calculated for load along the tibial axis of the gait signal, in addition to the cumulative power spectrum. The cumulative power spectral density is calculated using Equation 1.1. 99 % of all power lay below 4.2 Hz (Figure 1.7b). Similarly, for step up/down (accessed 27th June 2012, file name: k5r_060809_1_58p-step_up_step_down.akf, measured with an instrumented TKR), 99 % of all power lies below 4.6 Hz. Therefore, including some margin, the implant should measure all frequencies up to at least 5 Hz.

$$P_c = \frac{1}{P_{tot}} \int_{0}^{fmax} P \, d(f) \tag{1.1}$$

where:

P_{tot}	total power for all frequencies up to f_{max}
f_{max}	the maximum measured frequency
P	power per frequency
f	frequency

During stair climbing, forces range from 45 to 2335 N, with peak forces during walking/jogging at 4×BW at 8 km/h [11].

Although the load distribution between the two condyles changes during flexion and extension, this effect is not very large, and the loading per condyle can can be approximated by 50% of the total load on the knee [8, 26, 44]. The peak forces experienced *in vivo* are higher than cyclic forces: the largest peak force measured in an *in vivo* hip replacement was approximately 8 × BW, when stumbling [45]. It is important to clearly distinguish these peak forces from normal forces during normal use because they occur less frequently, may result in harmful loading of implants, and their frequency components are unknown.

1.8 Design Objectives

The primary aim of *in vivo* force measurement in the knee is to obtain accurate loading data about functional knee loading. This data can be used to provide information about function, disease progress, inform modelling studies, and additionally provide feedback about the status of the knee implant, and possibly subject-specific data for use in rehabilitation. The primary aim of this work is to provide information regarding how to construct an instrumented mobile UKR implant that measures loads in the knee. Existing instrumented TKR implants are very expensive (the implant shown in Figure

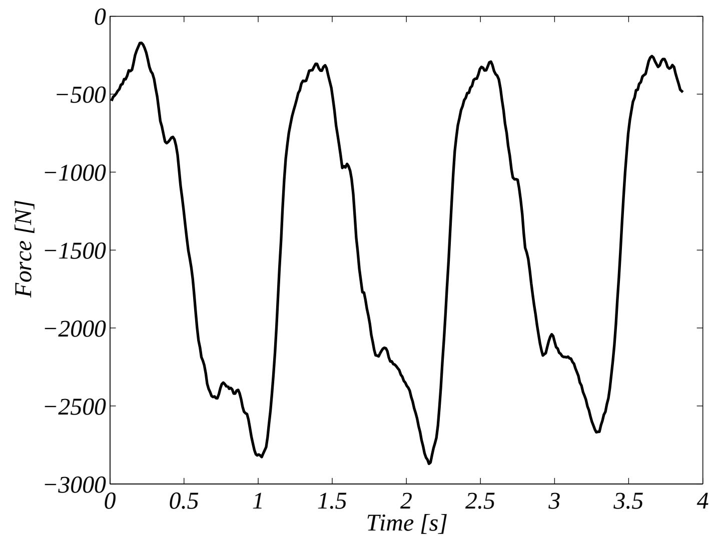

(a)

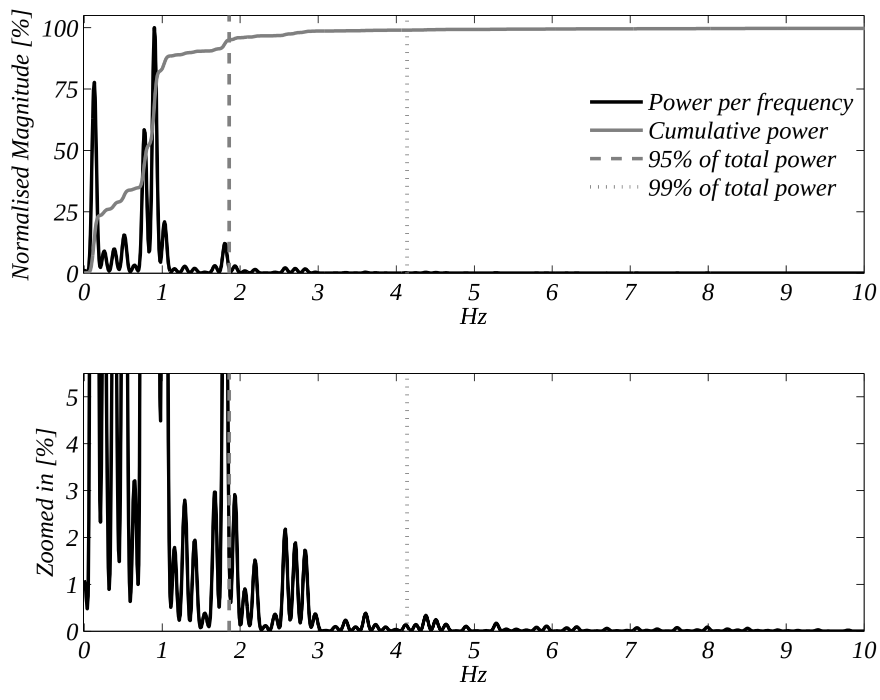

(b)

Figure 1.7: *(a) Gait forces parallel to the tibial axis for three steps, measured with an instrumented TKR [42, 43], and (b) the power spectral density of this gait signal, normalised to the maximum power, with the cumulative power spectrum, indicating that 99% of the total power lies within 4.2 Hz.*

1.5b cost approximately $1M to create [46]). They also require additional structures to be removed in order to fit and need custom tools during an operation [26]. There is a need for an implant that can measure force more cost effectively and require no or little adjustment of the implant and operation methods. The instrumented implant should function under the same conditions as a normal implant. This means that the implant has to function wirelessly, expose only biologically neutral material to the body tissue, and be resistant to wear. Furthermore, it should be able to measure the full range of load that can be expected during use. A maximum peak force of 8×BW has been reported earlier [45], and to create some margin, the maximum criteria considered for this implant will be 10×BW. Because no published information could be found about the maximum frequency of the frequency spectrum for peak force activities [42], twice the maximum frequency of gait, 10 Hz, (for more information see Section 1.7) should be measured.

1.9 Requirements

The following requirements have been set for the instrumented Oxford UKR:

Requirement	Description
1	No measurement instrumentation material, except for UHMWPE or other biologically neutral materials, may be in contact with the body.
2	Sustained wear of the bearing for 30 years, at a predicted mean wear rate of 0.02 mm/yr must not expose embedded components.
3	The measurement data must be transmitted wirelessly.
4	The bearing must be able to operate or be recharged using a power source outside of the body.
5	The instrumented bearing must be able to measure a maximum equivalent of 10 Body Weights of force.
6	The maximum frequency that can be measured should be at least 10 Hz, in order to capture peak forces.
7	The instrumented UKR must be cost effective.

1.10 Thesis Overview

The goal of this project is to provide information regarding how to construct an instrumented mobile UKR that can measure loads *in vivo*. There are many challenges that need to be faced in order to measure loads. The chapters in this thesis reflect the different aspects of this work.

In order to measure loads, a suitable sensor type needed to be chosen. Therefore in Chapter 2, several commonly used sensor types are discussed and two suitable sensor types were identified. In order to choose the most suitable sensor, a loading experiment with a UKR bearing was performed with the goal of measuring the strains under load. The capacitive sensor was chosen because it was the only sensor type that could withstand the high strains that are experienced by the bearing material ultra high molecular weight polyethylene (UHWMPE).

Because the load sensor was embedded in UHMWPE, the load measurement greatly depends on the reaction of UHMWPE to load. Specifically, in order to measure loads, the elastic response of UHMWPE to load should be as linear as possible. Because UHMWPE is a viscoelastic material, and specific data regarding the viscous behaviour was missing, as well as specific data regarding the elastic behaviour of UHMWPE in Chapter 3 experiments were performed that provided information about under which circumstances UHMWPE could be used so that it would react linearly to load.

Not only the material surrounding the load sensor was of influence on the load sensor output, but also where it was placed, in addition to the geometry of the bearing. In Chapter 4 the bearing geometry was simulated in a finite element study. In this study the location of the sensor was varied, in addition to the dimensions of the bearing, based on manufacturing tolerances. The primary goal of this chapter is to find the optimal location to embed the sensor within the bearing to get the maximum capacitive signal. Additional goals were to assess the influence of the position of the sensor on the output magnitude, and finally, the sensor output needs to be measured and processed by an electronic module, further discussed in Chapter 7. Simulations were run in order to find the optimal location for the module.

Chapter 5 provides data on how the sensor was developed, constructed and tested. Loading tests were performed with the bare capacitive sensor and the sensor embedded within UHMWPE, first with sinusoidal loads to determine the frequency response of the sensor, and then with physiological representative signals. Because of the viscoelastic properties of UHMWPE, a novel load estimation method needed to be developed and verified. Two load estimation methods were developed and compared.

The electronic measurement system generates digital data that has to be transferred wirelessly. In order to do so, in Chapter 6 the requirements of wireless communication were outlined, and a suitable wireless transceiver (*trans*mitter and re*ceiver*) was identified. *In vitro* tests were performed to assess how well the transceiver performed in a worst case situation representative of the knee, as well as tests with a custom flexible antenna. Additionally, inductive power experiments were performed to assess if it were possible to wirelessly power the implant.

In Chapter 7, the entire measurement system is discussed. New components were identified to measure kinematics. Calculations were made regarding power usage and physical volume of the system, as well as instructions on how to assemble the system. Finally, recommendations for future research are made.

2 Considering Sensor Options

2.1 Introduction

In this chapter, various methods of measuring loads *in vivo* using the mobile UKR are discussed, with their advantages and disadvantages.

Several parameters were considered; an important parameter is the life span of the sensor, which should exceed 3.6×10^7 loading cycles (see Chapter 1). An important consideration in this chapter is that the life span of a sensor is mostly determined by the strains it experiences. For that reason, it is vital that the magnitude of these strains is known. Therefore, an experiment is described that was performed to find out how much a bearing deforms under load and several sensor types to measure load were identified, of which two were chosen. A method to wirelessly measure capacitance is discussed. One sensor was dismissed after performing an experiment, and the capacitive sensor was chosen as the most suitable sensor type.

2.2 Aims

The following aims were set for this chapter:

1 Present a literature review on a selection of appropriate sensors

2 Determine how much strain a load sensor must be able to withstand.

3 Identify a suitable sensor to measure load.

2.3 Literature Review

The following sensors were considered, based on their small size and previous use in other research: magnetoresistive sensors, piezoelectric sensors, piezoresistive sensors, strain gauges, resistive wire and capacitive sensors. Additionally, inductive readout of capacitive sensors is discussed. At the end of this section, two suitable sensor types for measurement of loads within a UKR bearing will be chosen.

2.3.1 Magnetoresistive Sensors

The resistance of a magnetoresistive sensor changes as a result of a changing magnetic field in its vicinity. This effect has been used create an instrumented TKR bearing, in which all the electronics and the magnets were contained [47, 48]. By positioning the magnets proximally and the sensors distally within the UHMWPE, by measuring the change in resistance, the compression of the UHMWPE was measured, although not *in vivo*. The danger of using materials with grossly dissimilar elastic moduli, which is the case when embedding electronic components within UHMWPE, is that stress concentrations can occur within the polyethylene surrounding the stiffer object, which may lead to bearing wear or fracture [49, 50]. Additionally, because of the dissimilarity in elastic moduli, some of the load may bypass the sensor, introducing an error in the load measurement [51]. Therefore, this type of sensor is not very suitable for measurement of force within a UKR knee replacement.

2.3.2 Piezoelectric Sensors

In piezoelectric sensors, an electrical signal is generated by the material under the influence of strain. Piezoelectric sensors have been used to instrument a tibial component of a TKR, although not *in vivo* [51–54]. Metallic piezoelectric sensors should not be used within the bearing, because there is a large mismatch between the elastic moduli (the elastic modulus of the sensor is 44 GPa, whereas that of UHMWPE is 1 GPa [52]). Polymer piezoelectric materials have been used to create pressure sensors, using polyvinylidenefluoride (PVDF), however, for very small loads (<5N). A further disadvantage is that these sensors can only measure dynamic loads [55]. Therefore, this type of sensor is not very suitable for measurement of force within a UKR knee replacement.

2.3.3 Piezoresistive Sensors

In piezoresistive material the electrical resistance changes under influence of applied strain. However, again, the sensor has a very high elastic modulus, resulting in all the disadvantages that were discussed earlier. Furthermore, metallic piezoresistive sensors have to be bonded to a surface in order to measure strain [56]. Piezoresistive film sensors have been used to measure contact stress in the knee joint of cadavers, but not *in vivo* [57]. The sensor is constructed as a layered foil with conductive ink sandwiched in between. When pressure is applied, the conductivity increases. This sensor is flexible, which removes the problem of dissimilar elastic moduli between bearing material and the sensor. However, the drawbacks of this type of sensor are that conductive ink sensors have a limited life span [58], have a non-linear response, and therefore are highly dependent on an accurate calibration protocol [59, 60], drift [61], creep [62], gradual loss of sensitivity [62], and hysteresis [63, 64].

2.3.4 Strain Gauge Sensor

A strain gauge is a construct of a thin metal foil bonded to a flexible surface. By straining the foil, the metal is stretched, resulting in a decreased diameter and a resistance change of the gauge. The resistance change to strain change is proportional, and by measuring the resistance change, the strain may be measured. Strain gauges come in many forms, and the most widely used material for strain gauges is constantan, an alloy of 55% copper and 45% nickel. It is also the only material that is used in strain gauges with low drift, low temperature dependence and the capacity to withstand large numbers of cycles [65]. Strain gauges have been used on a polymer substrate to measure small forces [66] and also forces in the bearing of a TKR [67, 68].

2.3.5 Resistive Wire Sensor

Strain in the bearing can be measured by measuring the resistance change of a resistive wire, wrapped around the bearing, which will stretch when the bearing is compressed. Resistive wire comes in different materials, for instance constantan, which has the disadvantage of not being able to withstand the strains occurring in the bearing. Another material to consider is nitinol, which is an alloy of nickel and titanium. Nitinol has been used widely in the medical industry because of its biocompatibility and durability. Nitinol is a hyperelastic material, which means that it has an elasticity that is about ten times higher than the elasticity in ordinary materials [69]. It is linearly elastic up to a strain of approximately 1 %, and then for increasing stress, shows a flat stress relieving strain response where stress remains constant and strain increases up to approximately 8 %. Nitinol also shows the unique behaviour that once it is deformed beyond the 'knee' at 1 % into the flat region, and shows plastic deformation, it can be reheated and it will return to the original form in which it was 'programmed', provided that 8% strain has not been exceeded. Programming is a process which involves high temperatures, up to several hundred degrees.

Additionally, within the flat constant stress region, intermittent peak loads will introduce permanent plastic strains, introducing a permanent shift of the hysteresis loop to a new location, that can only be shifted back to the original location by heating the nitinol above the temperature zone. In theory, the nitinol could be programmed to regain the original shape at a temperature lower than the body temperature, but it is unclear how long that will take, and what the influence on the fatigue life would be.

This sensor could be used for sensing circumferential change of the bearing, ensuring the mechanical integrity of the bearing, which is an advantage.

Fatigue testing of combined tension and compression showed that fatigue life of nitinol extends past 10×10^7 cycles, as long as the dynamic strain remains below ±0.4 %, with rapidly decreasing fatigue life above (only 10×10^5 at ±0.5 % dynamic strain).

Interestingly, fatigue life can be increased by applying a static strain >1.5 %, with a maximum dynamic strain component of 0.8 %, resulting in a fatigue life of at least 10×10^7 cycles [70]. In another test, a purely tensional wire test, the fatigue life also exceeded 10×10^7, but only if the static strain was >6 % and the dynamic strain <0.5 % [71].

Concluding, even though nitinol wire can withstand higher strains than other materials, in order to guarantee continuous faultless operation for the lifespan of the bearing, the strains have to fall below a certain strain level. The magnitude of this strain level will be measured and estimated in Section 2.4. Furthermore, when opting for this type of sensor, there is no possibility to add extra sensors in order to measure load distribution in the future, because it can only measure circumferential change of the bearing.

2.3.6 Capacitive Sensors

A capacitive sensor can be used to measure compression of a material under the influence of load. A capacitor, consisting of two parallel, identically sized conductive plates, can be described by the following equation (Equation 2.1):

$$C = \frac{\epsilon 0 * \epsilon r * A}{d} \tag{2.1}$$

where:

C Capacitance [F];

ϵ0 Dielectric permittivity of vacuum [F/m], e.g., 8.85E-12

ϵr Relative dielectric permittivity of material [dimensionless];

A Area of the plates that is parallel to each other [m^2];

d Distance between the plates [m].

Decreasing the distance between the plates of a capacitor increases the capacitance (Eq 2.1), which is approximately inversely linearly related to the distance between the plates for small changes. When capacitance is expressed in percentage change, all constants ($\epsilon 0$, ϵr) and A can be ignored, and a change of d (Δd) results in (Eq 2.2):

$$C(i,j) = (\frac{1}{d - \Delta d(i,j)} - \frac{1}{d}) \times d \times 100[\%] \tag{2.2}$$

where:

C(i, j)	is the change in capacitance for every sensor coordinate i, j [%]
d	is the distance between the two plates of the sensor [m]
Δd(i, j)	is the distance change between the two plates [m]

Therefore, if the material between the plates is compressed under influence of load, the distance between the plates reduces, and the capacitance increases. Provided that the material between the plates is durable, this type of sensor can measure any strain desirable. Therefore, this type of sensor has none of the problems with strain life that was encountered by the other types of sensor.

Capacitive sensors have been used previously in the tibial component of a TKR [72], although there are no publications regarding *in vivo* use. In an instrumented bearing, a tibial plate was manufactured out of two plates with one axis of movement in the proximal-distal plane; with the proximal plate and distal plate each acting as a electrode (Figure 2.1). The device had six sensors, positioned near the edge of the tibial plate. The function of the device was to measure unequal tibial loading. Instrumenting a TKR poses disadvantages that were discussed earlier in this chapter.

Capacitive sensors are a suitable sensor type for instrumenting a UKR bearing, provided that the sensor does not damage the surrounding bearing material. Damage of the bearing material can be prevented by choosing a flexible sensor with an elastic modulus that is not too dissimilar from the elastic modulus of UHMWPE. That should be possible by choosing a suitable polymer for the dielectric layer. Flexible capacitive sensors have been demonstrated before, made from polyimide (PI) [73–75], polydimethlysiloxane (PDMS) [76–78] or mylar [62]. With PDMS, the maximum force that can be detected is below 10 N. With PI it is possible to measure loads in excess of 3 kN [73]. Therefore, PI is considered as a candidate for measurement of capacitance. With the proper configuration of the electrodes, shear forces can also be detected [75, 79]. The repeatability of this type of sensor is high, but a drawback is that creep behaviour occurs in these sensors [62]. The main determinant of the life span of this sensor is the mechanical integrity of the dielectric separating the electrodes, and the conducting electrode material. Given that the yield strength of PI (270 MPa [80]) is higher than that of UHMWPE (21-28 MPa [81]), it is unlikely that PI will experience any loading outside of the linear elastic region that may lead to early failure. No publications have been found that indicate that PI has a limited life span under cyclic loading below the yield strength. A potential weakness of this type of sensor is that while the dielectric material may withstand large strains, the electrode and the leads to the electrodes are made from metal and may not. However, electrode material can be constructed with stress-relieving methods to prevent over stressing. A further disadvantage of using polymer material is that loading-unloading hysteresis is introduced [75]. With this sensor type, it is possible put multiple capacitive sensors into an array, so that load distribution can be measured [78]. However, measuring load distribution is not one of the goals of this thesis.

There are two ways in which a load sensing capacitor may be constructed; by concentrating the electric field directly between two parallel electrodes, or by extending the electric field to couple from two adjacent electrodes, via the metal of the femoral component or tibial component, back to the electrode, similar to a 'floating electrode' [78, 82, 83]. An illustration of this is shown in Figure 2.1b.

Concluding, this type of sensor seems most suitable for measuring loads; the material that is under strain may be chosen so that is performs better than the UHMWPE of the bearing in regards to longevity and durability. It also provides the flexibility of measuring load on several sites, so that load can be measured directly as compression,

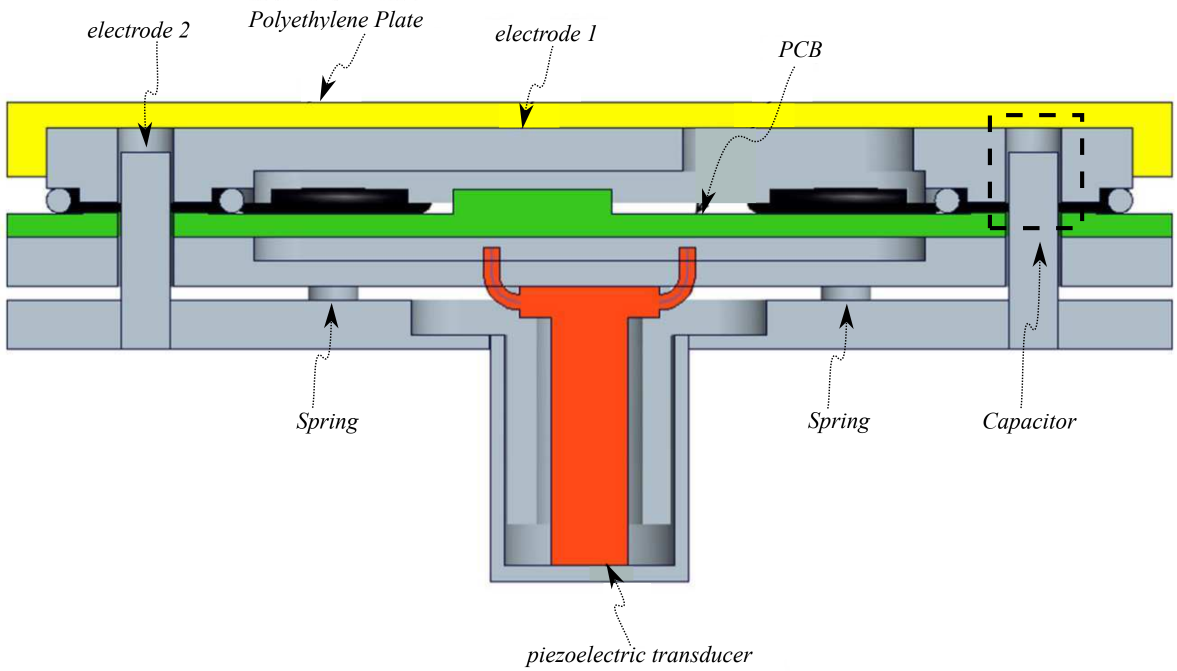

(a)

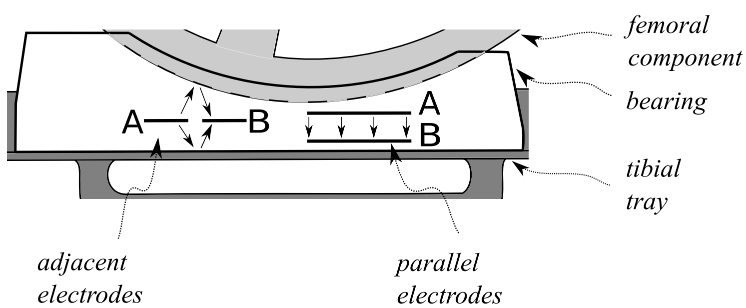

(b)

Figure 2.1: *(a) Instrumented knee replacement bearing with wireless antenna, electronics, and capacitive sensor array (adapted from [72]). The springs ensure that the lowest metallic part can move in respect to the upper metallic part. These two parts are electrically insulated and form the two electrodes of a capacitor. The capacitance changes because a pillar slides in or out of a chamber under influence of load, effectively increasing or decreasing the area between the electrodes.*
(b) A side view of an instrumented UKR bearing design, with part of the femoral component and tibial tray. Two possible capacitive sensor configurations are drawn: adjacent electrodes and parallel electrodes. The path of the electric field between the electrodes A and B follows the straight arrows. In the first sensor configuration, during compression of the polyethylene the femoral component comes closer to the electrodes, shortening the electric path between A and B via the femoral component, and increasing the capacitance. In the second sensor configuration, loading compresses the distance between the two electrodes directly, increasing the capacitance.

rather than indirectly by measuring the expansion of an object under compression.

2.3.7 Inductive Coupling

Although measurements using inductive coupling do not describe a sensor type similar like the previous sections, this method is used to transfer information in other research, and as such warrants a short description. When two conductors are placed as such that a current change through one wire induces a voltage across the ends of the other wire, the conductors are referred to as being inductively coupled. Typically, the conductors are configured as a coil, to increase the signal magnitude. To transfer information from the implant to the outside world, the implant has a sensor coil, which is coupled to an external reader coil. When a capacitive sensor is connected to the coil, a resonant circuit is created that resonates at a certain resonance frequency when the circuit is excited by the reader coil. The deviation of frequency is directly related to the change in capacitance. This method can be used to transmit through non-conducting barriers. Therefore, if this method could be used to transfer information regarding capacitive change, then this would be a very simple method to measure loads. However, there are great disadvantages [84]. Firstly, besides desired sensor changes, the measured values depend on distance and alignment of the sensor- and reader coil (Figure C.1) [85, 86]. The coupling error can be reduced to 1 to 8.8% of full scale per millimetre [87, 88], however a medial unicompartmental knee bearing under load bearing conditions moves between 4 to 8.5 mm in the sagittal plane [27], resulting in a theoretical full scale error of 4 to 74%.

Secondly, non-conducting [86] (Figure 2.2), and conducting materials influence coupling and parasitic capacitance [89, 90]. See Appendix C for a table of common *in vivo* dielectric constants.

Thirdly, metallic components closer than 10 mm to one of the coils make precise readout impossible [86, 87], which applies here because the femoral component and

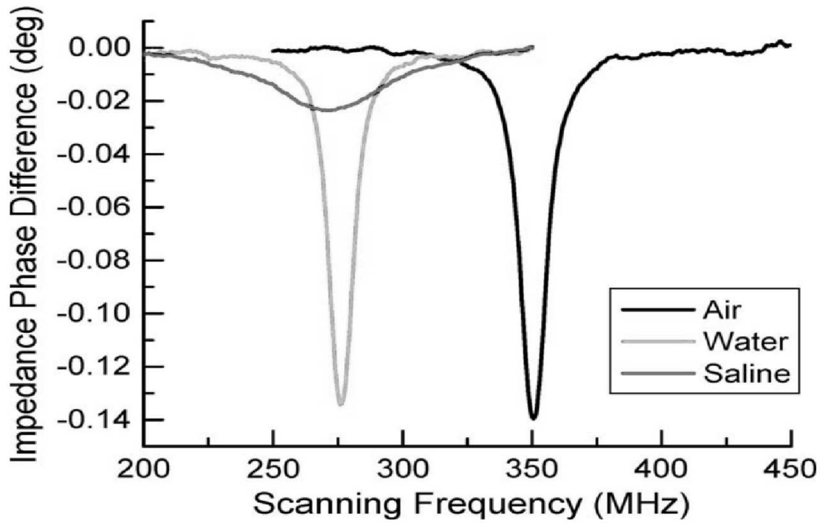

Figure 2.2: *Inductively coupled transponder voltage supply for different distances and materials, illustrating the effect of conducting transmission media on a resonating circuit [89].*

tibial tray are both made from metal.

Concluding: although inductive coupling would be a very straightforward method to measure capacitance change, the disadvantages do not make it a viable way of measuring capacitive sensor data, and an electronic measurement system will have to be used to measure and wirelessly send data. This system is further discussed in Chapter 7.

2.3.8 Conclusion Regarding Sensor Types

Several suitable sensor types were discussed. The magnetoresistive sensor, piezoresistive sensor, piezoelectric sensor are dismissed from further consideration. The strain gauge, resistive wire (Nitinol and Constantan), and capacitive sensors are are considered to be potentially usable. Following this section will be an analysis of the best location for a load sensor, and compression experiments with an actual bearing will then be used to make a choice for the best sensor in this application.

2.4 Bearing Strain Measurements

In order to find out how much strain there is within a bearing during compression, compression tests of a mobile UKR bearing were performed. The outcome of this experiment was a measure of how much strain was generated inside a bearing perpendicular to the long or vertical axis of the bearing.

A material under vertical load will expand in all perpendicular directions, in a ratio determined by the Poisson's ratio. Using a Poisson's ratio of 0.46 [81], and assuming that the bearing expands identically to a solid cube of UHMWPE, the perpendicular strain can be calculated by multiplying the vertical strain by the Poisson's ratio.

2.4.1 Method

Materials

Five 'large size 7 anatomically correct' UKR bearings (Biomet UK Ltd, Swindon, UK) were loaded under compression using a metal component with the same radius and width as a large femoral component (Biomet UK Ltd, Swindon, UK).

These bearings were not standard bearings; they were instrumented with capacitive sensors, identical to the ones used in Chapter 5. Compression took place with a Dartec DC10 servohydraulic test machine (Zwick Testing Machines Ltd, Leominster, UK), controlled by Tiab measurement software version SR2 v2.06.17 (TIAB Ltd, Middleton Cheney, UK).

Bearing thickness between the centre of the bearing concavity and the bottom of the bearing was measured using the internal linear voltage differential Transducer (LVDT) of the Dartec machine, full scale = 80 mm, resolution 0.001 mm, uncertainty ± 0.03 mm (Zwick Testing Machines Ltd), using a load of 10 N. Compression measurements were performed with a calibrated external LVDT: the Solartron AX/1/S LVDT, full scale = 2 mm, resolution = 5 μm (Solartron Metrology, Bognor Regis, UK) (see calibration test in Appendix A).

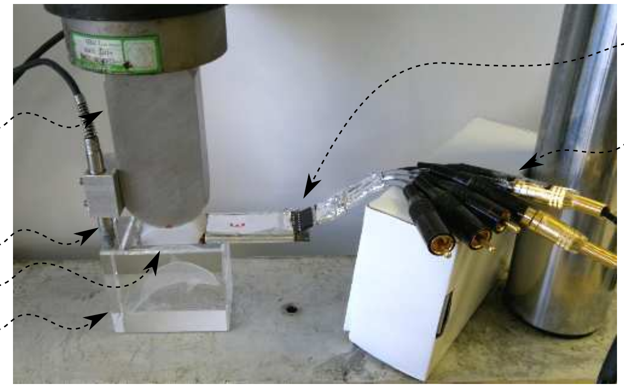

Figure 2.3: *Close up of the instrumented bearing loaded with the with the femoral component, the LVDT compression sensor, the glass base, the miniature connector to connect the C2D to the sensor, and the electrode connector, to connect to the correct electrode. The sensors and actuator are connected to a personal computer.*

Compression was measured and synchronised by the TIAB measurement system. A close up of the loading rig is shown in Figure 2.3.

Loading

The bearings were compressed with 1×BW or -392.5 N for 15 minutes, from now on referred to as "pre-loading". This was done because UHMWPE is a visco-elastic material and the viscous response takes up to 12 minutes to fully respond to a step change in loading (see Chapter 3). After 15 minutes, a gait signal was applied using the loading rig, the gait signal consisted out of three steps, and was repeated five times within one measurement. The gait signal was obtained from [42] (file name: k1l110108_1_80p_gait.akf), and normalised for an average patient (Figure 2.4a, see Figure 5.15 for the load signal and see Section 1.7 for more information about the definition of one BW), and then divided by two to get the loading for a single condyle. The gait signal applied had maximum load of 1.4 kN, or 3.67 BW. After each measurement, 15 minutes of non-loading was observed. The compression experiment was repeated 11 times, and experiments that had sudden jumps in the compression signal were excluded.

Data Processing

All data procesing was performed in MATLAB 8.2 (R2013b) (The Mathworks Inc, Natick, Massachusetts, USA). All data were measured at 100 Hz and the preloading LVDT data were smoothed in MATLAB, using a moving average filter (MOF) with coefficient of 100 samples. The dynamic load and LVDT data were smoothed using a MOF with a coefficient of 5. The minimum and maximum of the LVDT data were measured, and the span was calculated (the span is the difference between the minimum and maximum of the LVDT data).

Strain was calculated by dividing each compression signal of the LVDT by the thickness of each bearing. The Poisson's ratio was used to calculate the strains perpendicular to the strain in the long axis of the sample; the strains in the length of the sample were multiplied by a Young's Modulus of 0.46 to get the strains parallel to the bottom surface.

Given that impulses during loading may reach to 10×BW (see Chapter 1.9), the maximum impulse strains were calculated by dividing the measured maximum strains by the maximum load, and multiplying by the equivalent load at 10×BW, assuming a linear material response of UHMWPE up to 10×BW. It is unclear if UHMWPE responds linearly up to 10×BW, given that for higher stresses, the relative increase in strain reduces (see Figure 4.3). Therefore, in reality, the true strains of UHWMPE at 10×BW may be lower, and the current calculations result in a worst-case number.

Five types of strain were calculated:

1 The static strain
2 The difference between the maximum and minimum strain for gait loading
3 The estimated span for loading with 10×BW
4 The maximum total strain for dynamic loading
5 The maximum total strain for dynamic loading at 10×BW

The static strain is defined as the maximum strain measured after 15 minutes of loading. The difference between the maximum and minimum strain for gait loading (the 'span') will be used to calculate the estimated span for 10×BW. Differentiating between maximum static and dynamic strain is important because some sensors are more sensitive to dynamic strains in terms of reduction of life time of the sensor. The maximum strains are calculated by adding the maximum static strain and the maximum dynamic strains.

Calculation of the span: (Equation 2.3)

$$\epsilon_{span} = \epsilon_{dynamic,max} - \epsilon_{dynamic,min} \tag{2.3}$$

where:

ϵ_{span}	The difference between the maximum and minimum of the dynamic strain
$\epsilon_{dynamic,max}$	The maximum of the dynamic strain
$\epsilon_{dynamic,min}$	The minimum of the dynamic strain

Calculation of the span at 10×BW: (Equation 2.4)

$$\epsilon_{span,10\times BW} = \epsilon_{span} \times \frac{F_{10\times BW}}{F_{gait}} \tag{2.4}$$

where:

$\epsilon_{span,10\times BW}$	The difference between the maximum and minimum of the dynamic strain at $10 \times BW$
ϵ_{span}	The difference between the maximum and minimum of the dynamic strain
$F_{10\times BW}$	The maximum load at 10×BW.
F_{gait}	The maximum load during gait.

The maximum total strain for gait loading is calculated as follows:

$$\epsilon_{max} = max(\epsilon_{static}) + max(\epsilon_{dynamic}) \tag{2.5}$$

where:

ϵ_{max}	The maximum strain during gait
ϵ_{static}	The maximum static strain
$\epsilon_{dynamic}$	The maximum dynamic strain

The maximum total strain for 10×BW loading is calculated as follows:

$$\epsilon_{max,10\times BW} = \epsilon_{static} + max(\epsilon_{dynamic}) \times \frac{F_{10\times BW}}{F_{gait}} \tag{2.6}$$

where:

ϵ_{max}	The maximum strain during gait
ϵ_{static}	The maximum static strain
$\epsilon_{dynamic}$	The maximum dynamic strain
$F_{10\times BW}$	The maximum load at 10×BW.
F_{gait}	The maximum load during gait, 1.4 kN or 3.67×BW

For each of the calculated strains, the strain parallel to the bottom of the bearing was calculated:

$$\epsilon_{par} = \epsilon_x \times \nu \tag{2.7}$$

where:

ϵ_{par}	strain parallel to the bearing bottom
ϵ_x	uncorrected strain (i.e. $\epsilon static, \epsilon dynamic, \epsilon_{span}, \epsilon_{max}$)
ν	Poisson's ratio, 0.46

Given that the five bearings used had unknown radii, depending on the mismatch of the femoral component radius and the bearing concavity radius, the strains that were measured in this experiment may have been a factor two smaller than if a bearing with a larger radius were used (See Chapter 4.4.4).

Therefore all strains obtained in this experiment were multiplied by 2, and labelled "corrected strain" or $\epsilon corr$ (Equation 2.8).

$$\epsilon_{corr} = \epsilon_x \times 2 \tag{2.8}$$

where:

ϵ_{corr} corrected strain

ϵ_x uncorrected strain (i.e. $\epsilon static, \epsilon dynamic, \epsilon_{span}, \epsilon_{max}$)

2.4.2 Results

There were 36 suitable measurements (6 for sensor B, 8 for sensor G, 9 for sensor L, 3 for sensor O, 10 for sensor Q), other measurements were excluded because of intermittent jumps in the signal, attributed to the high sensitivity of the measurement equipment to cable movement. The bearing thickness ranged from 7.414 to 7.863 mm, average 7.661 mm. Measured pre-loading vertical strain at 15 minutes ϵ_{static} showed a minimum of 1.1×10^{-3}, a median of 2.1×10^{-3}, and a maximum of 4.4×10^{-3} (Figure 2.4b).

Dynamic strain span $\epsilon_{dynamic}$ ranged from 6×10^{-3} or 0.6% to 11×10^{-3} or 1.1%, with a median of 7×10^{-3} or 0.7%.

The maximum total strain ϵ_{max} was 10 or 1.0% during gait. The maximum total strain for 10×BW was 28 or 2.8%.

Parallel Plane Strains

The worst case correction results are shown in Table 2.1, in the column "Uncorrected Strain".

Worst Case Correction

The worst case correction results are shown in Table 2.1, in the column "Corrected Strain".

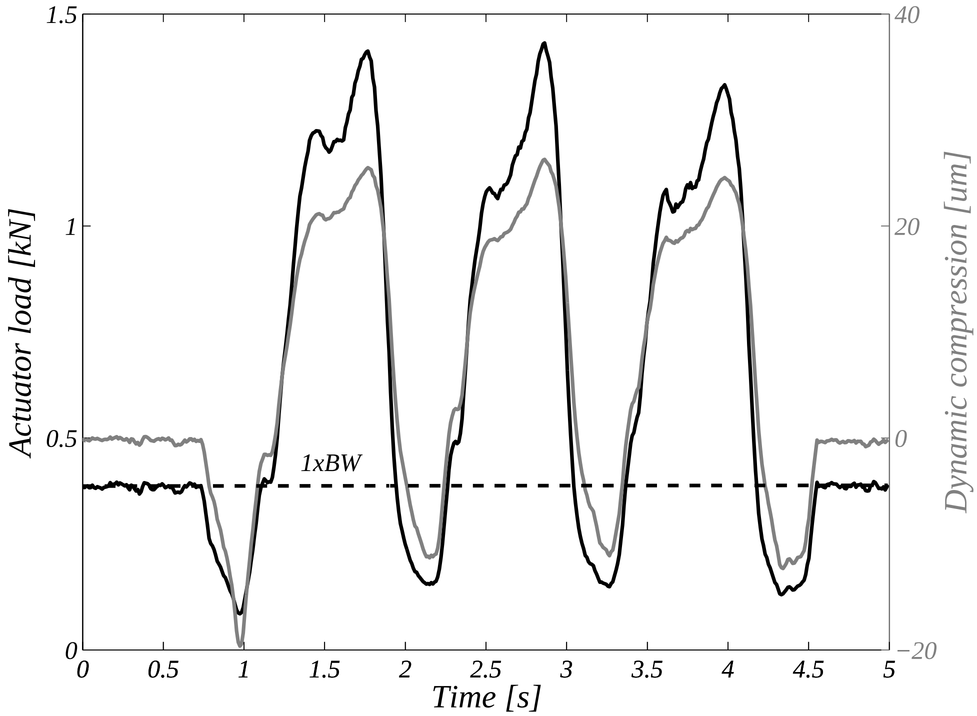

(a)

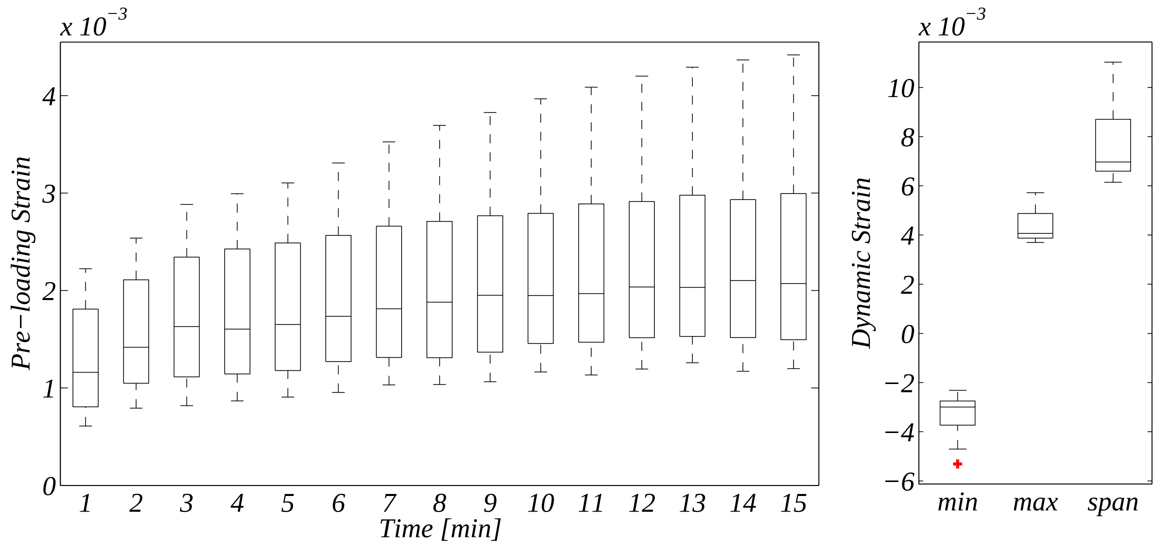

(b)

Figure 2.4: *Bearing compression measurement: (a) the gait signal (see Section 2.4.1) that was applied as a dynamic signal, with 1×BW depicted as a stippled line, and a typical example of the resulting dynamic bearing compression (LVDT measurement). (b) (left) Bearing strain during pre-loading with 1×BW or -390 N for 15 minutes and (right) the minimum and maximum strain, and the span (difference between max and min) of the dynamic signal.*

	Uncorrected ϵ [%]	**Corrected** ϵ [%]
perpendicular static ϵ, ϵ_{static}	0.44	0.88
perpendicular dyn. ϵ span, 3.67×BW, ϵ_{span}	1.1	2.2
perpendicular dyn. ϵ span, 10×BW, $\epsilon_{span,10\times BW}$	3.0	6.0
perpendicular max ϵ, 3.67×BW, ϵ_{max}	1.0	2.1
perpendicular max ϵ, 10×BW, $\epsilon_{max,10\times BW}$	2.8	5.6
parallel static ϵ	0.20	0.40
parallel dynamic ϵ, 3.67×BW	0.51	1.0
parallel dynamic ϵ, 10×BW	1.4	2.8
parallel max ϵ, 3.67×BW	0.46	0.92
parallel max ϵ, 10×BW	1.3	2.6

Table 2.1: *The uncorrected and corrected strain (ϵ) measurement results. The perpendicular strains are the maximum results from the bearing compression measurements. The parallel strains were estimated from the perpendicular strains using the Poisson's ratio. The corrected strains are calculated by multiplying the uncorrected strains by two. The correction factor 2 was obtained from Chapter 4 and depends on the uncertainty of the ratio of the femoral component radius to the bearing concavity radius due to manufacturing tolerances.*

2.4.3 Discussion

This experiment was performed to measure the typical vertical strain in a mobile UKR bearing, for the purpose of estimating how much strain a load measurement sensor may experience. At the end of the experiment, the trend of the strain was nearly flat, however the maximum strain level was still increasing. Therefore, the maximum strain should be taken with some reserve, in order to allow for additional strain increase. Additionally, given the large effect of the radius of the femoral component to the bearing concavity radius, in order to be absolutely safe in the estimations, a correcting multiplication factor of 2 was applied to all results. With the results of this section, all following sensor types could be analysed for suitability; if they cannot withstand these strains they should not be used. These bearings had capacitive sensors embedded. These sensors were made from polyimide, which has an elastic modulus which is approximately 2 to 3× larger than that of UHMWPE, and therefore may have partially restrained the perpendicular expansion of the bearing. Therefore, for the purpose of determining the minimum strain that all the sensors have to survive, the results of this section should be taken as the absolute minimum.

Referring back to Section 2.3.8, three types of sensor were identified as being suitable for measuring loads. With the strains identified in this section, each sensor is considered again.

There is no evidence that the capacitive sensor cannot cope with the strains that were measured here, given that the layer under compression is polyimide.

Strain gauges made of constantan have a very limited life span if the experienced strains are too high. The fatigue life of constantan is 10^5 cycles at $\pm 1.8 \times 10^{-3}\ \epsilon$ [65]. Therefore, both the perpendicular and parallel strains are too high to measure with this type of sensor. Since resistive wires are made of the same material, this also applies to constantan wire. Even for Nitinol wire, the dynamic strains are too high (parallel dynamic strain >0.4, compare Section 2.3.5 with Table 2.1). To demonstrate beyond a doubt that resistive wire cannot withstand the strains experienced in the bearing, an experiment with resistive wire was performed.

2.5 Resistive Wire Strain Experiment

To confirm that resistive wire would fail prematurely, a strain experiment was performed with one bearing and a constantan wire.

2.5.1 Method

A constantan wire was wrapped five times around a large size 6 anatomically correct bearing (Biomet). The wire (type RW80) was obtained from Alloy Wire International (Brierley Hill, UK). The diameter of the wire was 254 μm, and the specific resistance was 2140 Ω/m. The wire was secured with cyanoacrylate glue, parallel to the bottom surface of the bearing, 2 mm above the ground plane of the bearing. The wire was not

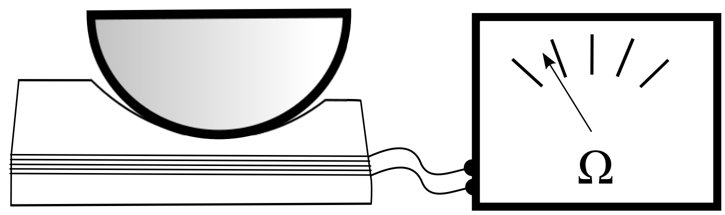

Figure 2.5: *Schematic representation of the resistive wire surrounding the circumference of the bearing, measured by a resistance (Ω) meter.*

pretensioned. The identical loading setup was used as in Section 2.4.1. The maximum load experienced with 10×BW is approximately 3.87 kN, however, as mentioned before, depending on the ratio of the bearing concavity radius in respect to the femoral component radius, the compression of the bearing may change by a factor of two. To compensate for that, the maximum load of 3.87 kN was multiplied by 2 to be absolutely sure that the bearing indeed underwent the maximum compression possible. The bearing was loaded in increasing and decreasing loads of 1, 2, 4 and 8 kN for 5 seconds per step. The resistance was measured using the Universal Transducer Interface board by Smartec (Smartec BV, Breda, the Netherlands). The data were analysed in MATLAB.

2.5.2 Results

The maximum resistance change was 1.3 %. The resistance before the measurement was 1.25 kΩ. After four loading cycles with 8 kN, after 217 seconds, the wire fractured in two places (Figure 2.6). Therefore, the resistive wire is not useful for this project.

2.5.3 Discussion

Four and especially eight kN is an enormous load for a UKR bearing, and would only very occasionally be experienced by a bearing, but this test was intended to be a worst-case study. In this study, the wire broke within minutes. Therefore, a resistive wire should not be used to measure loads in the UKR bearing, given that it must be able to withstand millions of cycles. Additionally, the strains are larger than those that strain

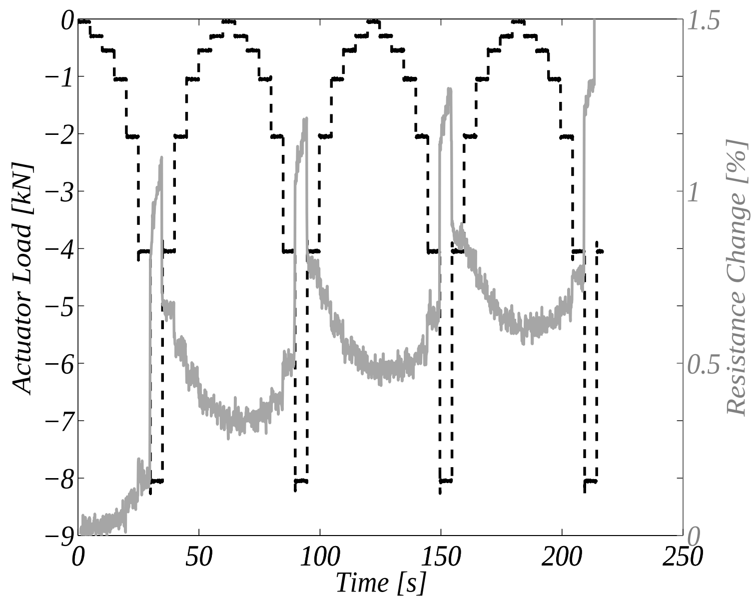

Figure 2.6: *Compression test results, measured with three loops of 254 μm thick constantan wire around the middle of the bearing, secured with glue, parallel to the bottom surface of the bearing. At t=217 seconds the wire broke, as can be seen by the sudden increase in resistance.*

gauges can withstand.

2.6 Conclusion

The aim of this chapter was to choose a suitable sensor type to measure load.

The most important requirement of load measurement within the UKR bearing is that bearing function is not impeded, for instance through wear or cracking, or changing the elastic behaviour. Therefore, sensors that have a high elastic modulus compared to UHMWPE have a high risk of damaging UHMWPE, and should not be used. This reduces the options of sensors to flexible or compliant sensors, such as foil sensors (piezoresistive, piezoelectric, capacitive, strain gauges, resistive wire). Another important requirement of load measurement is life span of the sensor and repeatability of data gathered with the sensor. The most important factor that determines the life span of a sensor is the maximum strain that is experienced by the sensor. Piezoresistive and piezoelectric foil sensors suffer from poor repeatability and accuracy or limited life span. Measurements have been performed to measure maximum static and dynamic strain for gait, a common loading condition. The results show that the strains within the bearing are too high for strain gauges, constantan wire, and nitinol wire. To be absolutely certain that resistive wire is not a suitable sensor for measuring load, a loading experiment was performed which confirmed that the strains of the bearing are too high.

There were several reasons, that capacitive foil sensors were chosen as the sensor type in this project. There was no reason to suspect the continuous strains will damage the sensor or that the sensor will damage the bearing; A capacitive sensor has an approximately inversely linear relationship between compression of the sensor and output value. Finally, a capacitive sensor can be made small and in any shape desired.

Finally, inductive sensing should not be used as a method to measure capacitance change, instead an electronic system must be used to measure and transmit the information from within the bearing.

3 Material Properties of UHMWPE

3.1 Introduction

The aim of this project is to investigate how to measure load *in vivo*. It is not possible to directly measure force (or load), but it is possible to measure the effect of a force on a deformable body. Thus by measuring deformation of the bearing, the applied load across a knee replacement may be estimated (a sensor of which the output is measured under influence of loading to estimate the load that was applied is therefore often called a load sensor). This requires the load/deformation relationship to be repeatable. In order to use the deformation to load relationship to estimate load the material properties of the bearing must be known and stable. If a sensor that is used to measure deformation is embedded within a material under load, then the material in which it is embedded influences the localised load acting on the sensor material. In that case, not only the surrounding material characteristics, but also the geometry of the surrounding material influences the load/deformation relationship. This is discussed in Chapter 4.

The sensor will be embedded in the UKR bearing material. The bearing is made from Ultra High Molecular Weight Polyethylene (UHMWPE). In this chapter, first the background of UHMWPE will be discussed, followed by a discussion of external factors that influence the elastic behaviour of UHMWPE under load. Because the compression of UHMWPE is directly related to the load through the elastic modulus or the stiffness, load measurement by measuring compression is directly influenced by changes in stiffness. Ideally, the elasticity of a material is identical for loading and unloading, but this is not the case for UHMWPE; it displays hysteresis. An experiment was performed to determine the magnitude of the hysteresis during repeated loading. Temperature increase decreases the stiffness of UHMWPE, and the knee experiences temperature changes. Therefore, temperature directly influences the magnitude of the sensor output under influence of load changes.

Another important property of the elastic behaviour of UHMWPE is that it is visco-elastic. On a very short time scale (<1s) it behaves linearly elastically, whereas on a longer time scale (>seconds) it behaves like a viscous substance. Linear elasticity is very simple to model, and displays highly repeatable behaviour. Since during activity, usual loading occurs with a static component (i.e. standing), and a dynamic component with a relatively high frequency in respect to the static average load (i.e. gait, see Figure 1.7), it is vitally important to know within what time range the viscous part acts.

To illustrate this: in Chapter 5 a method is discussed in which loads can be estimated from capacitive measurement data, as long as the average load is unchanging. However, at the transition between two activities, for instance going from sitting to gait, the average load changes. The viscous response to change in average loading change occurs within a certain time. Before reaching the end of this response time, both viscous and elastic responses to quick changes occur simultaneously, and loads estimated from capacitance changes within this time period will therefore have an error if they are based on linear response only.

Creep experiments were performed to determine after how much time the viscous behaviour stabilises and can be ignored. If viscous behaviour can be ignored, once a static load has been applied for a sufficiently long time, any dynamic loading around a mean load will only result in a linear elastic response.

3.2 Aims

The following aims have been set for this chapter:

1 Present a literature review on the background of UHMWPE.

2 Present a literature review on elastic behaviour.

3 Determine the influence of temperature change on the elastic modulus.

4 Determine the influence of stimulation frequency on the elastic modulus.

5 Determine the hysteresis behaviour of UHMWPE.

6 Determine after how much time the viscous behaviour can be ignored in the case of a constant static and changing dynamic load.

3.3 Background of UHMWPE

This chapter discusses the material properties of the UKR bearing, which is made from Ultra High Molecular Weight Polyethylene (UHMWPE), a polymer. The generic chemical formula for polyethylene is -$(C_2H_4)_n$-, where n is the degree of polymerisation, which are in excess of 200,000 ethylene monomer repeat units in UHMWPE. Compared to the lower density polyethylene types, UHMWPE has superior ultimate strength and impact strength, and is significantly more abrasion and wear resistant, important properties for clinical applications. The molecular chain of UHMWPE can be visualised as a very long tangled string of spaghetti. The chain can consist of several orientations; amorphous regions, in which the chain is tangled in a disordered manner; and crystalline regions, in which the chain is folded in an ordered structure with lamellae, a regularly folded section. When the folecular weight of polyethylene increases above 500,000 g/mol, such as is the case for UHMWPE, the entanglement of the immense polymer chains prevents it from flowing. The polymerisation of UHMWPE was commercialised by Ruhrchemie AG, based in Germany, during the 1950s. Ruhrchemie is still referred to in the denomination GUR which is part of the name of many types of UHWMPE, standing for granular UHMWPE Ruhrchemie, such as in the commonly used GUR4150 in the orthopaedic industry. The main ingredients for the polymerisation are ethylene, hydrogen, and a catalyst, and the resulting material is UHMWPE powder. UHMWPE products are usually produced by machining from ram extruded bar stock, or compression moulding techniques. In direct compression moulding, the polyethylene powder is placed into individual moulds to create components. This technique has the advantage that an extremely smooth surface finish is possible, with a complete absence of machining marks. Additionally, investigations of UHMWPE morphology suggest that compression moulded material has an isotropic crystalline orientation, whereas in ram extruded UHMWPE the morphology varies slightly as a function of the distance from the centre line. Similarly, crack propagation in moulded UHMWPE is found to be more isotropic compared to extruded and thereafter machined UHMWPE. UHMWPE has been widely used in knee replacement components since the late 1960s, initially only resurfacing the individual condyles of the femur and the tibia. The first TKR and UKR implants were developed in the 1970s [81].

The literature contains a large number of reports on material tests of UHMWPE, however the majority are concerned with failure criteria such as yield strength and strain, and fatigue [91–96]. For orthopaedic use *in vivo*, it is assumed that the yield stress is not exceeded, although there are reports that exceeding of the yield stress has led to pitting and delamination [97]. However, the latter is not the focus of this thesis. Furthermore, in many regular UHMWPE stress-strain investigations, the relaxation or creep behaviour of UHMWPE is ignored, and those parameters are very important for this work. This means that parameters obtained with monotonically increasing or yield exceeding tests do not provide the relevant information about the mechanical behaviour (relaxation/creep) during normal use *in vivo* [98]. Additionally, there are many types of UHMWPE, which may have dissimilar characteristics. Therefore, as part of the work of this thesis, specific tests were performed to measure these parameters. First the theoretical aspects of stress/strain and temperature effects are discussed before the experimental methods are described.

3.4 Theory Elastic Behaviour

3.4.1 Stress-Strain Behaviour

For repeatable force-deformation behaviour, it is necessary to define environmental conditions under which the UHMWPE is used; although a polymer has a complex stress-strain relationship with creep and nonlinear characteristics, it is possible to define specific conditions under which the force-deformation characteristics are repeatable.

Most materials behave elastically or approximately elastically under small stresses. Purely elastic materials reverse back to their original state (length, width, depth) after a load is removed, provided that the load is (well) below the *yield stress*, the stress magnitude below which a material changes from elastic to plastic behaviour. For plastics, the yield stress is not a fixed value but rather a trajectory. After plastic deformation, the material does not fully return to the original state. In some materials, the strain continues to increase for a short period after the load is fully applied and then remains constant under that load, but a permanent strain remains after removal of the load. This strain is called the plastic strain [99]. Some materials exhibit elastic behaviour provided that loading is sufficiently rapid, but then show a slow and continuous increase of strain at a decreasing rate. After removal of the stress, a continuously decreasing strain follows an initial rapid elastic recovery. In such materials the stress or strain rate influences the final strain, and these materials are also called time-dependent materials.

Time dependent behaviour of materials under a quasi-static state is mostly studied by means of three types of experiment; creep (including recovery thereafter); stress relaxation, and constant rate stressing or straining. Creep is a slow continuous deformation of a material under constant stress, but may be described in three stages; *primary creep* occurs at a decreasing rate, followed by *secondary creep*, which occurs at a nearly constant rate, and occasionally a *tertiary creep* stage can be observed, which occurs at an increasing rate, terminating in fracture. After removal of the load, the elastic strain portion will be recovered rapidly, followed by a continuously decreasing creep strain rate. If left unloaded for long enough, some plastic materials may recover fully to their original state. Analogous to creep there is also relaxation; these are two similar yet distinct mechanisms. Creep is an increase in strain under constant stress, and relaxation is a decrease in stress under constant strain. Creep and relaxation may happen simultaneously under combined loading.

Linear viscoelastic materials are materials for which the superposition principle holds; two arbitrary additive loads result in the sum of the loads, provided that the loads are not too large. For increasingly large loads, the material may start behaving elastically but nonlinearly, and loads that exceed the yield stress exhibit plastic behaviour. However, under loads occurring for a very short time, many plastics behave linearly even at stresses at which normally considerable nonlinearity occurs. [99].

3.4.2 Stress-Strain Behaviour UHMWPE

UHMWPE exhibits viscoelastic properties. The tensile yield strength of UHMWPE lies between 21-28 MPa [81]. When UHMWPE undergoes cyclic loading, the material can soften [93, 98, 100], (Figure 3.1a), or can harden [94]. Depending on the amount of stress that is applied (Figure 3.1b); for higher maximum stress, the secondary creep curve tends to decrease more than with lower stresses, and this effect is more pronounced with increasingly radiated UHMWPE [94].

Standard material tests are performed with “dog bone” geometry according to ASTM D638-01, ASTM D638-03 or its equivalent ISO 527-1 [92–94, 101], but with a small specimen size, the risk of buckling is too great, and cylindrical samples of various dimensions are used [91, 96, 98, 100, 102–108].

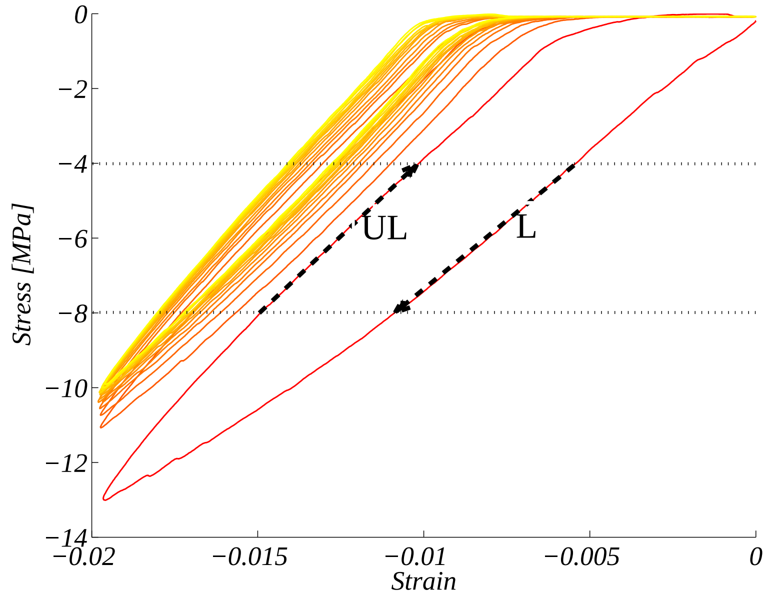

(a)

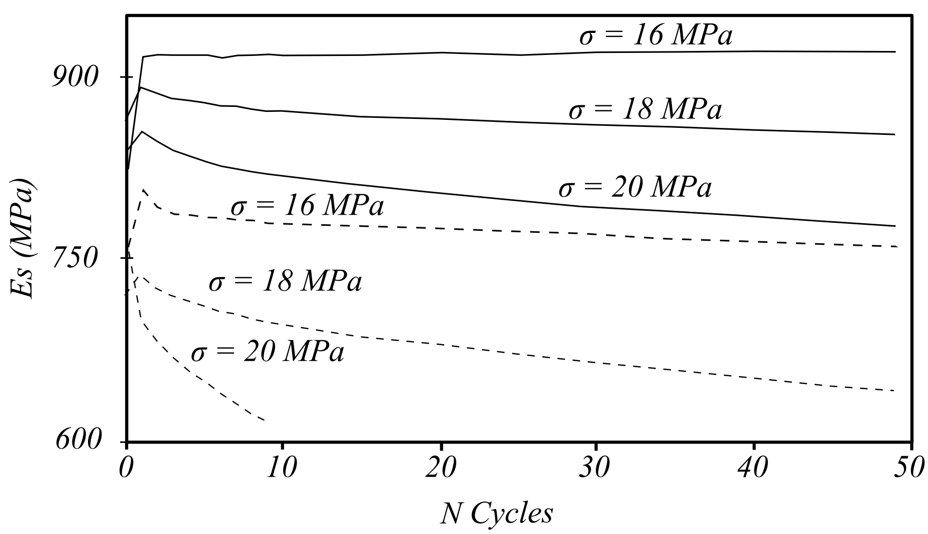

(b)

Figure 3.1: *(a) A typical result from a stress-strain experiment, with loading (L) and unloading (UL), performed as part of this work. As the experiment progresses, the curve is coloured lighter. This figure shows that the hysteresis becomes smaller over time, and that the material becomes stiffer, noticeable by the steeper slope between 4 and 8 MPa. (b) Immediate elastic modulus per cycle for three stress levels calculated at 1% strain versus cycles obtained in short-term tests for nonirradiated specimens (dotted line) and specimens radiated at 150 (∗) kGy (solid line). For loading stress (16-20 MPa) closer to the yield stress of approximately 20 MPa the curves show a decrease in stiffness Es. Adapted from [94].*

3.4.3 Frequency Effects

Under influence of increasing frequency, the elastic modulus of UHMWPE changes. For GUR405 an increase in frequency from 1 to 10 Hz will result in an elastic modulus increase of 10 % [109]. No data was found for GUR1050, the material of the Oxford unicompartmental bearing. Therefore experiments will have to be performed to measure the magnitude of stimulation frequency on the elastic modulus. The physiological frequency was determined to be zero to five Hertz (see Section 1.7). As a safety margin, frequencies up to 10 Hz will be measured.

3.4.4 Temperature Effects

The magnitude of the elastic modulus E of UHMWPE is dependent upon temperature [93, 104]. Published values for GUR1050 could not be found in the literature, whilst values for GUR405 have been published. Both materials are assumed to have similar characteristics. E decreases with increasing temperature at a rate of approximately -10 MPa/°C for GUR405 [109]. The elastic modulus for GUR1050, the base material that was used in the experiments described in this chapter is around 800 MPa at 24°C, depending on the irradiation dose [94]. The main reason for temperature change of a knee replacement bearing is friction due to motion against other components and mechanical loading. In case of mechanical loading, a hysteresis loop upon loading/unloading results in plastic work ($\triangle W_p$), which can be described by Equation 3.1. Part of the plastic work is dissipated in form of heat, while the rest of the work results in a reorientation of the molecular chains within the UHMWPE [110].

$$\triangle W_p = \oint (\sigma) \ d\epsilon_p \tag{3.1}$$

where:

$\triangle W_p$	plastic work done per cycle, the integral of all stress integrated over strain
σ	stress along the path
ϵ_p	accumulated plastic strain

In a UKR joint, the temperature of the synovial fluid increases by at least 3°C during moderate activity [111]. As much as half of the increase occurs during the first 6 minutes of walking [112, 113]. Reliable *in vivo* maximum temperatures for UKR are not available, but the maximum reported temperature increase for metal on UHMWPE hip implants is 10°C [112–115].

Ambient temperature also influences joint temperature. An ambient temperature of -3°C can lower the intra-articular temperature of a normal knee by as much as 3.6°C during activity [116].

Finally, body temperature may change due to inflammation. The skin temperature after a TKR operation rises from approximately 33.5°C preoperatively, to 36.5°C 2 weeks post-operation, and drops to about 35°C after 26 weeks [117–119].

Summarising, the most extreme temperature values found in literature range from -3.6 to 37°C, therefore, the temperature *in vivo* (henceforth called Body Temperature Range or BTR) is expected to lie between 33 and 47°C.

3.5 Methods

3.5.1 UHMWPE Specimens

Newly manufactured unicompartmental UHMWPE bearings in various sizes were obtained from an orthopaedic implant manufacturer (Biomet UK Ltd, Swindon, UK). Importantly, these samples had undergone all the processing that implanted components receive. The UHMWPE base material was GUR1050. From these bearings, samples were manufactured. Because of physical constraints imposed by the size of a bearing from which the material was salvaged, 10×15 mm (D×H) cylindrical samples were machined, identical to the size in other studies [91, 107, 120].

3.5.2 Compression Test Materials

Uniaxial compression tests were performed on a Dartec DC10 material testing machine (Zwick Testing Machines Ltd, Leominster, UK), controlled by TIAB measurement and control software version SR2 v2.06.17 (TIAB Ltd, Middleton Cheney, UK). Compression measurements were performed with a calibrated Solartron AX/1/S Linear Voltage Differential Transducer, with a full range of 2 mm, and a resolution of 5 μm, (Solartron Metrology, Bognor Regis, UK) (see calibration test in Appendix A), and room temperature was measured using a thermocouple thermometer (similar to SE002 Type K, Pico Tech, Eaton Socon, UK). Sample height was measured using the internal LVDT of the Dartec machine, with a full range of 80 mm, a resolution of 0.001 mm, and an uncertainty of $\pm$0.03 mm (Zwick Testing Machines Ltd). Load was measured using a DSCRCM-15KN load cell (Zwick Testing Machines Ltd), calibrated to a full range of 10 kN, and a resolution 0.5 N. All measurement data (load, temperature, compression) was measured and synchronised by the TIAB measurement system.

The loading rig can be seen in Figure 3.2.

3.5.3 Stress-Strain Behaviour UHMWPE

The measurement protocol was as follows: the sample was preloaded with 10 N in compression to get a stable initial height, then after 5 minutes the sample height was measured. Based on that, maximum compression in μm was calculated. Then a triangular load pattern with a strain rate of 0.01 ϵ/s was applied for 15 minutes, similar to [121], but to a maximum strain of 0.01 ϵ; earlier tests had shown that this

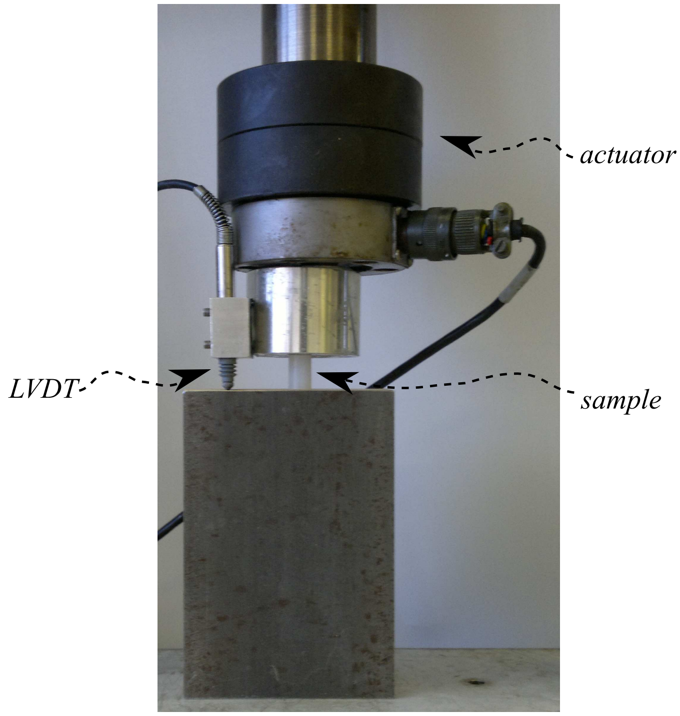

Figure 3.2: *A close up of the servohydraulic loading rig actuator (top), the LVDT compression sensor, the metal base, and the sample. The sensor and actuator are connected to a personal computer for measurement and control.*

strain magnitude corresponds to a stress level that remained well below the yield stress. Each test was repeated four times. Engineering stress and strain were calculated in MATLAB 8.2 (R2013b) (The Mathworks Inc, Natick, Massachusetts, USA). For every load and unload cycle, E was calculated by taking the tangent of the stress-strain curve between 4 and 8 MPa, a trajectory that consistently provided an approximately linear slope over all experiments.

3.5.4 Temperature and Frequency Tests

Further characterisation of the UHMWPE material was performed by the Oxford Silk Group, Department of Zoology, Oxford University. Dynamic Mechanical Analysis (DMA) was performed on a calibrated TA Q800 instrument (TA instruments, New Castle, DE, USA). A DMA applies a sinusoidal load to a specimen in a temperature controlled environment and measures resulting strain and phase differences. Five specimen bars with dimensions 36×6×2 mm, were machined for 3 point bending, and five specimen bars with dimensions 30×6×2 mm for tension tests and creep tests, because of clamping constraints, as per requirements of the test machine. Care was taken during machining to prevent heating of the UHMWPE. The DMA tests were done using their standard protocols and settings. The DMA provides storage modulus, which is often used to describe the immediate E. Single-cantilever clamps were used with a combined deformation of tension, bending and compression. The settings for temperature scan were from 0 to 70°C at 3°C/min at 1 Hz frequency and 0.1% dynamic strain. The creep test was performed from room temperature 27 to 70°C at 5°C temperature interval. Temperature was applied to the sample for 10 minutes. At the equilibrium of each temperature, 10 MPa of static stress was applied for 10 minutes, followed by a relaxing time of 30 minutes before the next temperature. Each resulting creep curve was normalised to 100% to focus on the time to reach the secondary creep stage, removing the effect of the temperature on the absolute value of the storage modulus, discussed in the previous paragraph. Then the difference in respect to the 36°C curve was calculated.

For the purpose of this chapter, "relatively constant" is defined as a maximum variation of 10% of the Elastic Modulus.

3.6 Results

3.6.1 Stress-Strain Curves

A loading test starts at zero stress and zero strain (top right corner of Figure 3.3a). For the first loading curve, the tangent fit for loading (L) and unloading (UL) is shown, between -4 MPa and -8 MPa of stress. The figure shows that UHMWPE had hysteresis behaviour; the slope for loading was different than for unloading. The hysteresis became smaller when the experiment progressed (Figure 3.3). The maximum stress for this experiment was -13 MPa, well below the yield stress for this material (21-28 MPa). The difference in Elastic Moduli for loading and unloading never exceeded 5%.

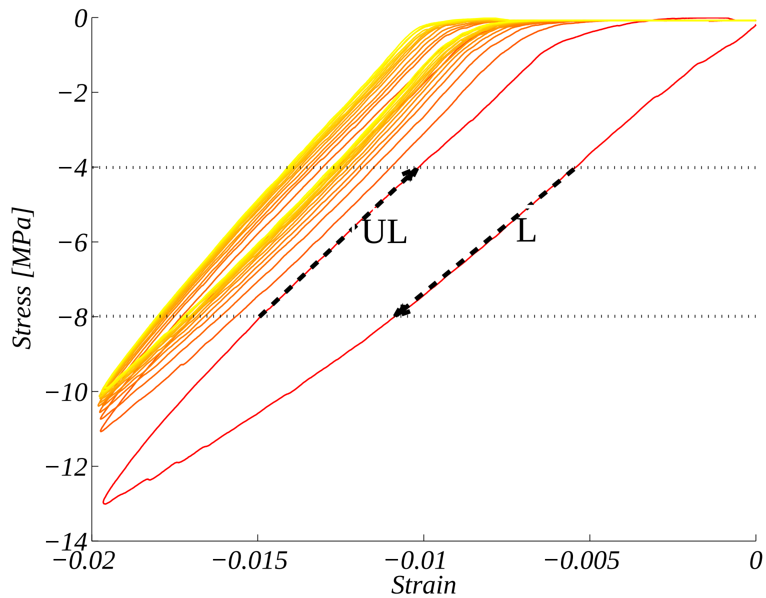

(a)

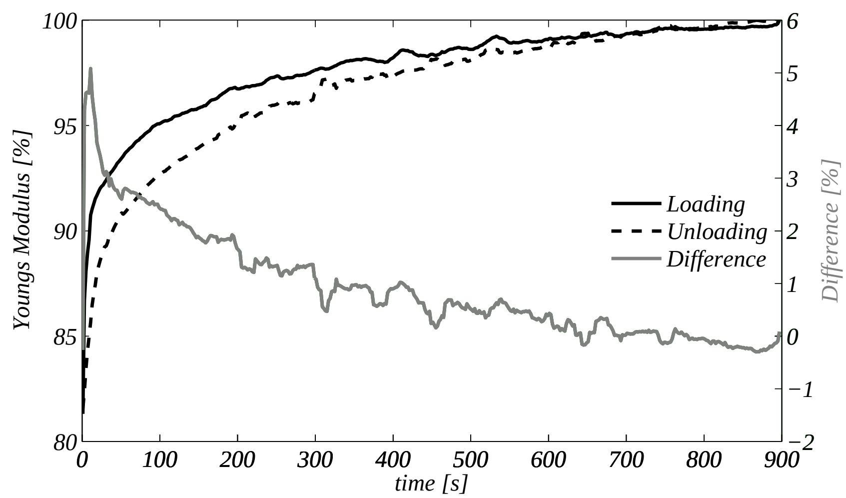

(b)

Figure 3.3: *(a) Loading (L) and unloading (UL) curves of UHMWPE for one sample (the curves are coloured lighter per minute). (b) Calculated Elastic Moduli for loading and unloading, averaged over all samples and tests. In (a), the -4 and -8 MPa lines depict the delineation of the region which was used for fitting a tangent to obtain E. As the experiment progresses, the hysteresis lessens and the tangents become steeper. Simultaneously, in (b) the slopes obtained with the tangent become larger, and the difference between the obtained E decreases as the experiment progresses.*

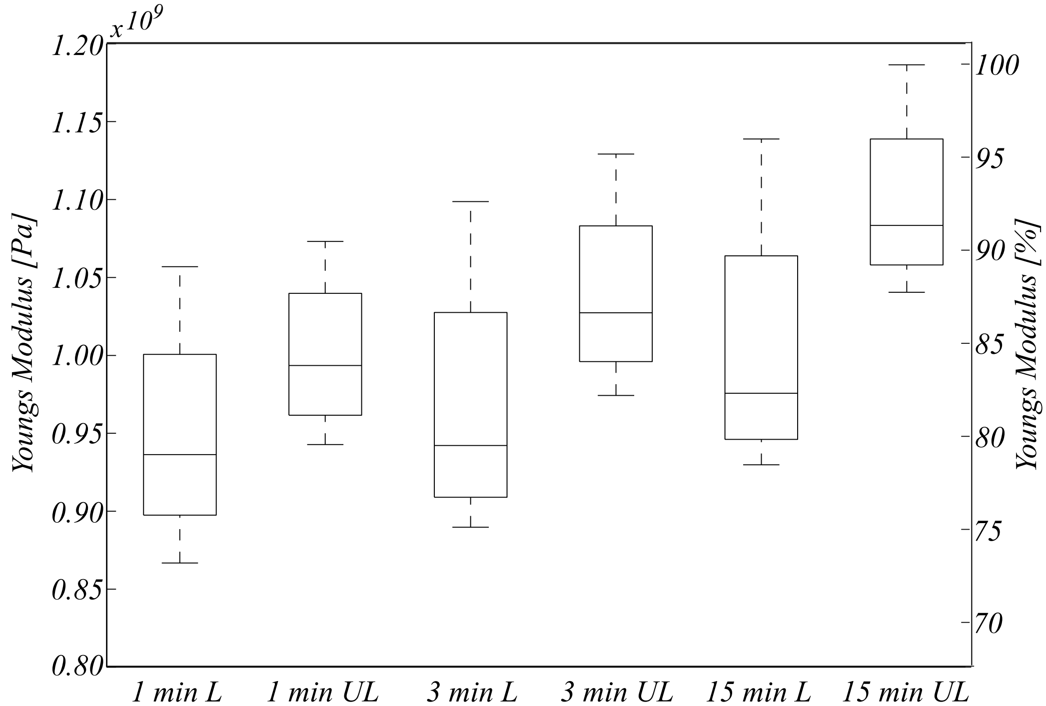

Figure 3.4: *Loading (L) and unloading (UL) distributions for all measurements. The right hand axis displays the identical Elastic modulus, but expressed in percentages.*

From Figure 3.3, three time points were selected for plotting using a box plot; after 1 minute, 3 minutes and 15 minutes (Figure 3.4, this plot is an average of four experiments, the first experiment showed significantly different results than the following tests, which was thought to occur during settling in of the UHMWPE at first time use). For the loading slope, but also the unloading slope, E increased during the experiment, exactly as seen in Figure 3.3b. The median of every loading E was lower than every median of unloading E. The increase in percentage of the median between 1 minute and 15 minutes was 4.0% for loading and 8.3% for unloading. In this experiment, Figures 3.3 and 3.4 indicate that after about 700 seconds or 12 minutes the hysteresis reached a state of reduced increase of E.

3.6.2 Frequency Effect on E

The stimulation frequency at a maximum stress of 10 MPa was varied from 1-10 Hz (Figure 3.5, and Table 3.1). Higher stimulation frequencies resulted in an increased E. The increase in E was not linear, but became less with increasing frequency.

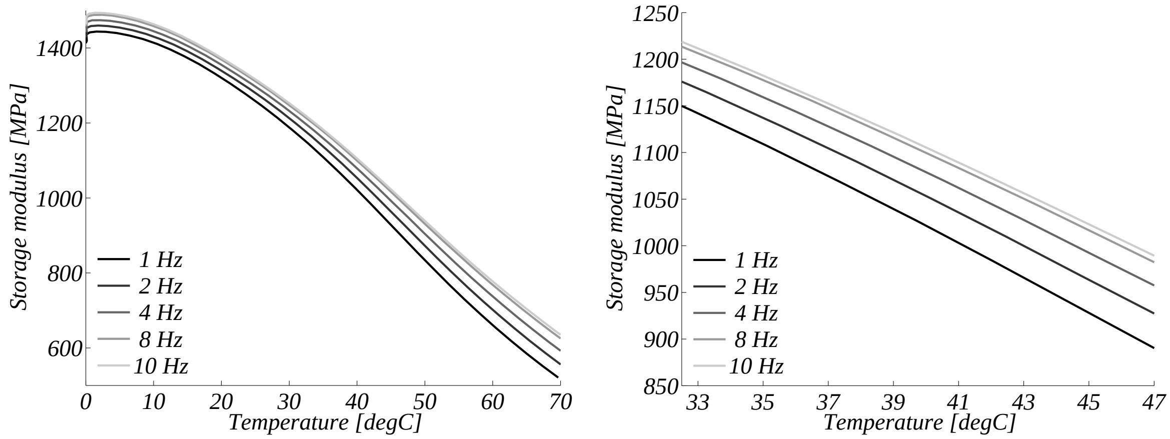

(a) (b)

Figure 3.5: *Storage modulus and tan Delta of UHMWPE (a) over the temperature range 0-70°C and (b) the Body Temperature Range of 33-47°C.*

	E [MPa]		E Change	E Change	E increase from 1Hz [%]	
	33°C	**47°C**	[%]	[%/°C]	**33°C**	**47°C**
1 Hz	1142	890	-22.0	-1.6	0	0
2 Hz	1169	927	-20.6	-1.5	2.3	4.2
4 Hz	1189	957	-19.5	-1.4	4.2	7.5
8 Hz	1206	982	-18.6	-1.3	5.6	10.3
10 Hz	1212	989	-18.3	-1.3	6.1	11.1

Table 3.1: *Storage modulus results at the limits of the Body Temperature Range for several loading frequencies. For all stimulation frequencies, the E changed more than 10% between 33 and 47°C. Furthermore, for 8 Hz and 10 Hz, at 47°C, E changed more than 10 %.*

3.6.3 Temperature Effects on E

This phase of the experiments focused on the temperature influence on the E of UHMWPE. In Figure 3.5 E is shown in overview and zoomed in on the defined body temperature range (BTR) between 33 and 47°C (Figure 3.5). In the BTR, the storage modulus (E) decreased monotonically. The results within the BTR are shown in Table 3.1. For all stimulation frequencies, the E changed more than 10% between 33 and 47°C. Furthermore, for 8 Hz and 10 Hz, at 47°C, E changed more than 10 %.

3.6.4 Temperature Effect on Creep

During the creep experiment, after every unloading cycle, there was a residual strain, from which a new loading cycle commenced (Figure 3.6a-b).

The normalised strain response (Figure 3.6c-d) shows more clearly that creep rate was influenced by temperature; the higher the temperature, the faster the strain reached its equilibrium plateau. For temperatures from 32°C to 41°C, the differences to the 36°C curve stayed within ± 2%, while for a temperature of 46°C, the change remained within 5 % (Figure 3.6e-f). The creep response occurred for the most part within the first seconds after removing the load, and then the rate of change reduced (Figure 3.6c-d). For loading around BTR, 90% of the end value was reached within 2.5 minutes, and at 95% after about 5 minutes. For unloading, these values were 4 minutes and 8 minutes. For higher temperatures, the strain change was quicker than for lower temperatures.

3.7 Discussion

3.7.1 Stress-Strain Behaviour UHMWPE

Relaxation

To date, no experiments have been published of loading and unloading below the yield stress that took long enough for relaxation to occur. The uni-axial compression test confirmed that UHMWPE shows viscoelastic behaviour and hysteresis (Figure 3.3, Figure 3.4).

The tangent to the E curve did not become constant in this test, as can also be seen in (Figure 3.3); even after 15 minutes of relaxation, the tangent to the Elastic Moduli was

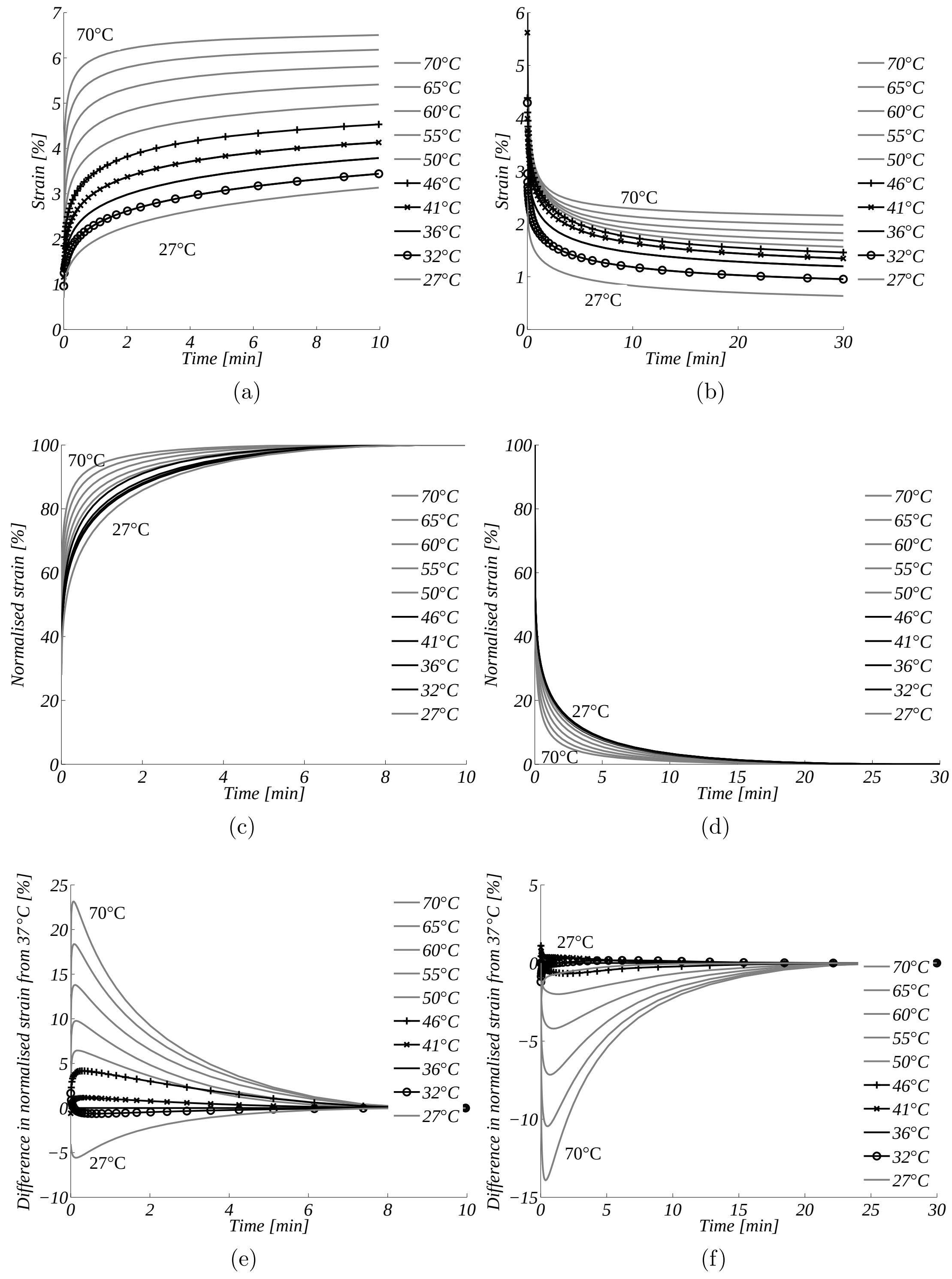

Figure 3.6: *Creep test loading: (a) storage modulus loading and (b) unloading, (c)-(d) normalised to maximum-minimum, and (e)-(f) difference in respect to the 36° C curve. In (c-d) is shown that for higher temperatures, UHMWPE changed quicker. In (e-f) is shown that within the BTR, all differences in respect to 36° C remained within 5%.*

still not horizontal. However, the change in E was very small, compared to the rapid change in the first 3 minutes. After about 300-400 seconds, the increase in E became approximately linear for both loading and unloading, indicating that even though the elastic moduli kept on increasing, a quasi-stable increasing state was reached.

This trend of increasing E can also be observed in Figure 3.4. After the experiment, E returned to lower values. If plastic strain were occurring, then the E values at the beginning of the experiment would not return to a lower magnitude, therefore, the yield stress was not exceeded in this test. Whether the secondary relaxation stage (analogous to secondary creep behaviour) resulted in a positive or negative slope was dependent on the stress that was applied to the material in respect to the yield stress; for lower maximum stress and UHMWPE with higher radiation doses (and thus a higher yield stress), the slope tended to be positive (Figure 3.1b). The data in the current experiment all showed positive slope; confirming that the maximum stress was indeed sufficiently below the yield stress.

Hysteresis

At the same time as creep behaviour could be observed in an ever slower increasing Elastic Modulus, it was also related to a hysteresis that became smaller over time, for the duration of the experiment. After unloading the sample for a sufficiently long time, the hysteresis returned to earlier values, as could also be observed from the lower E values at the beginning of the experiment (Figure 3.4). The stiffness during unloading was up to 10 % higher than during loading. This effect was similar to what others have found [107], which is to be expected, because it is inherent to the hysteresis. Hysteresis is an undesirable effect, because any dynamic load signal will experience different rates of compression and expansion, and therefore a load signal that is estimated using deformation with hysteresis will be distorted.

Magnitude of E

The Storage Moduli (E) from this study were higher than in the previous study that tested GUR1050 [94]. However that experiment was performed with tensile stress, and E obtained through a tensile test can be up to 22% lower than that obtained in a compressive test ([107]). Similar difference could be observed between the results of the current study and [94], depending after how much loading time the difference was observed. Also, the values that were obtained in the strain-controlled Figure 3.4 and DMA tests (Figure 3.5) were similar. Therefore, there is no reason to suspect that the values that were obtained in this study are incorrect.

DMA test: Frequency effect on Storage Modulus

An increased stimulation frequency resulted in an increased E. This effect remained smaller than 10% between 1 and 10 Hz for all frequencies and temperatures except at 46°C at 8 and 10 Hz. Therefore, temperature sensing and correction is still advisable. The change in E in response to an increase in frequency was a bit less compared to those obtained for GUR405 (+13.5 %) [109], but at a lower elastic modulus (which was almost twice as low in [109]). Given that a different UHMWPE was used, a better conclusion cannot be drawn.

How much influence the stimulation frequency has on deformation and therefore estimation of load based on deformation will be the subject of further measurements in Chapter 5.

DMA test: Creep

Similar to the results obtained for relaxation, the creep test showed a constantly increasing compression during the secondary relaxation stage (analogous to the secondary creep stage) for loading and constantly decreasing decompression during the secondary relaxation stage during unloading. After eight minutes, the tangent to the loading and unloading curve became approximately linear.

Limitations

In other studies, UHMWPE was forcably cooled to reduce or stabilise temperature rise because of dissipation of the UHMWPE [100, 104]. This was not done in this study, to simplify the experiment. However, in the current experiment, the UHMWPE samples were small, with therefore a relatively high contact surface with the surroundings, which was directly in contact above and below with solid metal parts of the hydraulic test machine, thereby providing an efficient temperature sink. Furthermore, the maximum stress and strain rate were very small (frequency similar to [94]), limiting the generation of heat, after the experiment the specimens were not noticeably warm. Therefore, the results in this study should not be much different from those that would be obtained in a temperature controlled study.

3.7.2 Temperature Effects on UHMWPE

DMA test: Temperature effect on the Storage Modulus

The temperature difference between 33°C and 47°C caused a decrease of 18-22%, well above the 10% that was set as a goal. However, the slope was linear, and therefore the temperature effect could be easily corrected by taking into account the data from a temperature sensor that measures the temperature change of the UHMWPE during measurements of deformation. The temperature difference was similar to that obtained for GUR405 (±20%) [109].

DMA test: Temperature effect on Creep

Within the approximate BTR, the differences to those at 37°C stayed within ± 5%, and therefore the temperature effect on the strain rate can be ignored for temperatures within the BTR.

Limitations

Although only one sample was used for this experiment, the results that were obtained are most likely representing a realistic trend. As Figure 3.4 shows, there was a lot of spread in values between samples, but the overall behaviour was similar. Therefore, it is not expected that more repeats with different samples (since this was a destructive test) would have resulted in a more accurate conclusion.

3.8 Conclusion

Given that UHMWPE is a viscoelastic material, the time constant of the viscous response was sought, as well as parameters that influence its elastic response, such as temperature changes, and loading frequency. A body temperature range (BTR) from 33 to 47 °C was identified which theoretically could be experienced by the bearing. Furthermore, a frequency loading range from zero to five Hz was identified in Chapter 1. Suitable data could not be found within the literature, and has now been obtained from several experiments.

Although temperature effects on creep can be ignored within the BTR, the effects on E can only be ignored if the temperature change is small; within the full BTR a temperature sensor should be used to correct for changes in E caused by temperature changes. *This answers aim 3: Determine the influence of temperature change on the elastic modulus.*

Stimulation frequency has influence on E, but only increases beyond 10% at temperatures above 47°C, and how much influence this poses on deformation of the bearing needs to be investigated more thoroughly using an instrumented bearing. *This answers aim 4: Determine the influence of stimulation frequency on the elastic modulus.*

For dynamically changing signals, hysteresis reached an intermittent stable state after about 700 seconds or 12 minutes. After that the hysteresis became smaller still, but it is unclear after how much time the final stable state, if any, is reached. *This* *answers aim 5: Determine the hysteresis behaviour of UHMWPE.*

At the same time, the relaxation reached a quasi-stable state, indicating that relaxation and hysteresis are closely coupled. When applying a constant load, the compression reached a stable state after 8 minutes; however one in which some compression still continues, albeit at a very slow rate. *This answers aim 6: Determine after how much time the viscous behaviour can be ignored in the case of a constant static and changing dynamic load.*

In summary:

It is absolutely vital to understand that the outcome of these experiments is that the viscous response to the application of a stable load reaches a quasi-stable state after about 12 minutes. After that time, both the hysteresis and creep response are suitably small to ignore for dynamic load measurements. This state could be achieved by having the person with a knee replacement walking or standing for at least 12 minutes before the measurement. Since UHMWPE is a viscoelastic material, thereafter faster changing signals can be applied, which are expected not to result in a viscous response.

Furthermore, a temperature sensor should be used to compensate for the influence of temperature on the elastic modulus.

4 Mechanical Modelling

4.1 Introduction

In the previous chapter, the mechanical behaviour of UHMPWE under load was measured. However, the mechanical properties alone do not determine the behaviour of an object under load; the distribution of material, i.e. the shape plays an important role too. In this chapter, the focus lies on modelling the deformation of the UKR bearing under load, and finding the optimal position for a capacitive load sensor. The capacitive sensor was simulated at various locations within the bearing, and the influence of changes in the geometry on the change in capacitance was investigated.

4.2 Aims

The following aims were set for the work described in this chapter:

1 Determine the optimal mesh size for the finite element models.

2 Determine which position of the load sensor results in the largest output signal.

3 Determine the influence of geometric properties on the output signal.

4 Determine the influence of temperature change on the output signal.

5 Determine the influence of wear on the output signal.

6 Determine the influence of embedding an electronic module into the bearing on the mechanical behaviour of the bearing and the sensor output.

4.3 Mesh Convergence Study

4.3.1 Introduction

In finite element modelling (FEM), mathematical models are created of physical objects. In FEM, each object is divided up into a finite number of smaller *elements*, such as tetrahedrons or cubes in three dimensional FEM, for which the loading equations are relatively easy to solve. The total of these solutions together form the solution

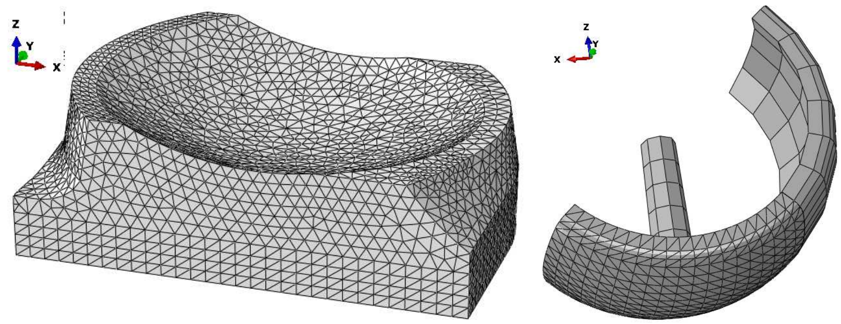

(a) (b)

Figure 4.1: *Mechanical model meshing illustration, not drawn to scale a) of the bearing, and b) of the femoral component.*

for the entire model. One application that FEM is often used for is simulation of the response of objects to loading, such as compression of the object.

The elements are linked together in a mesh. As the mesh is made finer, and more elements are created, the solution tends to become more accurate initially, and then converges to a stable solution. However, as the number of elements increases, so does the time it takes to solve the greater number of equations for the model. Therefore, in a mesh convergence study, the accuracy of the most important outcome is monitored as the mesh is made finer, and as soon as the model approaches the desired accuracy level, that mesh size will then used for modelling.

4.3.2 Method

A three dimensional finite element model of an instrumented bearing was created, based on the manufacturer's technical drawing of the Oxford UKR bearing, large, size 6, Phase 3, Bio-anatomically Correct (left side, Serial No# 159557, Biomet, Swindon, UK) and the accompanying large femoral component (Figure 4.1). The length of the bearing was approximately 36 mm, and the width approximately 24 mm. The distance from the bottom of the bearing to the lowest point of the bearing concavity was 6.5 mm. The radius of the femoral component was 25.63 mm, and the edge of the femur was rounded with a fillet radius of 2 mm.

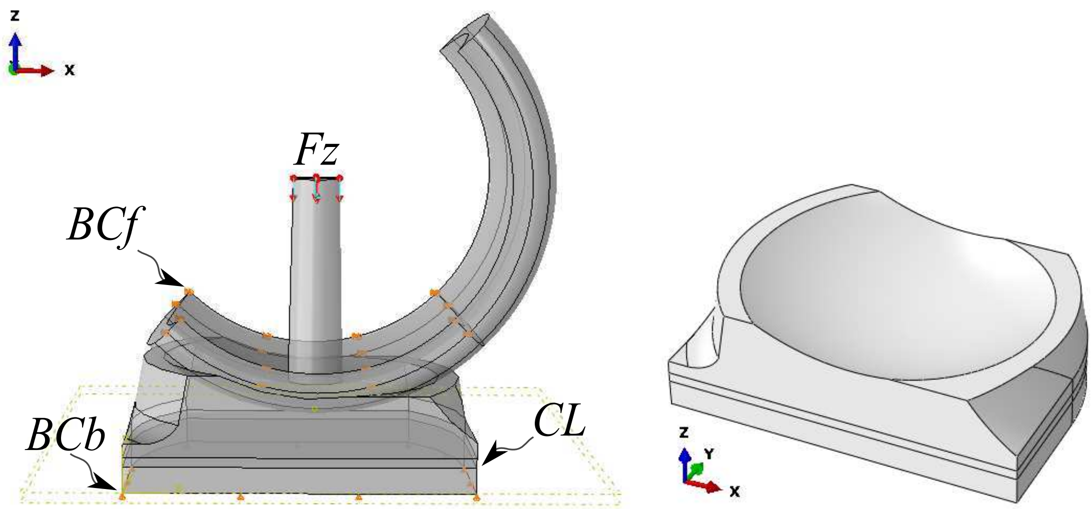

(a) (b)

Figure 4.2: *(a) Simulation setup with the femoral component on top, and the bearing at the bottom. The arrows represent compressive load (Fz), and the stippled lines represent the simulated capacitive layer (CL). The orange triangles represent boundary conditions (BC); the femoral component was constrained in the x and y direction (BCf), and the bottom of the bearing was constrained in the z direction (BCb). (b) The simulated bearing in more detail. Clearly the capacitive layer can be seen as two parallel lines parallel to the bottom surface of the bearing.*

Simulation Settings

The model was established and solved in Abaqus FEA 6.11 (Simulia, Rhode-Island, USA), and created using the python scripting language for Abaqus (Python version 2.6, Python Software Foundation, NH, USA). The femoral component and bearing were oriented corresponding to a knee in flexion (Figure 4.2). The femoral component was constrained in the X and Y direction only. The bearing component was constrained in the Z direction only. No rotational constraints were applied. One loading step was applied with a load of 3925 N (10×BW, see Section 1.8) in the Z direction. Loads were applied to the top of the peg of the femoral component. The explicit direct solver was used for solving the models. Each loading step was stabilised with a dissipated energy fraction of 0.0002, adaptive stabilising ratio 0.05, and correction for large geometry distortion. Contact was modelled using the 'general contact' method of Abaqus.

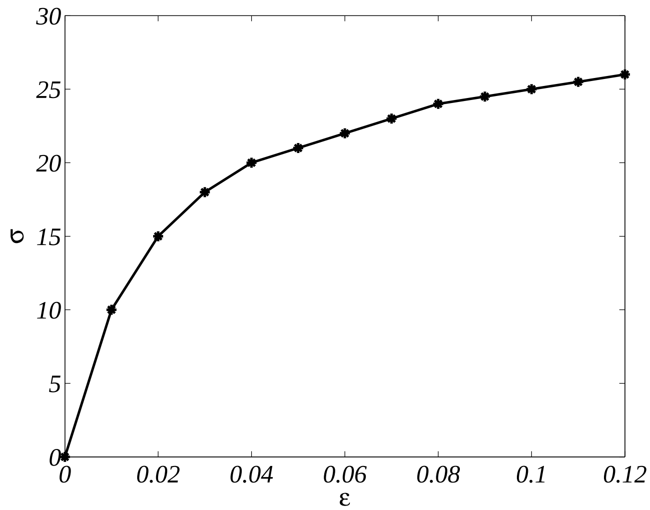

Figure 4.3: *Multilinear material model for UHWMWPE used in FEM, with stress (ϵ) and strain (σ) [107].*

Material Models

The mechanical response to load was simulated with a validated multi-linear model for GUR4150 (Figure 4.3) [107]. GUR4150 has approximately the same elastic modulus as GUR1050, the UHWMPE that is used for the Oxford UKR bearing. Although the behaviour of UHMWPE is more complex in reality (Chapter 3), a multi-linear model was chosen to represent the linear behaviour of UHMWPE, in order to achieve a compromise between realistic behaviour and computational time. For the femoral component, a linear elastic model was used with the properties of cobalt chrome steel; E = 200 GPa, with a Poisson's ratio of 0.3 [122, 123]. All materials were assumed to be homogeneous and isotropic.

Capacitive Layer

A capacitive layer was used to simulate a sensor within the bearing (Figure 4.2). The capacitive layer had a thickness of 1 mm and was centred at exactly half the thickness of a "size 6" bearing; 3.25 mm above the bottom plane of the bearing. The capacitive layer was divided into an array of capacitors with 100 sub-capacitors over the length of the bearing and 71 sub-capacitors over the width of the bearing. After the simulation, for every of the sub-capacitors, the thickness of the layer was stored to a file, which was then processed in MATLAB 8.2 (R2013b) (The Mathworks Inc, Natick, Massachusetts, USA). Capacitance was calculated by using Equation 2.2, with d (the distance between the electrodes) set to the thickness of the capacitive layer, and Δd set to the amount of compression of the capacitive layer.

Meshing

The bearing and the femoral component were meshed using the elements that were most applicable to their shape to minimize the computational time; the bearing was meshed with quadratic tetrahedrons (C3D10) (Figure 4.1); the femoral component was meshed with quadratic hexagonal elements for the part that did not experience direct compression (C3D20R), quadratic wedge-shaped elements for the peg (C3D15), and tetrahedral elements (C3D10) for the part that was under compression (the highlighted part in Figure 4.1). The bearing was meshed with tetrahedrons because they are most suitable to model complex shapes. A mesh refinement study was performed. The mesh size was varied for the bearing component and also for the femoral component. First a suitable mesh size was selected for the femoral component (2 mm), and then the bearing mesh size was varied from 0.1 to 1 mm in steps of 0.1 mm. The criteria for selecting the optimum size were: minimum capacitance change (of the entire transverse capacitance layer), maximum capacitance change, average capacitance change, and visual inspection of the plot of the final capacitance change plot. For the minimum, maximum, and mean, the outer five elements of the capacitive layer array were ignored, because limitations of FE modelling resulted in fringe effects at edges. Fringe effects express themselves in minute warping of the edge in a sinusoidal pattern of the edge of the layer. The best result of the bearing mesh variation results was picked (1 mm), and the femoral implant mesh size was varied from 0.1 mm to 2 mm. Prior tests showed that a larger femoral mesh size was found to introduce a mesh shaped indentation pattern into the top layer of the bearing, although this was not directly evident in the capacitive layer results.

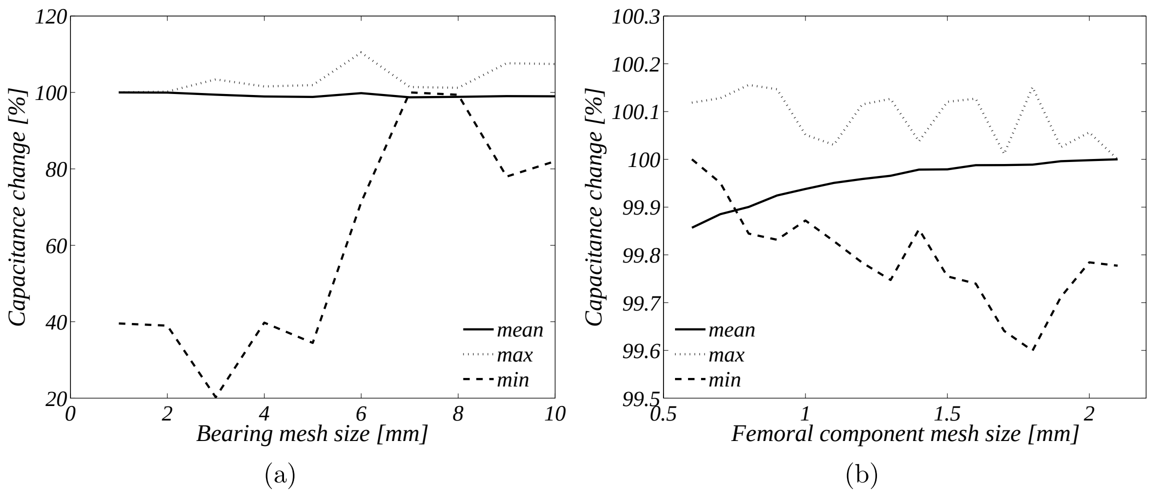

Figure 4.4: *Meshing convergence results on the minimum, mean and maximum of the entire transverse capacitance layer within the bearing, with a) results for the bearing mesh size, and b) results for the femoral component mesh size*

4.3.3 Results

The average time to solve a single compression problem was typically 11 minutes, using three cores on a quad core work station, running with a frequency of 2.86 GHz.

Bearing mesh size

As the mesh size refined, the minimum of all the elements of the capacitive layer diverged from the mean and maximum. Around a mesh size of 5 mm, the change became more constant, and it settled around 1 to 2 mm (Figure 4.4).

Femoral component mesh size

The changes in minimum, mean, and maximum capacitance of all the elements of the capacitive layer were much smaller for variations in the mesh size, compared to changing the mesh size of the bearing. Minimum, mean, and maximum were within 0.4 % of the mean.

The mean stabilised at an element size of approximately 2 mm.

4.3.4 Discussion

A typical change of the capacitance in the capacitive layer can be seen in Figure 4.5. As the minimum of the capacitance change should be close to zero, and the maximum should equal the top of the compression 'hill' (Figure 4.4), the minimum and maximum of the capacitance of all elements this layer should diverge, which was also observed when the mesh size became sufficiently small. Using a mesh size of 1 mm for the bearing, and 2 mm for the femoral component, a suitable convergence was achieved. Mesh size for the femoral component was found not to affect the outcome greatly, except for larger femoral mesh element sizes, therefore, a larger value was chosen to reduce computing time.

4.4 Parametric Model Study

4.4.1 Introduction

Each UKR is fabricated with certain tolerances, in addition wear can change its dimensions. Therefore the dimensions of the bearing were varied to investigate their influence on a capacitive sensor.

4.4.2 Method

The bearing was constructed identically to that used for the mesh convergence test. Unless specified otherwise, all models were run at a load of 1×BW (-392.5 N, see Chapter 1) and 10×BW (-3925 N), the femoral component radius was set at 25.53 mm, and the bearing radii between 25.73 and 26.43 mm were used, which represent the outer limits of the bearing radius tolerance. These tolerances were obtained from the datasheet of the manufacturer (serial N# 159557, Biomet).

The following parameters were investigated:

Bearing Concavity Radius

The femoral component articulates against the bearing inside the bearing concavity. The radius of the bearing concavity has a manufacturing tolerance of 25.73 to 26.43 mm, while the radius of the femoral component varied from 25.63 to 25.73 mm (datasheet serial N# 154602, Biomet). The influence of varying this radius on the contact area between the femoral component and the bearing was investigated, as well as the influence on simulated capacitance change. The load was varied from 1×BW to 10×BW in steps of 1 BW. In addition to calculating the compression of the bearing and the sensor, and the capacitance change, the contact area between the femoral component and the bearing was also determined.

Femoral Component Radius

The manufacturing tolerance of the femoral component ranges from 25.63 to 25.73 mm. To assess the influence of the femoral component radius on the capacitance change, the model was run for both for a bearing radius of 25.73 to 26.43 mm for loads of 1×BW and 10×BW.

Sensor Vertical Position

The effect of the height of the sensor above the bottom plane of the bearing was investigated. The height was varied from 0 mm to a maximum of 3.75 mm in steps of 0.25 mm.

Bearing Wear

One of the requirements of this work was to ensure that with an average annual wear rate of 0.02 mm the electronics would not be exposed after 30 years' worth of wear (see Section 1.5). This was calculated to be 0.6 mm. Thin layers were removed from the bottom of the bearing for the wear simulation in steps of 0.1 mm up to a maximum of 0.6 mm.

Bearing Thickness

Although the bearing that was simulated was a size 6 bearing, the large bearing is supplied in sizes 3 to 9, which corresponds to a distance between the bottom of the bearing to the bottom of the bearing concavity of 3.5 to 9.5 mm, respectively. The sensor was positioned exactly at half the distance between the bottom of the bearing to the bottom of the bearing concavity for every bearing size from 3 to 9.

Variation in Elastic Modulus

As described in Chapter 3, the elastic modulus of UHMWPE can change under influence of temperature and loading history. The elastic modulus curve, shown in Figure 4.3 was varied by ±10% by multiplying every value of the multi-linear model by 0.9 or 1.1. The model was for a range of loads between 1×BW and 10×BW, measuring in steps of 1×BW.

Rotation of the Femoral Component

The femoral component may rotate ±5° around the tibial axis [27] (Figure 1.1). This rotation was changed in steps of 1°.

4.4.3 Results

In general, the capacitance change of the entire transverse capacitive layer was highest in the middle of the bearing, directly underneath the centre of the bearing concavity (Figure 4.5).

Bearing Concavity Radius

Increasing the radius from 25.75 to 26.43 mm resulted in an increase of the contact area of approximately 40 to 50 %, depending on the load magnitude (Figure 4.6). When the contact area was larger, the bearing compressed up to 50 % less (Figure 4.7). The equi-compression lines (lines connecting regions where the compression was identical) were more horizontal for the smallest bearing concavity radius (Figure 4.8).

The capacitance change of the capacitance layer parallel to the bottom surface of the bearing (depicted in Figure 4.8) was highest in the centre of the bearing, where the compression was highest (Figure 4.5). Although capacitance was inversely related to

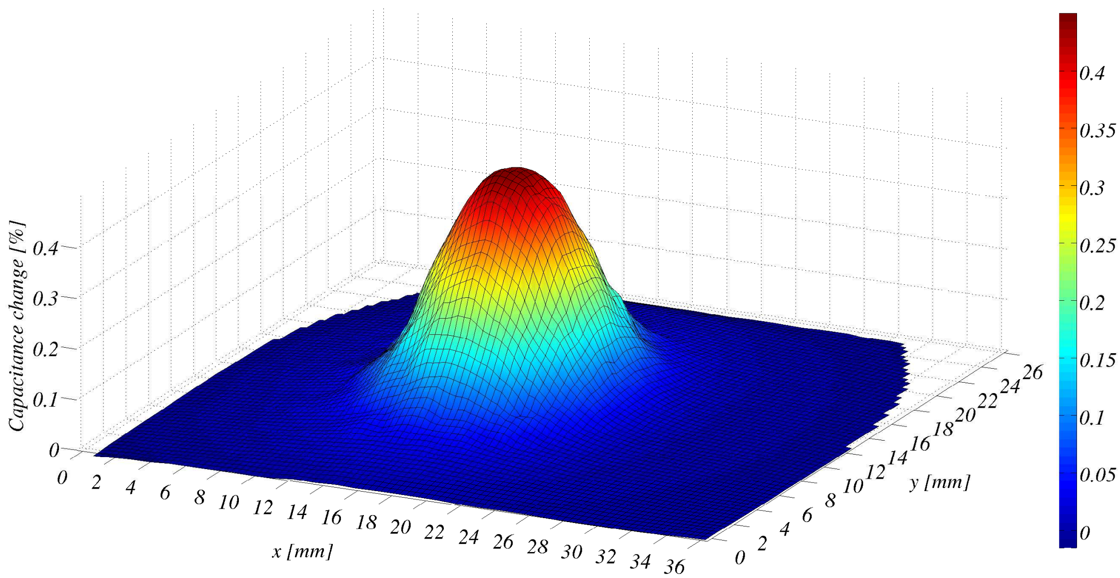

Figure 4.5: *Capacitance change expressed in percentage for each of the sub-capacitors of the simulated capacitance layer for a bearing concave radius of 26.43 mm and a load of 1 BW. Clearly shown is the highest capacitance change in the middle of the array, directly under the centre of the bearing concavity.*

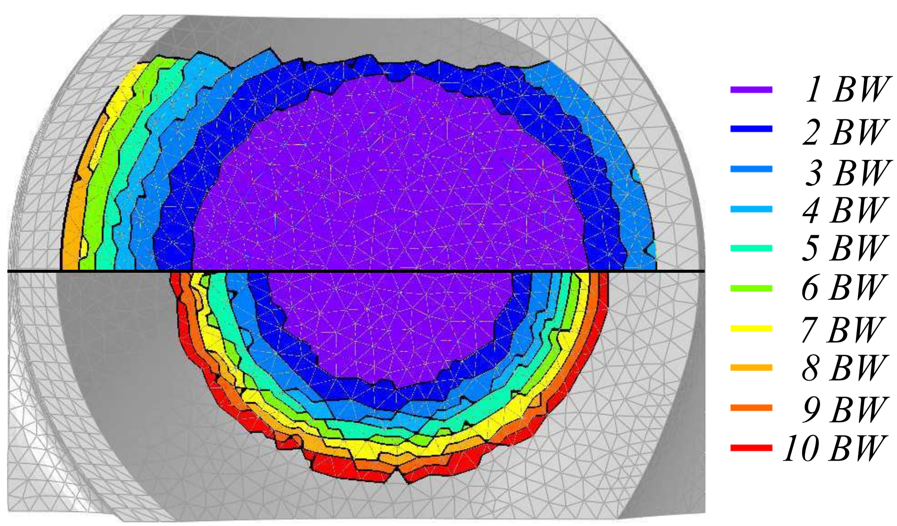

Figure 4.6: *Composition of the contact area between the bearing and the femoral component for the minimum and maximum limit of the bearing radius manufacturing tolerance (25.73 and 26.43 mm), for increasing load from 1 BW (purple) to 10 BW (red). Above the black line, a bearing with a concavity radius of 25.73 mm is shown, and under the black line a bearing with a concavity radius of 26.43 mm. As the load increases, so does the contact area. For the larger bearing radius, the contact area was smaller for all loads, compared to the smaller bearing radius.*

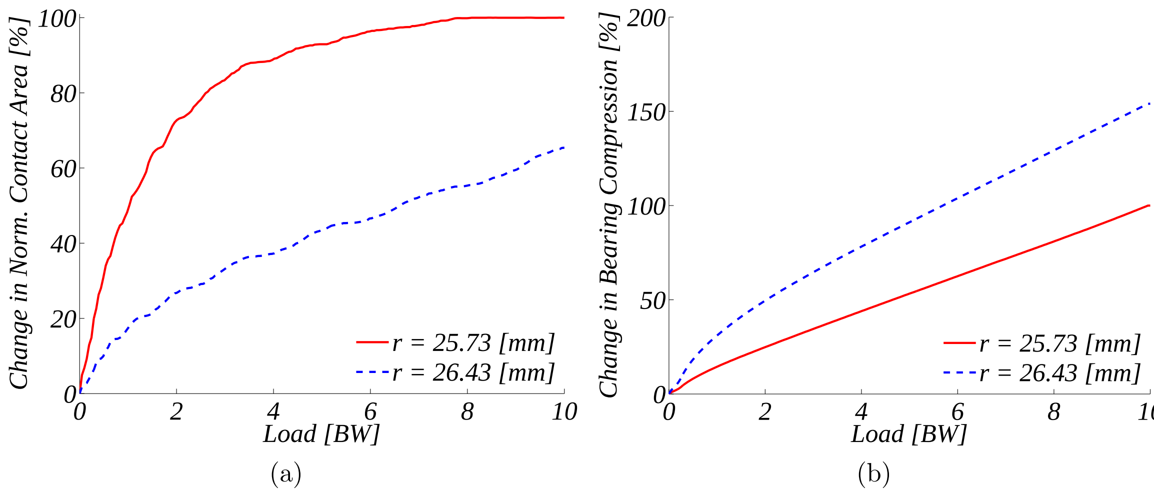

Figure 4.7: *Load, expressed in body weights (BW) vs (a) the magnitude of the contact area, normalised so that maximum compression of a bearing with a concavity radius of 25.73 mm equals 100 %, and (b) the vertical movement of the femoral component (bearing compression), normalised so that the maximum compression of the bearing at the centre of the bearing concavity for r=25.73 mm equals 100 %, for the minimum and maximum limit of the bearing radius manufacturing tolerance. For the smaller radius, the contact area was larger and the relationship between force and femoral movement (bearing compression) was more linear.*

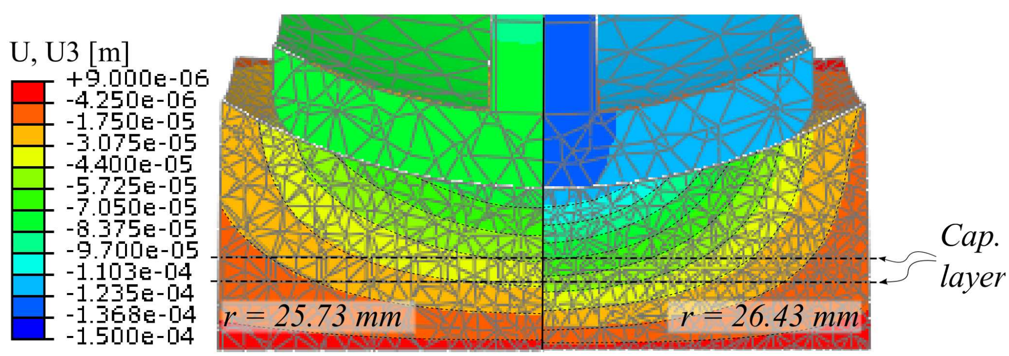

Figure 4.8: *Composition of the cross cut bearings at the medial-lateral mid line for vertical compression of the bearing (U,U3) [m], at the minimum and maximum limit of the bearing radius manufacturing tolerance (25.73 and 26.43 mm), for 10 BW load. Additionally, the capacitive layer ("cap. layer") is shown, the compression of which was used to calculate capacitive change. For the larger bearing radius, the compression was larger and more concentrated around the vertical mid-line of the bearing. In other words, for the smaller bearing radius the iso-compression lines (dotted lines) were more more parallel to the bottom surface of the bearing.*

the distance between the electrodes (Equations 2.1 and 2.2), the capacitance change was very small and was therefore linearly related to the compression (Figure 4.9a). The capacitance change was also linearly related to the bearing compression, although in this case the bearing compression and capacitance change deviated up to ±1.5% from the ideal linear relationship (Figure 4.9b).

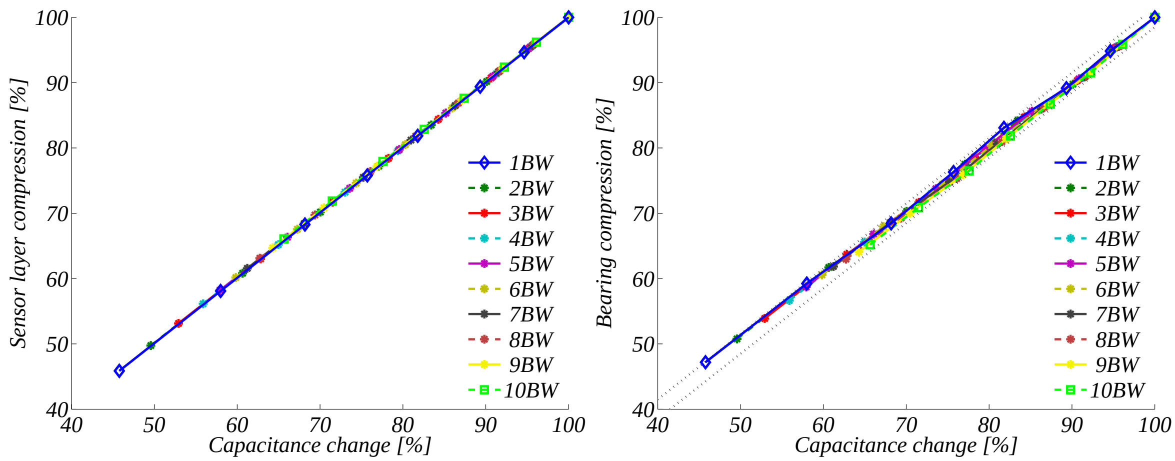

(a) (b)

Figure 4.9: *Capacitance change versus (a) sensor layer compression and (b) bearing compression. All percentages were normalised to the maximum per BW, and all locations were directly under the centre of the bearing concavity, with a square shaped simulated electrode, with dimensions 1×1 [mm]. The stippled lines indicate the maximum deviation of the ideal linear relationship between capacitance and bearing compression, with a magnitude +1.5 % and -1.5 %, in which all errors fell.*

The effect of the bearing concavity radius on the compression of the middle layer showed directly in the capacitance change of the simulated capacitive layer; for smaller bearing concavity radii, the capacitance change was less than for larger radii. This effect was largest for a sensor that was centred directly under the centre of the concavity (Figure 4.10).

Femoral Component Radius

Changing the radius of the femoral component from 25.63 to 25.73 mm at 1×BW resulted in a change from -43.9 % to -5.7 % for a bearing radius of 25.73 to 26.43 respectively. For 10×BW, these changes were from -9.6 % to -4.2 %.

Vertical Position of Sensor

The effect of varying the vertical position of the sensor within a size 6 bearing resulted in changes in capacitance that were within 5 % (Figure 4.11b), irrespective of changing the bearing diameter from 25.73 mm to 26.43 mm and loading with 1×BW and 10× BW.

Wear

Wear of the bottom surface of the bearing resulted in approximately 1 % capacitance change per 0.1 mm. For a smaller concavity radius this change in capacitance (compared to no wear) was more linear than for a larger concavity radius (Figure 4.12a).

Bearing Thickness

The capacitance change of the sensor was highest for the thinnest bearing, and for thicker bearings, the capacitance change decreases, initially by approximately 13 to 15 % per mm increase in thickness, a change with a slope that gradually reduces (Figure 4.12b). The compression for 1×BW had a magnitude of 13.76 μm for a bearing concavity radius of 25.73 mm and 28.76 μm for a radius of 26.43 mm. This corresponds to a strain of 1.8×10^{-3} and 3.8×10^{-3} respectively.

Change in Elastic Modulus

Increasing the elastic modulus of the material model by 10 % resulted in a capacitance increase of 6 to 10 %, and decreasing the elastic modulus by 10 % resulted in a capacitance decrease of 6 to 8 %, compared to the results obtained using the normal elastic modulus (Figure 4.13a).

Femoral Rotation

The influence of femoral rotation on the measured capacitance was less than 0.3 % of the maximum capacitance change (Figure 4.13b).

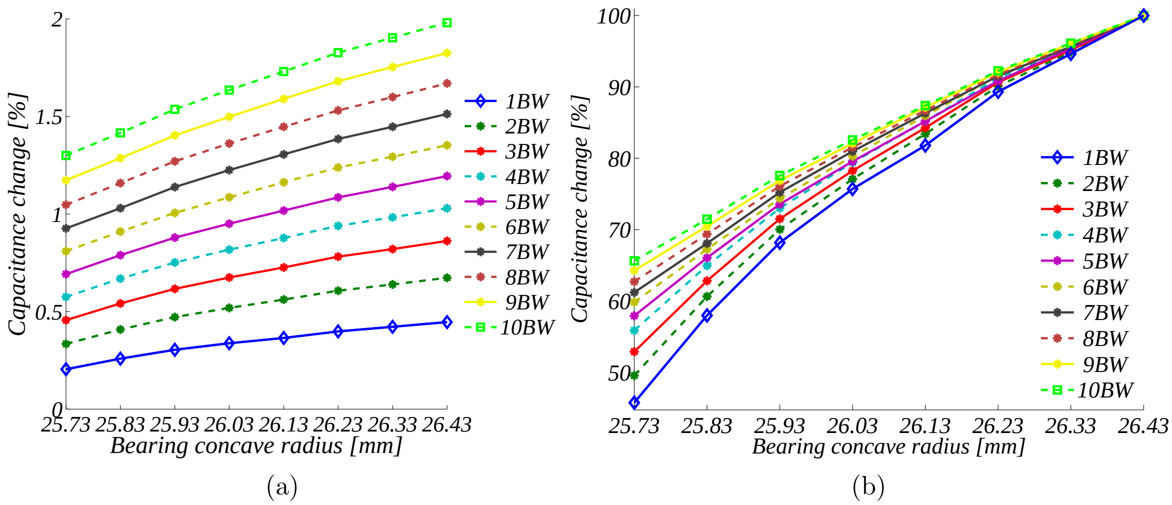

Figure 4.10: *Bearing concavity radius change: capacitance change, (a) expressed as a percentage of the capacitance with various loads, and (b) expressed as a percentage of the maximum capacitance for a radius of 26.43 mm, per loading magnitude. In both figures the effect of an increased bearing concavity radius resulted in an increased capacitance change. This increase became less prominent for higher loads, as is clearly visible in (b); for 1 BW load the change in capacitance relative to the maximum change was approximately 55%, compared to approximately 35% for 10 BW.*

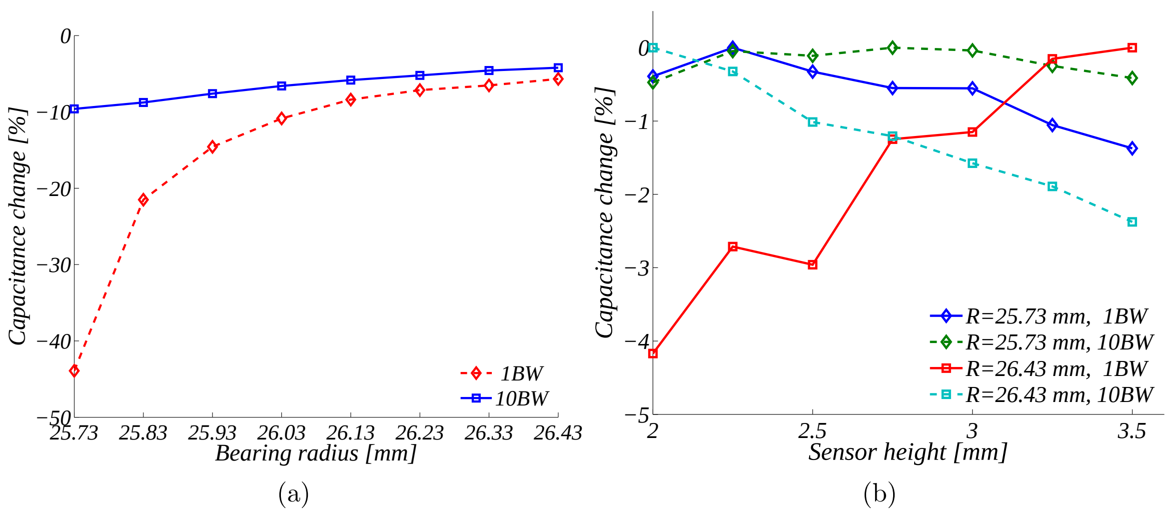

Figure 4.11: *Femoral component radius and sensor height change. (a) Change in capacitance for a femoral component radius of 25.73 mm, compared to the results of a radius of 25.63 mm, for 1×BW and 10×BW and several bearing radii. Especially at lower bearing radii, this effect is strong. (b) Vertical position of the sensor: Influence of changing the vertical position of the capacitive sensor to the bottom plane of the bearing, expressed in percentage of the maximum change of each individual curve. All changes remained within 5%*

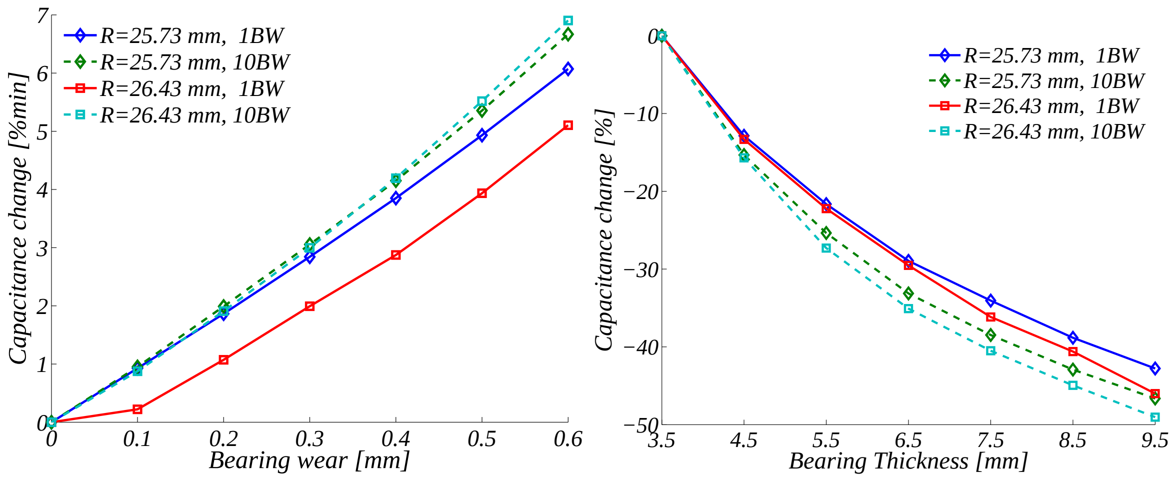

(a) (b)

Figure 4.12: *Wear and thickness results: capacitance change, expressed as an increase in respect to capacitance with no wear, for (a) a bearing radius of 25.73 and (b) 26.43 mm. A wear level of 0.6 mm equals 30 years' worth of wear. All wear was assumed to occur at the bottom of the bearing. For both radii, the increase in capacitive magnitude equaled approximately 1 % per 0.1 mm.*

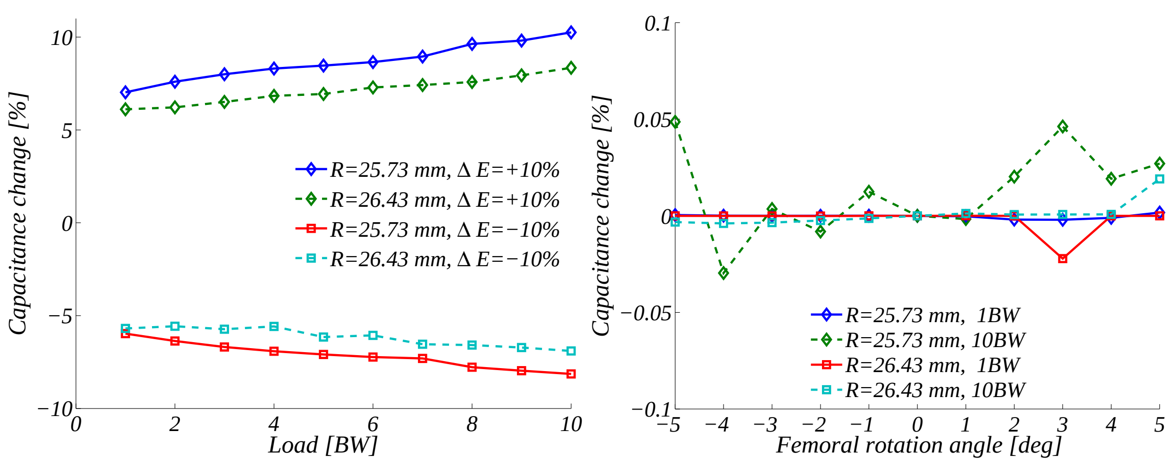

(a) (b)

Figure 4.13: *Elastic modulus change and femoral rotation: (a) Influence of changing the elastic modulus (E) with ±10% on the capacitive change, in respect to capacitive change simulated with an E shown in Figure 4.3, for a bearing concavity radius (R) of 25.73 mm and 26.43 mm. The capacitance changed with 5-10 % for both increased and decreased modulus. (b) Influence of the femoral medial-lateral rotation on measured capacitance, expressed in percentage of 0 degree rotation. All changes were within ±0.05 %.*

4.4.4 Discussion

Two types of changes in capacitance measurement were considered; changes that occur between individual bearings, and changes that occur within one bearing during use. This distinction was made because even though changes in measured capacitance may occur between bearings before calibration, they will disappear post calibration, whereas changes during use may not be correctable through calibration.

Furthermore, all changes that were less than 5 % were considered insignificant.

Bearing Concavity Radius

The bearing concavity radius can change approximately ± 1.15 %, because of manufacturing tolerances, but it resulted in a large difference in contact area (60 %) and bearing compression (50 %), and therefore also capacitance change. Therefore, every bearing needs to be calibrated individually to account for this. There was a linear relationship between compression of the simulated capacitive layer and the resulting capacitance change, even though the relationship between compression and capacitance change is non-linear (Equation 2.1). The relationship between load and capacitance was nonlinear, and the amount of non-linearity was dependent on the mismatch between the radii of the femoral component and the bearing concavity. The bearing concavity radius was determined during manufacturing. One of the influences on the radius after the bearing is implanted is wear, but wear was modelled as a separate parameter.

Femoral Component Radius

As with changing the bearing concavity radius, changing the femoral component radius by 0.1 mm resulted in substantial change in contact area and hence capacitance, resulting from the increase in the contact area between the bearing and femoral component. This effect was strongest at identical bearing concavity and femoral component radii; even for the lightest loads, the contact area was at its maximum. The femoral component radius was determined during manufacturing, therefore only one calibration is necessary, because the femoral radius will not change during the life of an implant.

Vertical Position of Sensor

This parameter provided an indication of the change in capacitance output between bearings if the capacitive sensor deviates somewhat from the ideal position. The influence of this parameter was less than 5 %, so this was considered insignificant. Furthermore, the vertical position of the sensor is determined during manufacturing, therefore only one calibration should be needed.

Wear

This was an effect that does take place during bearing use, and therefore multiple calibrations would be necessary. However, although the change in capacitance exceeded 5 %, the time required for the capacitance to change greater than 5 % occurred was determined to be approximately 25 years, and as such it was considered that this effect could be ignored.

Bearing Thickness

The modelling results showed that for thicker bearings the capacitive change decreased. Furthermore, the vertical strains for a "size 7" bearing were 1.8×10^{-3} to 3.8×10^{-3}, and were comparable to the strains obtained in an experiment, described in Section 2.4, where a median strain of 2.1×10^{-3} was obtained (Figure 2.4b). This gave confidence in the results obtained with this parametric study. The bearing thickness is determined during manufacturing, therefore only one calibration should be necessary. (The bearing thickness may change during service, due to wear, but that was discussed as a separate parameter).

Elastic Modulus

Elastic modulus may change up to 22 % due to temperature changes (Chapter 3). And for an elastic modulus change of 10 % the capacitance also changed between 5 to 10 %. Therefore, this simulation confirmed that a temperature sensor has to be used to measure temperature, in order to correct for this effect. It was considered likely that this effect changes during the life time of the bearing, depending if the material prop-

Parameter	**Changes > 5 % due to manufacturing ?**	**Changes > 5 % during short term use? ***	**When calibration?**
Bearing Radius	yes	no	once
Femoral Radius	yes	no	once
Vertical Position	no	no	once
Wear	no	no	after 20 yr
Bearing Thickness	yes	no	once
Elastic Modulus	no	yes	always**
Femoral Rotation	no	no	unnecessary

Table 4.1: *Summary of each varied dimensional parameter and how much it affects the capacitive change.*
** during the course of a single experiment.*
*** dynamic compensation of the measured capacitance using data obtained during calibration, based on real-time readings from a temperature sensor. The temperature calibration map may only have to be calibrated once.*

erties of UHMWPE change, for instance due to crystallisation. However, investigating this was part of future work.

Femoral Rotation

Femoral rotation does occur during use, but the magnitude of the capacitive sensor changed only approximately ±0.05 % in response to an angle change of ±5° and therefore was considered insignificant.

Conclusion

Most effects of geometry variation were not significant, except for variations in the bearing concavity radius and the femoral component radius, which resulted in large changes. This means that every instrumented bearing will need to be individually calibrated. Additionally, a temperature sensor was considered very important to ensure that a calibrated instrumented bearing will provide the correct loading data.

4.4.5 Limitations

The material model for UHWMPE that was used was assumed to be isotropic and homogenous, however, it is known that this material does exhibit non-isotropic behaviour [124].

4.5 Calibration Protocol

Based on the analysis of the last section, a calibration protocol is proposed. A bearing will be instrumented with a sensor, and calibrated using a material test machine, using the femoral component of which the dimensions very precisely determined. Various dynamic loading patterns will be applied, at temperatures that may occur *in vivo* (Chapter 3) so that the bearing will be completely characterised. For improved accuracy, the loading parameters may be based on the patient's weight. Then the bearing will be implanted. During the operation the bearing will be immediately ready for use, and could be used to determine if the correct pre-tension of the knee was performed. Calibration after implantation may be complex, and no method has yet been devised for that scenario. This will be part of future work.

4.6 Embedding a Sensor

4.6.1 Introduction

In the previous section, the capacitive sensor was modelled using a capacitive layer with a thickness of 1 mm, made from UHMWPE. However, in reality a prototype instrumented bearing was made using a sensor made from polyimide (PI) (Chapter 5) with a thickness of 0.1 mm. PI has dissimilar material properties compared to UHMWPE. Applying a load to dissimilar materials that are in contact results in stress concentrations at the boundaries of the materials. If the stresses become too high, then the material may degrade. In this section, a simulation was performed with a PI sensor embedded within a bearing, and the maximum stresses were compared to the stresses that were obtained without an embedded sensor, in order to discuss possible degradation of the bearing.

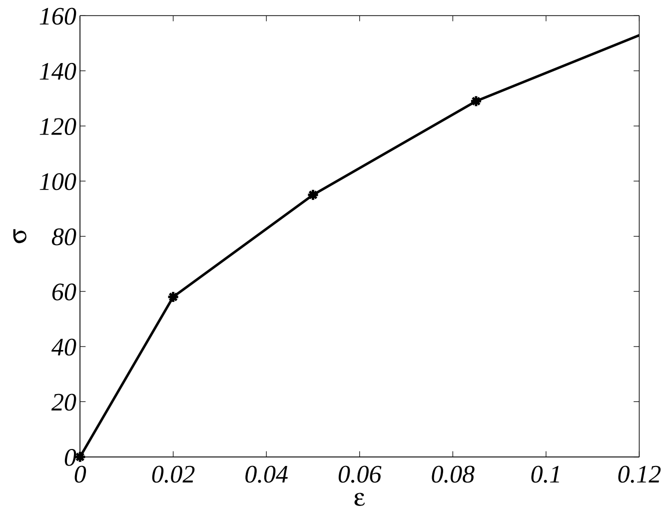

Figure 4.14: *Multilinear material model used for PI, with stress (ϵ) and strain (σ) [126].*

4.6.2 Background

Layers of material have been embedded in knee bearings before; when a complete layer of UHMWPE fibres is embedded within UHWMPE, wear rate increases, although in some cases, only by a factor of two, and in case of failure, the cause was delamination, thought to occur due to poor bonding at the interface between the fibres and bulk material [125].

The capacitive sensor that was used is made from polyimide (PI, Chapter 5). This material has an elastic modulus of approximately 2.5 GPa and Poisson's ratio of 0.34 [126]; these material properties are different than those of UHMWPE (Figure 4.14), and therefore these materials behave differenly under load.

Therefore, it is expected that stress concentrations will occur around the sensor. Stress concentrations, especially tensile stress concentrations, have led to increased wear. Therefore, the magnitude of these concentrations needed to be investigated.

4.6.3 Method

To simulate how much stress occurs around a capacitive sensor made from PI, a 2×2 mm sensor was embedded within the bearing model described earlier in this Chapter.

Sensor Model

A capacitive sensor was modelled with dimensions 2×2×0.1 mm. The sensor was modelled as homogenous PI, using the multilinear model shown in Figure 4.14). The sensor was meshed using standard quadratic tetrahedral (C3D10) elements, with an element size of 0.1 mm. The bearing was meshed with an element size of 1 mm. To provide a smooth transition between the two mesh sizes, two transition regions were created that surrounded the sensor, the first with a size of 5 × 5 × 0.5 mm, which was meshed with 0.25 mm elements, and the second with a size of 7 × 7 × 1 mm, which was seeded with 0.5 mm elements. A schematic view of the meshing is shown in Figure 4.15.

Stress Measurement

The maximum principal stress of the UHMWPE of the entire bearing was determined for loads of 4×BW and 10×BW for a bearing radius of 25.73 and 26.43 mm. A load of 4×BW was chosen because that is the maximum load that may occur during regular use of the bearing.

4.6.4 Results

The maximum principal stress was highest in the surroundings of the sensor, both for tensile and compressive stress. For a bearing radius of 25.73 mm and a load of 4×BW, the maximum principal stress ranged from -6.3 to +12.5 MPa. In comparison, the maximum stress for the identical bearing without the sensor ranged from -4.1 to 3.8 MPa. Adding a sensor resulted in an increase of tensile stress by a factor of 3.3.

For a bearing radius of 26.43 mm and a load of 4×BW, the maximum principal stress ranged from -6.4 to +10.0 MPa. In comparison, the maximum stress for the

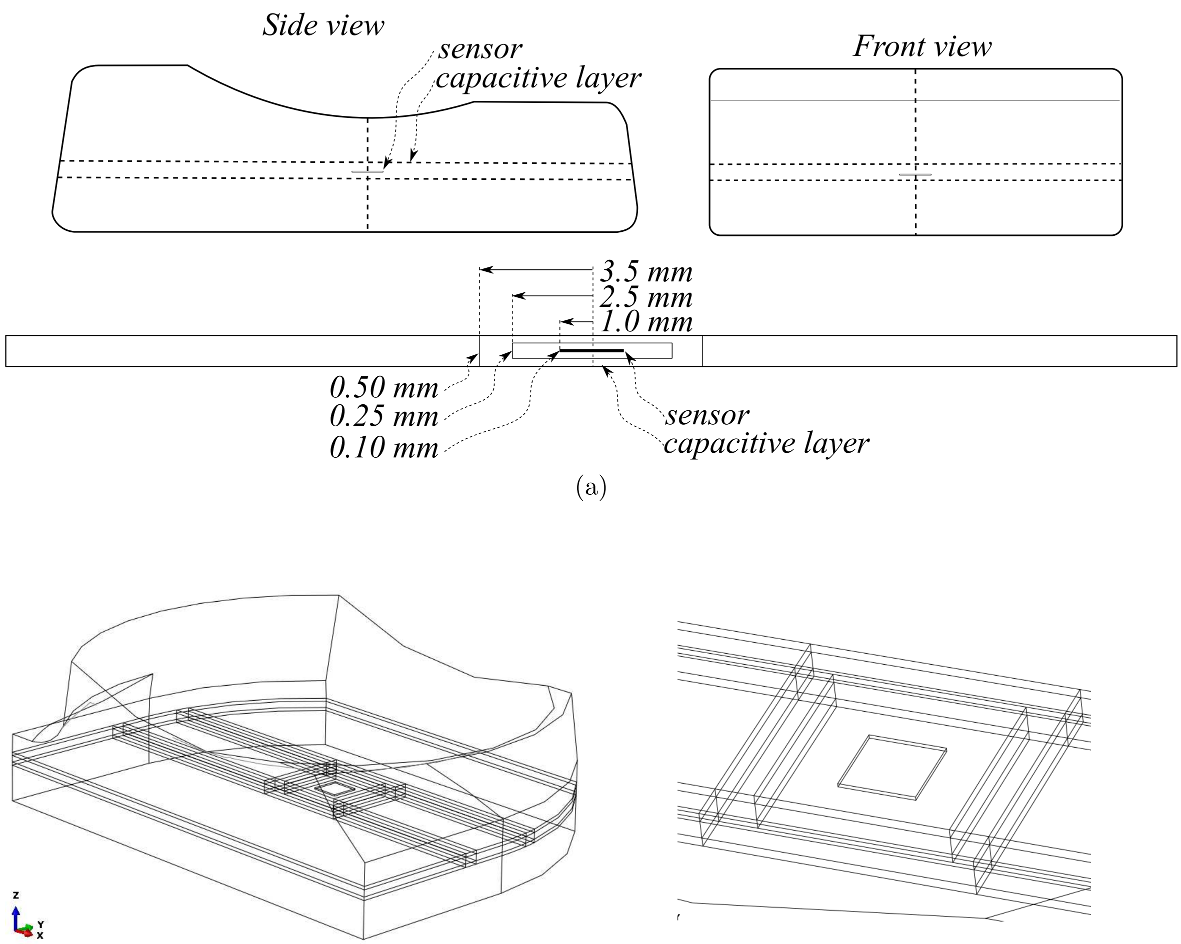

(a)

(b) (c)

Figure 4.15: *Embedded sensor model. (a) position of the sensor within the capacitive layer, with the width of the bounding boxes shown and their mesh sizes. (b) A 3D wireframe model of the bearing, with the layers. (c) a close up of the sensor and the surrounding meshing volumes.*

identical bearing without the sensor ranged from +3.8 to 9.9 MPa. Adding a sensor resulted in an increase of tensile stress by a factor of 1.01.

4.6.5 Limitations

In multi-layered foils, the adhesive layer has dissimilar properties to PI and therefore the material behaviour of the entire composite layer could be different to that of pure PI [126, 127]. Similarly, a simple material model was used for UHMWPE.

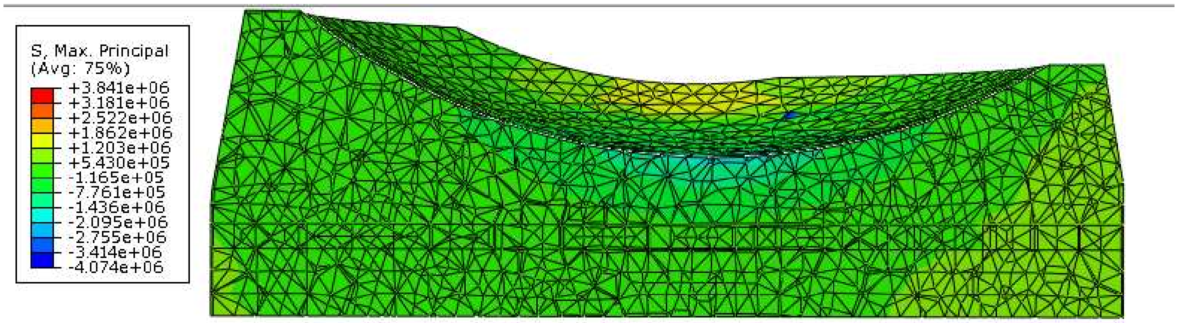

(a)

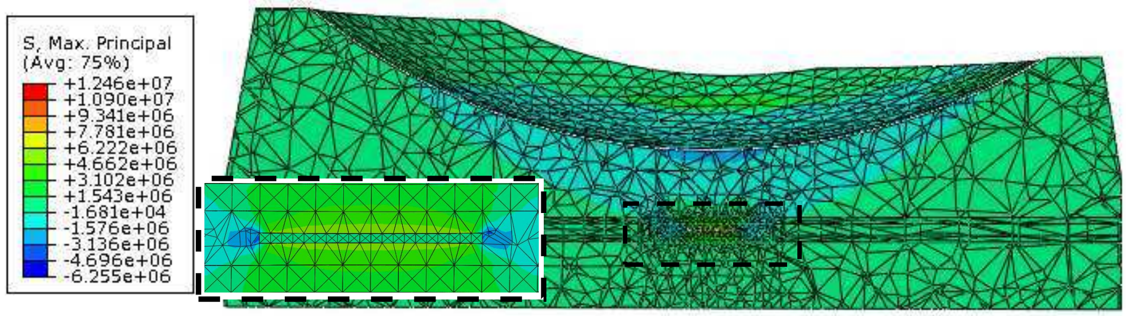

(b)

Figure 4.16: *Maximum principal stress within the bearing, for a concave radius of 25.73 mm and a load of 4×BW. (a) For a bearing with no sensor, and (b) for a bearing with a sensor. Inset: close up of the area surrounding the sensor. The maximum tensile stress (red) is a factor 3 times higher with a sensor.*

4.6.6 Discussion

It is reassuring that the reported stresses do not exceed the yield strength, even at an impulse load of 10×BW. However, it is worrying that the maximum stress increased up to a factor of 3 as a result of the presence of the embedded sensor.

The stress was highest directly underneath the centre of the bearing concavity, therefore it may be wise to move the sensor radially away from the centre of the bearing. However, there the compression would be decreased, and in accordance to that the capacitive sensor output would be decreased. Then the issue arises if there will be sufficient capacitive signal to noise ratio. This question is part of future research.

Given that UHWMPE in reality has very complex behaviour, much of which is still unknown, wear tests have to be performed in the future that show whether embedding a sensor within the bearing significantly weakens the bearing. These wear tests take a very long time to run, and as such are not part of this thesis.

4.7 Embedding an Electronic Module

4.7.1 Introduction

The capacitive sensor needs to be connected to electronic components for measurement and communication. The volume calculations are detailed in Chapter 7. All electronic components will be housed in one module, in which all components are surrounded by potting material, Bis-GMA, which has an elastic modulus of 10 GPa [128, 129]. The optimal position of the electronic module was identified as the front of the bearing (Chapter 6), given that the electronic module has to be in close vicinity of the antenna.

4.7.2 Method

In addition to the bearing model presented earlier, an electronic module was modelled with an elastic modulus of 10 GPa and a Poisson's ratio of 0.46. The block had dimensions 13 mm$\times$7.5 mm$\times$ 3.5 mm, and was positioned 0.6 mm above the ground plane, in line with wear requirements of 0.02 mm per year for 30 years (Section 1.9). The module was inserted from 0 to 5.5 mm into the front of the bearing in increments of 0.5 mm. The question that was considered was to what extent the vertical compression of the bearing and the capacitance measurement was changed by insertion of the electronics module. The vertical compression of the bearing was calculated directly under the centre of the bearing concavity, and the capacitance change was measured in a square area of 1$\times$1 mm in the capacitive layer, directly underneath the centre of the bearing concavity. The loads for which the change was measured were at 1 BW (392.5 N) and the maximum dynamic load experienced during gait and step up/down of 4 BW (1570 N) (Figure 5.15).

4.7.3 Results

Compression and Capacitance Change

The influence of inserting an electronic module into the bearing and loading with one body weight (392.5 N) resulted in a change in compression of the bearing and measured capacitance change of approximately 5 % (Figure 4.17). A much larger change in compression and capacitance resulted from changing the bearing concavity radius; at the largest concavity radius the bearing compression was approximately 50 % larger than at the smallest concavity radius. As a whole, for all bearing concavity radii, the compression and capacitance change occured above a depth of 1.5 mm (Figure 4.17). Comparable results were seen for a load of 4×BW, that the influence of bearing concavity radius on bearing compression and capacitance change was 40 % instead of 50 %.

Local Stress Levels

The stress levels within the UHMWPE within the immediate surroundings of the electronic module ranged from 0.57 MPa at an insertion of the electronic module of 5.0 mm and a bearing radius of 25.73 mm, to 4.1 MPa for an insertion of the electronics module of 0.5 mm and a bearing radius of 26.13 mm. Therefore, the stresses within the bearing are lowest when the electronic module is completely embedded within the bearing, with a stress level of approximately 1 MPa for all bearing concave radii (Figure 4.18).

Total Bearing Stress Levels

Within the bearing, the highest tensile maximum principal stress was in the side of the bearing, with a range of typically 2 MPa for a bearing with a radius of 25.73 mm, up to 3 MPa for a radius of 26.43 mm, both for a 4×BW load (Figure 4.20).

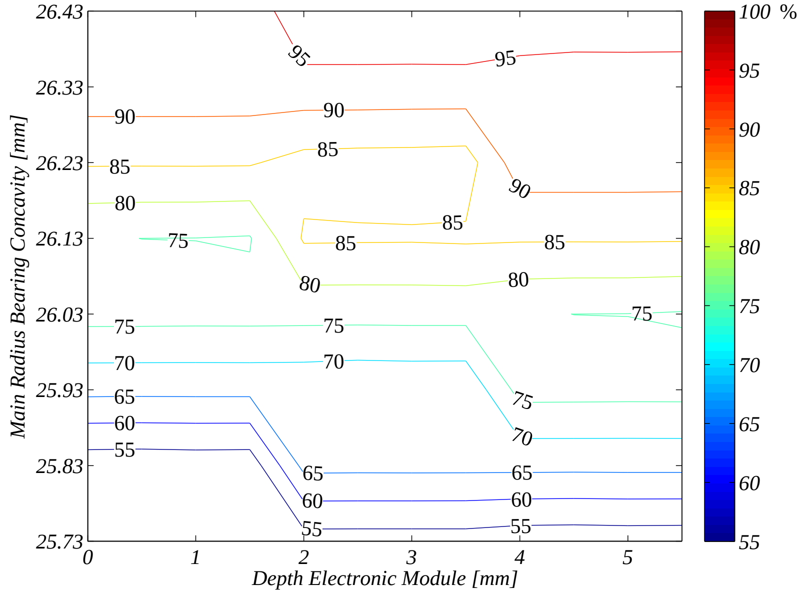

(a)

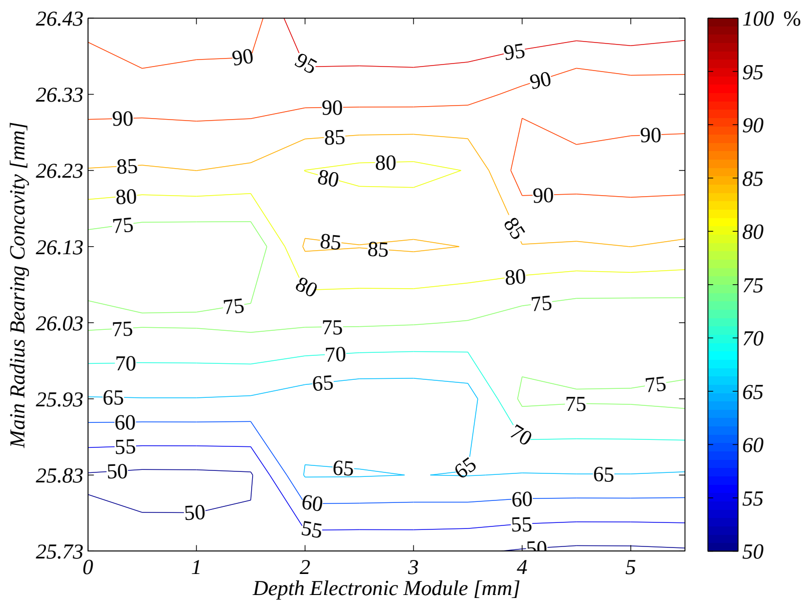

(b)

Figure 4.17: *Bearing compression (a) and capacitance change (b) normalised to the maximum change = 100 % (at a radius of 26.43 mm and insertion with 5.5 mm), under influence of varying the depth of the electronics module and the bearing concavity radius for* ***one*** *body weight. Inserting the module typically resulted in a change in compression and capacitance of 5 %, whereas changing the concavity radius lead up to a change of 50 %.*

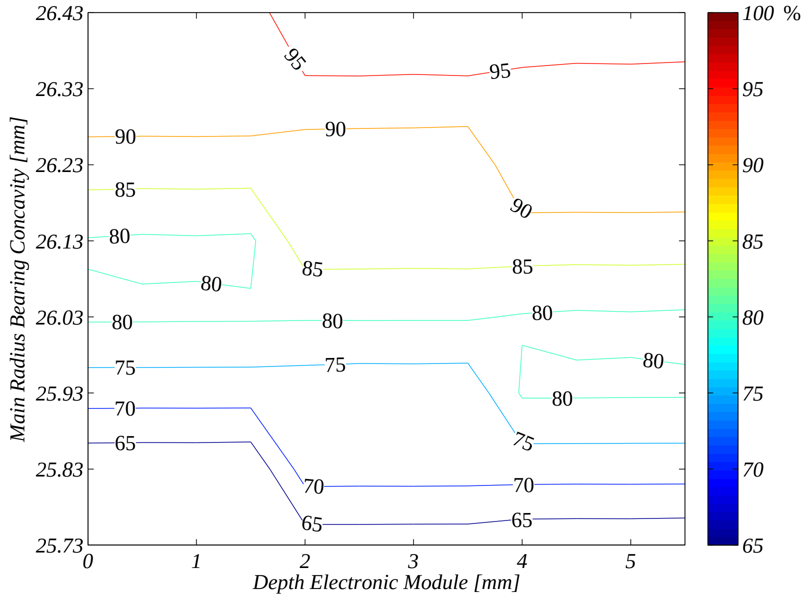

(a)

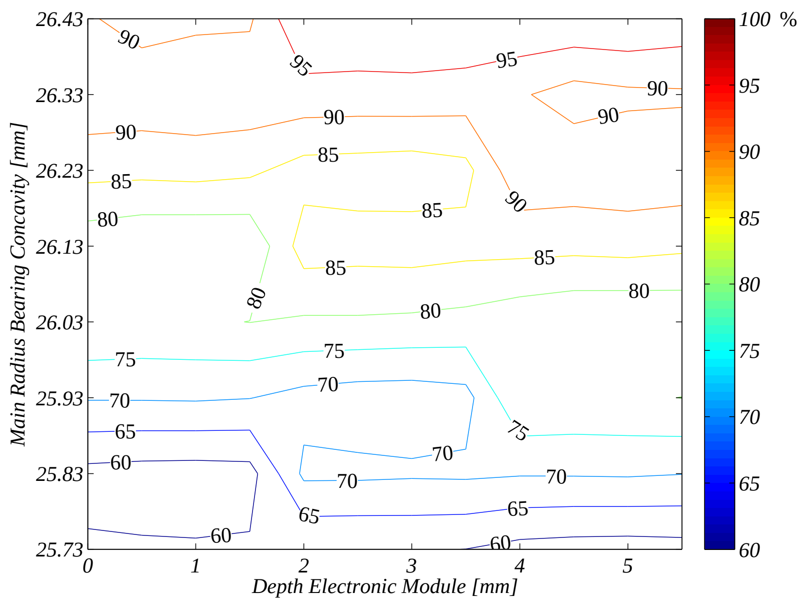

(b)

Figure 4.18: *Bearing compression (a) and capacitance change (b) normalised to the maximum change = 100 % (at a radius of 26.43 mm and insertion with 5.5 mm), under influence of varying the depth of the electronics module and the bearing concavity radius for* ***four*** *body weights. Inserting the module typically resulted in a change in compression and capacitance of 5 %, whereas changing the concavity radius lead up to a change of 40 %.*

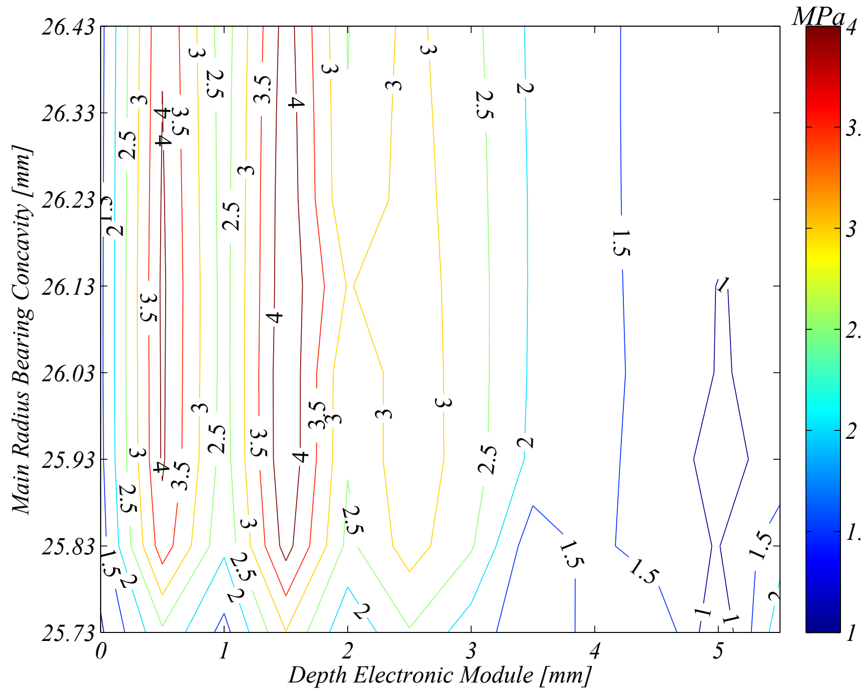

Figure 4.19: *Maximum principal stresses within the part of the bearing that surrounds the electronic module [MPa], at a load of four body weights. The stresses within the bearing were lowest when the electronic module was fully embedded within the bearing, and were highest when the module was only 0.5 mm within the bearing. The stress levels never exceeded 4.1 MPa, and the lowest stress level was 0.57 MPa.*

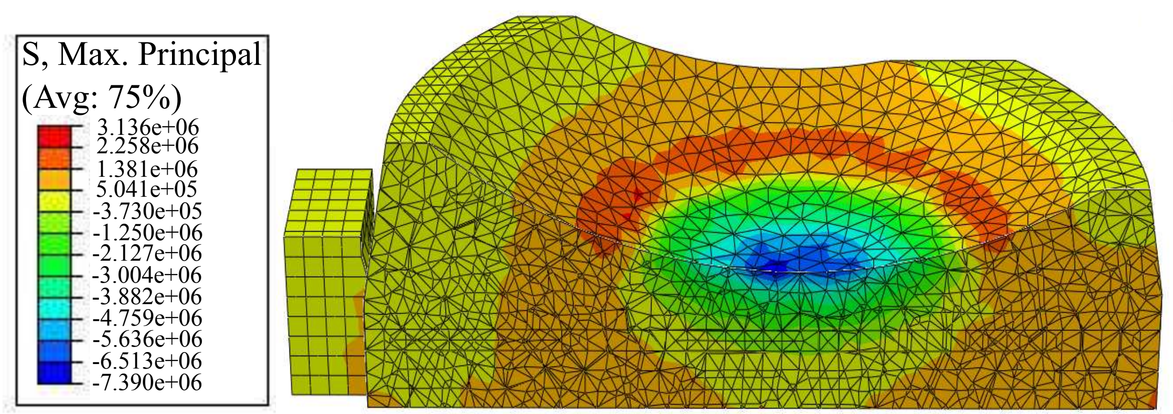

Figure 4.20: *Stress plot of the bearing, using maximum principal stress, for 4×BW load and a bearing radius of 26.43 mm. A negative stress level corresponds to compressive stress, whereas a positive stress corresponds to tensile stress. In this case, maximum tensile stress is approximately 3 MPa.*

4.7.4 Discussion

It was surprising, that inserting the electronic module into the bearing resulted in such small changes, for both loads of 1×BW and 4×BW. The bearing module should be inserted fully into the bearing, taking into account that at that depth the stress levels are lowest. Future tests are needed to establish how well the bearing performs when the module is fully inserted into the bearing, but these modelling results are very promising.

The maximum stress levels in the bearing surrounding the electronic module never exceeded 4 MPa, or 1/5th of the yield stress, at the maximum load during gait, and was approximately 1 MPa or 1/20th of the yield stress, for all the bearing concave radii. This means that according to the simulations, the bearing should have a very low risk of fracture if the module is fully inserted. However, physical wear tests have to be performed as part of future work to determine if this is observed in reality.

4.8 Chapter Conclusions

The strain results of the parametric study have been shown to be within the range of strain results obtained in an experiment, therefore the model was likely to give accurate results.

The most important conclusion of this chapter is that the capacitance increase of an embedded capacitive sensor is highest directly underneath the centre of the bearing concavity. *This answers Aim 2: Determine what position of the load sensor results in the largest output signal.*

The capacitive signal was found to be linearly related to the bearing compression, so in theory the capacitive sensor could also be used to measure bearing compression, besides load. Several geometric properties were investigated; most properties had influence on the capacitive signal, but could be taken into account by calibrating the bearing. *This answers Aim 3: Determine the influence of geometric properties on the* *output signal.* The femoral component and bearing concavity radii exerted a surprisingly large influence on the contact area and the compression of the bearing, together with the resulting capacitive change.

Temperature had a significant effect on capacitive output, and is the only one that can change during short term use, and therefore the capacitive sensor signal needs to be corrected with an embedded temperature sensor. *This answers Aim 4: Determine the influence of temperature on the output signal.*

The influence of wear is approximately 1 % per 4-5 years, so if a 5 % change is accepted then the bearing only needs to be recalibrated after 20 years. *This answers Aim 5: Determine the influence of wear on the output signal.*

Placing a capacitive sensor underneath the centre of the concavity is advantageous for getting a larger capacitive change, but on the other hand resulted in much larger stresses within the bearing, up to a factor three times larger. These stresses were still below the yield strength, but future mechanical wear testing should be performed in order to ensure reliability.

Placing an electronic module inside the bearing resulted in surprisingly little change on the mechanical behaviour of the bearing and the capacitive output, and the lowest influence on the mechanical behaviour of the bearing occurred when the module was positioned entirely inside the bearing. *This answers Aim 6: Determine the influence of embedding an electronic module into the bearing on the mechanical behaviour of the bearing and the sensor output.*

Conclusions for manufacturing: in order to get the maximum signal output of the capacitive sensor, the sensor should be placed directly underneath the centre of the bearing concavity. This does introduce extra stress inside the bearing, which is directly related to the position of the sensor. To what extent this stress would introduce bearing fracture remains to be tested during wear testing. If bearing fracture because of the sensor becomes an issue, it can be reduced by placing the sensor further away from the centre of the bearing concavity, in the plane parallel to the bottom of the bearing surface. To reduce the stress level of the electronic module, it is advised to place the module inside the bearing.

5 Capacitive Measurements

5.1 Introduction

This chapter presents the results of capacitive measurements of the bearing. No previous descriptions have been made about the use of a capacitive load sensor within an orthopaedic bearing. There are several advantages to using a load sensor within a UKR bearing, which are described in Chapter 1. Using a flexible capacitive sensor should increase the long term reliability of the instrumented implant compared to implants using a rigid sensor. This is because UHMWPE is a relatively soft material and embedding a rigid sensor results in an elastic modulus mismatch, which would introduce stress concentration gradients and therefore UHMWPE would be more easily damaged (see Chapter 4). Finally, UHMWPE is a polymer with a complex stress strain relationship, as already discussed in Chapter 3, and difficult to model, and direct measurement of load will provide information to verify finite element modelling results. A capacitive sensor could be placed in many different locations within the bearing, which would increase the knowledge of location specific loads, which in turn could help during design of new bearings, for instance to reduce wear. This sensor may also be of use for load measurement in total knee replacements, hip replacements, and shoulder replacements.

This chapter is divided up into the following sections:

Section 5.3) Load censor construction

Section 5.4) Pre-loading measurements

Section 5.5) Dynamic sensor characterisation

Section 5.6) Response to physiological loading

Section 5.7) Load estimation.

5.2 Aims

The following aims have been set for this chapter:

1 Determine how a repeatable sensor can be constructed and reliably embedded within a bearing

2 Determine if a pattern can be distinguished between sensor position and capacitive output magnitude.

3 Determine the creep behaviour of the bare sensor and the sensor embedded within the bearing

4 Determine the frequency transfer function of the sensor

5 Determine the response of the sensor to physiological signals

6 Determine how to estimate load from measured capacitance and the accuracy of load estimation

5.3 Load Sensor Construction

The theory of capacitance is discussed in Section 2.3.6. In Chapter 4, it has been shown that the maximum compression of the bearing occurs directly below the centre of the bearing concavity. Hence, a capacitive sensor that works by compression of a flexible material would have the highest output when it is situated in this location. To compromise the mechanical integrity of the bearing as little as possible, the sensor needs to be as small as possible. In order to achieve this and still obtain a capacitance value that is large enough to measure, the sensor electrodes must be placed vertically as close together as possible. Also, the electrodes must be placed directly over each other, with their planar axes parallel. Taking these factors into consideration, the decision was made to pre-assemble the sensor construct using foil; this enables highly repeatable electrode positioning, and means that a very small electrode surface area can be used because of the small thickness between the electrodes. For the foil material, polyimide was chosen.

5.3.1 Properties of Polyimide

Polyimide (PI) is a widely used material to create printed circuits, it has excellent mechanical properties; for instance BPDA-PDA, a commercially available electronics grade PI, has a glass transition phase which occurs at 360°C and a decomposition temperature of 620°C [130], it is highly resistant to solvents and body fluids, and therefore highly inert and non-toxic. Because of these properties, it is often used as an insulating layer. PI *in vivo* has only elicited mild foreign body reactions in several applications in the peripheral and central nervous system, showing good overall biocompatibility, for instance, it has been used in intraocular electrode arrays [131]. Electrical circuits in the form of copper traces can be applied as a thin film on top of PI by sputtering, electroplating, or etching on the surface. Additional layers can be added through adhesive processes. Vias (inter-layer interconnections) can be added by laser or conventional drilling methods [127]. PI has an elastic modulus of approximately 2.4 GPa, Poisson's ratio of 0.34, and similar visco-elastic behaviour to UHMWPE; hysteresis with associated increased unloading elastic modulus and temperature induced reduction of elastic modulus). In multi-layered foils the adhesive, with its own characteristics, also changes the mechanical properties [126, 127].

To establish the relationship between capacitance and load, compressive experiments using the capacitance change as measurand of strain were performed as part of this thesis. These experiments are described further on in this chapter.

5.3.2 Moulding Process

Before discussing the sensor design, first the moulding process is explained, since it had a major influence on the design, for reasons outlined further on. The moulding process starts by inserting UHMWPE powder in a mould form, and then applying compressive load and heat according to a process that differs between implant manufacturers. The sensor was designed as a foil with integrated leads, which were long enough to pass

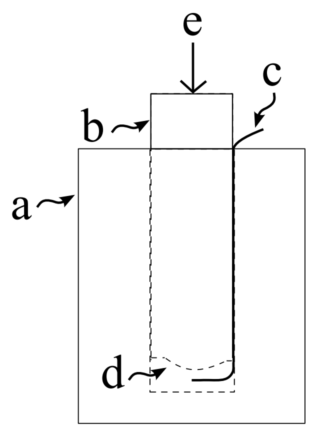

Figure 5.1: *A Schematic view of the compression moulding tool, with the (a) compression block, (b) plunger, (c) sensor foil, (d) UHMWPE powder, and (e) depicting the load that was applied.*

along a plunger that was used to compress the UHMWPE (Figure 5.1). The sensor foil experiences very high stresses during manufacturing, and is most likely to fail at this point. To embed the sensor within the UHMWPE, the only additional step to the moulding process was to insert the sensor foil within the UHMWPE powder prior to compression moulding. The sensor foil was placed between two layers of UHMWPE powder, which solidifies under pressure. No changes to the heat or load profile of the compressive process had to be made.

5.3.3 Sensor Design

The capacitance of a sensor depends highly on the geometry of the electrode, in both perpendicular and transverse directions (Equation 2.1). Due to this and the requirement to have a small sensor volume in order to preserve the bearing integrity as much as possible, the capacitive sensor was constructed in one part. Therefore the sensor was made with copper as the electrode material and PI as the inter-electrode layer. The sensors were designed using OrCAD 16.6.0 Lite software (Cadence Design Systems Inc, San Jose, CA, US), and saved to a standard printed circuit board file. Sensors were manufactured by Shenzen Yuzhixiang Electrons Co., Ltd (Shenzen, China). The sensor had four electrodes, each electrode had dimensions 2×2 mm, and each electrode was spaced 1 mm away from the others in the transverse plane. One electrode covers all four electrodes to form the other electrode, perpendicularly spaced at 0.1 mm distance. Sensor design took place in several iterations;

Iteration 1

The electrode leads were dual layered, and had straight thin leads (Figure 5.2b). The common electrode covered all four electrode areas. The common electrode layer also contained a shielding plane, that covered the sensitive electrode leads from one side. The sensor foil was inserted alongside the plunger (Figure 5.1). This often resulted in completely severed leads, because of stretching of the leads during compression of the UHMWPE and the associated downward movement of the plunger. Even lubricating the sensor leads with PTFE lubricant did not improve matters. Additionally, the copper traces on the leads were so thin that repair was difficult, taking up to an hour to solder by hand. The results were varied, but generally poor.

Iteration 2

To prevent shearing of the leads, a strain relieving pattern was introduced in the sensor leads, and the lead traces themselves were made wider (Figure 5.2c). This resulted in a better yield, and repairing the sensor was easier because of the wider traces, the result was acceptable but still sub optimal, as the leads would occasionally still shear partly or completely.

Iteration 3

Although iteration 2 provided acceptable results, the following concerns were identified in regards to interference with the electrodes:

1) the bearing would be powered by wireless induction at a later stage, introducing a probable cause of electromagnetic interference.

2) there was a minute possibility of an aberrant path from one electrode to the other via the surrounding metal components or body fluids.

Capacitive measurement generally occurs by applying a charge to one of the electrodes,

(a)

(b)

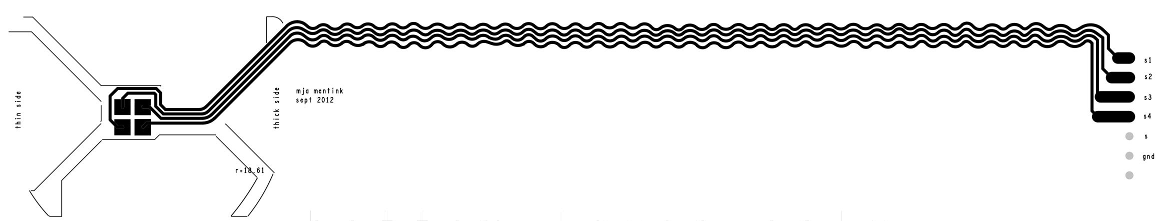

(c)

Figure 5.2: *Copper track layout of the individual layers of the capacitive sensor: (a) Common electrode layer, (b) straight sensor leads and (c) strain-relieved sensor leads*

and measuring the received charge on the other electrode, and both concerns can be remedied by surrounding the receiving electrode by the transmitting electrode, effectively forming a Faraday cage.[1] An additional advantage was that the sensor area per electrode could be made twice as small, because the effective surface area doubles in a triple layered configuration. The only disadvantage to the new design was that the increased lead thickness prevented the use of the tried and tested method of guiding the electrode lead alongside the plunger of the mould tool. This was overcome by cutting the lead to length, and introducing a 'harmonica' fold at the end (explained in the next section).

[1] A Faraday cage is an earthed metal screen surrounding a piece of equipment to exclude electrostatic and electromagnetic influences.

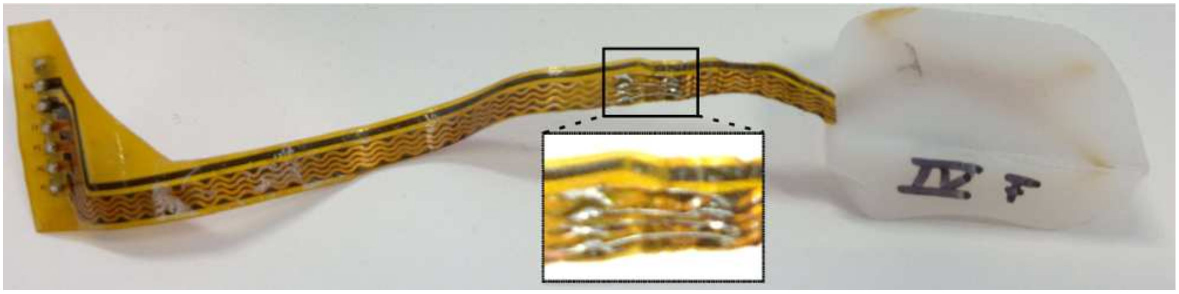

(a)

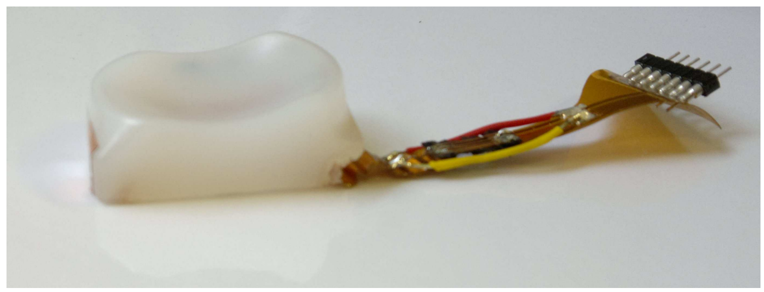

(b) (c)

(d)

Figure 5.3: *Bearing preparation, (a) earlier prototype, in which leads were still attached during moulding, which often resulted in damaged leads that needed to be repaired (inset) (b) new prototype, in which leads are extracted from the bearing after moulding; the left bearing shows the folded up electrode lead inside the bearing, and the right bearing shows the unfolded lead; (c) the bearing reconnected to the leads, and (d) securely packaged.*

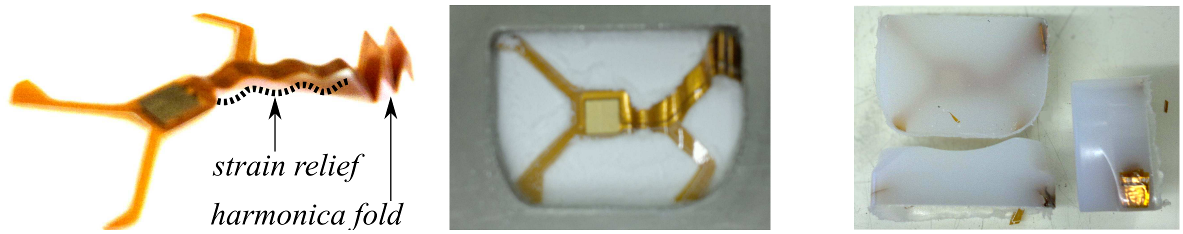

Figure 5.4: *Bearing moulding in all its stages: (a) prepared the sensor foil, with the folded sensor lead in the top right corner, (b) placing the sensor foil in the mould, on top of half the UHMWPE powder, (c) the finished product.*

5.3.4 Sensor Preparation for Moulding

The sensor lead was cut to the right length using a scalpel. Then a strain relieving 'harmonica' pattern was introduced in the transverse plane of the foil. At the end of the sensor leads, the leads were folded with a 'harmonica fold' several times, and cut (Figure 5.4a). The sensor foil was placed inside the mould tool, on top of approximately half the UHMWPE powder (Figure 5.4b). The rest of the powder was inserted into the mould, and the bearing was moulded using the normal procedure, resulting in a finished instrumented bearing as shown in Figure 5.4c. After the moulding procedure, UHMWPE was removed around the folded lead in the corner of the bearing with a hot tool to allow access to the lead, and the lead was unfolded. Bearing preparation, including soldering and testing the reliability of the connections is discussed in Appendix B.3.

5.3.5 Moulding Placement Validation

To verify that the sensors were embedded within the correct location, directly under the centre of the bearing concavity and in the middle of the bearing seen in lateral view, radiographs were taken of 18 bearings with embedded sensors, using a Siemens Multex top X-Ray machine (Siemens, Erlangen, Germany). To determine the position of the sensor in respect to the centre of the concavity, each bearing was placed on a

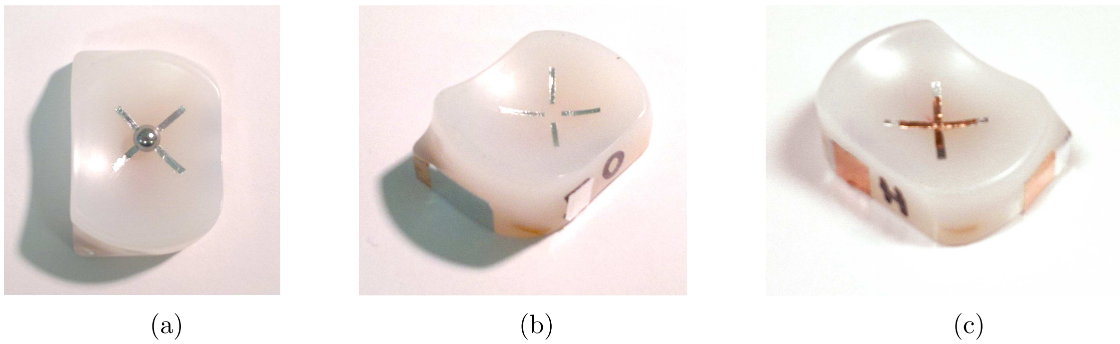

Figure 5.5: *Marking the centre of the bearing: placing a metal ball bearing in the concavity, and applying metal foil in two steps.*

horizontal surface, and a metal ball bearing, diameter 5 mm, was placed in the bearing concavity (Figure 5.5).

The resting position of the ball bearing was marked with two layers of copper foil (100 μm total thickness). A radiograph was then taken with the following settings: 40 KV, 4 mA, 20 ms exposure time. Two images were taken of each bearing: top view, and lateral view. The images were processed with MATLAB version 8.2.0.89 (R2013b) (The Mathworks Inc, Natick, Massachusetts, USA). The centres of the bearing concavity and the sensors were determined manually from the pixel coordinates of the images (Figure 5.7). The repeatability of finding the sensor locations was tested, and had an intra class correlation coefficient (ICC) of $r = 1.000$ (see Appendix B.2).

The mean position of each electrode was calculated, together with the 95% confidence interval (CI), using the Student-t distribution with N=18, assuming a normal distribution. The coordinate system that was used was anterior-posterior x, medial-lateral y, and proximal-distal (x). Similarly, the midpoint of the sensor foil was calculated by taking the mean of all the electrode coordinates. A calculation was performed to check if the height of the X-Ray source influenced the measurement accuracy (the 'penumbra effect', see Appendix B.1), but this effect introduced a maximum error of 0.0163 mm, which corresponded with $1/10^{th}$ of the pixel resolution of 0.168 mm, and

	x±CI [mm]	**y±CI [mm]**	**z±CI [mm]**
electrode 1	-2.25 ± 1.41	1.61 ± 1.73	3.30 ± 0.54
electrode 2	-2.23 ± 1.39	-1.00 ± 1.79	3.30 ± 0.54
electrode 3	0.39 ± 1.50	-0.96 ± 1.80	3.30 ± 0.54
electrode 4	0.38 ± 1.45	1.67 ± 1.75	3.30 ± 0.54
sensor assembly	-0.92 ± 1.43	0.33 ± 1.76	3.30 ± 0.54

Table 5.1: *x (anterior-posterior), y (medial-lateral) and z (distal-proximal) coordinates and their 95% confidence intervals (CI) for every electrode, and the complete sensor assembly. x and y are relative to the centre of the bearing concavity (Figure 5.7), and z in respect to the bottom of the bearing (5.6).*

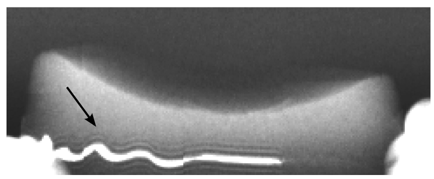

Figure 5.6: *Lateral radiograph of a bearing with an embedded sensor. Left = Anterior. The wavy transverse strain relieving pattern (see arrow) can clearly be observed in the sensor leads.*

therefore was ignored.

On average, the sensors were located slightly off-centre (Table 5.1). The sensor height was slightly below the desired height of 3.75 mm, on average approximately 0.5 mm, but this was not considered to be a problem. The height distribution 95% CI of ±0.54 mm was considered to be small, which indicates that the current technique of embedding sensors within a bearing functions adequately, especially because finite element simulations demonstrated that changing the vertical position of the sensor did not influence the capacitive change greatly (Figure 4.11).

5.4 Pre-Loading Measurements

During the pre-loading phase one body weight was placed on the sensor. Because of the viscous response of the bearing to a constant load, as discussed in Chapter 3, secondary creep (steady-state compression) occurs after a certain time interval. PI

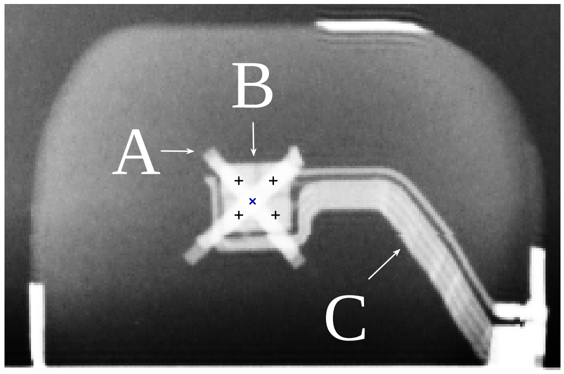

(a)

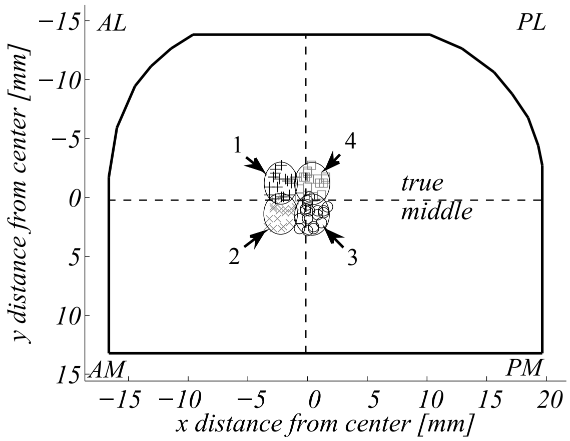

(b)

Figure 5.7: *(a) Bearing radiograph, top view, with (A) centre of concavity marker, (B) electrodes, (C) electrode leads, + marks the centre of each electrode, and × marks the centre of the bearing concavity. (b) Schematic view of the bottom view of the bearing, with centre of bearing concavity (dotted line), and each of the four electrode centres. The ellipses depict the expected centre for each electrode, at 95% confidence level. e1..4: the electrode numbers A=anterior, P=posterior, M=medial, L=lateral*

also shows creep/relaxation behaviour (see Section 5.3.1), for which the time constant was yet unknown. Additionally, the time for the bearing itself to reach a stable load response was unknown, because the shape of the bearing influences the stress/strain response (see Chapter 4). Therefore in this chapter, experiments were performed to determine the response of the bare sensor foil and the sensor foil embedded inside a bearing.

5.4.1 Methods

Loads were applied using a metal component with the same radius and width as a large femoral component (Biomet UK Ltd, Swindon, UK), mounted in a uniaxial hydraulic material testing machine (Dartec DC10, Zwick, Leominster, UK), controlled by TIAB software version SR2 v2.06.17 (TIAB ltd, Middleton Cheney, UK). Load data was sampled at 100 Hz, using a load cell (DSCRCM-15KN, Zwick, Leominster, UK, calibrated to 10 kN, resolution 0.5 N). For capacitive measurement, a Capacitance-To-

Digital (C2D) converter was used, the AD7746 v2.2.2 (Analog Devices Inc, Norwood, MA, USA). Upon request from the author, the manufacturer provided the source code for the software, and the software was adapted by the author to automatically zero capacitance offset at the onset of the measurement using the built in CAPDAC of the AD7746, log capacitance data with time stamps, and measure with a data rate of 90 samples per second. In all experiments, to lower the measurement noise, the C2D was galvanically isolated from the computer, using the ADUM4160EBZ USB optoisolator (Analog Devices Inc, Norwood, MA, USA). The C2D system was electrically grounded to the hydraulic test machine. The sensors were connected to the C2D using shielded leads. The C2D system was enclosed in aluminium enclosures. Room temperature was measured by an external thermocouple temperature sensor. All measurements were performed at room temperature. Before the start of an experiment, all equipment was allowed to warm up for 10 minutes. **The identical setup was used as depicted in Figure 2.3.**

To measure the time in which a quasi-stable compression rate is reached, a creep test was performed with the bare sensor foil and the embedded sensor.

Five different sensor foil samples were used, and of a total of 20 repeats. For the foil loading, a static load of 100 N was applied for 3 minutes. Five different bearings were used, and of a total of 36 repeats. For the bearing loading, a static load of 392.5 N was applied for 15 minutes.

5.4.2 Results

Bare Sensor Pre-loading

A typical pre-loading change of capacitance is shown in Figure 5.8. After 5 to 10 seconds, the capacitance was within 5% of the capacitance value (Figure 5.8b) that was measured at the end of the experiment The median of the loading increased over time.

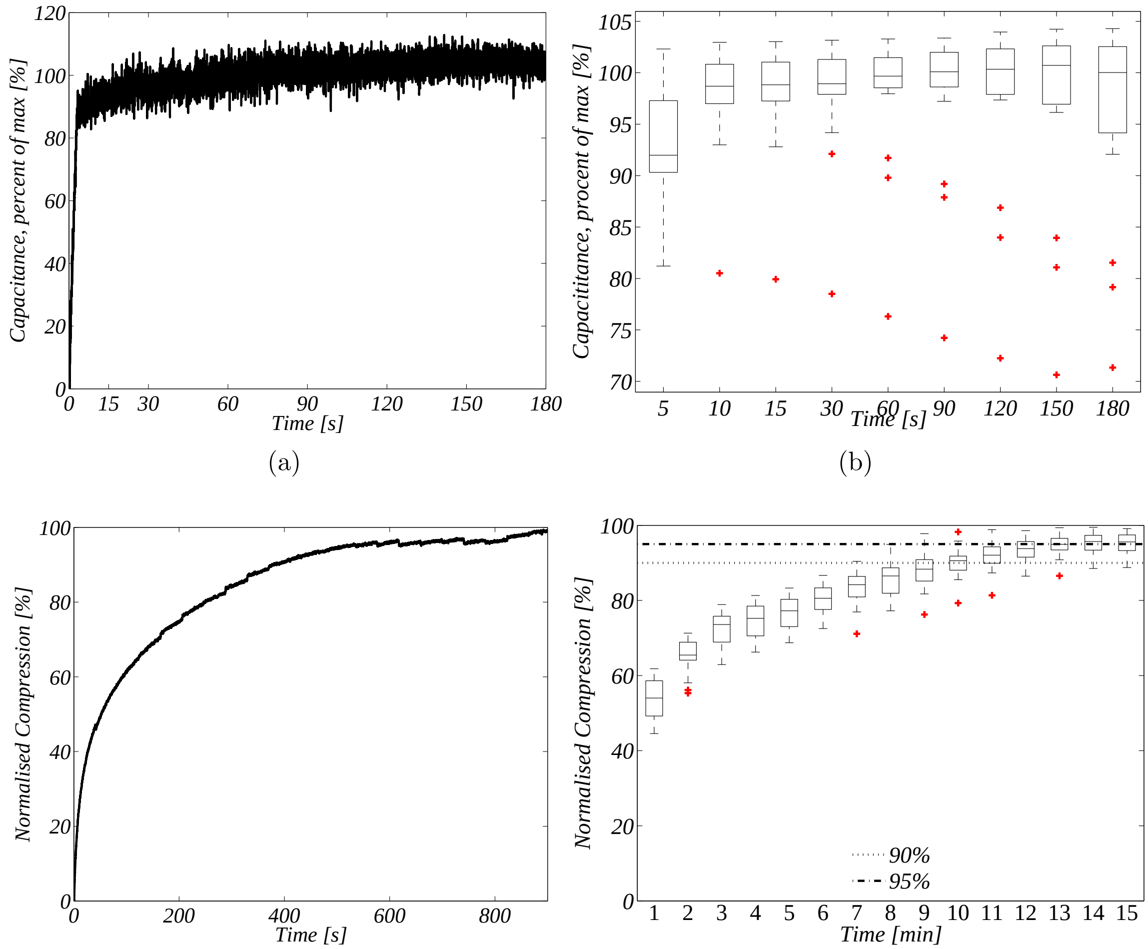

(a) (b) (c) (d)

Figure 5.8: *Pre-loading of the sensor foil and the bearing, with the y-axis normalised so that no load equals 0% and full load equals 100%, (a) a typical measurement for sensor foil, and (b) all measurements grouped. (c) a typical measurement for one sensor embedded within the bearing, and (d) all bearing measurements grouped.*

Bearing Pre-loading

A typical pre-loading change of capacitance is shown in Figure 5.8. After an initial rapid increase in compression, after 13 minutes the value was within 5% of the capacitance value that was measured after 15 minutes.

5.4.3 Discussion

Bare Sensor Foil

The foil sensor itself reached a quasi-steady state value within 5 to 10 seconds. During this phase, compression continued in an approximately linear fashion. At this point it was unknown how long this linear compression phase will continue, and if this linear compression stage will decrease after repeated use. This was something that may be investigated in the future.

Bearing Compression

15 minutes of loading was sufficient to reach a quasi-static compression of the bearing. This is in line with the findings of Chapter 2.

The results showed that PI responds far quicker to load than UHMWPE. That means that in a situation when a sensor made from PI is embedded in UHMWPE, the limiting factor that determines how much time is required before measurement is equal or greater than the minimum time that UHMWPE required to reach a quasi-stable compression state. In the bare foil measurements, over time the spread widened, and there were also some decreasing capacitance curves. This was probably due to slow drifting of the C2D. How much this was influencing measurements is something that has to be investigated in the future.

5.5 Dynamic Sensor Characterisation

5.5.1 Introduction

The hypothesis was that once the material is pre-loaded, all dynamic loads occur at a sufficiently high frequency that the elastic response to the load dominates, and the viscous response can be ignored (see Chapter 3).

This section describes the experiments that were performed to find out if the elastic response is linear over the relevant frequency range of loading.

5.5.2 Background

With an ideal load sensor, the frequency transfer would be completely flat from 0 Hz to infinity, but every physical sensor is frequency limited. For this application, the sensor should ideally be *low pass*; all frequencies up to a certain corner frequency should be unattenuated, and for frequencies higher than that frequency attenuation should commence.

A first order low pass filter has the following transfer function (Equation 5.1):

$$H = \frac{\omega_n}{\omega_n + 1} \tag{5.1}$$

in which:

ω_n	Corner frequency of the transfer function, $\omega = 2 \times \pi \times f$ [rad/s]

and a second order low pass filter with two poles at the same corner frequency has this transfer function (Equation 5.2):

$$H = \frac{\omega_n^2}{\omega_n^2 + \frac{\omega_n}{Q} + 1} \tag{5.2}$$

in which:

ω_n	Corner frequency of the transfer function, $\omega = 2 \times \pi \times f$ [rad/s]
Q	Quality factor

In the first part this section, the experiment is described in which sine waves with a frequency of 0.1 to 10 Hz were applied to the bare sensor foil and the bearing to measure the frequency response.

The second part of this section deals with finding out if any harmonic distortion takes place. In case of harmonic distortion, during stimulation with a frequency $f1$, a frequency $f2$ and possibly $f3..fx$ are generated which are a multiples of $f1$. Harmonic distortion is common in case of nonlinear transfer relationships. An ideal sensor would have no harmonic frequency generation.

5.5.3 Methods

Frequencies from 0.1 to 1 Hz in steps of 0.1 Hz and 1 to 10 Hz in steps of 1 Hz were applied to the bare sensor foil and the embedded sensor, each for 10 seconds, and the resulting capacitance was measured. The experiment was performed with the setup described in Section 5.4.1

Foil Frequency Response Measurements

5x5x5 mm glass cubes were bonded to 5 sensor foils with poly-acrylate adhesive. The glass cubes were used to separate the metal actuator of the testing machine from the electrodes, and also to ensure that stress was applied evenly to the electrode area alone, not the area surrounding the electrode. A static load of 100 N and a dynamic sine wave load of ±33 N peak were applied to the glass cube, where a compromise was made between applying a load that was as low as possible, yet high enough to exceed the system noise, which consisted mainly of actuator system noise.

Bearing Frequency Response Measurements

First, a static load of 390 N was applied for 15 minutes. This was followed by a test to obtain the frequency and phase diagrams as described in Paragraph 5.5.4; a static load of 390 N and a dynamic sine wave load of ±3/4 * 390 N peak were applied.

The sensors that were used were sensors labelled B, G, L, O and Q, 5 sensors of the group of sensors created in “iteration 3”. The sensor locations were all within 2 mm of the centre of the bearing concavity (Figure 5.9).

For alignment of data, each sine wave was alternated with an alignment square wave, as described in Appendix B.4. A MATLAB script was written for data processing; First the datasets were aligned and then to each frequency, a single sine model was fitted. From the fitted model, the magnitude difference and average phase delay be-

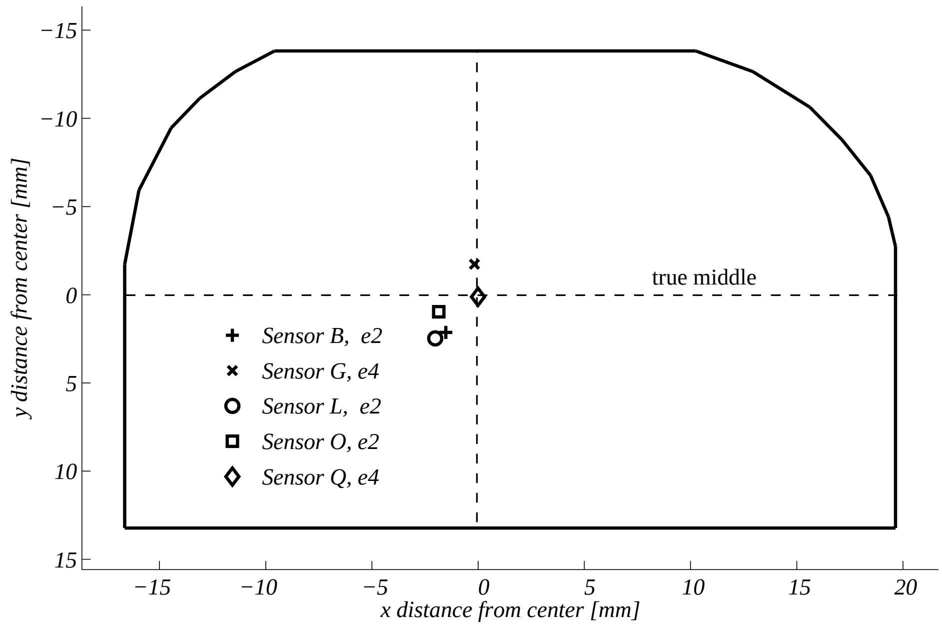

Figure 5.9: *The location of the electrodes, determined from the radiograph, such as in Figure 5.7.*

tween load and capacitance was obtained. Furthermore, the phase difference between the load frequencies and capacitance data was calculated.

Spectral Analysis

To further determine the frequency response, in MATLAB, spectral analysis (SPA) method was used to determine the transfer between the applied load and the resulting capacitance. Using the transfer function graph, the approximate characteristics of the transfer were determined graphically. The second order filter characteristics were determined using Equation 5.2. Each measurement was repeated 11 times. The individual spectra were averaged, and the averaged spectrum was smoothed with a smoothing parameter of 20, which was determined manually in order to smooth the peaks yet not deviate from the 0 dB too much. For input of the SPA algorithm, gait loading and capacitive data was used.

Harmonic Distortion Analysis

Additionally, a dual sine wave model was fitted to the measurement data, with amplitude and phase calculation that was independent from the first sine wave. An example of that is shown in Figure 5.13.

5.5.4 Results

Measurements Overview

Figure 5.10 shows the full measurement cycles for the bare sensor and embedded sensor. The measurement starts with a pre-loading phase, followed by sine waves, for the embedded sensor also followed by gait waves and step up/down waves, and finally unloading. Figure 5.10b shows that that the capacitance slowly increases during the pre-loading phase, and continues to increase during the sine waves, gait, and step up/down phases.

Frequency and Phase Response Measurements

The amplitude of the bare sensor foil did not deviate more than 0.5 dB from 0 dB up to 2 Hz, after which the median of the amplitude dropped in a linear fashion. The slope was approximately *-1.5 dB/Decade* (Figure 5.11a). The amplitude of the embedded sensor did not deviate more than -0.7 dB from 0 dB up to 1 Hz, after which the median of the amplitude dropped off in a linear fashion. The slope was approximately *-2.6 dB/Decade* (Figure 5.11b).

The phase of the sensor foil was just above 0 degrees up to 1 Hz, and then decreased to approximately -3 degrees at 10 Hz. The phase of the embedded sensor foil was approximately 15 degrees up to 1 Hz, and dropped off to approximately -30 degrees at 10 Hz.

SPA Calculated Frequency Response

The individual spectra using SPA are all plotted superimposed in Figure 5.12. Above 8 Hz, the individual calculated spectra had sharp peaks, but the spectra av-

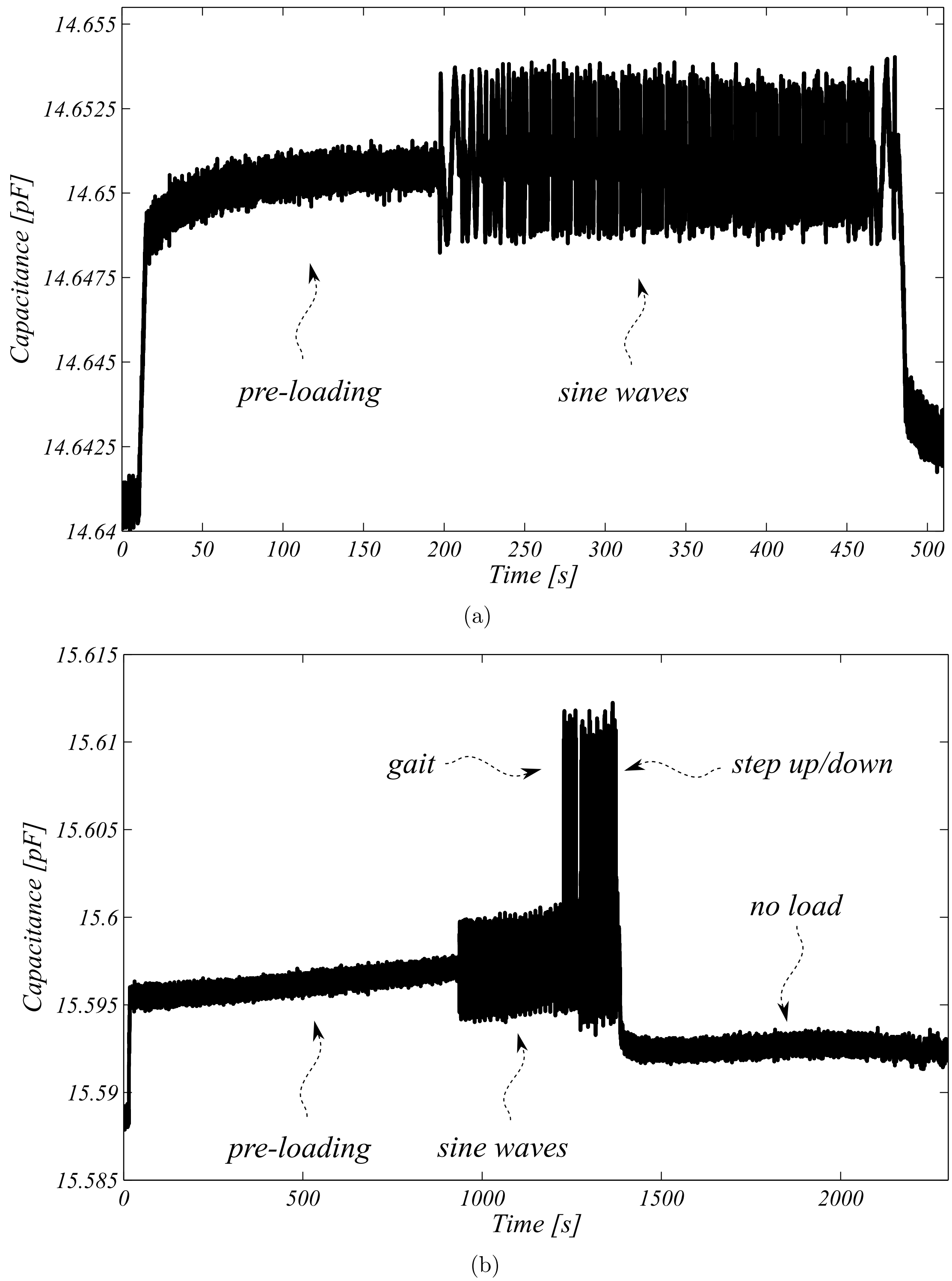

Figure 5.10: *A full measurement cycle of the loading test (a) for the bare sensor, and (b) for the embedded sensor, with 15 minutes of pre-loading, followed by sine waves for transfer function measurement, five repetitions of the gait signal and five repetitions of the step up/down signal, followed by post-loading for 15 minutes.*

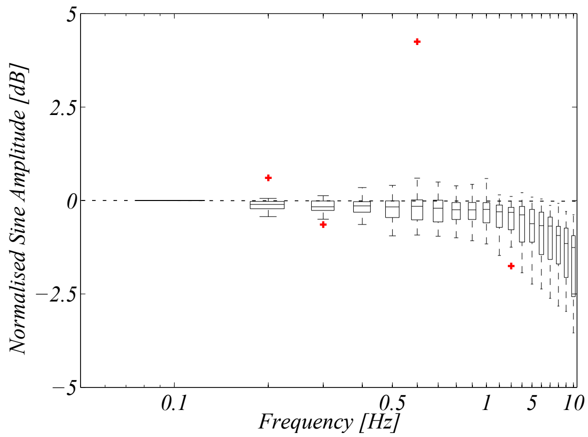

(a)

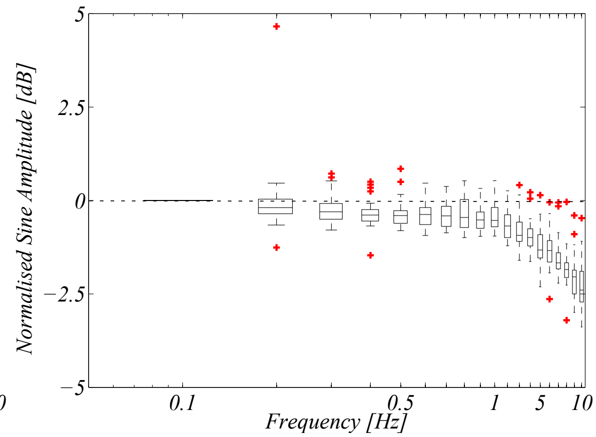

(b)

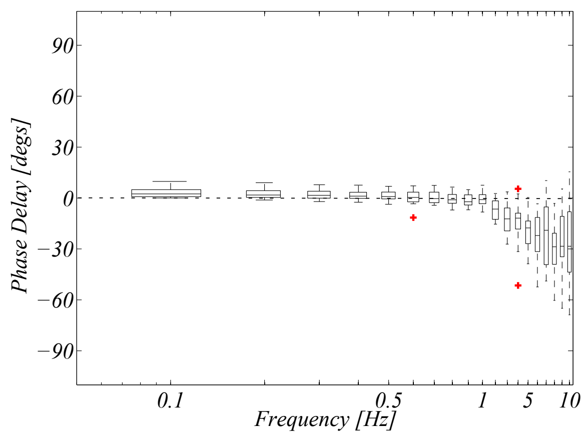

(c)

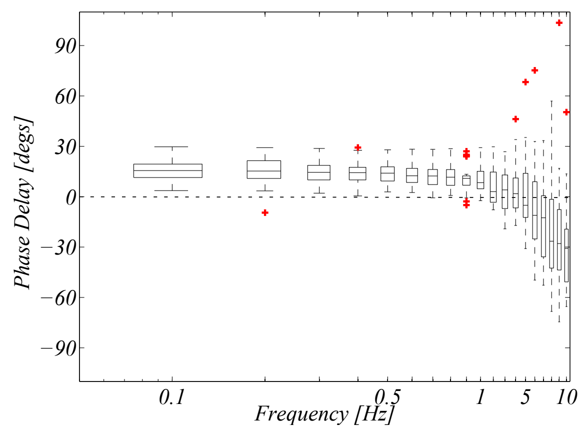

(d)

Figure 5.11: *Frequency spectrum from 0.1 Hz to 10 Hz, with (a) amplitude of the bare sensor, (b) amplitude of the sensor embedded within the bearing, (c) phase diagrams for the bare sensor, and (d) phase diagram for the sensor embedded within the bearing.*

eraged out to a much flatter response. The help lines show 0 dB, -40 dB, and the -40dB/dec relationship. In Figure 5.12(c), the measured amplitude response, as well as the simulated transfer functions with several Q are shown. A second order response with Q=0.707 fitted the data most accurately. The measured phase response and several simulated phase responses are shown in Figure 5.12(d). In this case a second order response with Q=3 fitted the data most accurately.

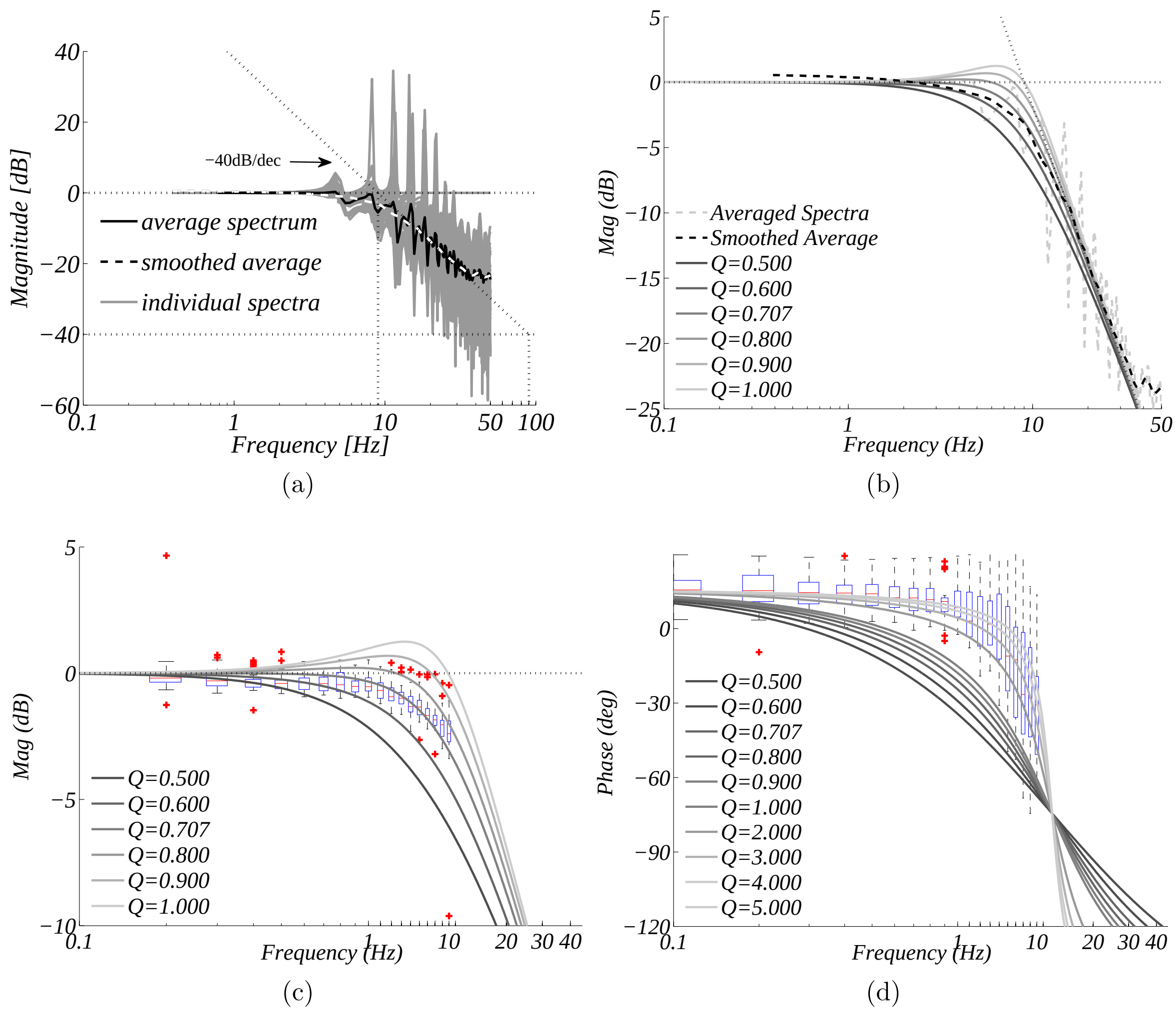

Figure 5.12: *(a) Calculated frequency spectra with SPA and their average of all measurements with associated interpretation lines; the grey peaks are all the individual calculated spectra. The black line is the average of those spectra, and the white dotted line is the smoothed average. In (b), the averaged and smoothed average of the spectra are shown, and superimposed the simulated second order transfers for a corner frequency of 9 Hz and several Q factors. (c) Dampening for a frequency transfer with a corner frequency of 9Hz and several Q values for the measured amplitude data and several simulated transfer functions with various Q factors, and (d) the measured phase data and several simulated phase responses with various Q factors.*

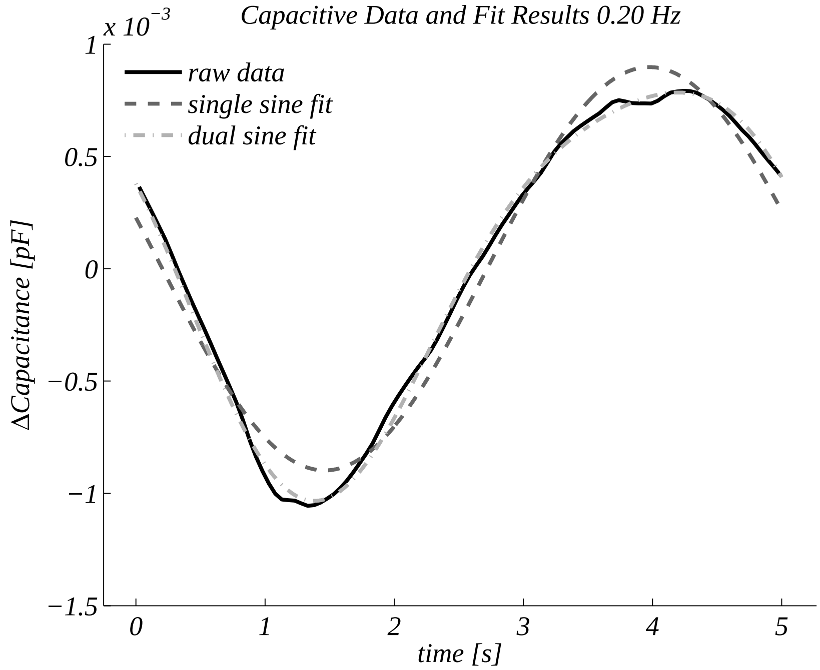

Figure 5.13: *An example of fitting a waveform (raw data) with two sine wave fits, one in which a single sine wave frequency was fitted, and one in which two sine waves are fitted.*

Harmonic Distortion Measurements

An example of fitting a single and dual sine wave fit to raw data is shown in Figure 5.13. In this particular case, the dual sine wave fitted the data more accurately than the single sine fit.

After applying a loading signal with a frequency f_1, the measured capacitive signal had the original frequency f_1 plus a second frequency f_2, at twice the frequency of f_1, also called the second harmonic (Figure 5.14). This harmonic frequency had a median amplitude of approximately 20, or 5% of the first harmonic for the bare sensor foil, and 20% for the embedded sensor. Above 8 Hz only the first harmonic was found.

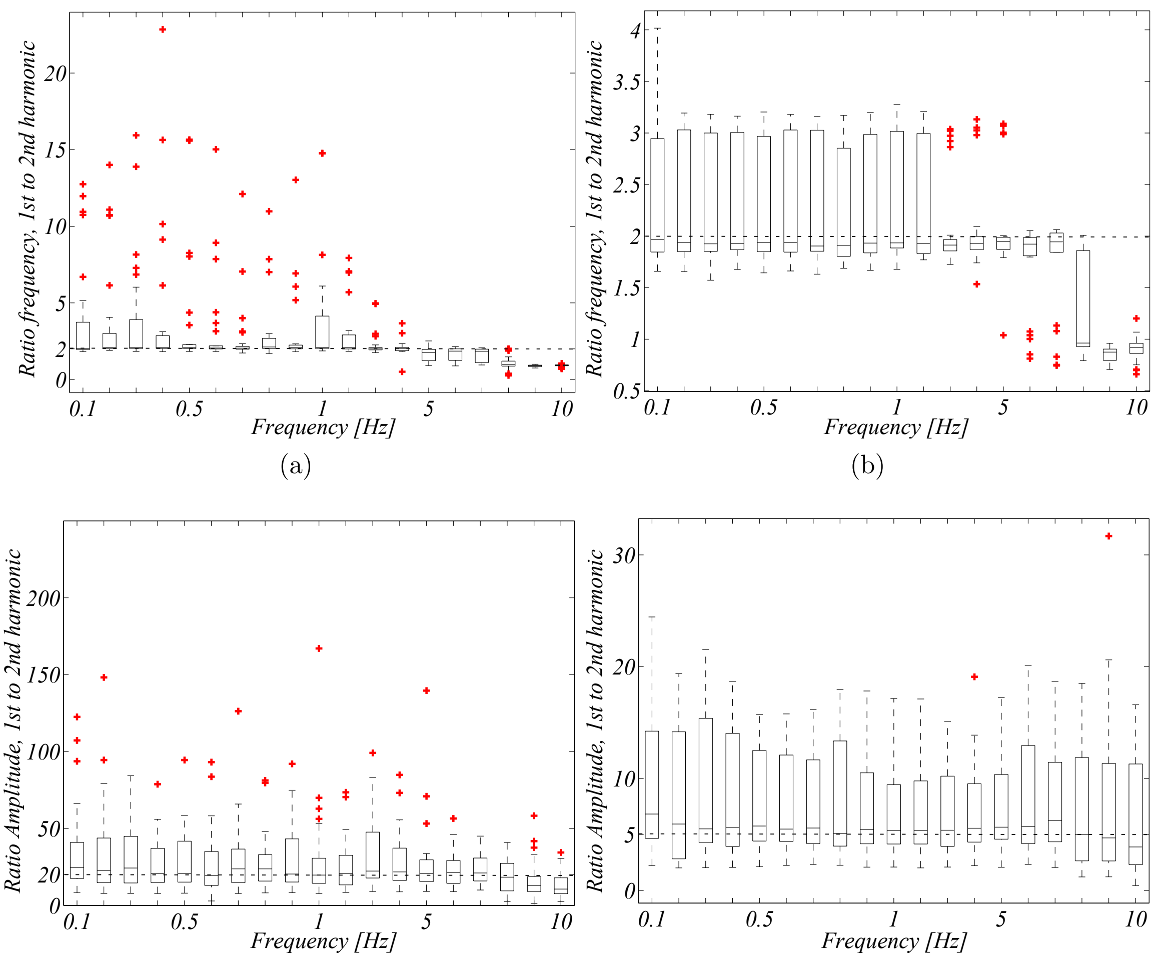

(a) (b) (c) (d)

Figure 5.14: *Results for the dual sine wave fitting (an example shown in Figure 5.13): the ratio of the frequencies for (a) the bare sensor, and (b) the embedded sensor, and the ratio of the amplitudes for (c) the bare sensor, and (d), the embedded sensor. The dotted line shows the best fit to the means of the distributions, which lies at 2x for the frequencies, indicating that for most dual frequency fits, the second sine that was fitted had twice the frequency of the first sine. Amplitudes: for the bare sensor foil the second harmonic had 1/20× or 5% of the amplitude of the first, and for the embedded sensor, the second harmonic had an amplitude that was 1/5× or 20% of the amplitude of the first.*

5.5.5 Discussion

Sensor Frequency and Phase Characterisation

There was a difference between the phase response of the bare sensor and the embedded sensor, most notably an increased constant phase lead of 15 degrees, which manifests itself as a delayed response to loading. This delayed response can only be caused by the UHMWPE (Figure 5.11b and d).

The amplitude magnitude decreases after approximately 1 Hz for both the bare sensor foil and the embedded sensor (Figure 5.11a and b). This was not a typical first order low pass filter behaviour. If that were true, then the slope of the amplitude decay above 1 Hz would be -20dB/dec. Therefore, the transfer characteristic had to be of a higher order.

Individual SPA spectra showed a lot of vertical peaks (Figure 5.12a), which were attributed to the decreasing magnitude of the sensor amplitude over 9 Hz and the associated reduced signal to noise ratio. Therefore these peaks were dismissed as artefacts of the SPA calculation, and they largely disappeared after averaging. The slope of the averaged and smoothed transfer characteristic was -40 dB/dec, indicating a 2nd order filter. This can clearly be seen in Figure 5.12a and b: the -40 dB/dec line crosses 0 dB at 9 Hz and -40 dB at 90 Hz. Simulated second frequency responses with fixed corner frequency of 9 Hz made apparent that a Q in the range 0.6 to 0.707 was the most likely quality factor (Figure 5.12b and c), since a Q of 0.707 occurs within a *critically damped* system, where the resulting peak at the corner frequency does not exceed the 0 dB line, meaning that there is no amplification of the applied load signal.

The Q factor also determines the phase behaviour, and the measured phase behaviour should be identical to the simulated phase for a Q of 0.6 to 0.7. Unfortunately, similar to the frequency response calculated by SPA, there were a great number of peaks in the calculated phase diagram, and because phase was bound between 0° and 360°, averaging the phases did not result in a useful average phase plot.

Simulated phase relationships for various Q factors (Figure 5.12d) indicated that for phase the best Q was in the vicinity of 3 to 4, contradicting the Q factor determined earlier. However, the phase fit did confirm a corner frequency of 9 Hz, since it matches the simulated phase transfers. It was unclear what caused such an apparently high Q in the phase measurement results. This could be caused by the complex dynamic behaviour of UHMWPE, introducing an additional phase lag. The sensor can be modelled by a second order low pass filter, with unity gain, a corner frequency of 9 Hz and a Q factor of 0.707. *This answers Aim 4: Determine the frequency transfer function of the sensor.* This is suitable for measuring physiological signals, given that 99 % of the frequency power lies below 5 Hz (Section 5.6.3).

In case the frequency response needs to be determined more accurately, the sine wave measurement should be repeated with higher frequencies. However, the current C2D was limited to a maximum measurement frequency of 90Hz, practically limiting the measured frequency to 10 Hz. Therefore, more sophisticated equipment will have to be used in future studies.

Harmonic Distortion

A second harmonic of 5% for the bare sensor foil was not very large and may be ignored, but a second order harmonic with an amplitude of 20% was large for the embedded sensor. Harmonic frequency generation is caused by the nonlinear load-strain relationship. The influence of this non-linear distortion may have a result on the shape of the loading signal. The response to physiological loading signals is analysed in the next section. A limitation was that above 8 Hz the method stopped working accurately; only the first harmonic was found. This was most likely due to signal to noise issues, rather than the absence of second order frequency generation.

5.6 Sensor Response to Physiological Loading

5.6.1 Introduction

To determine how the embedded sensor responded to common physiological signals such as gait and step up/down loading, experiments were performed. The main question was: how repeatable were the measurements?

5.6.2 Methods

Gait and step up/down data were obtained from Bergmann et al [42, 43] and normalised to an average BW for one condyle (see Section 1.7 for more information about the definition of one BW) by correcting for a different subject body weight, and divided by 2 for the load per condyle. The identical test setup was used to the one described in Section 5.4.1.

Five bearings (B, G, L, O and Q) were used. Each measurement was repeated 11 times.

Loading Protocol

For all gait and step up/down tests, first one BW was applied for 15 minutes, followed by the sine wave test, and then each gait and step/up down signal was applied 5 times, directly followed by an alignment wave. At the end, the experiment was specimen was left for 15 minutes with no applied load (Figure 5.10). In MATLAB, each gait and step/up down cycle was aligned and averaged to calculate the mean.

Data Fitting

Each pair of load corresponding capacitive samples was sorted according to increasing capacitive magnitude and to the resulting data set a first order relation was fitted, in order to calculate the slope and intercept of the relation to estimate load from capacitance. For the fit, a robust estimator was used.

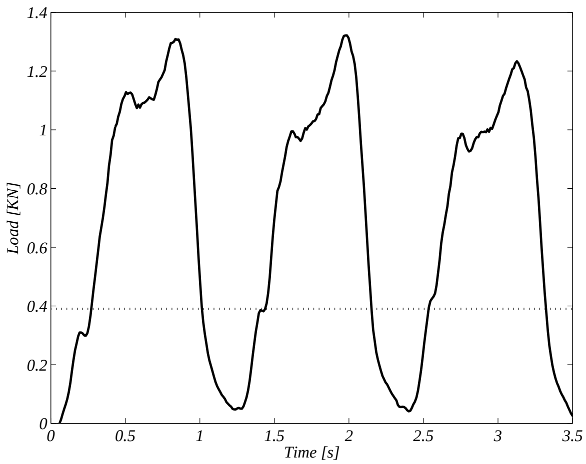

(a)

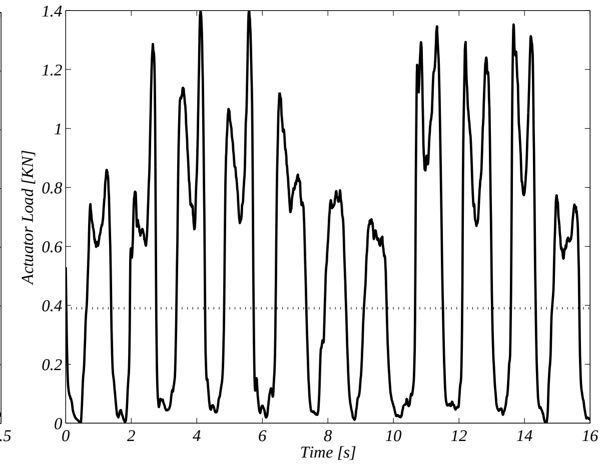

(b)

Figure 5.15: *Loads for gait (a) and step up/down (b). The dotted line depicts one body weight.*

5.6.3 Results

The gait and step up/down loads are shown in Figure 5.15. The dotted line shows the pre-loading weight of 392.5 N (1×BW). Therefore, the loading below that line represents unloading in respect to the dotted line. The maximum load of gait represents approximately 3 BW and for step up/down approximately 4 BW. The step up/down loading waveform had faster changes than gait.

For some sensors, the curves of the capacitance and load overlap more accurately in *magnitude* than others (Figure 5.16); for others, the maximum capacitance reaches comparable magnitude, but the minimum capacitance value varies.

Additionally, for some sensors, the curves of the capacitance and load overlapped more accurately in *time* than others (Figure 5.16); in some sensors the capacitance value corresponding to a peak in load occurred after a delay, whereas the capacitance value corresponding to the minimum load occurred within a shorter time interval or with no delay (Figure 5.17). There seemed to be no difference in the low peaks, but for the high peaks, either a large difference or no measurable difference from zero delay was found.

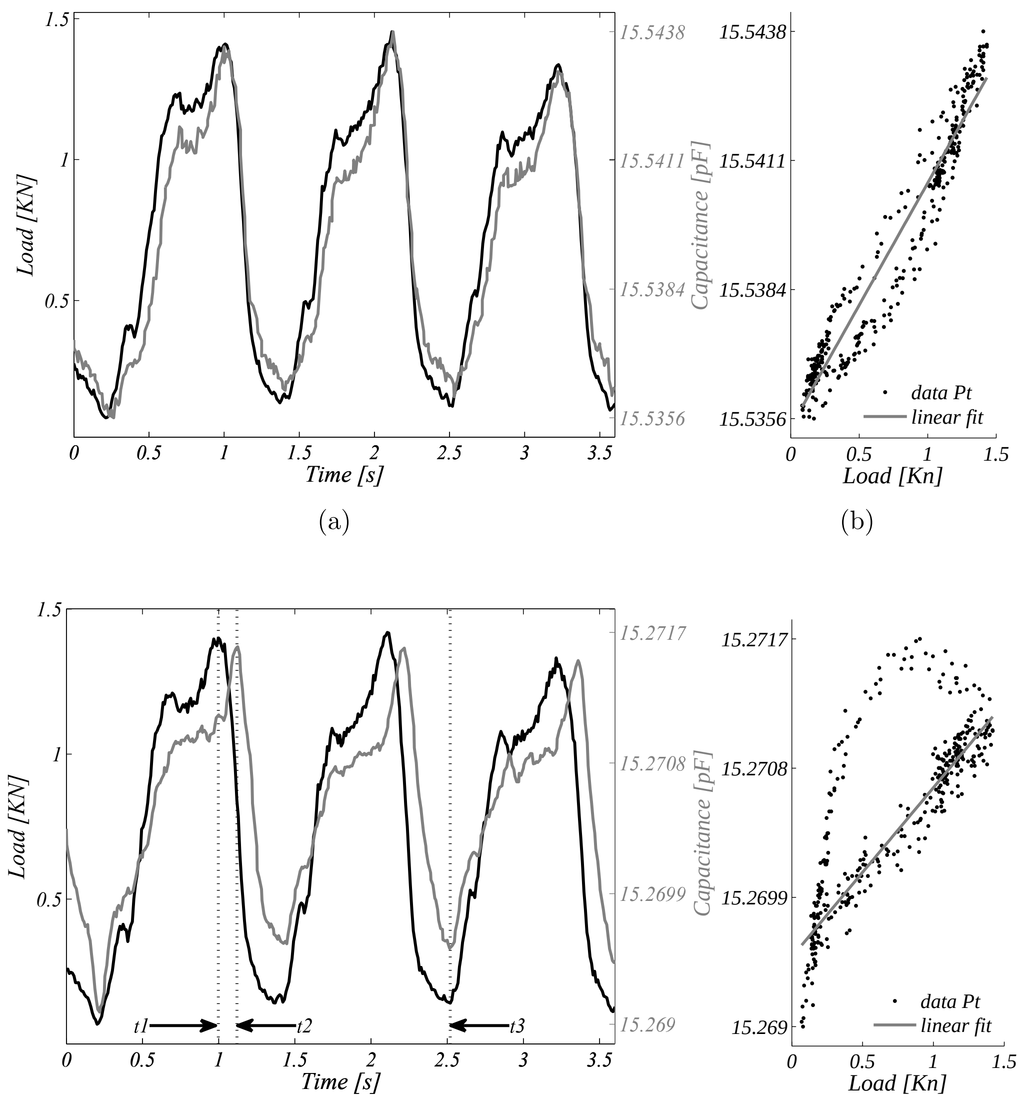

Figure 5.16: *Raw data of (a,c) load and capacitance vs time for gait and (b,d) load vs capacitance for two different sensors, showing a delay between load and capacitance in some sensors. t1-t3 corresponds to a local peak in the load or capacitance value.*

All the Gait and Step up/down results data can be seen in Appendices B.5 and B.6

5.6.4 Discussion

In some cases, the shape of the load-capacitance point cloud was fairly narrow around the approximating first order fit, but in other cases, the cloud widens, partially as a result of the lag in time of the capacitance behind the load (Figure 5.16). The lag time was virtually absent at the unloading minimum, but for some sensors, was considerable at the loading maximum. Since the lag occurs for a sensor that was exactly in the middle (Figure 5.9), but also for a sensor that was further away from the centre, so at first glance the lag magnitude does not seem to be connected to the location of the sensor. However this has to be verified with a larger number of sensor locations.

If it were related to the distance of the sensor from the centre of the bearing, it would probably be related to a combination of a different femoral component (FC) radius and bearing concavity radius, and the sensor being off centre: in case the FC conforms to the radius of the bearing concavity, at every point of the loading cycle, the contact area of the FC and the bearing was constant. This results in a direct load to capacitance relationship. Because the bearing has a larger concavity radius than the FC then only the centre of the bearing would always be contact with the FC, and area on a line radially away from the centre would only come in direct contact with the FC in case of higher loads (see Chapter 4, 4.6). However, this is part of future research.

This behaviour could also explain a changing relationship between load and capacitance; due to the complex relaxation behaviour of UHMWPE, temporarily the material at the centre may compress (relax) and decompress (regain former shape/stiffness) under the influence of a loading pattern. In that case, material located radially away from the centre may only experience direct contact with the FC after one compressive cycle has passed leaving the material directly under the centre compressed. These behaviours are very complex and make the process of estimating the load on the entire

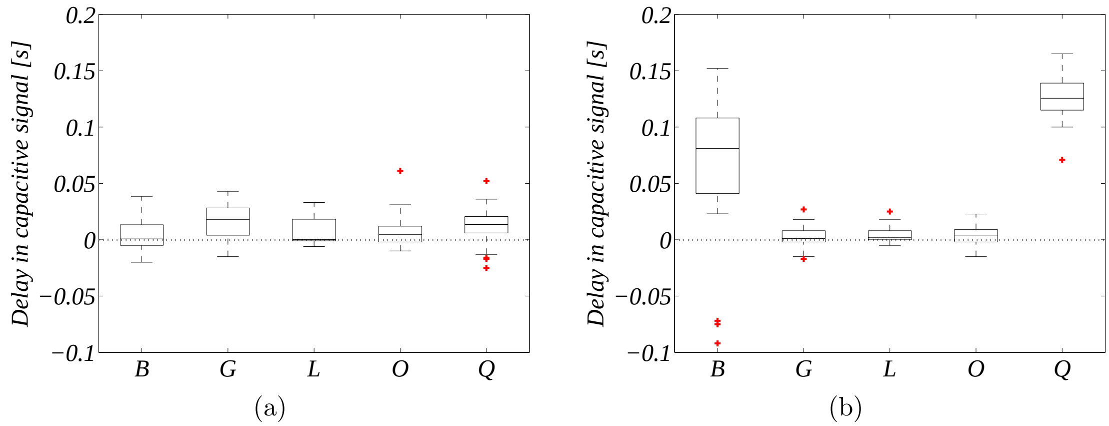

Figure 5.17: *Delay values per sensor between the peaks for gait loading (Figure 5.16), for (a) the three low peaks and (b) the three high peaks for every sensor.*

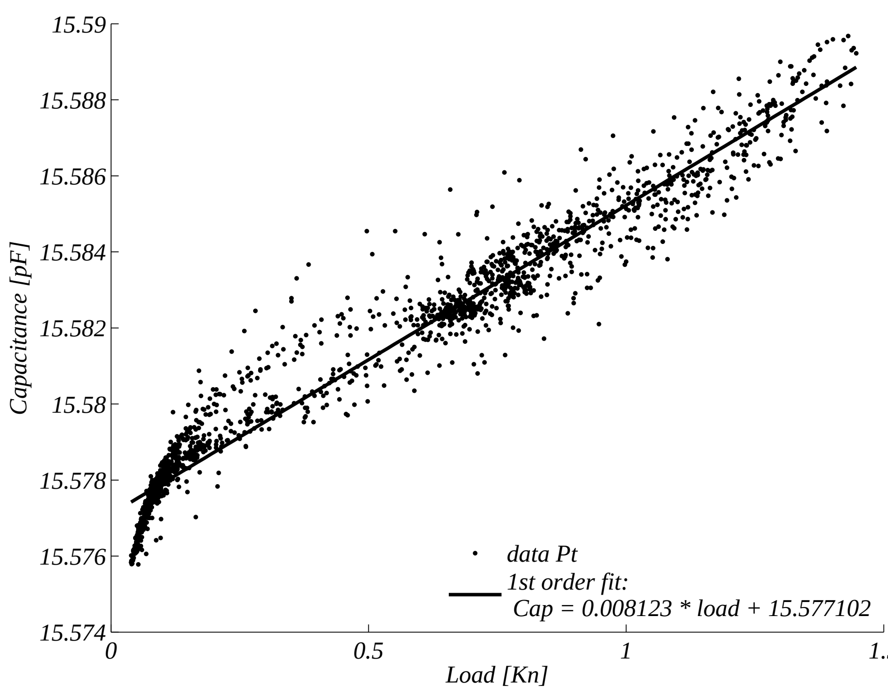

Figure 5.18: *Example of x-y plot of load vs capacitance, with 1st order best fit.*

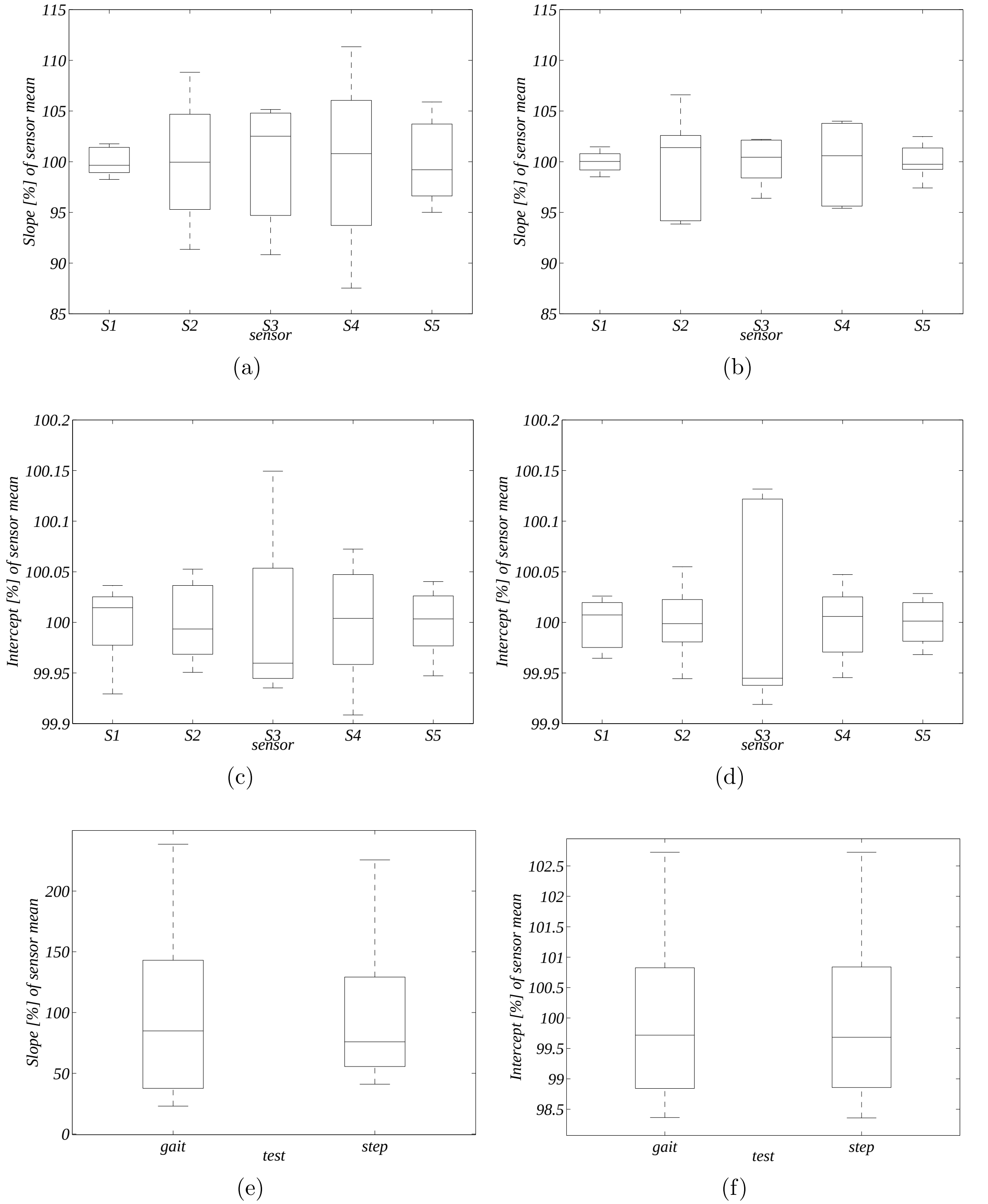

Figure 5.19: *Results for first order fit of load vs capacitance: (a) gait slope and (b) step slope, (c) gait intercept and (d) step intercept, (e) all slopes, and (f) all intercepts*

bearing difficult, however on the other hand, it gives a direct insight on the conditions that UHMWPE experiences under influence of shape and dynamically changing loads.

Slope and Intercept

Assuming that the slope and intercept are constant was only approximately true. In Figure 5.19a-b can be seen that the slope varies typically by approximately 10 % within one sensor. Therefore, should the slope be used to estimate capacitance from load, the load measurements would have an error of typically approximately 10 %. There was a large difference between sensors. In Figure 5.19e can be seen that every sensor had to be calibrated individually, because the slopes differ considerably between sensors. The intercepts (Figure 5.19c-d-f) do not change that much, however they change too much for an accurate estimation if they were to be used in the simplest load estimation by using a lookup table to estimate load from capacitance. Even during the measurement the baseline capacitance slowly changes (Figure 5.10b); therefore, to get a proper signal, the intercept has to be dynamically determined by establishing when the patient is not moving, and re-calibrating the intercept. In case this method were used, the average load estimation error would be 10 % or less. However, there are ways to improve these results, and they are discussed in the following paragraph.

5.7 Load Estimation

5.7.1 Introduction

The previous sections described the sensor characteristics. This section describes how measured sensor data can be used to estimate the load.

5.7.2 Theory

Chapter 2 described the static and dynamic properties of UHMWPE. Based on that information, for the estimation of load these assumptions were made; 1) the creep behaviour of UHMWPE and PI is repeatable and stable once 15 minutes of waiting time is observed prior to the actual measurement; 2) after this time also the dynamic behaviour of PI and UHMWPE is stable and repeatable; 3) the static or constant load acting on the sensor between dynamic loading is constant, with a magnitude of 1×BW.

If condition 1 is met, then any time that there is no dynamic load acting on the sensor, the sensor value will become constant, because of condition 3. Therefore, constant load can be determined during measurements. If condition 2 is met, then the magnitude of the estimated load signal will be correct.

5.7.3 Methods

Gait and step up/down data were obtained from www.orthoload.com [42, 43] (accessed 27th June 2012, file name: k1l110108_1_80p_gait.akf, and k5r_060809_1_58p-step_up_step_down.akf, both measured with an instrumented TKR) and normalised to an average BW for one condyle (see Section 1.7 for more information). For all gait and step up/down tests, first 1×BW was applied for 15 minutes, and each gait and step/up down signal was applied 5 times, directly followed by an alignment wave. For the dynamic estimation of load, only the first and last alignment wave were used to align the load data and capacitance data together. This resulted in a dataset with five repeated gait patterns, interspaced with zero load and an alignment wave. All load data was filtered using a 10th order low pass Butterworth filter at 20 Hz, and all capacitance data was low pass filtered with a 10th order low pass Butterworth filter at 10 Hz. All data was processed with MATLAB.
Five bearings (B, G, L, O and Q) were used. Each measurement was repeated 11 times.

Two methods of estimating load were compared;

Linear Estimation

In linear estimation (LE), the slope of the first order relationship between load and capacitance was used. The capacitance and load measurement data was detrended by subtracting the mean. The first order relationship was determined using a robust fit. The detrended capacitance data was multiplied by the slope. This data was then shifted back to the correct load level by adding the difference between the estimated load data at zero dynamic load points within the data, and the assumed 1BW load at those zero dynamic load points.

Dynamically Modelled Estimation (DE)

MATLAB had the option of automatically determining the dynamic response of an unknown system if the input (load) and output (capacitance) data were given, using the System Identification Toolbox. In dynamic system charactarisation, the capacitance was given as the input and load as the output. The dynamic system order was fixed to 2. Then the capacitance and load data was detrended, and the detrended data was used with the estimated signal, to estimate load. This data was then shifted back to the correct load level by adding the difference between the estimated load data at zero dynamic load points within the data, and the assumed 1×BW load at those zero dynamic load points.

Comparison of the Estimation Methods

For both LE and DE, the parameters to estimate load (slope for LE and the system matrices A, B, C and K for DE) were determined. This is called characterisation. Then, the average system parameters were calculated by taking the medians of the characterised system using gait data (called Median of Gait characterised Parameters, or MGP), and additionally, the average system parameters were constructed by taking the medians of the characterised system using step data (called Median of Step characterised Parameters MSP).

Three result outcomes were generated per test:

O1) for every experiment the system was characterised, and the load was estimated using the same experiment data. This method can not be used in real life, but served only to provide an optimal measure for comparison. This parameter was called an 'individual' result.

O2) for every gait experiment, the MGP was used to estimate load, and for every step experiment, the MSP was used to estimate load. Results from this method are labelled for instance lgg, standing for Linear method, estimating Gait load, using Gait charactisations.

O3) for every gait experiment, the MSP was used to estimate load, and for every gait experiment, the MGP was used to estimate load. Results from this method are labelled for instance lgs, standing for Linear method, estimating Gait load, using Step characterisations.

Option 3 is most representative of a real situation, where a system is characterised on data and later used to estimate load with other data.

For comparison between estimated and applied load, the Normalised Mean Square Error (NMSE) was used; the NMSE was subtracted from 1, which represented a perfect fit.

Level-Shifting Data

For both LE and DE, detrended data was used for the input. Therefore, after estimation, the data had to be 'level shifted' back to the correct load level. This was performed by identifying time instances where there was no change in load (representing a person standing still), measuring the load at those instances for both the input load data and the estimated load data, and subtracting the difference of those loads from the estimated data, effectively shifting the estimated load data back to the correct level.

The data that was shifted back was also compared with the input load data using the method described in the previous section.

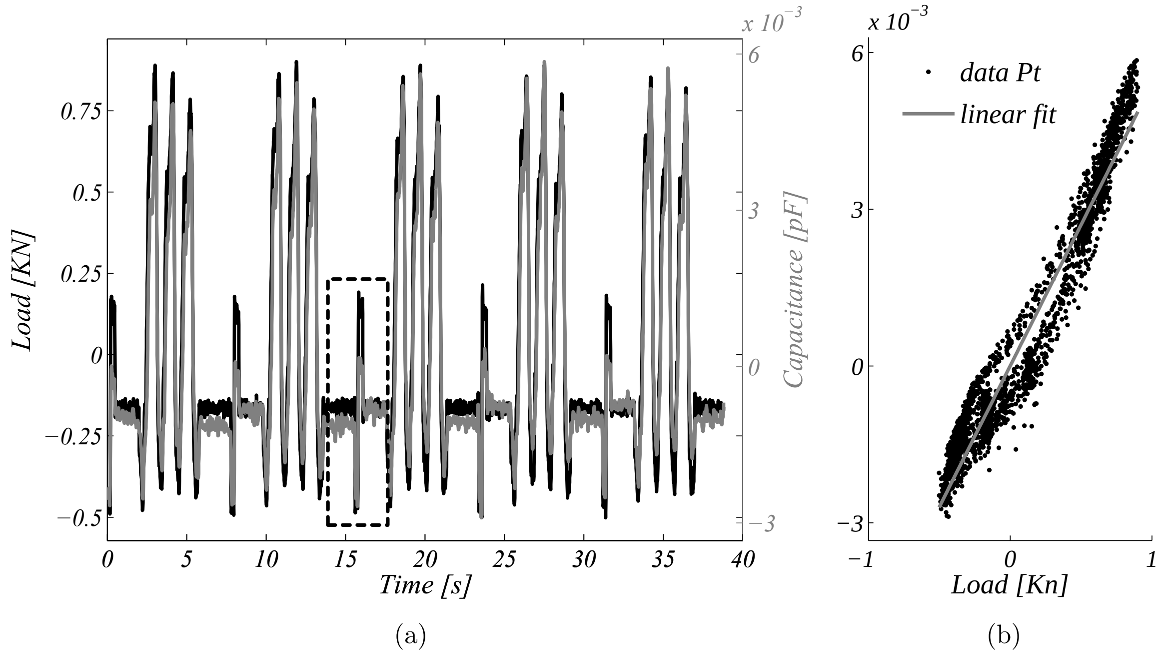

Figure 5.20: *Low pass filtered and detrended data of (a) load and capacitance vs time for gait and (b) load vs capacitance x-y plot. In (a), each gait cycle was interspaced with 'no load' and a synchronisation square wave (stippled box)*

5.7.4 Results

The detrended data was not centred around zero load, but above that (Figure 5.20a); -162 N for gait and -130 N for step up/down.

Furthermore, at a zero load level, interspaced with a calibration wave, the capacitance magnitude tended to be lower prior increased load, and slightly higher afterwards. This is clearly visible around the "synchronisation waves" shown in Figure 5.20a (the stippled box, see Appendix B.4 for more detail on synchronisation).

The load versus capacitance curve shows hysteresis, the same behaviour as discussed in Section 3.4.2, apparent in the white space of the curve around the linear fit line (Figure 5.20b).

All estimation data can be seen in Figures B.3 and B.4 in Appendix B.7.

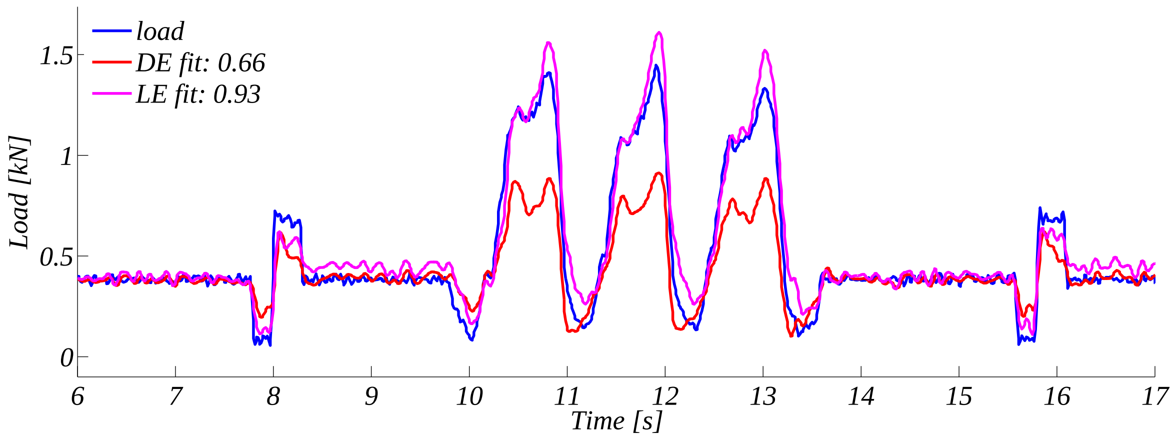

Figure 5.21: *Load estimation results for linear estimation (LE) and dynamic estimation (DE), after level shifting back to the correct 'static load' condition of 1×BW. For this figure, estimators were characterised with step data. The linear fit method resulted in the best fit. Before and after the gait signal there is an alignment wave. Clearly can be seen that after the alignment wave, the linear fit magnitude is slightly higher.*

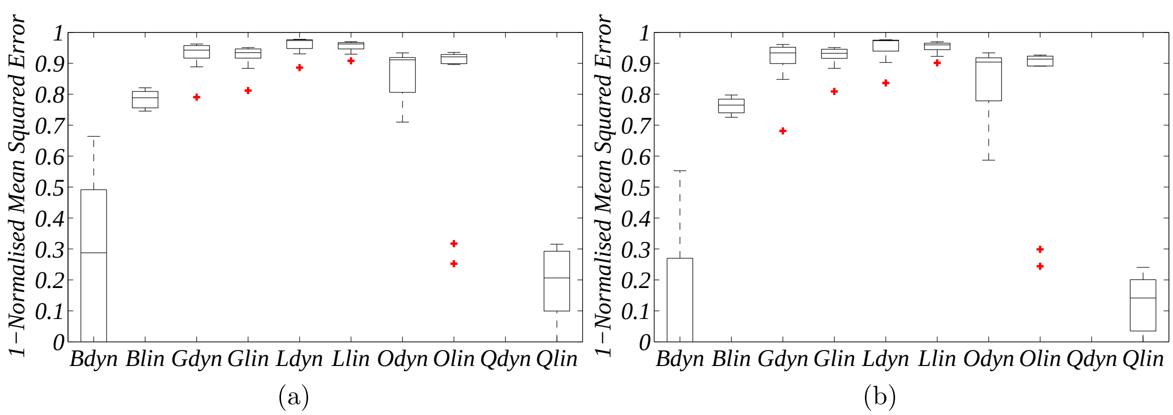

Figure 5.22: *Typical results for estimation of load using gait data, using the same data for characterisation and estimation (output parameter O1). B, G, L, O, Q = sensor, dyn = DE, lin = LE.*

Linear Versus Dynamic Estimation

Load estimations for sensors B and Q were typically worse than for the other sensors (Figure 5.22).

Linear estimation consistently resulted in higher fit result medians, however, the box plots of each result overlapped, indicating that a clear conclusion cannot be drawn from this (Figure 5.23). The results for O1 (*lgi,lsi, dgi, dsi*) were highest for DE using gait data (*dgi*), and also with a small distribution. However, for DE using step data (dsi), O1 was the smallest. For LE, there was not much difference for O1 between gait and step data.

Overall, the LE results were less variable, expressed by relatively unchanging box plots for O1, O2, and O3 (*lgi vs lgg vs lgs, and lsi vs lgs vs lss*). Or in other words: whether LE was characterised with gait or step data, it did not make much difference to the estimation results.

In contrast, for the DE method, O2 and O3 results were always worse than O1 and furthermore, O3 was worse than O2. Or in other words: when DE was run with pooled characterisation data, the results became worse, especially when different data was used for characterisation and estimation; and gait data estimation using characterisations based on step data was worse than step data estimation using characterisations based on gait data.

Level-Shifting Data

Level shifting introduced a slight reduction in estimation quality for both LE and DE, but not much (Figure 5.24).

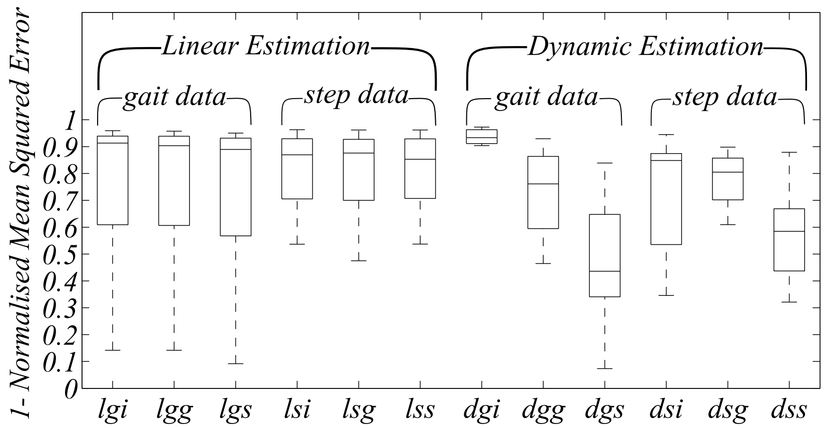

Figure 5.23: *Load estimation results for LE and DE after level shifting (Figure B.3 b,d,f and Figure B.4 b,d,f of Appendix B.7), grouped into gait data estimations and step data estimations. Each box represents the collection of medians from every sensor estimation. Symbol explanation: l = LE, d = DE, i = individually optimised calibration settings, g=pooled gait calibration settings, s = pooled step calibration settings. lgi, lsi, dgi, and dsi are estimations on the same data as the system characterisation and are provided to indicate the best possible response.*
The gait data estimation was always higher than the step data estimation. The data estimated with the LE method had less variability than those of DE. Additionally, the LE consistently resulted in better estimation results, except for DE for gait data, using individual calibration (dgi).

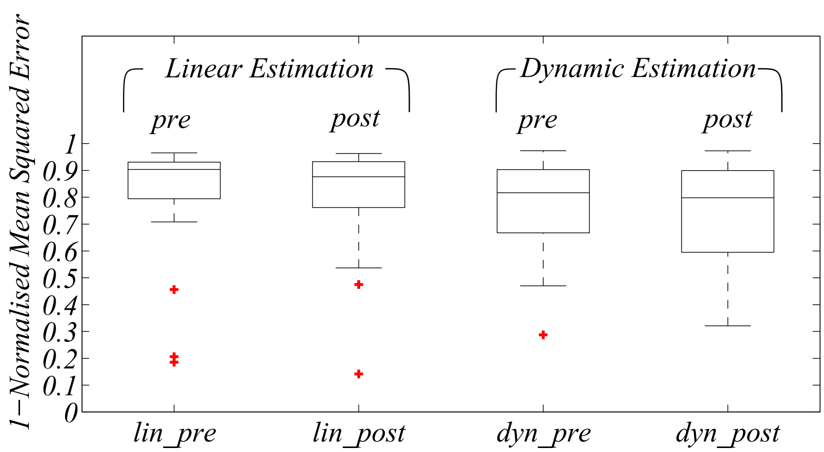

Figure 5.24: *Pooled results for LE and DE, pre and post level shifting. Each box represents the collection of medians of Figures B.3 and B.4; pre-shifting represents the data from sub-figures a,c,e, and post-shifting represents data from sub-figures b,d,f. Symbol explanation: lin = LE, dyn = DE, pre = pre shifting, post = post shifting.*
Shifting resulted in worse estimation results for both LE and DE, and LE performed better than DE in all cases.

5.7.5 Discussion

Fit Results

The estimation methods worked noticeably better for the sensors that had no lag (G, L, and O, Figures 5.17 and 5.22). This was because the lag introduced large errors during changing signals.

Overall, DE resulted in lower absolute estimation quality than LE. The only time when DE performed better was when the same experiment data was used to characterise the system and to then estimate the load. However, that is not a situation that happens in reality. In all other cases, LE performed better, with only minor dependence on what data was used to characterise the system. The estimation results approached the ideal results (load estimation on the same data as characterisation) very closely.

The level shifting method worked well; it hardly affected the quality of the estimation results.

Limitations

The load and capacitance signals were low pass filtered. However, as Figure 1.7 shows in Chapter 1, 99% of all signal power lies roughly below 5 Hz, therefore filtering at 10 and 20 Hz was acceptable, and not really a limitation.

5.8 Chapter Conclusions

A novel type of load sensor was developed, using inexpensive and standard production methods. The electrodes can be accurately and repeatably positioned within the bearing during a standard moulding process, however there are still some reliability issues regarding connecting test equipment to the sensors, resulting in failure and noise. *This answers Aim 1: Determine how a repeatable sensor can be constructed and reliably embedded within a bearing.*

It seems that there was a small bias between the four electrodes of the sensor, where electrodes e1 and e2 had a slightly higher signal, but this difference was not significant. *This answers Aim 2: Determine if a pattern can be distinguished between sensor position and output.*

The bare sensor had a creep response that reaches 95% of the end value within 5 to 10 seconds. However when the sensor was embedded within the bearing, this time increased to 11 to 15 minutes. *This answers Aim 3: Determine the creep behaviour of the bare sensor and the sensor embedded within the bearing.*

The sensor transfer was accurately determined as a second order low pass filter with a corner frequency of 9 Hz. *This answers Aim 4: Determine the frequency transfer function of the sensor.* This frequency range was sufficient for the commonly occurring patterns were used (gait and step up/down). There was variation in dynamic capacitive output magnitude between the electrodes, and also between sensors. Non-linear distortion was introduced in the capacitive output data; amongst which second order harmonics and hysteresis.

Two distinguishable groups of sensors were identified; one group in which a lag was generated between load signal and capacitive signal response, and one in which lag was hardly noticeable. For non-lagging sensors, the relation between capacitance and load was linear, and for the lagging sensors there was a degree of nonlinearity. *This answers Aim 5: Determine the response of the sensor to physiological signals.* A reason for this lag was not been found yet, but the hypothesis is that this may have been caused by the test setup, in which the bearing was inadvertently placed slightly off-axis.

Two load estimation methods were tried, a linear estimation method and a dynamic estimation method. The linear method works best overall. Estimation of load was a straightforward process resulting in a signal with a fit quality of 0.9 or higher for sensors in the 'no lag group', using averaged sensor parameters. *This answers Aim 6: Determine how to estimate load from measured capacitance and the accuracy of load estimation.*

6 Wireless Communication and Power

6.1 Introduction

The previous chapters dealt with the sensor and the bearing material in regards to measuring loads. It was established earlier that capacitance cannot be sent directly over an inductive link as an analogue change (see Chapter 2.3.7). Because this project is still in the prototype phase, it is most convenient to use off-the-shelf components, in order to save time and reduce cost. In a future prototype, a microprocessor will be used to control the semiconductor integrated circuit that measures the capacitive sensor (See Chapter 7). This measurement generates digital data. Additional digital data will also need to be sent, and communication should ideally be bi-directional (from the implant to an external device and vice-versa), to increase the flexibility and functionality of the implant. For instance, the software that runs on the microprocessor of the implant may need to be updated, a greater number of individual tasks could be performed, and stored information on the implant could be requested and accessed. In this chapter a suitable wireless transceiver (*trans*mitter and re*ceiver*) was chosen, and the test results are presented.

Besides sending information wirelessly, the implant also has to be powered wirelessly. An experiment was performed to test whether wireless powering of the implant would be possible with a small size coil.

6.2 Aims

The following aims have been set for this chapter:

1 Determine the most suitable off the shelf wireless transceiver

2 Determine how much influence body tissue has on the transfer of data

3 Determine how much influence antenna separation has on the transfer of data

4 Determine if it is possible to transfer power using an inductive link

6.2.1 Requirements

Wireless communication components need to consume low amounts of power, be small, cost effective, and uncomplicated to implement. Wireless communication has been used in implants before to send data *in vivo* [47, 132–134], but their lack of proper description and/or complicated assembly would result in extensive development time and money, which pushes their usefulness outside of the scope of this project. This reduces the options to wireless solutions that can be built using off-the-shelf components. Several off-the-shelf wireless transceivers are commercially available. To find the transceiver that was most suitable, first the requirements for 'normal use' were determined.

Communication Protocol

The data from the sensors needs to be transmitted. Data transmission occurs in packets (Table 6.1). A packet was defined with the following contents; a packet identifier identifies up to 4 devices simultaneously, in case multiple devices are within wireless communication reach. The packet type indicates what kind of packet it is; depending on the experiment, different packet types can be defined. For instance, for an experiment, only accelerometry data may be useful, whereas it may also be useful to define packets to read stored memory contents. The packet number is helpful to detect communication errors and to request a re-send of that packet. The sample time indicates either the differential time since the last measurement or the absolute time; for instance in case of 20 packets per second, this timer increments up to 20 and then starts at 0. The load and acceleration data needs to be transmitted at least 20 times per second, in order to measure a maximum frequency of 10 Hz, following Shannon's sampling theorem (see Section 1.7). A packet that consists of load, acceleration, and other data was 160 bits long.

For a sample rate of 20 packets per second, an effective data rate of $160 \times 20 = 3200$ bps or 3.13 kbps is required. It is beneficial to send data with the highest transfer rate possible, because sending and receiving data costs a relatively large amount of power,

Function	Description	N bits
Identifier	Identifies device (2 bits), packet type (4 bits) and packet number (10 bits)	16
TempC	Temperature sensor data	8
Vin	Input voltage measurement	8
AccX	Accelerometer X axis data	16
AccY	Accelerometer Y axis data	16
AccZ	Accelerometer Z axis data	16
MagX	Magnetometer X axis data	16
MagY	Magnetometer Y axis data	16
MagZ	Magnetometer Z axis data	16
Cap	Capacitive sensor data	16
Time	Sample time	16
total		160

Table 6.1: *Contents of the standard measurement communication packet with the most common information, to be sent at at least 20 times per second. Each bit gives* 2^n *possibilities, and each bit* 256^n *possibilities.*

and if data can be sent quickly the transceiver can remain in a low power state for a longer time. Optimisations such as sending data of multiple sample times in larger packets are not considered at this moment.

Several transceiver integrated circuits are listed in Table 6.2. In the case where multiple transmission rates were available, only the most power efficient results are shown, and the lowest transmission power settings are used. Some manufacturers have several transceivers, in that case only the lowest power option was displayed. For calculations, only the lowest voltage was used. To save energy, the following communication protocol was assumed: the implant sends an 'keep alive' packet once every second, and then waits in receive mode for 10 ms for a reply from the base station. The 'keep alive' packet was assumed to be 16 bits (just the identifier, see Table 6.2), bringing the total data to be transmitted to 3.14 kbps. Average power during standard communication was calculated using Equation 6.1. The total power consists of the time and power spent transmitting, receiving, and standing by.

Transition times between idle and Rx (receiving data) or Tx (transmitting data) state are assumed to be 0 seconds. For the sake of simplicity, the communication time between the microprocessor and the transceiver was ignored.

$$P_c = V_s \times \left(I_s \times (1 - \frac{B_{req}}{B_{norm}} - t_{rx}) + \frac{B_{req}}{B_{norm}} \times I_{tx} + t_{rx} \times I_{rx} \right) \tag{6.1}$$

where:

P_c	Power at required bit rate [mW]
I_s	Sleep current, during non-transmission time
V_s	Supply voltage, assumed to be 3 Vdc
B_{req}	Required bit rate
B_{norm}	Standard bit rate
I_{tx}	Current during transmission of data
I_{rx}	Current during reception of data
t_{rx}	The time spent waiting in receive mode, 10 ms.

When the device is not transmitting or receiving, it will be in idle mode, for comparison defined as: retaining all register values, retaining control of all digital inputs/outputs and ready to return to Rx or Tx mode within 1 ms.

Device	**Comm. Freq. [MHz]**	B_{norm} **[kbps]**	I_s **[μA]**	$I_{tx,norm}$ **[mA]**	Irx **[mA]**	P_c **[mW]**	**Size [mm]**
ADF7023 [135]	862-928, 431-464	300	160	7.9	12.8	0.81	5×5
AT86RF233 [136]	2400	2000	300	7.2	11.8	0.77	5×5
CC2500 [137]	2400	500	160	11.1	17	0.71	4×4
MAX7030 [138]	315,434	66	3000	3	6.2	6.37	5×5
MC13201 [139]	2400	250	1500	38	45	4.79	5×5
MRF49XAT [140]	433, 868, 915	250	1200	13	15	3.27	5×5
nRF24L01+ [141]	2400	2000	320	7	12.3	0.86	4×4
SI4438 [142]	425-525	500	0.05	75	14	1.1	4×4
SX1211 [143]	863, 902, 950	200	80	21	3.5	0.93	5×5
ZL70102 [144]	402-405, 433-434	515	0.01	5.3	4.3	0.15	4.3×3.2

Table 6.2: *Commercially available wireless transceivers, their communication frequency, supply voltage, transmission data rate, standby current, normal transmission current, normal reception current, average communication power usage calculated using Equation 6.1, and their package size. The ZL70102 scores best overall, the main determinant being average power usage.*

In several areas, the ZL70102 (Microsemi Corporation, Aliso Viejo, CA, USA) performed best. It had the lowest standby current of all, the best combination of low transmission/reception current, the lowest power dissipation for standard use, and the smallest footprint size. Additionally, it was designed specially for medical implant communication, and was medically certified. It was designed to be used in pacemakers, implantable cardioverter defibrillators, and various other short-range body area networks (BAN). It utilises the medical implantable communications service (MICS) frequency band, which spans from 402 to 405 MHz. It uses a very small number of external components.

To assess the suitability of the ZL70102, the Zarlink ZL70102 ADK v2.1.1 (Microsemi) development kit was tested, from now on referred to as 'the base station'. The base station was connected to a personal computer, which ran the software to control the ADK. The ADK also came with an 'implant module', which ran on batteries.

Within the instrumented UKR, the ZL70102 would be surrounded by body tissues and fluids, and metals. These materials all potentially have a negative impact on wireless communication, such as reduced signal to noise ratio (SNR) and shifting resonance frequencies. These effects have been measured in an experimental setup using a HP8753E vector network analyser (VNA)(Agilent Technologies UK Ltd, Wokingham, UK), using several porcine body tissues, NaCl solution, metal foil and the antennas that were supplied with the development kit, and an experimental antenna. The experimental antenna is described in Section 6.4.2. The reason that an experimental antenna was developed was because the supplied antennas were far too large for embedding in the bearing. Additionally, for several communication protocols, the SNR, the number of transmission errors, and effective communication speeds were measured using the same tissues and materials, the supplied antennas, the base station, and an experimental antenna.

6.3 Background Information

6.3.1 *In Vivo* Propagation of Radio Waves

The Maxwell equations are described in Appendix D.1. They dictate that an electromagnetic wave that propagates through a material is attenuated depending on the propagation constant β, which is dependent on the dielectric constant ϵ and the dielectric permeability μ of the material.

6.3.2 Small-scale Fading

In addition to attenuation of an electromagnetic wave through a lossy medium, fading can play an important role in the attenuation of waves. "Small scale fading is a characteristic of radio propagation resulting from the presence of reflectors and scatterers that cause multiple versions of the transmitted signal to arrive at the receiver, each distorted in amplitude, phase and angle of arrival" [145]. The resulting signal at the receiver is a constructive or destructive addition of these signals, resulting in a signal that is strongly and seemingly randomly dependent on the location of the receiver to the transmitter. In case of a small distance between the sender and receiver, and body tissue with a small thickness, small scale fading becomes more dominant in the attenuation of electromagnetic waves. The range of amplitude variation can range up to 70 dB [145].

6.3.3 Properties of Body Tissue

Between an external antenna and the antenna within the polyethylene bearing, skin, fat and body fluids and UHMWPE may be present. UHMWPE, being an insulating polymer material, was assumed to have a negligible effect on wave propagation and was not tested.

Skin covers most of the outer layer of the body. Skin consists of two layers: the epidermis and dermis. The thickness of skin varies from 1.55 to 2.54 mm depending on the location on the body. The skin thickness for the knee was not found in literature, but the thigh region has a skin thickness of 1.5 mm and the waist 1.91 mm [146]. In comparable experiments porcine tissue was utilised as a surrogate for human tissue [147, 148]. At approximately 500 MHz, the relative permittivity (in respect to the absolute permittivity of vacuum) of porcine skin ranges from approximately 90 to 110, and the conductivity from 0.3 to 0.5 [S/m]. The relative permittivity of porcine fat extends from approximately 6 to 18 and the conductivity from 0.05 to 0.4 [S/m] [149].

6.3.4 Antenna Location

All the instrumentation components of the instrumented UKR have to be physically isolated from body materials, both to ensure that the components are not damaged by corrosion and/or wear, but also to prevent the introduction of toxic materials into the tissues and body fluids. Practically, this means that all components have to be embedded within the UHMWPE, and that the location for these components has to have low or no wear and be exposed to the lowest possible stresses and strains to prevent damage to both the instrumentation components and the bearing. Several locations exist around the perimeter within the medial UKR bearing, where the antenna could be located; on the anterior, posterior or medial side in respect to the knee. Laterally is not a good location because of the close presence of the metal rim of the tibial plateau, which may have a negative impact on both transmission and reception of electromagnetic waves, but also the risk of exposure due to wear due to possible impingement between the bearing and the rim. Similarly, an antenna around the circumference of the bearing is not advisable either, given the dissimilar elastic moduli of metal and UHMWPE. Because of the Poisson's ratio, a bearing under normal load will expand in the transverse plane (see Section 2.4.1). There are several ways in which dissimilar expansion of UHMWPE and metal under load might lead to failure: the metallic material of the antenna could impinge on the UHMWPE, 1) damaging/fracturing the material of the antenna or 2) damaging the material of the bearing or 3) not damaging the bearing but constraining the lateral expansion of the bearing during loading, hence altering the mechanical load/deformation behaviour of the bearing. Therefore, to prevent failure of the bearing and the instrumentation components, the components have to be located where the stresses and strains are low. The most optimal places for this are at the front and the back of the bearing, in an extension of the current bearing shape. Within an extension, the further away from the centre of the bearing (the source of the stresses), the smaller the stresses become. Given that the space directly behind the knee is reduced during flexion, this is not an ideal location for an external antenna. Additionally, because the space behind the bearing during flexion is filled with tissue from the upper leg, during gait, the electromagnetic waves have to travel through varying materials during flexion/extension of the knee, which is may not beneficial for a constant transmission of electromagnetic waves.

By elimination, the front of the bearing is the best location for an antenna. During flexion and extension of the knee, the position of the external antenna can be kept constant when the external antenna is fixed to the lower leg.

6.3.5 Antenna types

The Zarlink ADK was provided with two types of antenna; a helix antenna for the base station and a square loop antenna for the implant (Figure 6.1). Given the dimensions of the antennas, the antennas work in normal mode, which means that the electromagnetic field of the helix antenna is shaped like a half torus and the electromagnetic field of the square loop is shaped like a torus. The radiation patterns are shown in Figure D.1 in Appendix D. For maximal signal transmission the radiation patterns of both antennas have to be aligned so that they overlap. The helix antenna has the advantage that it has good directivity, and good gain, but the disadvantage is that it is easily detuned by

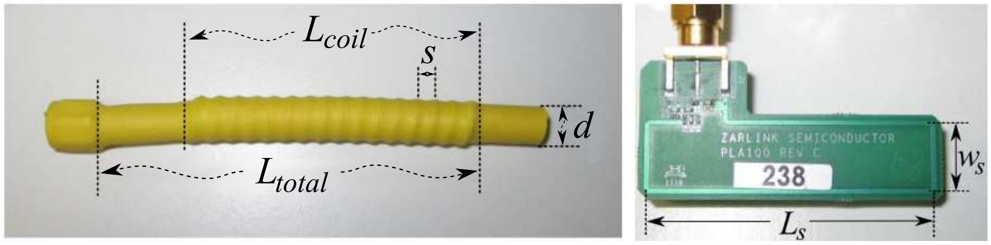

(a) (b)

Figure 6.1: *Antennas, supplied with the ZL70102 ADK (not shown to scale): (a) helix antenna, with s = 3 mm, d = 7 mm, L_{coil} = 48 mm and L_{total} = 72 mm, and (b) loop antenna with L_s = 44 mm and w_s = 10.5 mm.*

body tissue. The loop antenna has the advantage that it is cheap, small and relatively insensitive to surrounding tissue, but is very narrow band, which makes tuning to the exact frequency extremely critical. Another disadvantage is poor gain [150, 151]. The square loop antenna was too large for the bearing. Therefore, a custom antenna was designed.

6.3.6 Zarlink ZL70102

Communication Modes

The ZL70102 in the base station should always be ready to send or receive packets. The ZL70102 in the implant can be configured to 1) continuously transmit and receive ('normal mode'), 2) remain in a dormant state and monitor a special 'wake-up' frequency on which the base station transmits, after which it returns to normal mode, or 3) it can sleep and send packets to the base station without prompting. In all measurements, the wake up frequency was used to initiate communication.

Modulation Schemes

The ZL70102 can use three different modulation modes to send data, two frequency shift keying (2FSK), where two frequencies are used to encode a '0' or '1', two frequency shift keying high sensitivity (2FSK), and four frequency shift keying (4FSK), where four different frequencies are used to send two bits of data at once, i.e. '00','01','10' and

'11'. The modulation mode 2FSK provides a faster data rate than 2FSK HS, but has a lower sensitivity and thus functions less well with a noisy transmission link. The minimum sensitivity of mode 2FSK HS is -99 dBm, that of 2FSK is -94 dBm, and that of 4FSK is -84 dBm.

Received Signal Strength

In the ZL70102, the received antenna signal at a frequency between 402 to 405 MHz is internally multiplied by a signal at the same frequency as the carrier wave and then low pass filtered with a corner frequency of 450 kHz so that only the modulation signal with a bandwidth between 0 to 450 kHz is retained. The sum of the power of the remaining signal is then measured by the ZL70102 using an external 12-bit analog to digital converter (ADC) or a 5-bit internal ADC, and can be obtained by requesting the received signal strength indicator (RSSI). Unfortunately, RSSI is a dimensionless number, and the gold-standard of signal power representation is in dBm, the signal power in respect to 1 milliWatt (Equation D.22). Therefore, the relationship between RSSI and dBm needs to be calibrated per device.

Error Correction

Data is sent in packets. Each packet consists of a packet preamble, a packet header, and up to 31 data blocks. Each block consists out of 113 bits data (the 'payload'), 12 bits for the cyclic redundancy check (CRC), and 30 bits for the error correcting code (ECC). The packet preamble and header are used to define the start of the packet and to identify a packet, for instance, in case of retransmission. The CRC is a number that is calculated by dividing the input data by a known polynomial. The resulting CRC checksum is then added to the packet and sent. Upon arrival, the CRC is calculated by the receiver, and compared to the CRC that was attached. If they differ, then an error is generated, which may prompt a repair action using ECC.

6.4 Methods

The goal was to assess how well the ZL70102 would perform within a UKR knee replacement, and the most important outcome was the effective data rate. Data and error rate are dependent on the signal to noise ratio (SNR) of the system, which is strongly dependent on the antenna characteristics, such as attenuation and resonance frequency location, which in turn are dependent on the presence of body tissues and fluids. Therefore, to characterise the system the following bottom-up approach was used: 1) the antennas were measured in the presence of air and several body materials; 2) the transfer characteristic between the two antennas was measured in the presence of air and several body materials; 3) the data and error rate of the entire system was measured in the presence of air and several body materials.

6.4.1 Body Materials

Porcine tissue was used in the characterisation tests, because of the similar properties to human tissue [149]. Porcine skin and fat were obtained from a local abattoir. The skin was measured to be 2 mm thick. Two types of test construct were made: one with >2 mm skin and >5 mm fat, and the other >15 mm fat, with a surface area of at least 200×100 mm (L×W), in order to fully cover the loop antennas. The reason for having a skin specimen with fat attached was because of the difficulty in separating skin and fat without damaging the skin. To prevent contamination, the constructs were fully covered in polypropylene foil with a thickness of 50 μm (Figure 6.2). The foil was assumed to have no measurable effect on the electromagnetic propagation. To simulate body fluids, a solution of 0.5M NaCl solution was used.

6.4.2 Custom Antenna Simulations

Because the antenna that was supplied with the Zarlink development kit was far too large for embedding within the bearing, a custom antenna was designed. The custom

(a) (b) (c)

Figure 6.2: *(a) fat specimen with implant module attached, wrapped in aluminium foil. The antenna was embedded completely by the fat. (b) skin specimen. (c) The antenna immersed in NaCl solution.*

square loop antenna (henceforth called custom foil antenna) was designed using Sonnet 13.55-Lite software (Sonnet Software Inc, NY, US). The dimensions were set to fit within the width and height of the front of the bearing, 23×5.5 mm. Double layer polyimide (PI) was utilised with four loops per side, to maximise signal reception power. The copper track thickness was 0.1 mm, the commonly used minimal width in PCB design. Any connection will detune the antenna. To simulate the connection, a transmission line equivalent was simulated, by adding a capacitance in parallel and inductance in series, and varying their values. Capacitance was increased between 0 and 50 pF in steps of 10 pF, and inductance was increased between 0 and 50 nH in steps of 10 nH (Figure 6.3).

The printed circuit board layout of the antenna was drawn using OrCAD 16.6.0 Lite (Cadence Design Systems Inc, San Jose, CA, US), and manufactured from the same PI as the capacitive sensor.

6.4.3 Antenna Characterisation

Antenna characterisations were performed to determine attenuation at frequencies between 30 Hz and 3 GHz. The square loop antenna, the helical antenna and the custom foil antenna were characterised using air, encapsulation with the body materials and

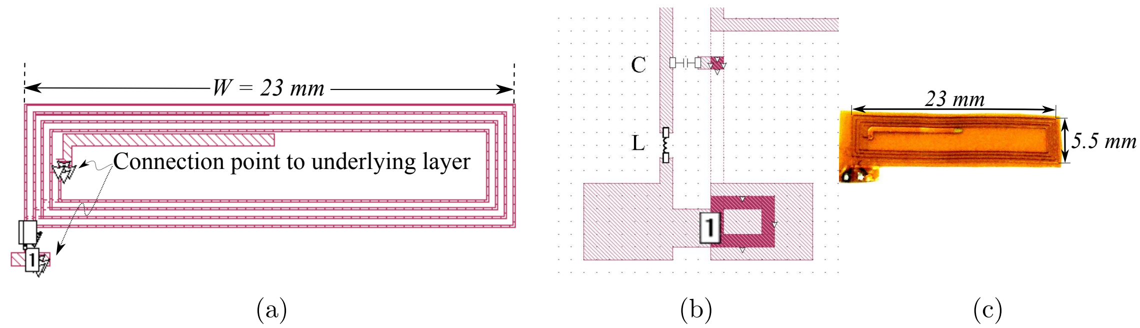

Figure 6.3: *Overview of the finite element simulation setup for the double sided custom foil antenna, with (a) a complete overview (stippled lines: bottom layer), and (b) zoomed in to the left bottom corner of figure (a) to show the load components C and L that were used to simulate the external loading that occurs when the antenna is connected to a receiver. '1' in both pictures is the simulated connector. The reverse side is practically identical to the front side. c) a photo of the actual antenna, depicted to true scale.*

adjacent aluminium foil. The antennas were connected to a calibrated vector network analyser (VNA) (HP8753E, Agilent Technologies UK Ltd, Wokingham, UK). The VNA frequency was set to sweep from 30 Hz to 3 GHz, and all other settings were set to standard. The calibration standards for the VNA were: open 'SMA' type connector [2], closed 'SMA' type connector, and a 50 ohm <=20 GHz resistor; Vishay Thin film, Farnell ref: 1109049 (Farnell Electronic Components, Leeds, UK). The capacitance of the open connection C0 was 3.66 pF; measured using a calibrated inductance-capacitance-resistance (LCR) databridge 9343M (Racal-Dana, Bracknell, UK). All antenna connectors were SMA type, and the connection from the 7 mm connectors of the VNA to SMA were made using an adaptor. The location of the resonance frequencies, and the attenuation at the wake-up frequency of 2.450 GHz (Section 6.3.6) were measured. Before measurement in tissues, the antenna was tuned in air to a frequency of 405 MHz by adding 45 mm of insulated parallel conductors, with conductor thickness 0.5 mm and wire separation of 1 mm.

[2] This is a commonly used coaxial connector

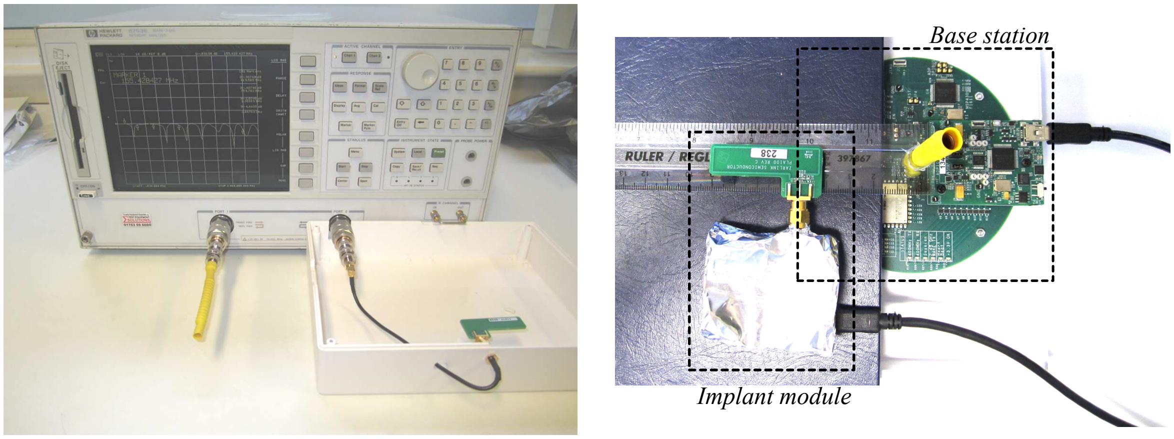

(a) (b)

Figure 6.4: *(a) Setup of the measurement jig to determine the transfer functions of the antennas, with on the left the helical antenna and on the right the square loop antenna. (b) The jig for testing received signal strength and transfer speed at several antenna separations, with on the right the base station and on the left the implant module, wrapped in aluminium foil.*

6.4.4 Antenna Transfer Characterisation

The transfer between the two antennas was determined using the same setup as described in the previous section. The antennas were placed in a custom rig that held the antennas at 0.2 m separation ure 6.4). The helical antenna was connected to port 1 and the implant antenna was connected to port 2 of the VNA, and in a second setup, the custom designed foil antenna was connected to port 2. The transfer function (S21) was measured between the two antennas.

6.4.5 RSSI Measurements

Additionally, the Zarlink ZL70102 software was modified to save the received signal strength indication (RSSI) to file for every measurement. The ZL70102 'implant module' ran on battery power, and was not connected to the measurement computer. The ZL70102 'base station' was optically isolated from the computer on which the control software ran using the ADUM4160EBZ USB optoisolator (Analog Devices Inc, Norwood, MA, USA). The carrier wave frequency was set to 402.15 MHz, Channel 0. The following variables were changed: 1) the body tissues were changed, and the aluminium foil was placed directly underneath the square loop antenna; 2) the distance between the antennas was changed from 0.02, 0.05, 0.1, 0.15, 0.20, 1 and 2 m. The output power of the wireless output stage was set to the lowest transmit power setting of -12.5 dBm. Each experiment was repeated ten times. All data were processed in MATLAB. All RSSI was measured using a 12 bit ADC.

6.4.6 RSSI Calibration

The calibration of RSSI is discussed in Appendix D.3; as well as the method to transform RSSIext to received power expressed in dBm. The calibration correction factor to calibrate the ZL70321 to the values according to the manufacturer's datasheet [144] was determined to be -40.93 dBm by measuring the RSSI simultaneously with the antenna voltage (see Appendix D.3).

6.4.7 Data Rate Characterisation

The identical setup as in Section 6.4.4 was used to measure the change data rate of the ZL70102 whilst varying the distance between the antennas. The base station transmitted at the lowest power setting. The implant module in conjunction with the square loop antenna was used to send data, and the base station was used in conjunction with the helical antenna to measure RSSI and data rate, the number of ECC packets, and the number of CRC errors (see the ZL70102 datasheet 6.3.6). The packet length was set to 113 bits, and the number of packets was 10,000 per change in parameter. Each experiment was repeated ten times. Preliminary measurements showed that 4FSK resulted in so many missing packets that the effective data rate dropped below that of 2FSK and 2FSK HS; therefore the experiment was performed with only 2FSK and 2FSK HS. The effective data rate is the amount of 'payload' data that is sent per second; therefore the preamble, header, CRC and error correction bits were not counted. Packets that could not be repaired were discarded, but successfully retransmitted packets were included in the calculation. The average and confidence interval (CI) were calculated for 10,000 packets that were sent, where the CI was calculated assuming a normal distribution with N=10,000.

6.5 Results

6.5.1 Custom Antenna Simulations

There were several resonance peaks for the simulated custom foil antenna, around 170, 460, 960, 1610 and 2880 MHz. Adding a capacitive (C) or inductive (L) load to the antenna terminals led to the following effects; increasing C led to emphasis of lower resonance peaks and de-emphasis of higher resonance peaks (Figure 6.5a), with a some lowering of the resonance frequency (Figure 6.5b). Increasing L led to emphasis of lower resonance peaks, but not so much de-emphasis of higher resonance peaks (Figure 6.5c), the main effect was lowering of the resonance frequency (Figure 6.5d). By changing the capacitive or inductive load at the antenna terminals, the amplitude of the resonance peak could be changed with a factor of 20 dB.

6.5.2 Antenna Characterisation

The standard antennas of the Zarlink ADK do not have their resonance frequency (F_{res}) at the carrier wave frequency of 403.5 MHz (see Table 6.3).

The square loop antenna was tuned best for air, was more detuned for skin and fat, with comparable resonances, and was worst for NaCL solution. The amplitudes ($|A|$) at resonance range from -21.4 to -18.9 dB, while at the required carrier frequency they range from -15.8 to -10.1 dB. The resonant peak does lie in close enough vicinity that it aids transmission (Figure 6.6a, marker 1 and 2). The resonant frequency around 2.45 GHz lies close to 2.45 GHz. The resonant peaks around 400 MHz and 2.45 GHz are the most obvious resonances, although there was some variation in amplitude between

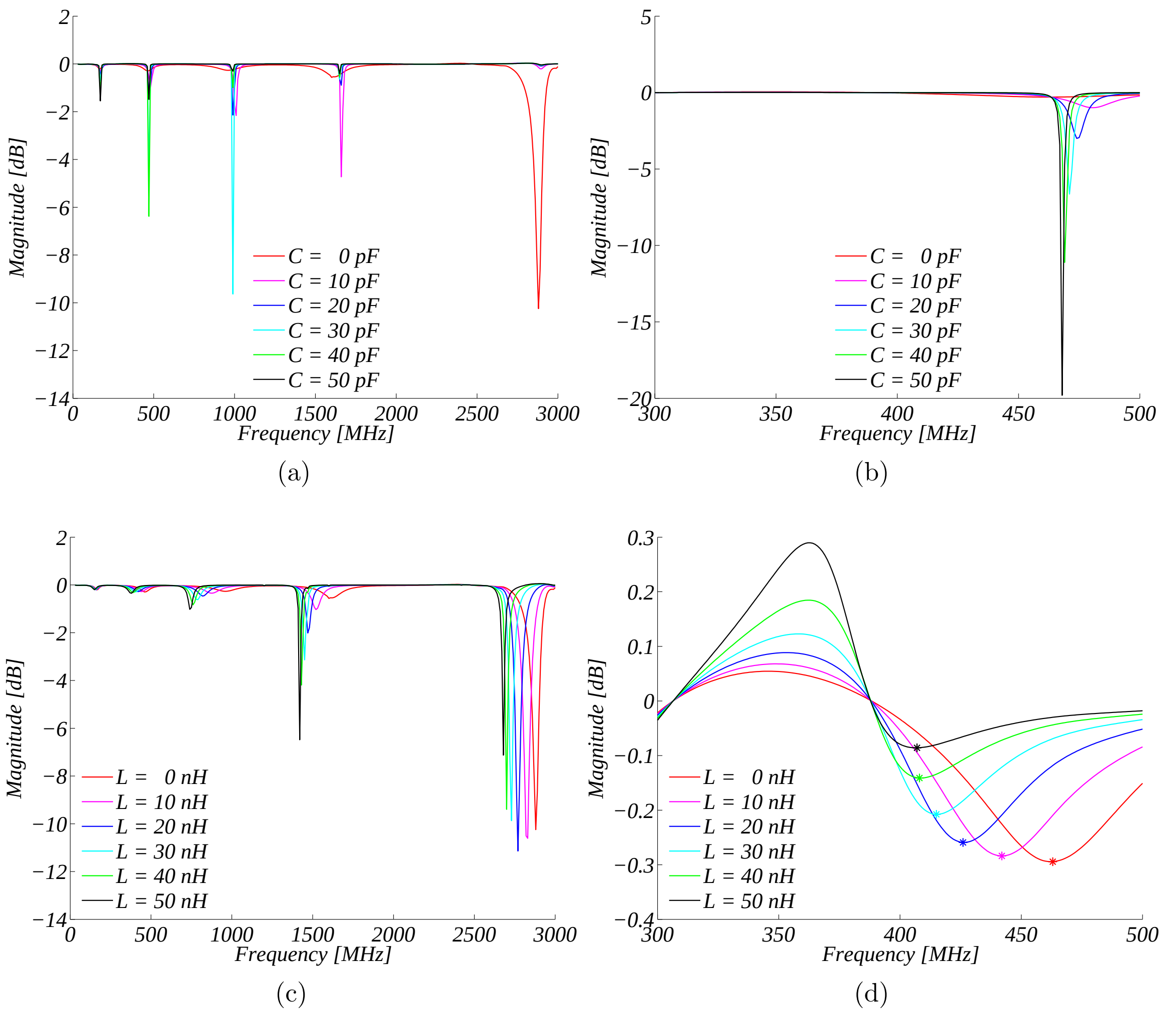

Figure 6.5: *Simulated amplitude responses for the custom foil antenna, whilst varying C and L. Increasing C leads to emphasis of lower resonance peaks and de-emphasis of higher resonance peaks (see a), with a some lowering of the resonance frequency (see b). Increasing L leads emphasis of lower resonance peaks, but not so much de-emphasis of higher resonance peaks (see c), the main effect was lowering of the resonance frequency (see d), the resonance peaks are accentuated.*

Medium	$\mathbf{F}_{res}$ [MHz]	$\|A\|_{res}$ [dB]	$\|A\|_{403.5MHz}$ [dB]	$\|A\|_{2.45GHz}$ [dB]	$Z_{403.5MHz}$ [Ω]
Air	390.4	-19.0	-15.8	-15.0	64.8 - j13.1
Fat	346.6	-21.4	-10.6	-26.5	80.0 - j24.8
Skin	345.1	-17.4	-10.1	-21.8	74.3 - j31.5
NaCl	315.1	-18.9	-14.0	-14.0	66.5 - j43.3
			(a)		
Air	317.5	-10.0	-1.2	-9.9	124.3 - j269.3
			(b)		

Table 6.3: *Measurement results for the (a) square loop antenna and (b) the helical antenna; resonant frequency (F_{res}), amplitude ($|A|$) (lower is better) at the carrier frequency of 403.5 MHz and wake up frequency of 2.45 GHz, and complex impedance (Z) at the carrier frequency of 403.5MHz. The resonant frequency was not at the desired frequency of 403.5 MHz, indicating that the standard system was unoptimised for use in vivo and needs to be optimised. This was especially so for the helical antenna which was designed to be used in air. Additional optimisation can be gained in the antenna impedance; which ideally is 50 Ω.*

them, where the transfer ideally should be 0 dB.

The helical antenna was more detuned than the square loop antenna, and the resonance amplitude was higher than those of the square loop antenna. Additionally, the antenna impedance was about 2.5× higher than the standard 50 Ω.

The custom foil antenna was tuned closer to the desired carrier frequency of 403.5 MHz, except for air and the NaCl solution. There was less variation in resonance frequency under influence of different materials for the custom foil antenna than with the square loop antenna (31.2 vs 75.3 MHz respectively) (Table 6.4). The custom foil antenna had more resonant frequencies than the square loop antenna between the carrier and wake up frequencies. Furthermore, at 2.45 GHz, the closest resonant frequency was too far away to provide lower SNR (Figure 6.6b).

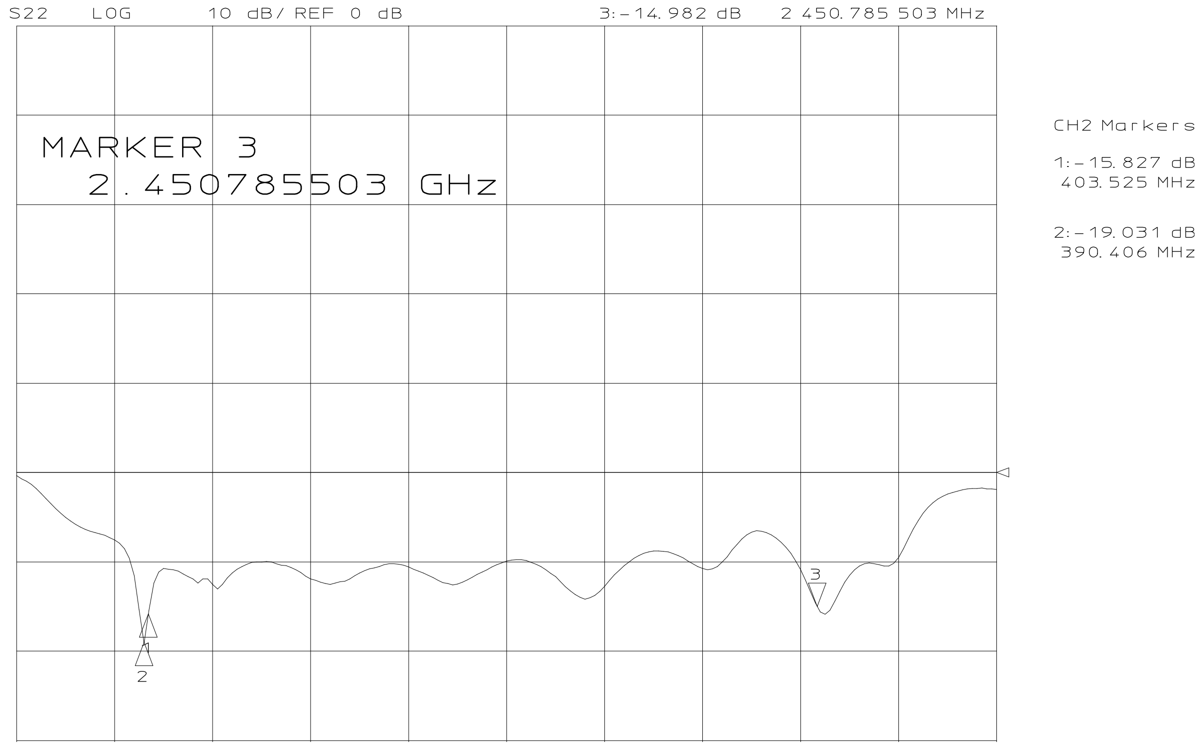

(a)

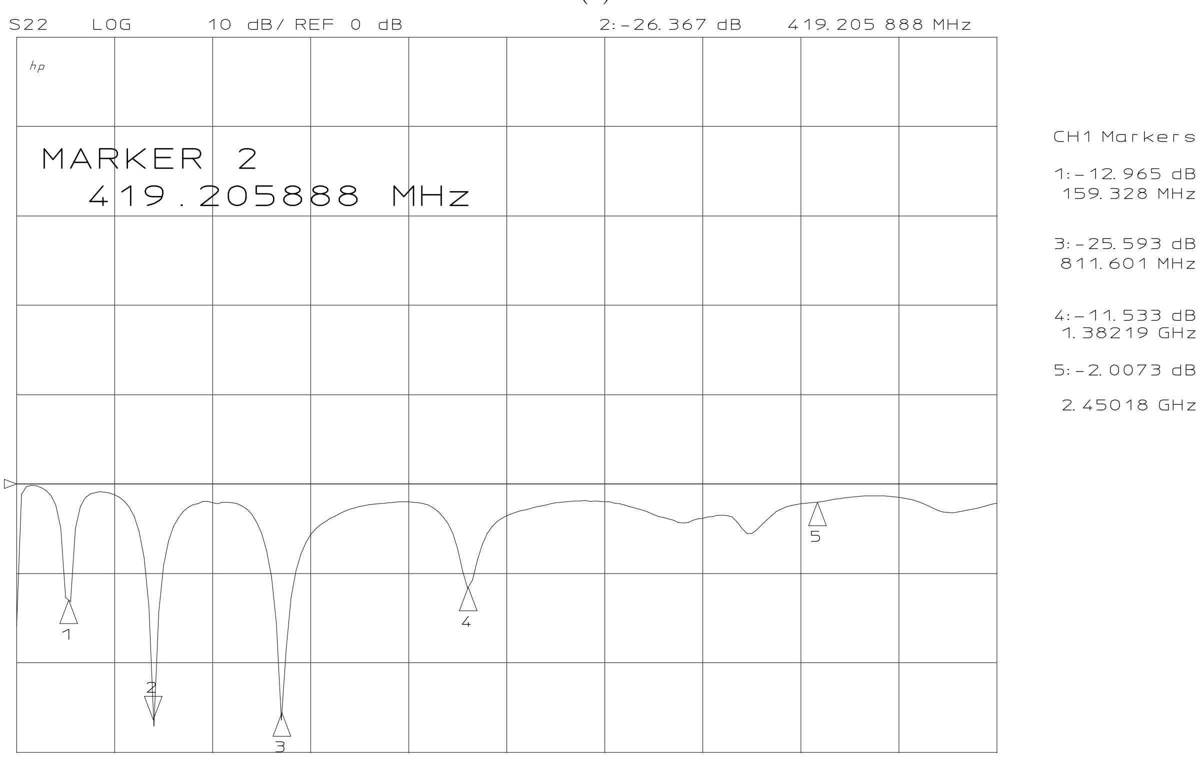

(b)

Figure 6.6: *Amplitude response of (a) the square loop antenna and (b) the custom foil antenna in air. Every marker was set to a resonant frequency, at which transmission was most favourable, and the last marker was set to the wake up frequency of 2.45 GHz.*

	$\mathbf{F}_{res1}$ [MHz]	$\|\mathbf{A}\|_{res1}$ [dB]	$\mathbf{F}_{res2}$ [MHz]	$\|\mathbf{A}\|_{res2}$ [dB]	$\mathbf{F}_{res3}$ [MHz]	$\|\mathbf{A}\|_{res3}$ [dB]	$\mathbf{F}_{res4}$ [MHz]	$\|\mathbf{A}\|_{res4}$ [dB]	$\|\mathbf{A}\|_{2.45}$ [dB]	$\|\mathbf{Z}\|_{res2}$ [Ω]
Air	159.3	-13.0	419.2	-15.0	811.6	-25.6	1382.2	-11.5	-2.0	46.0
Fat	149.4	-16.0	405.7	-26.5	763.9	-16.7	1306.0	-7.7	-2.4	35.6
Skin	149.4	-17.8	405.7	-21.8	763.9	-22.7	1306.0	-12.6	-3.9	38.8
NaCl	149.4	-14.5	388.0	-14.0	700.3	-18.0	1037.5	-10.3	-2.6	41.6

Table 6.4: *Measurement results for several materials in the vicinity of the custom foil antenna; resonant frequency (F_{res}), amplitude ($|A|$) and complex impedance (Z). There are multiple resonant frequencies, and F_{res2} was around the desired frequency of 403.5 MHz. Additional optimisation can be gained in the attenuation at 2.45 GHz ($|A|_{2.45}$), which is ideally higher, and also in the antenna impedance at 403.5 MHz, which is ideally 50 Ω.*

6.5.3 Antenna Transfer Characterisation

For signal transfer amplitude the attenuation between the helical antenna and the square loop antenna was generally higher than when using the square loop antenna with the custom foil antenna, which means that signals are attenuated more, resulting in a higher SNR for the custom foil antenna (Table 6.5). The typical attenuation of the signal between the sent and received signal was between -40 and -30 dB, with an exception for the custom foil antenna in air, which was higher.

A typical transfer for the custom foil antenna is shown in Figure 6.7. Unfortunately, the VNA could only display amplitudes down to -50 dB. The markers show the location of the resonance peaks of the custom foil antenna, which were determined earlier in (Table 6.4). The area around the carrier frequency of 403.5 MHz was relatively flat,

Medium	$\|\mathbf{S}\|\mathbf{21}_{square}$	$\|\mathbf{S}\|\mathbf{21}_{custom}$
Air	-36.4	-47.7
Fat	-37.2	-36.4
Skin	-39.2	-37.4
NaCl	-39.6	-33.2

Table 6.5: *Measurement results of the typical attenuation between the helical antenna and the square loop antenna, and between the helical antenna and the custom foil antenna at the carrier frequency of 403.5 MHz. Less attenuation is better. The custom foil antenna typically had less attenuation, except for in free air.*

which makes the transfer relatively insensitive to a change in the carrier frequency.

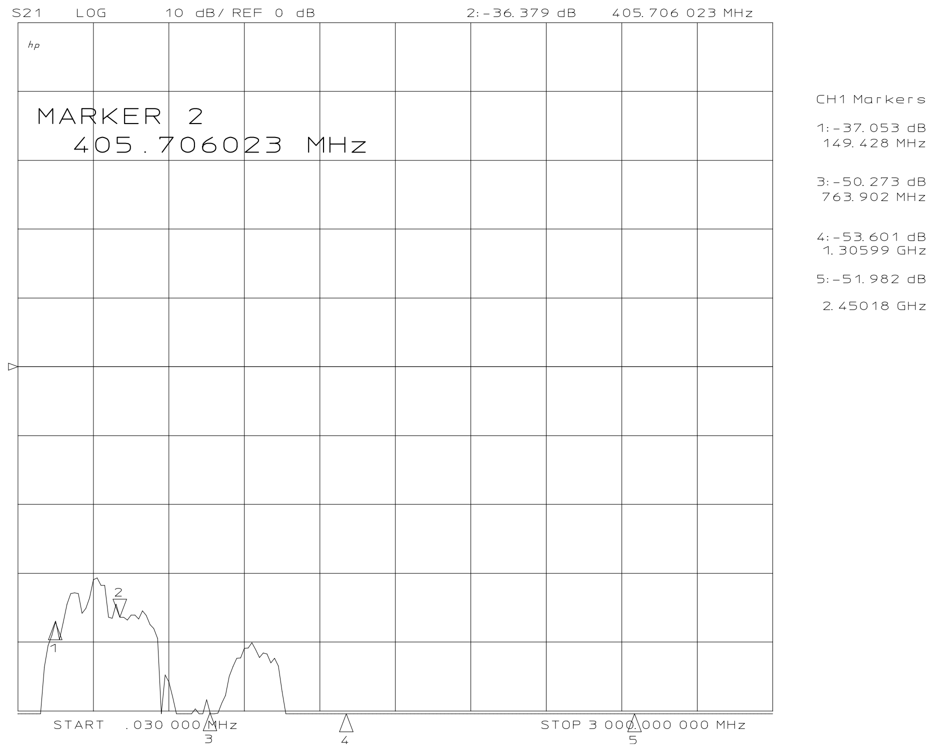

Figure 6.7: *Example of a typical transfer amplitude response between the custom foil loop antenna, surrounded by porcine fat, and the helical antenna. The attenuation(marker 2) was relatively constant around the carrier frequency. The other markers indicate the resonance frequencies that were found for the custom foil antenna (Table 6.4). The amplitude at those frequencies does not show as a peak in this figure, which is favourable for the frequency at markers 3 and 4 but unfavourable for 5*

6.5.4 RSSI Measurement

For the signal transmission between the base station with the helical antenna and the implant with the square loop antenna, the received power was reduced the most by the porcine skin sample, except at a distance of 2 m, where porcine fat provides more attenuation. At distances up 0.2 m, all received signal strengths are above -82 dBm, with typical variations in signal strength at a distance below 1 m within 2 dBm under influence of the surrounding tissue. When the square loop antenna was swapped for the custom foil antenna at a distance of 1 m in air the signal strength was about 1

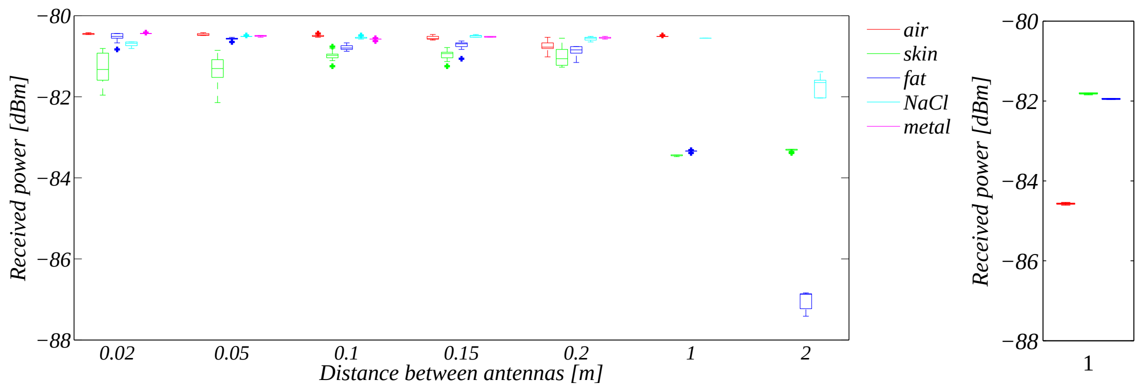

(a) (b)

Figure 6.8: *Received signal power at the antenna terminal, expressed in dBm, for various distances and surrounding materials by the implant module (a) for the square loop antenna and for several antenna separations, and (b) by the custom foil antenna at 1 m antenna separation.*

dBm weaker, but for skin and fat the transmission was about 2 dBm weaker, compared with the square loop antenna results (Figure 6.8).

6.5.5 Data Rate Characterisation

Error Rates

More detailed error rate tables can be found in Appendix D.4, given here is the summary. Using 2FSK modulation, below 1 m antenna separation, typically less than 50 packets per 10,000 packets are damaged but recoverable using ECC, versus typically 1 per 10,000 for the 2FSK HS modulation scheme. Communication between the implant module to the base station required even less recovery actions.

Typically less than 2 per 10,000 packets were unrecoverable and were resent for modulation scheme 2FSK, and less than 1 per 10,000 packets for modulation scheme 2FSK HS. Packet resends were typically less than 1 per 10,000 in the direction base station to implant.

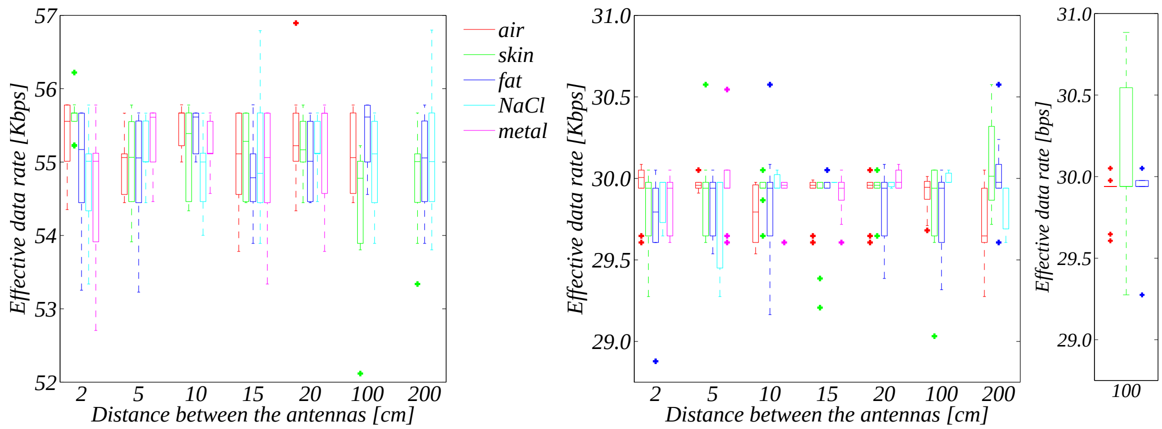

(a) (b) (c)

Figure 6.9: *The measured data rate from the base station using the helical antenna to the implant module using the* ***square loop antenna*** *for several surrounding materials, and antenna separation distances, for (a)* ***2FSK*** *modulation and (b)* ***2FSK HS*** *modulation (c) results for* ***2FSK HS****, using the* ***custom foil antenna*** *instead of the square loop antenna.*

Data Rates

The data rate for both the square loop antenna and the custom foil antenna was around 55 kbps for 2FSK modulation and just under 30 kbps for 2FSK HS modulation (Figure 6.9). The custom foil antenna had comparable data rates to the square loop antenna at an antenna separation of 1 m.

6.6 Discussion

The ZL70102 ADK was been tested in the vicinity of tissues with a thickness that represent worst case scenarios of typical *in vivo* conditions. The goal of the test was to asses how much transfer rate was influenced by antenna separation between the implant module and the base station in the vicinity of several materials that occur within a knee replacement, and two communication modulation schemes, 2FSK and 2FSK HS. The standard ADK antennas were used, as well as a custom foil antenna. First, the attenuation and the change in the transfer characteristic was measured per antenna. Secondly, the transfer attenuation from one antenna to the other was measured. Thirdly, the number of recoverable and unrecoverable packets during transmission and the effective transmission speed was measured. Fourthly, the received signal strength by the Zarlink ADK was measured.

6.6.1 Custom Antenna Simulations

The simulation provided guidelines how to tune the custom foil antenna; adding more inductance mainly helped in tuning the resonance frequency to the correct frequency, while adding more capacitance mainly emphasised the lower frequency peaks, and aided in fine tuning the resonance frequency. It was helpful that adding capacitance provided a means to fine tune the resonance frequency, since it is relatively easy to add capacitance in parallel; this could even be done after embedding the antenna in the bearing by adding capacitive load using electronic switches.

The simulation was limited in that it was only performed for air. Future simulations could include different surrounding materials such as fat and skin. Additionally, it was regrettable that this version of the software was only enabled to do a linear sweep of one parameter at a time. However, for the purpose of finding out the effects of adding capacitive or inductive load it was sufficient. High frequency components such as antennas are very dependent on the environment in which they are in, and therefore there is a point where doing more detailed simulations will not be more helpful than taking measurements on the device itself. Eventually the standard conditions *in vivo* will have to be determined, and the antenna had to be tuned to that environment. Additionally, the ZL70102 is not very demanding when it comes to correctly tuned antennas using 2FSK and 2FSK HS modulation, and if the antennas are tuned correctly, potentially 4FSK modulation could be used.

6.6.2 Antenna Characterisation

The standard antennas of the ZL70102 ADK and their compensation circuits were not tuned to their maximum potential. If the resonance peaks were tuned to the carrier frequency, then higher SNR would be possible (Table 6.3). The square loop antenna did have a better behaved spectrum between the main peaks of 403.5 MHz and 2.45 GHz (Figure 6.6a). This was good because ideally frequencies that lie in this region should be damped. If the antenna has a large amplification for this region, then the system may receive signals in that spectrum which overload the receiver and result in bad communication.

In comparison, the foil antenna was tuned much better to the carrier frequency (Table 6.4), and had a higher resonance peak, making higher SNR possible (Figure 6.6b). However, at 2.45 GHz the antenna was detuned, and should be relocated. The spectrum between 403.5 MHz and 2.45 GHz had two large resonances, which may be unfavourable for the receiver, depending on the 'pollution' of the frequency spectrum.

Additionally, the variation in impedance was much lower in the foil antenna. The impedance relates directly to received signal strength, since the antenna impedance and the impedance of the receiver form a voltage divider.

In a UKR, the bearing translates in the anterior and posterior direction. Therefore, the distance between the antenna and the knee tissue changes, and the volume that was previously occupied by bearing will immediately be filled with fluid. Therefore, it is favourable that the resonance frequency and the impedance are relatively insensitive to changes in adjacent tissue. In that regards, the custom foil antenna should result in better performance at low SNR conditions.

Summarising: The custom foil antenna had better SNR at 403.5 MHz and should result in better SNR during transmission of data.

6.6.3 Antenna Transfer Characterisation

The custom foil antenna had higher attenuation than the square loop antenna, but not dramatically so. It is doubtful that the difference will be noticeable in the data rate.

6.6.4 RSSI Measurement

Up to and including 0.2 m antenna separation, all antenna received signal strengths are between -82 and -80 dBm, and mostly above -81 dBm. Given that a -3dB equals multiplying by a factor 0.5× and all the variation up to 0.2 m lay within 1 dB, the signal power was relatively insensitive to surrounding tissue. Only at 1 m and 2 m, the damping became higher, but still only with approximately 6 dB, which is not much, given the fact that by tuning the antenna correctly, a factor 5 dBm (Table 6.3) can be gained (dB measured by the VNA was in dBV units, each change of 2 dBV equals 1 dBm change).

In this experiment, the custom foil antenna performed a little worse than the square loop antenna, but the difference should not be noticeable.

6.6.5 Data Rate Characterisation

The number of recoverable packets was considerably higher for 2FSK than 2FSK HS, but typically, the number of packet errors per 10,000 was still very low. Data transmission under the influence of fat at 0.2 m resulted in a large amount of faulty packets for 2FSK, however, at 1 m it became much less again. The sudden isolated attenuation at 0.2 m might be due to multipath fading effects. 2FSK HS results in a very low amount of packets that are broken. For high reliability, it was decided it was best to use 2FSK HS modulation, however for high speed, it was best to use 2FSK.

The data rate of 2FSK was hardly affected by the surrounding tissue, even at large antenna distances. The biggest change that was introduced was a slowing down of the bitrate from 55 Kbps to approximately 52 Kbps, which is equal to a reduction of approximately 5%. The data rate of 2FSK HS was also hardly affected, with the largest change equal to about -1 Kbps, equal to a reduction of approximately 3%, both for the square loop antenna and the custom foil antenna. There were no obvious correlations between antenna separation and data rate for any material. Future measurements will have to determine how well the custom foil antenna performs at 2FSK, but given the better performance of CRC and ECC for the custom antenna it is unlikely that the custom foil antenna will perform worse.

6.6.6 Limitations

The experiments were performed in a laboratory environment. It remains unclear to what extent the environment influences the measurements. However, the implant is likely to be used in an environment where less reflecting surfaces are present (i.e. a large room for gait analysis). Future tests will have to show how the wireless communication functions then.

For the custom foil antenna, only preliminary measurements were possible, due to time constraints. Since the custom foil antenna is also a square loop antenna, it was expected that their responses are similar. Additionally the effective data rate, which is the most important parameter, was equally good for both antennas, at a distance of 1 m.

6.7 Wireless Power Transfer

6.7.1 Introduction

Because of reasons given in greater detail in Chapter 7, the instrumented UKR bearing needs to be powered using inductive power transfer. An inductive coil, located external to the body, will be placed in close proximity of the implanted instrumented bearing (Figure 6.10, "inductive antenna").

The external coil generates an electromagnetically changing field, which radiates

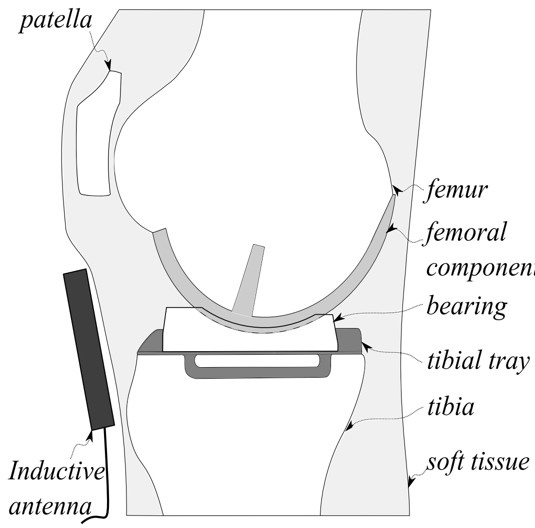

Figure 6.10: *A schematic view of the knee with a UKR and an external antenna providing inductive power to the implant.*

through the body tissue, and which is picked up by a coil within the bearing, so that an alternating current is generated inside the coil. This current can then be used to power the implant. The goal was to reach an induction of 32 mW of power (see Section 7.6.6).

6.7.2 Method

An experiment was performed with a primary and secondary coil, set up so that the coils were parallel and the centres of the coils were in line. The aim was to find out the relationship between coil separation and induced power for several coils. The primary coil was round, with a radius of 20 mm and 5 windings of 0.5 mm lacquered copper wire. A series of secondary coils with dimensions 4×20 mm and 25, 33, 50, 66, 75, and 100 windings of 50 μm lacquered copper wire were used. The voltage on the secondary side was measured by a PM2521 true RMS multimeter (Philips Electronics UK Ltd, Guildford, UK), over a 250 Ω and 500 Ω resistor (accuracy 1%). The signal on the primary side was supplied by a simple custom class B power amplifier, driven by a signal generator. The secondary coils were tuned to a resonance frequency within 5 kHz of 152 kHz. The carrier frequency of 152 KHz allowed the radiated power to fall within the OfCom legal limits in the UK [152]. For each experiment, the signal generator was tuned to provide the maximum secondary voltage (resonance). Secondary power was calculated by the formula P = V^2/R, with V = voltage measured over the resistance, and R = resistance. All data was processed in MATLAB.

The equivalent internal resistance R_{in} was calculated by using Equation 6.2, and then substituting V_{in} in Equation 6.3 with Equation 6.2 for two measurements with changing R_{load}. This is possible because in this model the generating voltages V_{in} of both measurements are identical, regardless of the load resistor R_{load}. The resulting inequality was then solved in MATLAB for each paired measurement, and for every coil and coil separation, and a quadratic polynomial was fitted to the data. The quadratic polynomial was then used to calculate V_{in}, using Equation 6.2, to estimate the maximum voltage that is generated during low load conditions.

$$V_{in} = V_{out} \times \frac{R_{in} + R_{load}}{R_{load}} \tag{6.2}$$

where:

V_{in} Generating internal voltage [V]

V_{out} Voltage over the load resistor [V]

R_{load} Load resistance [Ω]

R_{in} equivalent internal resistance of coil [Ω]

The equivalent internal resistance of the secondary coil is an important factor to determine to what magnitude the secondary voltage will increase when faced with a large load resistance, for instance, when the sensors are not enabled and thus do not draw any current. The minimum current that will always be present is the sleep current of the microprocessor, (see Chapter 7) which typically 6.3 μA.

turns	$\mathbf{R}_{dc}$ [Ω]	$\mathbf{L}_{ser}$ [μH]	$\mathbf{C}_{par}$ [**nF**]	$\mathbf{f}_{res}$ [**kHz**]
25	12.1	18.64	52	158
33	16.15	30.64	34	148
50	23.56	69.01	27	152
66	31.85	110	10	149
75	36	133	6.6	152
100	43	191	5	146

Table 6.6: *Secondary coil measurements for a coil wire diameter of 50 μm, with coil dimensions 20×4 mm (L× W). The table shows results for resistance (R_{dc}), serial inductance (L_{ser}), parallel capacitance (C_{par}) required for resonance, and resulting resonant frequency (f_{res}).*

The voltage over the load resistance may be approximated by the following formula:

$$V_{out} = V_{in} \times \frac{R_{load}}{R_{in} + R_{load}} \tag{6.3}$$

where:

- V_{load} Voltage over the load resistor [V]
- V_{in} Generating internal voltage [V]
- R_{load} Load resistance [Ω]
- R_{in} equivalent internal resistance of coil [Ω]

6.7.3 Results

As the number of coil winding turns increased, the serial DC resistance and serial inductance increased as well (Table 6.6). The capacitance that was required to tune to the correct resonant frequency decreased.

The voltage and the power that was induced in the secondary windings was dependent on the load. For a load of 250 Ω, the induced voltage was approximately 1.5× smaller, and the induced power was approximately three times smaller than for a load of 500 Ω (Figure 6.11).

The equivalent internal resistance of the secondary coil was found to follow a second

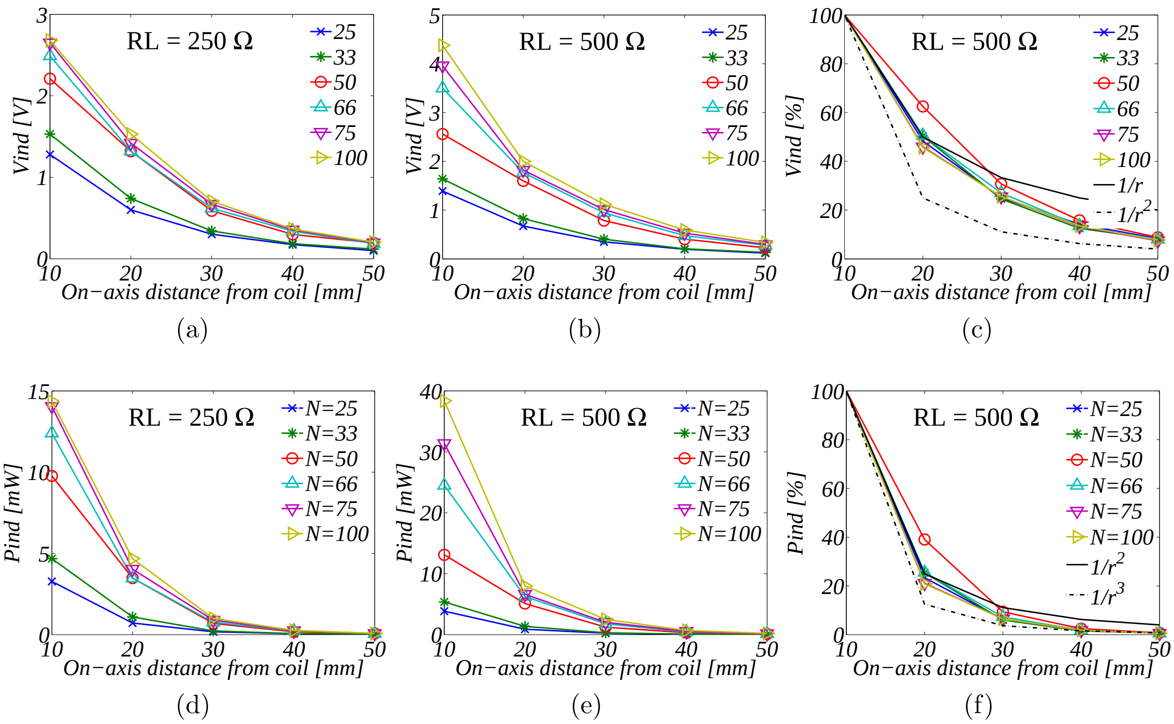

Figure 6.11: *Induced voltage (a-c) and power (d-f) in the secondary air core at an increasing number of secondary windings (N) and distance from the primary core, a,d) for a load of 250 Ω, b,e) 500 Ω, and c,f) expressed in percentage of the maximum power. In c) additionally first and second order decay, and inf f) second order and third order decay over distance has been plotted, based on measurement b and e respectively). Voltage drop off occurs between first and second order decay over distance, whereas power drops off between second and third order. More than twice the amount of power is induced in the 500 Ω load compared to the 250 Ω load.*

order polynomial that depended on the number of secondary windings: $0.0603N^2$ + 1.2437×N - 4.8933, with N is the number of windings (Figure 6.12). The data points spread out further from the polynomial fit for coils with more turns. The estimated internal voltage V_{in} can reach as high as 11 V_{ac} at 10 mm coil separation for a coil with 100 windings.

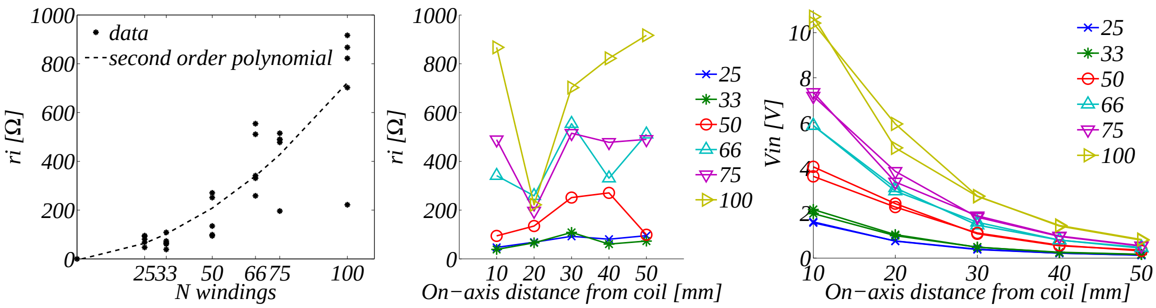

(a) (b) (c)

Figure 6.12: *Equivalent internal resistance, a) the amount of windings versus equivalent internal resistance, b) the coil separation versus equivalent internal resistance, and c) the calculated internal voltage V_{in} using the polynomial shown in a), and using the data from both load measurements. The internal equivalent resistance increases in a second order power: 0.0603N^2 + 1.2437$\times N$ - 4.8933, where N is the amount of windings. For lower number of windings, the internal resistance shows unchanging dependence on coil separation. For higher number of windings the same cannot be said. The estimated internal coil voltage V_{in} increases to over 10 V_{ac} for a coil with 100 windings at a coil separation of 10 mm.*

6.7.4 Discussion

The equivalent internal resistance increased with the number of windings. On the other hand, the output voltage and power increased with the amount of windings. This meant that the output voltage was extremely load dependent. The internal resistance calculation was very sensitive to the voltage measurements, but it seemed to be relatively independent from the coil separation, except at 20 mm, where suddenly the internal resistance dropped. This can be attributed to the slightly higher voltage at 20 mm for the 250 Ω load, compared to the 500 Ω load (compare Figure 6.11a with b). Given the relatively flat internal resistance for 25 and 33 windings, it can be justified that the internal resistance was independent of coil separation. Additionally, since power was calculated with P=V^2/R it maked physical sense. Power at a separation of 25 mm did not reach 32 mW. However, this does not mean that it is not feasible to induce the amount of power necessary, merely that more power needs to be induced on the primary side. Typical induction efficiency of 0.35-1.49% [152] means that for an efficiently tuned primary transmitter the primary induced power should be roughly 9 W for secondary induced power of 32 mW, which is very feasible, given that transmission power of 15 W has been reported [152].

6.8 Chapter Conclusions

The ZL70102 was identified as the most suitable bi-directional wireless transceiver. *This answers Aim 1: Determine the most suitable wireless transceiver, based on data from manufacturers.*

Even though the data rate was affected by the tissue, there was no clear correlation between decreasing data rate and increasing distance between the antennas or decreasing data rate and tissue. All changes remain within 5%. *This answers Aim 2: Determine how much influence body tissue has on the transfer of data, and Aim 3: Determine how much influence antenna separation has on the transfer of data.*

Therefore, experiments have shown that the ZL70102 performs as described in the data sheet. Overall, the ZL70102 shows a remarkable tolerance for badly tuned antennas, and there should be no issues concerning wireless communication *in vivo* using the custom foil antenna. [3]

The inductive power transfer measurements showed that it was possible to transfer the required power to the implant. *This answers Aim 4: Determine if it is possible to transfer power using an inductive link.*

[3]For more information about the experiments that were performed, please contact the author for an unpublished internship thesis for the University of Twente, the Netherlands: "Tanuhardja, R R, Medical Implantable Wireless Communication", reporting about work performed under supervision of the author.

7 System Design

7.1 Introduction

This chapter describes how a prototype might be constructed. It incorporates data gathered in previous chapters; using the optimal location of the capacitive sensor and the electronic module (see Chapter 4), and the wireless communication power requirements and wireless power measurement results (see Chapter 6).

First a brief overview of the electronic system is given, followed by a discussion of several quantities that can be measured besides load measurement, along with reasons why their measurement is advantageous. After that the system that enables obtaining data from the sensors measuring these quantities is discussed in detail, including assembly of the system, wireless communication and powering of the system.

After that, methods of manufacturing and sterilising the instrumented bearing are discussed. At the end of this chapter, the main conclusions of this thesis are summarised and conclusions are drawn, and finally recommendations for future work are made.

7.2 Aims

The following aims have been set for this chapter:

1 Determine which additional quantities can be measured and their requirements in terms of power and physical size.

2 Determine the power requirement of the complete implant.

3 Determine if and how the power requirements could be met.

4 Provide a possible method to construct the implant.

5 Summarise the conclusions of this dissertation.

6 Provide future work recommendations.

7.3 System Overview

This section briefly describes an overview of the system. The system to measure *in vivo* loads should have the components presented in Figure 7.1. Capacitance, already discussed in Chapter 5, is measured using a capacitance to digital converter (C2D). Additional measurements from an accelerometer and magnetometer could provide the angle of the tibial plate in respect to the gravitational vector, and the angle of the tibial plate in respect to the femoral component. Temperature should be measured in order to compensate for temperature influence on the load sensor output. The microprocessor is the connecting hub in the system to which all peripheral components are connected (Figure 7.1). It takes care of communication with the peripherals and doing calculations. Data will be transmitted bi-directionally using a wireless transceiver, already discussed in Chapter 6. Additionally, a uni-directional wireless data link can be provided as a back up data link. Power should be delivered to the system using an inductive power link, also discussed in Chapter 6. In the following sections, each of the components will be discussed in more detail.

7.4 Possible Measurable Quantities

The aim of this project is to measure loads *in vivo*, but there may be other important factors that could be measured. This section aims to determine if the information provided by the extra sensors significantly outweighs the cost of increasing the volume of the implant by adding those sensors. For power calculations, the required power for the slowest necessary update rate (20 Hz, see Section 1.9) and the fastest possible update rate of the capacitive to digital converter will be used as a minimum and maximum requirement.

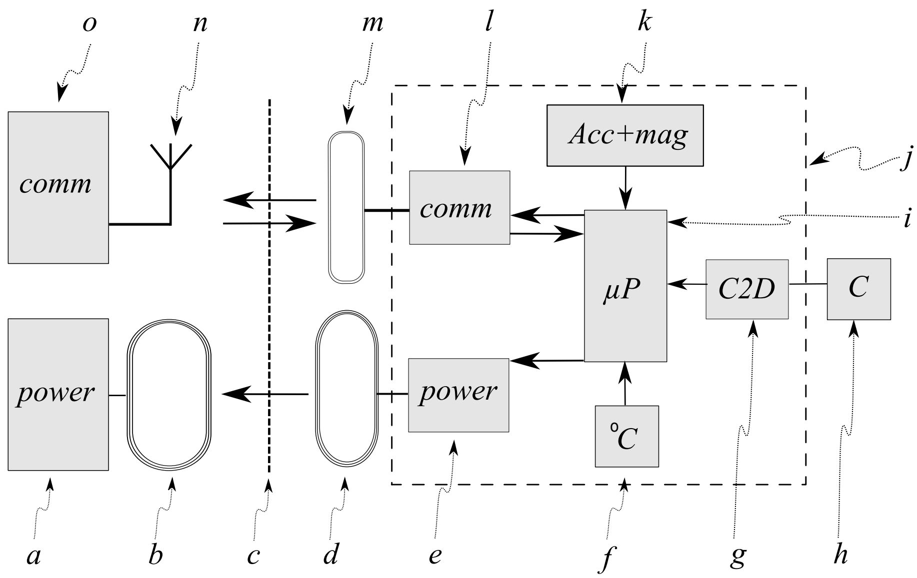

Figure 7.1: *Electronic schematic of the instrumented bearing, with arrows indication a data link. a) the external power supply, b) the external inductive antenna, c) the body boundary, d) the internal inductive antenna, e), power module (the arrow from the microprocessor to the power module indicates the inductive communications link), f) temperature sensor, g) capacitance to digital converter, h) capacitive sensor, i) microprocessor, k) accelerometer and magnetometer, l) wireless tranceiver, m) internal antenna, n) external antanna, and o) external communication (and data processing).*

7.4.1 Capacitance

Capacitance is measured to estimate load (Chapter 5). Several other groups have used custom integrated circuits (IC) capacitance measurement devices [51, 153, 154], or discrete components [155–157], but always with poorer accuracy and physical size than the device that was used in this project, or custom made. The C2D that was used is the AD7746 (Analog Devices Inc, Norwood, MA, USA), which has been used in capacitive pressure measurements before [158]. It was the highest resolution semiconductor C2D available, with resolutions down to 4 atto Farad (aF), in a package size of only 6.4×5×1.2 mm [159]. The AD7746 uses an average current of 700 μA. Power consumption is 2.1 mW, at a supply voltage of 3 V_{dc}. There is a temperature sensor on-chip with a resolution of 0.1°C and an accuracy of ±2 °C, but at a cost of reducing the capacitive sample rate, and compared to a discrete temperature sensor, at a far higher current (Table 7.1). Temperature compensation of the AD7746 itself is unnecessary, given that it has an offset error of approximately 14 aF between 33 and 47°C, or 1 aF per °C, approximately a thousand times less than the typical dynamic capacitive change during gait at 9×10^{-3}pF peak-to-peak, (Figure 5.20).

Internally, the AD7746 measures at a fixed sampling frequency, but it has a 3rd order digital filter that provides a more filtered signal when a longer filter processing time is chosen. The update rate is discrete in a number of steps, and the closest setting to the minimum sampling frequency (20 Hz, see Section 1.9) is 26.3 Hz, with a -3dB low pass frequency of 21.8 Hz. The maximum sampling frequency is 90.9 Hz, with a -3dB low pass filtered frequency of 87.2 Hz.

The AD7746 has a full input range of ±4 pF, but it has a built-in CAPDAC register which can be programmed to provide a stable additive offset up to 17 pF, increasing the maximum capacitance to 21 pF. During all experiments in this thesis, during startup the CAPDAC register was set so that the initial capacitance before the measurement was nulled.

The AD7746 uses the I^2C protocol for digital communication at a maximum speed of 400 kHz. I^2C defines two data lines for communication [160], and the AD7746 provides an extra 'data ready' pin that changes output state when a new sample is ready. One sample update cycle in which a microprocessor requests for a capacitance value which is then returned by the AD7746 takes about 100 μs. For a sampling frequency of 26.3 Hz, this results in a total communication time of 2630 μs per second and 9090 μs per second for 90.9 Hz update rate.

There are C2D converters that can measure multiple capacitances, such as the AD7147, which was tried in a measurement but resulted in capacitance measurements that were too noisy. Perhaps in the final application the noise may be lower, given the smaller distance between sensor and C2D. Measuring multiple capacitors could provide information about load that is not distributed exactly in the centre of the bearing concavity, for instance, during shear. Perhaps it might possible to integrate a multiplexer [156] to measure different capacitances individually using one AD7746.

7.4.2 Temperature

Temperature should be measured because it was found to influence the mechanical behaviour of UHMWPE under load (see Chapter 3). Discrete temperature sensors provide the following advantages over use of temperature sensors that are provided as secondary function in another IC: 1) they take less time to read, 2) they consume smaller amounts of power, 3) are more accurate. The demands that were placed on an external temperature sensor were: 1) small physical size, 2) accurate to ±1 °C or better, 3) low power usage, 4) occupying a low amount of pins on the microprocessor, 5) provide digital output. Concerning demand 4): fewer pins that are occupied on the microprocessor also means a lower amount of printed circuit board is occupied by PCB copper tracks to the sensor. Concerning demand 5): digital output is more immune to electromagnetic interference on the data and provides more flexibility for microprocessor selection, since the microprocessor need not have an analog to digital converter. Based on these requirements, several commercially available temperature sensors are shown in Table 7.1. Another method of transferring information is using pulse width modulation (PWM), in which the ratio of the high and low of a square wave on one line is used to encode temperature data. PWM can be read with very low time and current requirements, explained in Section 7.5.3. Power usage of the temperature sensor compared to other components was very low, therefore this parameter was not considered as the most important parameter to choose a temperature sensor. Temperature sensor TMP05 was considered as most suitable given the small footprint, and the PWM interface type occupies only one pin.

	Res. [°C]	ϵ [°C]	$\mathbf{I}_s$ [μA]	$\mathbf{I}_c$ [μA]	ΔT [ms]	**P** [μW]	**L×W** [mm]	μ**P Pins** [N]	**IFT**
MAX6667[161]	0.08	-0.5	-	142	33	426	2.8×1.9	1	PWM
LM73[162]	0.25	±1	8	300	14	45	3×3	2	I^2C
TMP05[163]	0.025	±0.1	12	30.9	170	101.9	2.2×2.4	1	PWM
TMP112[164]	0.0625	±0.5	1	7	35	3.6	3×3	2	I^2C

Table 7.1: *Overview of some commercially available digital output temperature sensors, with resolution (res), inaccuracy (ϵ), standby current (I_s), conversion current (I_c), conversion time, including sending data (ΔT), power usage (P), dimensions ($L \times W$), number of pins to interface with the microprocessor (μP pins), and interface type (IFT). The inclusion criteria were: no more than ±1 °C inaccuracy between 33 °C and 47°C, no more than 500 μA current usage during conversion, digital transmission of data, no more than 2 pins used on the microprocessor (μP), and package dimensions no larger than 3mm. Power consumption (P) per second is calculated for 1 measurement per second, including conversion and transmission time, the rest of the time spent in idle mode. All reported currents are typical currents.*

7.4.3 Linear and Angular Kinematics

If the angle of the tibia and femur could be measured, then this would provide a much more detailed picture of loading of the knee.

Accelerometers

Accelerometers are used to measure acceleration of limbs, for instance during heel strike [165]. Knee acceleration cannot be accurately measured using external accelerometers, because of the problem of reliably fixing the accelerometer to the leg. There will always be some motion artifacts because of the movement of soft tissue [166, 167]. Accelerations during normal gait have been reported with a mean of -5.9 g, and with peak accelerations as high as -12 g at the ankle [165]. It is likely that the peaks are less at the knee, but it is unclear to what extent. Accelerometer signals are suggested to be filtered at a maximum frequency of 29-35 Hz, depending on the axis of measurement [168]. Therefore, ideally accelerometer signals should be measured at a frequency higher than 70 Hz, or twice the maximum filtered frequency.

Additionally, an accelerometer measures the gravity acceleration vector of the earth (Figure 7.2, v1), which can be used to calculate the angle of the tibia in respect to the

	Acc$_{noise}$ [$\mu g/\sqrt{Hz}$]	**Acc**$_{max}$ [g]	**Gyr**$_{noise}$ [$°/\sqrt{Hz}$]	**Gyr**$_{max}$ [±°/s]	**Mag**$_{res}$ [μT]	**Mag**$_{max}$ [±mT]	**L×W** [mm]	**μP Pins** [N]
KXG02	150	2-8	0.03	256-2048	-	-	4×4	2
KMX61G *	?	2-8	?	2000	0.146	1.2	3×3	2
MPU-6500	300	2-16	0.5-0.5	250-2000	-	-	3×3	2
MPU-9150	400	2-16	0.005	250-2000	0.3	1.2	5×5	2
MPU-9250 *	?	2-16	0.01	250-2000	0.15	4.8	3×3	2
LSM330DLC	220	2-16	0.03	250-2000	-	-	4×5	2/3-4
LSM9DS0		2-16		245-2000		0.2-1.2	4×4	2/3-4

	I$_{acc}$ [μA]	**I**$_{gyr}$ [μA]	**I**$_{mag}$ [μA]	**P**$_{acc}$ [mW]	**P**$_{full}$ [mW]	**ΔTC**$_{acc}$ [μs]	**ΔTC**$_{full}$ [μs]	**IFT**
KXG02	250	3750	-	0.75	12	17	31	I^2C
KMX61G *	130	-	350	0.39	1.44	17	31	I^2C
MPU-6050	70	3700	-	0.21	11.31	56	104	I^2C
MPU-9150	70	3400	875 ?	0.21	10.41	140 ?	380 ?	I^2C
MPU-9250 *	200	3200	?	0.60	10.20 ?	140 ?	380 ?	I^2C/SPI
LSM330DLC	350	6100	-	1.05	19.35	140	260	I^2C/SPI
LSM9DS0	350	6100	?	1.05	19.35	140	380	I^2C/SPI

Table 7.2: *Overview of some motion sensing integrated circuits. * means preliminary data, - means not available, ? means unspecified or estimated. Currents: whenever possible for an update rate of 26.3 Hz. Power: calculated at 3 Vdc. Power was calculated using $P = 3V \times I$.*

gravity acceleration vector.

Gyroscope

Another method of measuring the angle of the tibia is by using a gyroscope, which can be seen as an angular axis accelerator. A 3D gyroscope can measure angular rotation in 3 axes, for instance the rotation of the knee (Figure 1.1). A gyroscope does not provide absolute angles, just change in angles. A drawback of a gyroscope is that there is drift during dynamic movements, so the data has to be continuously referenced against known angles, such as full extension of the knee. A major drawback of using a gyroscope compared to other types of sensor is that it requires a significant amount of power (Table 7.2).

Additionally, just as with the angle of the tibia measured in respect to the earth, it is unclear what the angle of the femoral component in respect to the tibia is, because the angle of the femoral component can not be measured with a gyroscope located within the bearing.

Magnetometer

A magnetic sensor is designed to measure the direction and magnitude of the earth's magnetic pole in three axes. However, it also measures external magnetic fields, and therefore manufacturers advise to keep currents (which generate magnetic fields) higher than 10 mA at least a few millimeters away from the sensor [169]. Three sources of external field were identified: 1) the earth's magnetic field, 2) the external field of the inductive coils for power transfer (see Chapter 6) an external static magnet (see Chapter 3).

The earth's magnetic field ranges from 25-65 μT, however, since inductive coupling is used to power the bearing, and the external coil has currents up to 1 A just centimeters away from the bearing, an embedded magnetometer will pick that field up in addition to the earth's magnetic field. The magnetic field B generated by the external coil is estimated to have a magnitude of 167 μT, calculated using Equation 7.1, using N = 5, I = 3.75 A, a = 2.5e-2, z = 2.5e-2. Therefore, the magnetic vector would point to the external coil field instead. This field cannot be used for accurate determination of the angle of the bearing with respect to the coil; since this field is only 3-7 times larger than the earth's magnetic field, the earth's magnetic field would still have a significant influence on the reading, depending on the orientation of the patient with respect to the magnetic north pole of the earth. A more powerful magnet would reduce that error.

An external static magnet in combination with a magnetometer has been used to measure knee angles in a TKR, with a maximum error of 5° in flexion-extension, and 0.93° in abduction-adduction, although not *in vitro* [67]. A magnet disc was mounted behind a femoral component, which was found to have a small effect on magnetic field strength, and two magnetic sensors were mounted in the knee bearing to measure the direction of the magnet.

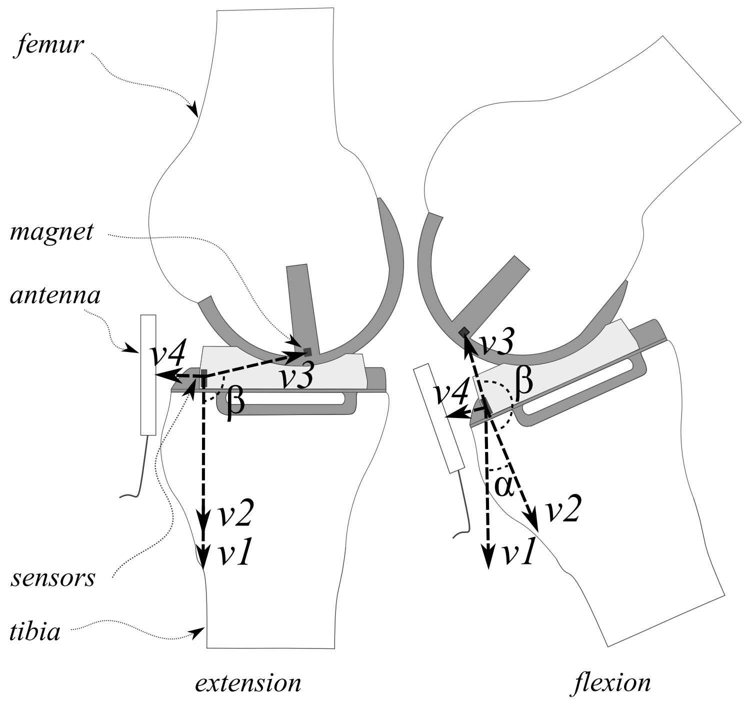

Figure 7.2: *The angles of the femur and tibia during flexion and extension. v1, v2, v3 and v4 denote the gravity vector, the perpendicular axis of the tibial plate, the location of the magnet, and the location of the inductive antenna. α and β show the angle between v1-v2 and v2-v3 respectively. v1 may be measured using an accelerometer, v2 is known, and v3 may be measured using a magnetic sensor. v4 may be a cause for interference for measurement of v3.*

$$B = \frac{\mu 0 \times N \times a^2 \times I}{2 \times (a^2 + z^2)^{3/2}} \tag{7.1}$$

where:

B magnetic field [T]

$\mu 0$ Vacuum permeability, $4{\times}\pi \times 10^{-7}$ [T×m/A]

N Number of windings of the coil

a Radius of the coil [m]

I Current [A]

z Axial distance from the centre of the coil [m]

There are three options of measuring the position of the bearing: fixing a magnet to an external reference system, to the tibial reference system, or to the femoral reference system. The first option is not very practical, given the quadratic fall-off of the magnetic field. It were fixed to the tibial reference system, for instance by fixing to the tibial component, the rotation along the long axis of the tibia could be measured, and also the anterior-posterior translation of the bearing, provided that the field strength of the magnet is within the range of the magnetic sensor. If it were fixed it to the femoral component, two movements can be measured: rotation of the femoral component around the perpendicular axis of the bearing, and rotation of the femoral component in the anterior-posterior plane during flexion/extension of the leg.

If the flexion angle could be measured during gait, then this would be a powerful addition to load measurement. Not only would the normal force in respect to the tibia be known, but also exactly at what part of the gait cycle this occurs. Posture determination with accelerometers and gyroscopes on the femur and tibia has been shown to be an inexpensive alternative to optical motion analysis systems [170], and angle measurement using a magnetometer could be an alternative to sensors attached to the femur. Additionally, it could replace X-Ray imaging in kinematic studies.

The conjunction of measurement data from the implant (angle of the tibia, angle of the femur, force) allows for full gait characterisation.

Feasibility

If the magnet is mounted in the middle of the femoral component (Figure 7.2), the distance between the sensor and the magnet during flexion is approximately 23 mm, and during extension, approximately 30 mm. The magnetic field drops off with the square root of the distance from the magnet. If a magnet is used that creates a field strength of 1.2 mT at 23 mm then the minimum field strength at 30 mm is equal to 0.55 mT, roughly three times the size of the external magnetic field, and far above the minimum resolution of most magnetometers (Table 7.2). The accuracy may be negatively affected by the metal of the femoral component, but it is unclear to what extent until an experiment has been performed. Femoral components are typically made from cobalt chrome alloy, which may be described as non-magnetic [171].

Conclusion

Given that a gyroscope uses a lot of power, compared to an accelerometer or magnetic sensor, it is beneficial to use a magnetic sensor to measure rotation. In fact, there is one integrated sensor that internally calculates rotation directly based on magnetic readings (KMX61G, Kionix, Ithaca, NY, USA) (Table 7.2), although the use of a dedicated external microprocessor is required. The advantage of measuring angles using a magnetic sensor is that it does not suffer from drift, as the gyroscope does, because the measured angle is absolute.

Therefore, in addition to using an accelerometer to measure the acceleration/deceleration during gait and the angle of the tibia in respect to the ground, it is beneficial to measure angular rotation and position, to determine the angle between the tibia and femur.

7.5 Other System Components

7.5.1 Wireless Bi-directional Communications

Chapter 6 describes the experiments that were performed for wireless bi-directional communication with the ZL70102. In this section the power use during typical communication is calculated.

To estimate the current consumption of the ZL70102, three activity states were defined: *standby*, where the ZL70102 is waiting for a wake up signal from the base station, *idle*, where there is no wireless communication, but during which time the new data may be sent from the microprocessor to the ZL70102, and *transmission*, during which time the data is sent wirelessly.

For the ZL70102, the current during these three states is 10 μA, 1.1 mA and 5.3 mA respectively. The time that the microprocessor is occupied transmitting to the ZL70102 was calculated using Equation 7.2. During wireless transmission between the implant and the base station, assuming faultless communication, for a sensor update rate of 26.3 Hz and 90.9 Hz, the bit rates are 26.3×160 = 4208 bps and 90.9×160=14544 bps. For communication between the microprocessor and the transceiver 8 bits have to be added to each 160 bit packet for transceiver commands. Therefore between the microprocessor and the transceiver, this results in 26.3×(160+8) = 4419 bps, and for 90.9 Hz, 90.9×(160+8) = 15272 bps.

Since the transceiver has a 'wake up' functionality, provided in case the base station needs to send a packet to the transceiver, the requirement that the transceiver has to wait for 10 ms per second to wait for commands was omitted (Equation 6.1).

The results of the calculation using Equation 7.2, are shown in Table 7.3. Given the large amount of power and time spent during wireless communication in comparison to standby power, it was not surprising that the power at 90.9 Hz was 3.44× larger than at 26.3 Hz, since 90.9/26.3 = 3.45.

$$P_c = V_s \times \left(\frac{B_{TX}}{B_{TXeff}} \times I_{TX} + \frac{B_{ISP}}{B_{ISPmax}} \times I_{ISP} + (1 - \frac{B_{ISP}}{B_{ISPmax}} - \frac{B_{TX}}{B_{TXeff}}) \times I_s \right) \quad (7.2)$$

where:

P_c	Power at required bit rate [mW]
I_s	Sleep current, during non-transmission time, 10 μA
V_s	Supply voltage, 3 Vdc
B_{ISP}	Number of bps between microprocessor and transceiver
B_{ISPmax}	Maximum bit rate, 4 Mbps
I_{ISP}	Current during transmission of data to base station, 1.1 mA
B_{TX}	Number of bps to be transmitted by transceiver
B_{TXeff}	Effective transmission rate, 55 kbps
I_{TX}	Current during transmission of data from microprocessor, 5.3 mA

Communication between the processor and the transceiver uses the serial digital communication protocol SPI which defines four pins for communication; data in, data

	T$_{tx}$ **[ms]**	**T**$_{ISP}$ **[ms]**	**T**$_{s}$ **[ms]**	**P**$_{c}$ **[mW]**
26.3 Hz	76.5	1.1	922.4	1.29
90.9 Hz	264.4	3.8	731.8	4.44

Table 7.3: *Power calculation for the ZL70102 transceiver for two sensor update rates, using Equation 7.2.* $T_{tx} = B_{TX}/B_{TXeff}$ *(time needed for wireless communication),* $T_{ISP} = B_{ISP}/B_{ISPmax}$ *(time needed to communication between the processor and the tranceiver),* T_s = 1-T_{ISP}-T_{TX} *(time spent in stand-by).*

out, clock and chip select. Communication occurs at 4 Mbps.

Besides those four pins, there are two pins available for interrupts from the transceiver to the microprocessor about important events, such as a full buffer.

7.5.2 Wireless Uni-directional Communication

Unidirectional communication have been achieved using an inductive link at communication speeds up to 4.75 kbps [152], and the same link can be simultaneously used for powering the implant. Communication is possible by momentarily shorting out the voltage that is induced in the secondary coil with an electronic switch, with a modulation signal (m, Figure 7.3 block c), which induces a voltage in the primary coil. Therefore a signal can be transferred. The disadvantage is that for communication a part of the power generated in the secondary coil is dissipated. That power is required to power the implant components, and therefore to reach the same level of power generation during communication, more power has to be transferred to compensate for the loss.

At a communication speed of 4.76 kbps or 4874 bps, only the lowest update rate of 26.3 Hz can be used. Additionally, up to half of the available power that would otherwise be available for powering the implant would be dissipated in the form of heat, depending on the packet contents. For instance, if a packet contains more 'high' bits than 'low' bits, the switch would be on for a longer period, therefore dissipating more power.

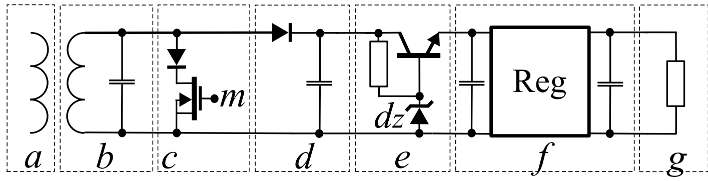

Figure 7.3: *Converting alternating current to direct current, with a) the primary coil, external to the body, b) the secondary coil with the tuning capacitor, inside the bearing, c) unidirectional communication block, with m denoting the communication modulation signal. d) rectification and smoothing, e) overvoltage protection, f) regulation to a stable output voltage and g) the rest of the system, symbolised by a load resistor.*

An advantage of this communication method is that only two additional components are required (Figure 7.3 block c). This communication link could be useful as a back up alternative to the wireless transceiver, or as a communications link that is only used when the implant is powered up before a measurement. In such a case over this link data would be sent regarding available voltage, and component functioning, until the processor gets a signal to switch to bi-directional communication using the wireless transceiver.

7.5.3 Micro Processor

Of all the different microprocessors, the MSP430FR series [172] has the best low power performance. It uses ferro electric memory (FRAM), which uses much less power than flash or EEPROM memory, two other types of memory that are used more often. The processor is non-magnetic and radiation resistant. Ferro electric memory has been shown to be resistant to radiation, including gamma radiation, and for that reason it is used in space flight [173].

In low power mode the main clock is disabled, and typically 6.3 μA is used at 3 Vdc, and at full power mode at 16 MHz approximately 1.3 mA.

Storage Memory

The MSP430FR family has internal FRAM memory up to 64 KB, which can be used for program code and storage of data. It is unclear how large the microprocessor program will be until it is programmed. The MSP430FR5738 has internal FRAM memory of 16 KB, which is four times smaller, but has the advantage of providing a footprint size of merely 2.04×2.24 mm, compared to 6×6 or 7×7 mm for 64 KB versions, and is the smallest package that is available. Therefore, a compromise had to be made between memory size and footprint size. In order to reduce the size of the instrumented bearing as much as possible, the MSP430FR5738 was chosen. Optionally at a later stage, external memory could be included, but this was not considered as being not vital, since for functioning, external power has to be supplied, and then it was thought to be only a small additional effort to include communications as well.

Clocking

To prevent the use of external crystals, which take up considerable volume, internal microprocessor sources were assumed to be used to generate clocks, and the measurement update rate would be clocked by responding to the 'measurement ready' interrupt of the AD7746 after each conversion. For each 'measurement ready' interrupt, the microprocessor will read the capacitance, followed by read out of other peripherals, data processing, and transmission to the transceiver. After that the microprocessor returns to low power mode.

Communication

Although for the power calculations the standard packet was defined, other packets may be defined, for instance to read out individual sensor data, change the update rate, read out memory contents, and to reconfigure the processor. The temperature sensor can be read using low power mode by connecting it to a pin on the microprocessor that generates an interrupt on change; when the PWM output of the TMP05 (see Section 7.4.2) changes state, an interrupt will be generated so that automatically a timer/counter register within the microprocessor will start counting clock cycles of a low power clock until the next interrupt. The clock that is available for this is generated inside the microprocessor, and has a typical frequency of 8.3 KHz. For the TMP05 sensor, this results in a resolution of approximately 0.5 °C per clock cycle. The microprocessor can remain in low power during the counting process, and only needs to be in full power mode to calculate the temperature.

The ZL70102 will be controlled using a dedicated SPI communications module, available within the microprocessor. Communication with the KMX61G and AD7746 will be controlled using a dedicated I^2C communications module, available within the microprocessor. Multiple I2C devices can be controlled using the same communication lines/signals.

Processing Time

To encompass all calculations, memory writes, transition states, it was estimated that the processor spends one extra millisecond per second in full power mode at 26.3 Hz update rate, and 3.4 ms per second at 90.9 Hz update rate 1 ms equals 16000 clock cycles, which is a considerable amount. Data processing will consist out of the following actions: calculate temperature, put the received data in the right order into a package (packaging), and perform data reduction calculations. For instance in the case of capacitance the dynamic change is in the order of femto farads, so instead of the full 24 bits of data, which describe the full range of the capacitive converter, only the change in capacitance may be saved, which results in smaller storage volume.

Peripheral Pin Count

The number of pins that the processor needs to provide for communication with the peripherals are shown in Table 7.4):

The MSP430FR5738 has 19 pins available for input/outputs.

	Number of pins
AD7746	3
TMP05/06	1
KMX61G	2
ZL70102	6
Vin[1]	1
ind. link[2]	1
total	13

Table 7.4: *Number of pins that the microprocessor needs to provide for communication with peripherals.* [1] *Vin is measured using an analog to digital converter internal to the microprocessor.* [2] *inductive unidirectional communications link*

7.6 Powering the Implant

7.6.1 Power Consumption

To estimate how much power will be consumed during normal operation, two scenarios have been determined:

1) operation at 26.3 Hz, capacitance, temperature measurement, and tibial/femoral angle determination.

2) operation at 90.9 Hz, capacitance, temperature measurement, and tibial/femoral angle determination.

For power calculations, it is assumed that when the microprocessor is not occupied, it is in low power mode. Furthermore, it is assumed that all sensors are read out consecutively, except for the temperature sensor, which can be read parallel to the other measurements using a specialised module, which can run in low power mode (see Section 7.5.3), and finally, since the calculations are performed for normal operation, the inductive link is not included in the power calculations. At an update rate of 26.3 Hz and 90.9 Hz, 4.66 and 7.81 mW are expected to be required (Table 7.5).

	$\mathbf{T}_{c,26.3Hz}$ [ms]	$\mathbf{T}_{c,90.9Hz}$ [ms]	$\mathbf{P}_{26.3Hz}$ [mW]	$\mathbf{P}_{90.9Hz}$ [mW]
AD7746	2.63	9.09	2.1	2.1
TMP05	0	0	0.1	0.1
KMX61G	0.03	0.14	1.44	1.44
ZL70102	0.8	3.8	0.98	4.2
MSP430	4.46	14.03	0.04	0.07
total			4.66	7.91

Table 7.5: *Power calculations for full sensor use; measurement of capacitance, accelerometry and magnetic sensor, and temperature at update rates of 26.3 and 90.9 Hz. The communication time (T_c) for the MSP430 microprocessor is the aggregate of all the T_c of the individual peripheral components, plus 1 ms of extra time, which is discussed in Section 7.5.3. MSP430 power calculations are explained in Section 7.6.1.*

7.6.2 Powering Methods

Implants can be powered using inductive power transfer, batteries, or motion based power generation. Only inductive power transfer and batteries have been used *in vivo*, because of their larger energy supplying capabilities [174]. For the same arguments as mentioned before in Chapter 2 (risk of changing the mechanical behaviour of the bearing and risk that components with a high elastic modulus damage the UHMWPE), power harvesting or storing components should be placed within the part of the bearing that experiences only minor loading. Because of the limited space and the risk of exposing the body to dangerous chemicals as a result of wear of the bearing, it was considered to be safest not to use a battery. Therefore, the implant should be powered using wireless induction. For reasons outlined in Section 6.3.4, the best location for the inductive coil is on the anterior side of the bearing.

7.6.3 Proposed Power Stage

The power stage that was proposed is shown in Figure 7.3. An inductive coil will generate alternating current (AC), which will be rectified by a rectifier and smoothed to direct current (DC). To protect the regulator that creates a stable output voltage from the input voltage from voltages that are too high, an overvoltage protection circuit should be used. Each of the elements will be discussed in more detail.

7.6.4 Inductive Coil

An inductive coil, located external to the body, will be placed in close proximity of the implanted instrumented bearing (Figure 7.2, "antenna"). The external coil generates an electromagnetically changing field, which radiates through the body tissue, and which is picked up by a coil within the bearing. Experiments have been performed with several inductive coils that demonstrated that the electronic power required by the implant could be generated (see Chapter 6.7).

7.6.5 Input Over-Voltage Protection

Because a regulator has a maximum input voltage, it needs to be protected from voltages that are too high. The estimated internal voltage was shown to increase over 10 V_{ac} (see Chapter 6.7), and therefore, to protect the voltage regulator, a limiting pre-regulation circuit is necessary.

Therefore, a simple active limiting circuit needs to be inserted before the regulator (Figure 7.3e). The limiting circuit is a series-pass regulator, that will pass all voltages below the voltage limit, but will limit all voltages above that to the limiting voltage. The zener diode ("d_z", Figure 7.3e) provides a stable voltage at its positive terminal when the voltage supplied by the resistor connecting to d_z is higher than V_z, the zener voltage. The transistor (the component above the zener diode) only conducts from the supply side of the circuit to the regulator when the voltage at the controlling terminal is higher than the output + the diode voltage drop V_{be} of the transistor.

Therefore, the output voltage can be calculated using Equation 7.3. With a typical V_{be} of 0.6, for a required output voltage of 5.5 Vdc, a zener diode with a zener voltage of 6.1 Vdc needs to be chosen.

$$V_{out} = V_z - V_{be} \tag{7.3}$$

where:

V_{out} Output voltage of limiting circuit

V_z Zener voltage

V_{be} Base-emitter voltage of series transistor

7.6.6 Voltage Regulator

The induced voltage is dependent on the distance between the primary and secondary coil (see Chapter 6.7). This distance is dependent on the flexion/extension of the knee, because the bearing moves anteriorly and posteriorly during movement.

Therefore, a regulator needs to be used to create a stable voltage output. There are two types of voltage regulator that create a pre-set output voltage: linear regulators, that provide series or parallel resistance regulation, and switching regulators, that switch the input voltage. In case of decreasing the input voltage, the converter is called a buck converter, and in case the output voltage is higher than the input voltage, a boost converter. A combination of the two is called a buck/boost converter. Boosting the voltage comes at the expense of reduced current. Additionally, for low currents, linear regulators are more efficient.

To find out what the typical efficiency of a buck/boost converter is, an experiment was performed with the TPS61200, and the typical efficiency was 25% if the input voltage was lower than the output voltage, and 50% if it was higher (see Appendix E.1). This means that the inductive power transfer has to transfer 200-400 % more power than required on the output of the boost converter, which for a power requirement of 7.94 mW corresponds to an induced power of 15.88 to 31.76 mW.

$$P = V^2/R \tag{7.4}$$

where:

P	Power
V	Voltage
R	Resistance

Power can be calculated using Equation 7.4, so load of 32 mW with a voltage of 3 V corresponds to a resistive load of R = 281 Ω, and a load of 16 mW results in R = 566 Ω. These numbers were used as equivalent loads in Section 6.7.

To estimate the efficiency of a linear regulator, a suitable regulator, the TLV717, was found, and the information from its datasheet was used to calculate the theoretical efficiency, using the following equation (equation 7.5):

$$P_{LDO} = V_d \times I_{out} + Vin \times I_{out} \times \beta + V_{in} \times I_q \tag{7.5}$$

where:

P_c	Dissipation of the linear regulator [mW]
V_d	voltage drop between input and output of the regulator [V]
I_{out}	Output current [mA]
V_{in}	Input voltage [V]
$V_d \times I_{out}$	Voltage regulation dissipation [mW]
$V_{in} \times I_{out} \times \beta$	Dissipation linked to output current of the regulator [mW]
$V_{in} \times I_q$	Quiescent dissipation of the regulator [mW]

Using V_{in} = 0.25 V, V_{in} = 3.1 V_{dc}, V_{out} = 2.85 V_{dc}, I_{out}=2.667 mA, and Iq = 0.035 mA, the dissipation of the TLV717285P is 1.235 mW.

$$\eta = \frac{P_{out}}{P_{out} + P_{diss}} \tag{7.6}$$

where:

η	Efficiency
P_{Out}	Output power
P_{diss}	Dissipated power

Using Equation 7.6, a delivered output power of 7.91 mW (Table 7.5), and a dissipated power of 1.235 mW, the efficiency is 0.86 or 86%.

Assuming a power requirement of the circuit of 7.91 mW at 2.85 Vdc, and a regulator efficiency of 86 %, an input power of 9.1 mW is required to compensate for a loss of power of 1.235 mW.

The voltage at is required at the input of the limiting circuit should be at least 3.7 V_{rms}, calculated using Equation 7.7.

$$V_{coil} = V_{in} + V_d + V_{drop} \tag{7.7}$$

where:

V_{coil}	Output voltage of the coil, at the input of the limiting circuit
V_{in}	Voltage at the input of the regulator, 2.85 V_{dc}
V_d	Voltage drop by the diode, 0.4 V_{dc}
V_{drop}	Voltage drop by the limiting transistor, 0.2 V_{dc}

7.6.7 Discussion

The efficiency of the boost converter is very low, compared to the linear regulator, especially for lower input voltages. At an efficiency of 25 to 50 %, in case of using a boost converter, the coil needs to deliver two to four times the amount of power, and therefore needs to have more windings too; just as would be necessary to create

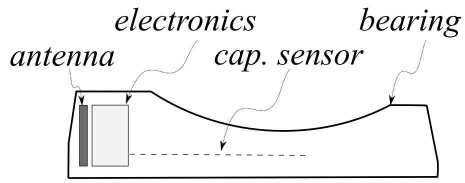

Figure 7.4: *Knee replacement bearing, with internal antenna, encapsulated electronics, and capacitive sensor.*

sufficient input voltage for a linear regulator.

Therefore, a linear regulator should be used, because of the higher efficiency. In order to compensate for power loss, fewer additional input coils would be necessary for the linear regulator compared to the boost converter, and additionally the heat production within the bearing would be lower.

7.7 Construction

7.7.1 Introduction

All the electronic components that were identified, and the supporting components that are required to enable them to function, need to be encapsulated in one module. That module connects to the capacitive sensor, the wireless antenna and the inductive power coil. The encapsulated electronics should be placed within a portion of the bearing that undergoes little direct mechanical compression during use (Figure 7.4). First the volume of the module was calculated, and then methods of embedding the module will be discussed.

7.7.2 Estimated Volume of the Implant Electronics

To estimate how much volume the full circuit would occupy, a full list of the components was made, based on the manufacturers' requirements. Then the smallest size package was chosen for that component, whilst still using standard IC packaging and enabling the use of standard manufacturing technology. The ZL70321 is a ZL70102 IC, packaged together with an external filter and matching components. Therefore this module was more suitable for prototyping.

Smaller component sizes are possible; but only when the *dies*, the silicon wafer integrated circuits within normal packages, are assembled using specialised bonding techniques. For instance, the ZL70102 in *die* form has dimensions of only 4.3×3.2×0.57 mm (however other components, like a filter and crystal are required). However, for prototyping this solution not practical, given that bonding techniques have to be utilised for connections, which is expensive, cumbersome, fragile, and prevents easy access for debugging. Using bonding, all components could be integrated within one or two IC packages, when only the necessary connections are connected. The reduction in volume could be 10-20 fold, but the process of assembly only becomes viable when the complete system is working faultlessly and when large quantities are required, to offset the large initial cost.

The resulting volume was 240 mm^3. For this calculation, the surface area occupied by the copper signal traces was ignored, as well as the volume of the PCB material itself. The wireless antenna was assumed to made out of the same material as the PCB, with dimensions 22×5 mm (see Section 6.3). All the outlines of the components are shown laid out in Figure 7.5. The ZL70321 module had roughly the same surface area as all other components, therefore these all fitted on the reverse side of the PCB. The resulting PCB had dimensions 13×7.3 mm.

The thickness of the multi layer PCB was assumed to be 0.4 mm. The entire assembly (two layers of components, and one layer of PCB) should have a maximum size of 13×7.3×5 mm (Table 7.7 and Figure 7.5). The overall theoretical volume increased from 239.86 mm^3 to 462.25 mm^3. The coil may have to be integrated in one potted package, or placed separately. Which solution is best is part of future research.

The influence of inserting the electronic module into a bearing was simulated in Chapter 4, resulting in 5 % change in bearing compression and capacitive sensor output.

	L [mm]	**W** [mm]	**H** [mm]	**A** [mm^2]	**V** [mm^3]	**ext. comp** [N]	$\mathbf{A}_e$ [mm^2]	$\mathbf{V}_e$ [mm^3]
AD7746	5.227	6.527	1.327	34.12	45.27	3[0]	0.90	0.387
TMP05/06	2.327	2.527	1.577	5.88	9.27	1	0.31	0.12
KMX61G	3.127	3.127	1.027	9.78	10.04	1	0.31	0.12
ZL70321[1]	**12.12**	**7.127**	**1.677**	86.37	144.86	8	2.48	0.94
MSP430[2]	2.167	2.367	1.027	5.13	5.27	4	1.24	0.47
ac/dc-C[3]	1.74	0.93	0.63	0	0	1	0.31	0.12
ac/dc-D	0	0	0	0	0	2[4]	1.93	1.14
ac/dc-E	0	0	0	0	0	3[5]	0.31	0.12
ac/dc-F[6]	1.177	1.177	0.527	0	0	2	0.62	0.24
subtotal	-	-	-	144.29	216.46	23	15.29	10.77
coil[7]	25	5	0.1	125	12.5	1	0.31	0.12
total	-	-	-	284.89	239.86	24	15.60	10.89

Table 7.6: *Dimensions (L,W,H), area (A), volume (V) of the electronic components, and number of supporting components (ext. comp) with their area (A_e) and volume (V_e).* [0] *using 0402 package: 1.127×0.627×0.427 mm.* [1] *The ZL70321 is the ZL70102 packaged together with a crystal, and several filter/matching components. The ZL70321 had the largest dimensions of all components.* [2] *MSP430FR5738* [3] *Components of block c of Figure 7.3* [4] *Components of block d of Figure 7.3, one of these had dimensions 1.74×0.93×0.63 mm.* [5] *Components of block e of Figure 7.3. Two of these had dimensions 1.88×1.83×1.03 mm.* [6] *Components of block f of Figure 7.3.* [7] *The coil was assumed to be a rectangular block, with outer dimensions 25×5×1 mm. Unless mentioned otherwise, each external component was assumed to have '0201' packaging, 0.6×0.3×0.25 mm. Each component was assumed to be spaced at least 0.005" (0.127 mm) apart from the next component, effectively increasing the volume. All component dimensions were increased by this amount.*

7.7.3 Moulding Process

One method of creating a bearing is by compression moulding, where UHMWPE powder is compacted under high pressure into the shape of the bearing, which is the standard method. Another method is to also use compression moulding but into a larger block, called a 'slug' from which the required component will be machined.

The standard compression moulding technique results in the minimum amount of changes to the existing method.

A typical protocol to manufacture direct compression moulding of UHMWPE is shown in Figure 7.6. UHMWPE is compacted, molten, and recrystallised. Tempera-

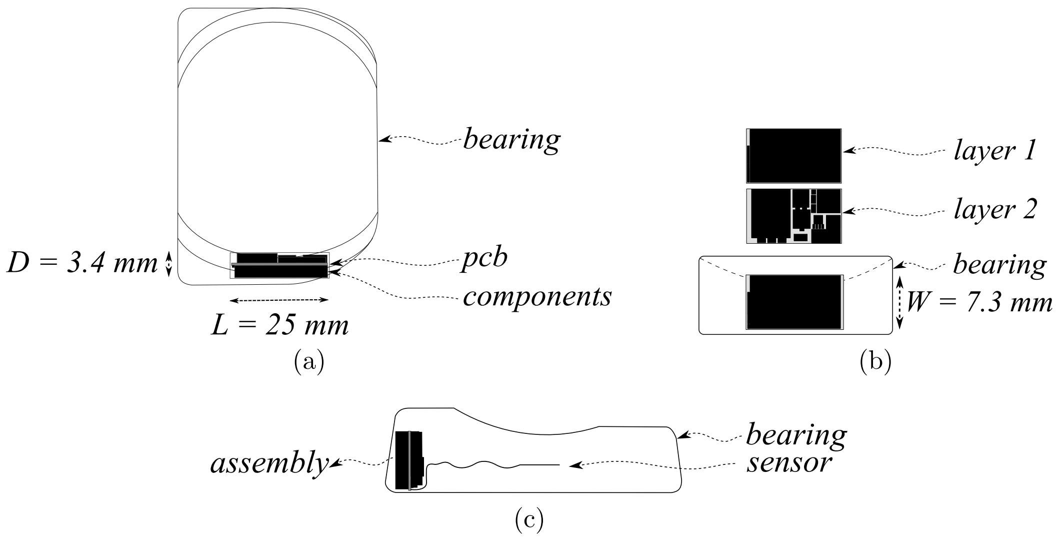

Figure 7.5: *Illustration of the instrumentation assembly, top view, with all the electrical components, drawn to scale. The large module on the PCB is the ZL70321, taking up roughly the same amount of surface area and volume as all the other components.*

	Description	**L [mm]**	**W [mm]**	**D [mm]**	**A [mm^2]**	**V [mm^3]**
layer 1	coil	13	7.254	1	95	95
layer 2	shielding	13	7.254	0.1	95	9.5
layer 3	ZL70321	13	7.254	1.68	95	159.6
layer 4	PCB	13	7.254	0.4	95	38
layer 5	components	13	7.254	1.57	95	149.15
layer 6	shielding	13	7.254	0.1	95	9.5
layer 7	antenna	13	7.254	0.1	95	1.5
total	-	-	-	4.95	-	462.25

Table 7.7: *Description and dimensions of the layers that compose the instrumented bearing electronics assembly, with length (L), width (W), depth (D), area (A) and volume (V).*

tures can reach up to 210 °C, and pressures up to approximately 40 MPa.

7.7.4 Sterilisation

After compression moulding, the bearing is sterilised. There are several methods to sterilise a UHMWPE component; through gamma radiation in low oxide conditions, vacuum, or nitrogen; using gas plasma; through annealing (heating below the melt temperature); or using ethylene oxide gas. The Oxford UKR bearing is sterilised using

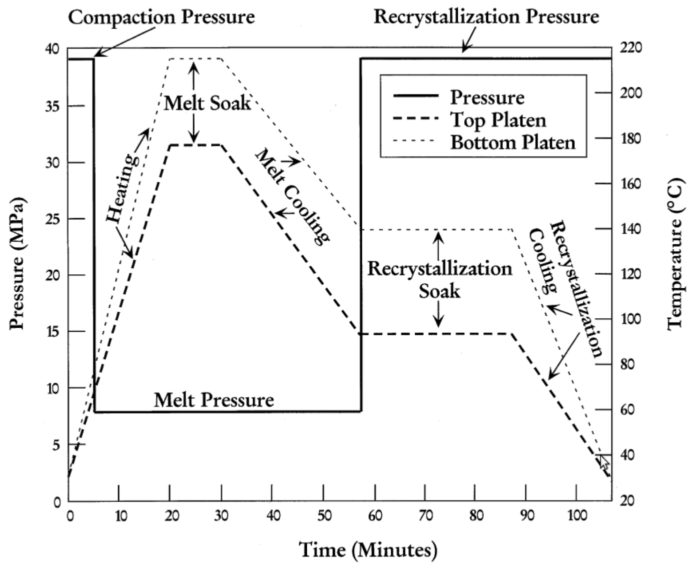

Figure 7.6: *A typical compression moulding process, in which UHMWPE powder is molten and compressed into a solid item. Pressure is applied with the top platen (Figure 5.1), and the top and bottom platen may have different heat profiles [175].*

gamma radiation in a low oxygen package. Gamma radiation changes the material properties of UHMWPE; it increases cross-linking, making the UHMWPE more resistant against abrasive and adhesive wear. However, this method is not suitable for repeated use, for instance in the case of intra-operative use, since after every radiation dose the material properties are changed. Ethylene oxide gas is highly toxic and neutralises bacteria, spores and viruses. Given the toxicity, the process needs to be performed under carefully controlled conditions. A typical sterilisation cycle takes up to 41 hours; 18 hours of preconditioning at 65 % humidity, followed by 5 hours of exposure to 100 % ethylene oxide gas, followed by 18 hours of forced air aeration. There are no reports of mechanical property changes for this type of sterilisation. Gas plasma, or ionised gas has been used to sterilise the surface of components. In comparison to ethylene oxide gas sterilisation, gas plasma does not leave toxic residues or involves environmentally hazardous byproducts. A gas plasma sterilisation cycle only takes 75 minutes. Also for this method there are no reports of mechanical property changes. Another common method of sterilisation, namely autoclaving: sterilising using steam, cannot be used with UHMWPE because it changes the material properties of UHMWPE; it promotes oxidation of UHMWPE, making it more brittle [175].

7.7.5 Embedding Electronics

For embedding the electronics within the bearing created using compression moulding there are three options: 1) adding the electronics to the bearing before the UHMWPE is compacted, 2) adding the electronics to the bearing after manufacturing, but before gamma irradiating 3) adding the electronics to the bearing after manufacturing and irradiating.

Option 1)

In this method, the electronics must be able to withstand temperatures up to 210 °C, pressures up to 40 MPa, and radiation with gamma radiation of about 40 kGy. No additional sterilisation is required since the electronics are fully contained within the UHMWPE.

Option 2)

In this method, the electronics must be able to withstand radiation with gamma radiation of about 40 kGy. No additional sterilisation is required since the electronics are already sterilised during irradiation.

Option 3)

In this method, the electronics must be able to withstand sterilisation only.

Embedding the electronics within a slug and machining the result into a bearing shape is similar to Option 1.

In every option, the electronic components and PCB need to be covered (*'potting'*) in a protective shell of resin. There are multiple reasons for this; solder starts melting at approximately 217 to 227 °C, depending on the SnCu alloy [176], so in *Option 1*, because the temperature used in compressive moulding approaches the melting temperature of solder, the electronic components need to be kept in place to prevent them from falling off the PCB. Additionally, solder joints typically shear off at a lateral stress of 20-40 MPa, depending on the surface area and composition [177–179]. Therefore, the potting needs to prevent compressive forces from shearing off the components from the PCB. In *Option 2* and *Option 3* the electronics need to be protected from bodily fluids, and additionally, the environment needs to be protected from contaminants, bacteria, viruses and spores, and possible bio-incompatible materials. Once fluid enters the seams, it may increase the risk of infection, or it may provide a conduit for metallic ions or particles, which may be toxic to the body.

The potting material needs to bio compatible, and ideally as stiff as possible to protect the electronic components from shearing, and, especially in case of option 1), needs a high melting temperature. The hardest known bio compatible materials that can be poured are used in dental reconstruction. The most commonly used dental restorative material is bisphenol A glycol dimetacrilate (Bis-GMA). Bis-GMA is a polymer, and in dental applications it is mixed with other materials such as glass to change the colour or mechanical properties, or to prevent bacterial growth (added fluoride). To improve mixing with other (and inorganic) materials, often triethyleneglycol dimethacrylate (TEGDMA) is used. Bis-GMA is cured with light. The glass transition temperature Tg, the temperature at which a polymer transitions from a hard glass-like state to a rubber like state, is dependent on the exposure time and the lowest reported Tg for Bis-GMA composites lies around 295 °C, with a maximum of 384 °C. Therefore, there is no risk that Bis-GMA will melt during compression moulding, as long as proper exposure times are observed [180]. The Youngs modulus of Bis-GMA composites can range up to 10 GPa [128, 129].

An impression of the potted electronic assembly is shown in Figure 7.7. The capacitive sensor and the inductive coil are not potted, as they need to be connected with an external connector. This connection could be a regular solder connection, which after

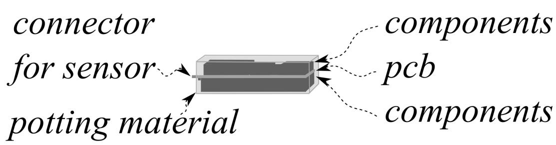

Figure 7.7: *An impression of the potted electronic assembly, sized 14×7.5×3.6 mm, shown to scale. On the left hand size of the block, a connector for the capacitive sensor protrudes from the potting. A similar connector will be placed for the inductive coil.*

soldering needs to be potted or covered in case construction option 2) or 3) is chosen.

Option 1 is the most advantageous in the sense of bio compatibility, because all the electronics are covered by UHMWPE. However, in this case the electronics get gamma radiated, and that may destroy or alter the functioning of the electronics. Future testing has to show how important this effect is. *Option 2* ensures that within the potting there are no surviving bacteria. However, Bis-GMA is not a porous material, and therefore any organism trapped within the potting should not be able to come out. However, bacteria that are trapped between the potting material and the bearing material do get irradiated, which results in better sterilisation. *Option 3* provides the least radiative stress for the electronics, but care must be taken that the device is reliably sterilised. Residual bacteria may be trapped between the potting material and the bearing, which may not be reached by gas sterilisation processes.

To find out how much influence embedding the electronics has on the measured capacitance, a finite element model simulations were performed (see Chapter 4).

7.8 Cost

The cost, including assembly of the printed circuit board but not counting potting material, the potting process itself, or inserting the assembly within the bearing after moulding, is estimated to cost approximately £50 excluding VAT, when ordered per 1000 (Table E.2 in the Appendix). Compared to the average total cost of a UKR implant, £1309 plus Value Added Tax (VAT), [181], the cost of instrumenting the UKR will most likely not exceed 5% of the uninstrumented UKR.

7.9 Chapter Conclusions

Besides capacitance and temperature, other useful measurable quantities are the angle of the tibia relative to the earth's gravity vector and possibly the angle of the femur relative to the tibia. Several off-the-shelf semiconductors have been chosen to measure these quantities, based on volume and power use *This answers Aim 1: Determine which additional quantities can be measured and how much power and volume their measurement requires.*

The resulting design for a UKR bearing is meant to be for the prototype only; smaller packaging solutions are possible with the same electronic circuits by integrating multiple circuits into one package.

The total power during a sample update rate of 26.3 and 90.9 Hz has been calculated. *This answers Aim 2: Determine the power requirement of the complete implant.*

Measurements have shown that it should be possible to power the implant with inductive power and that a linear voltage regulator should be used. *This answers Aim 3: Determine how and if the power requirements can be met.*

The electronic components should be potted inside a potting material to protect them from body fluids and tissue, and also to protect body fluids and tissue from possible contamination with toxic materials and bacteria.

It was concluded that the implant should be constructed in phases; first the implant should be created using off-the-shelf components and the module should be moulded into a slug, ready for machining into a bearing shape. Using a slug would result in a bearing with an integrated electronics module, which can be more reliably sterilised. When all the instrumentation errors have been eliminated, the electronic module should be inserted into the bearing at the moulding stage. *This answers Aim 4: Determine how the implant should be constructed.*

7.10 Thesis Summary

The main goal of this thesis was to investigate how to instrument a mobile Unicompartmental Knee Replacement (UKR) in order to measure load. Several conclusions were drawn in each chapter;

Chapter 1: loads measured with an instrumented mobile UKR would be more representative of normal knee loads than those measured with an instrumented TKR. In addition to that, because the UKR is mobile, the amount of axes of movement of the femoral component over the bearing is reduced from three to one, comparing the instrumented TKR to the instrumented UKR bearing. Therefore load measurement requires less sensors.

Chapter 2: commonly used sensor types are not suitable for long-term use in UHWMPE, because either the sensor would fail prematurely, or because of an increased risk of UHMWPE wear. A capacitive sensor was identified as being the solution to both problems.

Chapter 3: the load sensor was embedded within UHMWPE and because its mechanical response has a potential influence on load measurement, relaxation, creep, and frequency measurements were performed. The viscous response of UHWMPE to a change in constant load, the primary creep response, reaches 95 % of its final compression within 12 minutes. Thereafter, the change in compression is slow, however quasi-steady state. Frequency measurements indicated that for temperatures that can be experienced by an implant *in vivo*, stiffness could change by more than 10 % and therefore a temperature sensor for temperature compensation should be used.

Chapter 4: in this chapter finite element models of the instrumented bearing indicated that besides the material surrounding the load sensor, also changes in geometry of the surrounding material influence sensor measurements. However, it was concluded that even though between bearings such changes may lead to large changes, within one bearing during its lifetime most parameters can be ignored, except for temperature influence on the elastic modulus of UHMWPE. It was found that placing the capacitive sensor directly underneath the bearing concavity resulted in the largest sensor output magnitude. Additionally, simulations were performed to assess the influence on stress within the UHMWPE surrounding a sensor made of PI and an electronic module. The conclusion was that there are effects on stress, but that future wear tests have to be performed in order to assess the influence of this on bearing wear and component life.

Chapter 5: in this chapter the construction of the novel capacitive sensor was outlined and experiments were performed to assess its response to loading. In static loading experiments the finding of Chapter 3 was confirmed that, after observing a sufficiently long time after applying a step change in average loading, the viscous response reaches the ultimate compression value within 5 %. The frequency response of the sensor was shown to be second order low pass, with a corner frequency at 9 Hz, roughly twice the required maximum frequency of 4 Hz, determined in Chapter 1. The loads measured with the instrumented UKR do show non-linear second harmonic distortion generation with a relative amplitude of approximately 20 %. A novel load estimation method was developed, in which dynamic loads were estimated with a linear or dynamic estimator, using the detrended measured capacitance data, which were then shifted to the correct absolute loads. This method resulted in loads that could be estimated with an accuracy better than 90 %.

Chapter 6: in this chapter a suitable wireless transceiver was selected, the Micro-Semi ZL70120, and *in vitro* measurements were performed to assess how well this transceiver performed with supplied antennas and a custom designed foil antenna. For transfer modes 2FSK (55 kbps) and 2FSK-HS (30 kbps) all antennas worked well up to 2 meters distance (1 meter verified for the foil antenna using 2FSK-HS). The *in vitro* setup that represented the worst-case situation *in vivo* introduced changes to data rate smaller than 5 %. Additionally, wireless power experiments were performed that confirmed that the implant could be powered wirelessly.

This chapter: an overview of the electric system of the implant was given. Additionally, several other measurement modalities were suggested: measuring the angle of the tibial plateau towards the earth gravity vector, and the tibial plateau in respect to the femoral component. The total power consumption and physical volume of the entire system was calculated, and finally methods of how the entire system should be constructed were discussed.

7.11 Thesis Goals

To gauge to what extent the goals of this thesis were achieved, the requirements set out in Section 1.7 (and re-given in Table 7.8) will be discussed, one by one.

Requirement	Description
1	No measurement instrumentation material, except for UHMWPE or other biologically neutral materials, may be in contact with the body.
2	Sustained wear of the bearing for 30 years, at a predicted wear rate of 0.02 mm/yr must not expose embedded components.
3	The measurement data must be transmitted wirelessly.
4	The bearing must be able to operate or be recharged using a power source outside of the body.
5	The minimum amount of load to be measured is 0.2×Body Weight.
6	The maximum frequency that can be measured should be at least 10 Hz, in order to capture peak forces.
7	The instrumented UKR must be cost effective.

Table 7.8: *The requirements for an instrumented UKR, outlined in Chapter 1 of this Thesis.*

7.11.1 Requirement 1

No measurement instrumentation material, except for UHMWPE or other biologically neutral materials, may be in contact with the body. The final design of the capacitive sensor will be completely embedded within UHMWPE (see Chapter 5), as well as the electronics module.

At this stage it is unclear how reliably the bearing performs with an inserted electronics module; although it will be inserted into a part of the bearing that is not experiencing direct compression, the extra stresses that are generated may still result in premature failure of the UHMWPE. This may mean that the volume of the electronic module has to be decreased, or the existing bearing design may have to be extended to provide extra space, which will require a new regulatory approval as well as a new mould. Both options are very costly. Summarising: it is possible to house all the electronics within biologically neutral materials; for measurements made in cadaveric specimens or during trial implantations the electronic module will be moulded into a slug, which will then be machined into a bearing shape, but for studies involving permanent implantation of the instrumented bearing a redesign of the bearing may be necessary

7.11.2 Requirement 2

Sustained wear of the bearing for a 30 years, at a predicted mean wear rate of 0.02 mm/yr must not expose embedded components. The work described in Chapters 7 demonstrates that it is possible to house the electronics a greater distance than 0.6 mm away from the bottom and top surface of the bearing, thus for the expected mean amounts of wear [34], the instrumented bearing should be able to survive 30 years.

7.11.3 Requirement 3

The measurement data must be transmitted wirelessly. For an update rate of 26.3 Hz, data can be sent either with a unidirectional inductive link or with a bidirectional transceiver (see Chapter 6). For faster update rates, a wireless transceiver should be used. Tests have been performed with a ZL70102 transceiver which performed suitably within a simulated worst case *in vitro* test setup using body tissue to model the effects of signal attenuation.

7.11.4 Requirement 4

The bearing must be able to operate or be recharged using a power source outside of the body. Tests and calculations have been performed with inductive power transfer, and for the required power, the findings indicate that it is certainly possible to power the implant (see Chapter 7).

7.11.5 Requirement 5

The instrumented bearing must be able to measure a maximum equivalent of 10 body weights of load. Both the capacitive sensor itself, and the electronics module must be able to withstand this amount of loading.

The capacitive sensor which was developed for this work was made from polyimide, which has a higher yield strength than UHMWPE. Therefore, if the bearing can withstand this load, then polyimide certainly should. Even if the adhesive layer within the sensor were to fail, causing detachment of the sandwiched copper layers, the copper layer could not become displaced, as it is trapped inside the UHMWPE, and the sensor would continue to function.

Secondly, the electronics must be able to withstand ten body weights, and the bearing must not be damaged by the electronics during ten body weight circumstances. Finite element modelling has shown that for certain mounting positions of the electronics, the electronics module will only experience minor loading, and that there is only a very small mismatch in elastic modulus between the electronics and the bearing. Therefore, it is expected that there will not be significantly increased wear, as occurs in case of a significantly mismatch of elastic modulus. This is discussed in more detail in Chapter 4.

7.11.6 Requirement 6

The maximum frequency that can be measured should be at least 10 Hz, in order to capture peak forces. The results given in Chapter 5 show that the capacitive sensor starts to attenuate most clearly from a frequency of 9 Hz. The electronics have been designed to measure at at least 26.3 Hz, for an effective frequency of maximum 11.2 Hz.

7.11.7 Requirement 7

The instrumented UKR must be cost effective. The additional cost of the sensor and the electronic system has been shown to be less than 5% of an uninstrumented UKR bearing.

7.11.8 Conclusion

All the requirements that were set for this project were met. A novel capacitive sensor was developed for load measurement within a UKR bearing. Measurements have shown that after about 13 minutes of pre-loading the system can repeatably measure loads, with an accuracy of 90 % (see Chapter 5). All the aspects of the measurement system were investigated and wireless powering and communication was tested.

7.12 Future work

The main objectives of future work are (Table 7.9):

Objective	Description
1	Develop a prototype to be used *in vivo* for UKR
2	Improving post-processing methods for load estimation
3	Perform system testing of sensor and telemetry circuitry
3	Perform failure testing to ensure component integrity
4	Test the performance of the instrumented bearing in cadaver studies
5	Test its use as an intra-operative tool to aid surgeons achieve optimal balancing of the UKR
6	Use the bearing permanently *in vivo*

Table 7.9: *Different stages of future work.*

7.12.1 Developing a Prototype

All the components that were described in this Chapter need to be integrated into one prototype. Part of this work has already been performed: the I^2C protocol has been implemented in software for the MSP430 processor, and software control of the C2D has already been written, but control of the accelerometer, and especially the wireless transceiver needs to be programmed. Once the firmware has been written and the electronic design has been finalised, everything will need to be integrated into a low-volume prototype, as described earlier in this Chapter.

7.12.2 Improving Load Estimation

Currently, load estimation occurs by characterising the system using the average of five repeated gait cycles, with a detrending method of subtracting the mean of the measurement. This may be improved by changing the method to measure the deviation from the mean, and compensating for this prior to system identification. Similarly, during load estimation in the 'shifting back' stage, compensation for drift may improve estimation of loads.

Another possible improvement of load estimation is to use a multi-linear estimation of load from capacitance. Currently a linear fitting method is used as an estimator. However, the capacitance to load relationship is only approximately linear, and even shows hysteresis (Figure 5.20). Therefore, the estimation may be improved by constructing a piece-wise linear approximation that better matches the curvature of the point cloud, and possibly even having different characteristics depending on loading and unloading, to match the hysteresis curve.

7.12.3 System Testing of Sensor and Telemetry Circuitry

The performance of the load measurement of the instrumented bearing should be assessed in a servohydraulic rig, similar to the one described in Chapter 5.

To evaluate kinematic measurements, the instrumented bearing should be tested in a mechanical rig with the use of a phantom (saw bones). A rig should be used to provide flexion and extension of the knee joint, allowing for free motion of the knee. To track motion a magnetic tracker (WinTracker, VR-Space Inc, Woolloongabba, Australia) should be used to accurately track three dimensional motion and position of the femur and tibia. The data from the implant and the tracker should be compared.

Temperature sensor testing should be performed by immersing the bearing in a heated fluid bath. The temperature measurements of the integrated temperature sensor of the bearing and an external sensor that measures the temperature of the fluid bath should be compared for all temperatures in the physiological range (33 °C to 47 °C, see Chapter 3).

7.12.4 Failure Testing

Failure testing of the instrumented bearing is a crucial part of this project, to ensure that incorporation of the sensor device does not compromise the integrity of the UKR bearing. As the simulation results of Chapter 4 have shown, the stresses in the instrumented bearing can be higher than in a normal bearing. Therefore, it is possible that the instrumented bearing will fail earlier than a normal bearing under similar circumstances. Tests to failure should be performed for several instrumented and normal bearings, to see if instrumented bearings do fail prematurely. These tests should be performed using a servo-hydraulic test rig or similar, to ensure a controlled test environment. These tests should be divided into several parts: tests with only the sensor inserted, tests with a sensor and an electronic module fully inserted, and tests with sensor and electronic module inserted, post sterilisation.

7.12.5 Cadaver Studies

In vitro testing is intended to test the accuracy with which the device can measure loads and kinematics under simulated *in vivo* conditions using cadaver specimens. A UKR will be performed using routine surgical steps and an optimal size instrumented bearing will be inserted at the end of the procedure to assess the loads exerted on the bearing in extension and flexion. These measurements will be compared to the gold standard to assess ligament balancing (using feeler gauges). This will help establish the magnitude of the differences in the measured loads under influence of identical applied loads but with soft-tissue balancing that is too loose, optimal, or too tight.

A separate part of these studies are wireless powering and communication tests.

7.12.6 Testing for Intra-Operative Use

Subject to obtaining ethical approval, the instrumented bearing should be used at first intra-operatively. Similar to the cadaveric experiment the measurements of the instrumented bearing will be compared to the use of feeler gauges to assess balancing of the soft tissues. The use of an instrumented bearing to aid soft-tissue balancing during a joint replacement surgery is a significant advance in improving the surgical technique of UKR and therefore the outcome of surgery.

7.12.7 Using the Bearing Permanently *In Vivo*

Subject to obtaining ethical approval, the instrumented bearing should be implanted for permanent *in vivo* use. After that, experiments should be performed to assess bearing performance; for instance using three dimensional tracking of femur and tibia using optical markers to verify angles measurement; and using force plates to compare ground reaction forces to knee loads. After verification, experiments should be performed for various activities to compare the loads measured with an instrumented UKR to those measured using an instrumented TKR [3, 5, 8, 11, 182–185]. The ultimate aim is to measure the *in vivo* loads of the knee, to create accurate models of the normal knee, something which so far has not been satisfactorily done before.

Appendices

A LVDT Calibration

The Linear Voltage Differential Transducer (LVDT) was used to accurately measure the vertical position of the servohydraulic actuator above the ground plane, to measure the thickness of the specimen. This section describes the experiments that were performed to measure the accuracy of that measurement.

A.1 Method

A custom made calibration rig was manufactured, that could accurately change the LVDT tip position. The LVDT that was used was the Solartron AX/1/S standard PL (Solartron Metrology, Bognor Regis, UK), which is specified to a range of 2 mm, but has a total travel of 3 mm. The LVDT was connected to a measurement system by TIAB (TIAB Ltd, Middleton Cheney, UK, version SR2 v2.06.17). To provide an accurate reference displacement, a Mitutoya micrometer positioning stage was used (Del-Tron 201 MM, 203.778.2727, Deltron, CT, USA). The platform had a specified inaccuracy of 0.013 mm per 25 mm of travel, and provided a 0.01 mm minor pitch scale.

The LVDT was placed in the rig, and the principal axis of the LVDT and the micrometer stage was aligned. The LVDT was mounted so that an LVDT reading of 0.0 μm corresponded to 0.00 mm on the micrometer. Then the displacement was incremented in 0.01 mm steps up to 2.90 mm. This measurement was repeated three times. The LVDT data was multiplied by 1000 to convert from μm to mm. A robust fit was used to calculate the cross correlation between reference and measurement displacement. Furthermore, the difference between the reference displacement and measured displacement was calculated.

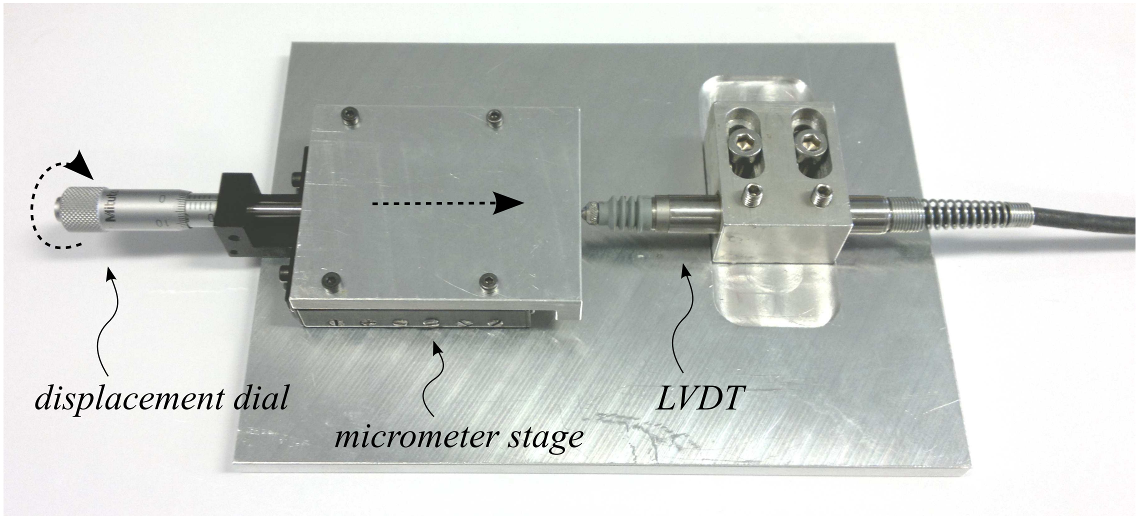

Figure A.1: *LVDT calibration rig, with the micrometer stage, and the linear voltage differential transducer. The dotted arrows indicate the displacement directions.*

A.2 Results

The cross correlation between the reference displacement and measured displacement was 1.0000 for all three tests for the specified range of 0-2 mm and the full measurement range of 0-3 mm. The maximum error between reference and measured displacements at the specification range of 0-2 mm was -0.0039 mm or 0.195 % of 2 mm, and for the full range of 0-3 mm was 0.0367 mm, or 1.22 % of 3 mm (Figure A.2).

A.3 Conclusions

The Solartron AX/1/S LVDT is very accurate, and is most accurate in the specified range of 0-2 mm.

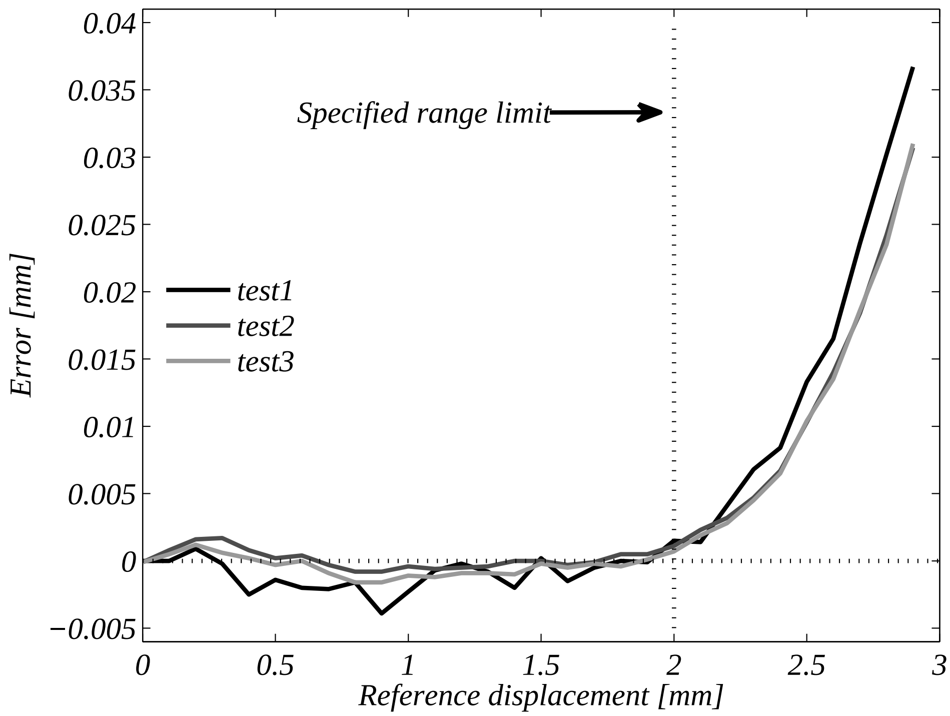

Figure A.2: *Calibration errors of three tests for the LVDT calibration, for the specified range (0-2 mm) and the full range (0-2.9mm) .*

B Appendices for Chapter 5

B.1 Sensor Placement Offset

The results from Table 5.1 were based on images taken with an X-Ray machine, which introduces particular errors. Since the bearing source can be likened to a point source, and the bearing image on the X-Ray foil can be likened to a shadow, placing the bearing further away from the perpendicular centres axis of the X-Ray source may lead to position errors (Figure B.1), also known as the penumbra effect.

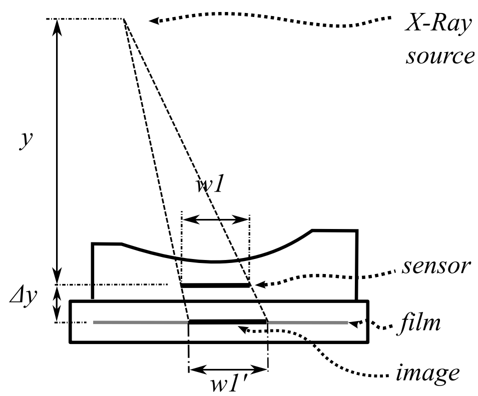

Figure B.1: *Schematic view of the X-Ray projection error*

B.1.1 Method

To calculate the magnitude of this error, the coordinates of the bearing that was furthest away from the centre of the X-Ray were measured, and an error calculation was performed using Equation B.1

$$w1' = (y + \Delta y) \times \frac{w1_a}{y} - (y + \Delta y) \times \frac{w1_b}{y} \tag{B.1}$$

in which (using symbols from Figure B.1):

$w1'$	Image of $w1$ on X-Ray film
y	Distance of X-Ray source above *w1*
Δy	Distance of $w1$ above X-Ray film
$w1_a$	First coordinate of *w1*, the centre of the electrode
$w1_b$	Second coordinate of *w1*, the centre of the bearing concavity

B.1.2 Results

The coordinates furthest away from the centre were: electrode coordinate: 163.31 mm, centres of bearing concavity: 164.94 mm, height of X-Ray source above bearing (Figure B.1: y) 1000 mm, height of sensor above the X-Ray film (Figure B.1: Δy) 10 mm.

Using the coordinates and Equation B.1, *w1* and *w1'* were calculated, resulting in an error of *w1 - w1'* of 0.0163 mm.

B.1.3 Discussion

An error of 0.0163 mm is approximately ten times smaller than the pixel resolution of 0.1680 mm/pixel. Therefore, this effect was ignored.

B.2 Repeatability of Finding Sensor Locations

B.2.1 Introduction

A test was performed to find out to determine the repeatability of the method of visually finding the centres of the bearing concavity and sensors (Figure 5.7).

B.2.2 Method

The process of finding the centre points was repeated three times by the same observer. That gave a data set of three times 18 bearing concavity centres, and for 18×4 electrodes with an x and y point, this gave three data sets of 4×36 points per sensor. It was assumed that any possible error for finding the centre of the electrode was equally large in x and y direction. An Intra-class Correlation Coefficient was performed on the collection of all x and y points for the centre of the bearing, and the centre of each sensor.

B.2.3 Results

The correlation coefficient for the centre of the bearing concavity was 1.0000, as well as for every electrode reading. The maximum difference found in all the paired readings was 2 pixels, corresponding to 0.336 mm.

B.2.4 Discussion

The sensors were placed within a bearing with a good accuracy, the current method works well. The method of determining placement works with high repeatability. Although this does not directly indicate good accuracy of the actual positions, it does indicate that the method of finding the sensor centres was repeatable.

B.3 Sensor Embedding Validation

B.3.1 Introduction

18 instrumented bearings were created, each with four sensors. The sensor foil was first folded, moulded, extracted, and then soldered to leads. This Section describes how many successful sensors resulted from this process, after describing in more detail how the sensors were prepared for measurement. Since the sensor lead consisted of a sandwich of three layers, of which the middle layer contained the sensitive leads, the end of the lead was heated with a flame. This enabled the top copper layer to be peeled back. Then, the individual sensor leads of the middle layer were carefully connected to their original counterparts on the lead that contained the connector (Figure 5.3c).

	A	B	C	D	E	F	G	H	I	J	K	L	M	N	O	P	Q	R
t1		1234	4	1 4	1234	12	1 4	123	123		1234	1234	2	1234	1234	14	1234	1234
t2		234		4	1234	1234	1234	12	12 4	1234	1	1234		1 4	1234	14	1 4	1234
t3		1234		124	1234	1 34	1234	123	234	1	12 4	1234	3	12	2	1	1234	23
t4	4	1234		4	1234	123	2 4	12	3	1	4	1234	2 4	2	1234	14	1234	12
t5	4	123		4	1234	2	1234	123	123	1 4	34	1234		1 4	12 4	1	1234	

Table B.1: *Result of the sensor embedding validation test, for each sensor (A-R) and test (t1-t5). A numbered entry (1-4) indicates a successful measurement of that electrode.*

Finally, the whole assembly was hot-glued to a tin platen to provide strain relief of the sensors and surrounded by aluminium foil to provide some shielding and to protect the fragile solder connection from outside mechanical disturbances (Figure 5.3d). Of the 18 bearings, two sensors had one electrode that could not be connected through soldering, their connection was 'open'.

B.3.2 Method

To find out how many sensors would work under dynamic testing, all sensors were loaded with one BW for two minutes, followed by a quick step loading cycle for synchronisation of load and capacitance (see Appendix , then unloaded for one minute, followed by loading for one minute. Each test was repeated five times. The resulting data was checked for intermittent noise, indicating a faulty lead.

B.3.3 Results

Over all measurements, electrode 1 had most successful measurements (59×), followed by electrode 2 (53×), electrode 4 (51×) and finally electrode 3 (42×). The best six sensors are (in order of good measurements) Sensor L, E, B, Q, O, and G. The results are presented in Table B.1. Unfortunately, even using these sensors, in order to get successful dynamic measurements some experiments had to be repeated a number of times because of intermittent noise, which was most likely due to motion artefacts from the moving leads. For instance, in order to get five faultless sine wave experiments (see Section 5.5.4), some experiments had to be repeated 11 times, even with the leads fixed in place and all experiments taken without removing and replacing the sensor between experiments.

B.3.4 Discussion

The method of re-soldering the leads resulted in variable reliability with room for improvement. A potential point of improvement would be to standardise the lead length within the bearing, instead of cutting it to length during the sensor preparation stage, pre-moulding. If the length were standardised, then solder-friendly connections could be made, which should improve the reliability of the leads. Another potential source of error would be a faulty connection within the bearing, but as long as the leads do not function faultlessly, this cannot be separated from the faults of the leads themselves. This is something that needs to be investigated in the future.

B.4 Lining Out Measurement Data

To properly align data series that have possible time retardation effects, for every measurement that needs to be aligned with another data source, dedicated alignment points are used. These alignment points signal a known time point in time, and have a shape that facilitates reliable and easy alignment. For accurate alignment, abrupt changes in the alignment shape result in the best alignment in the presence of noise, and abrupt changes imply a signal with a great deal of high frequency content. The square wave fulfills these requirements, because it has all odd-integer harmonic frequencies from zero Hertz up to the system bandwidth, and furthermore, it has a clear transition and stable state before and after the transition. Alignment is performed in MATLAB. The square wave that was used is shown in Figure B.2. First, the user has to define roughly where the square wave is located. Then the program automatically finds the start of the alignment wave as follows:

i	sampled time point number
$d[i]$	sampled Data region
$t[i]$	matching time signature to $D[i]$
$t_0, t_1, \cdots$	sample number at t=0 seconds, t=1 seconds, *i.e.*
$\overline{d[t1, t2]}$	average of d between $t1$ and $t2$

First, the function is given a copy of a region surrounding the position of the alignment wave, spanning from $-1.5s$ to $4s$ after the suspected start. For that region, the de-trended minimum and maximum values are calculated; $d_{min} = min(d - \overline{d})$ and $d_{max} = max(d - \overline{d})$. De-trending means removing the average value. Then a collection of square waves is constructed with amplitude d_{min} from 0 to 0.5 seconds, and d_{max} from 0.5 to 1 seconds, starting from t_0 to t_2:

$$\sigma(i) = \begin{cases} d_{min} & \text{for} \quad t + 0s \quad \leq |i| < t + 0.5s, \quad t_0 \leq |t| \leq t_2 \\ d_{max} & \text{for} \quad t + 0.5s \leq |i| \leq t + 1s, \qquad t_0 \leq |t| \leq t_2 \end{cases}$$

To find the start of the alignment wave, the only matter remaining now is to correlate the sampled de-trended square wave

$$\delta(t) = \left\{ \; d(t+0, t+1) - \overline{d(t+0, t+1)} \quad \text{for} \quad t_0 \leq |t| \leq t_2 \right.$$

with the constructed square waves σ by using the dot product;

$t_a = max\{\delta(n) \cdot \sigma(n)\} \quad for \quad 1 < n < N$

where N is the number of constructed square waves. The correlation will be at maximum at the time instance where the subset of data most closely matches a square wave. As can be observed in Figure B.2, this method of finding the alignment wave works really well, with a maximum time error of $Ts = 1/Fs$, where Fs is the sample

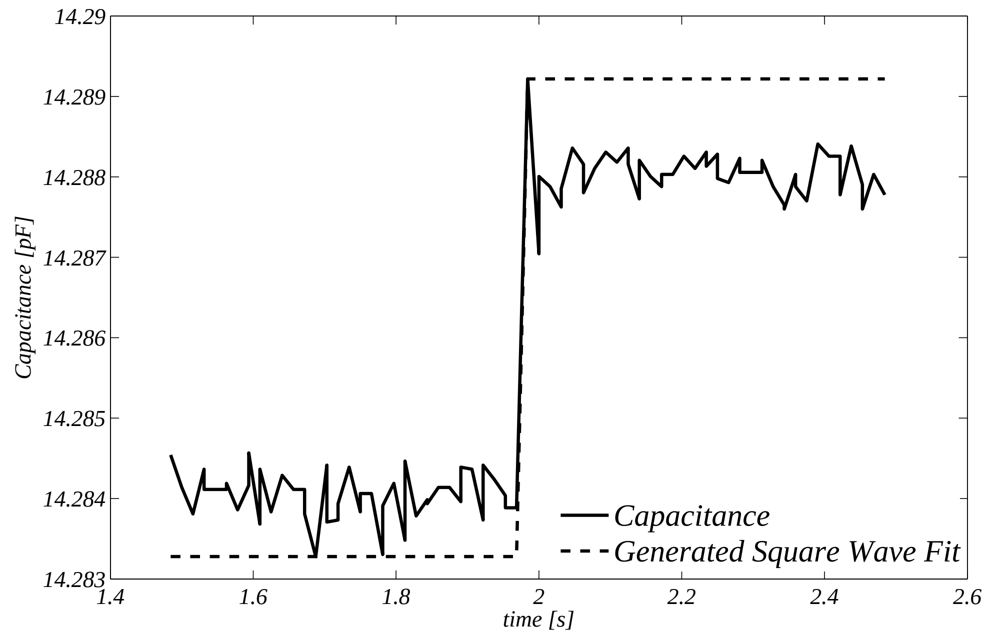

Figure B.2: *Example of an alignment measurement.*

frequency, which lies typically at 90-100 Hz.

B.5 Appendix: Bearing Gait Measurements

The bearing gait measurements are shown in Tables B.2 to B.4.

B.6 Appendix: Bearing Step Up/Down Measurements

The bearing gait measurements are shown in Tables B.5 to B.7.

B.7 Fitting Results

The fitting results for gait and step up/down are shown in Figures B.3 to B.4.

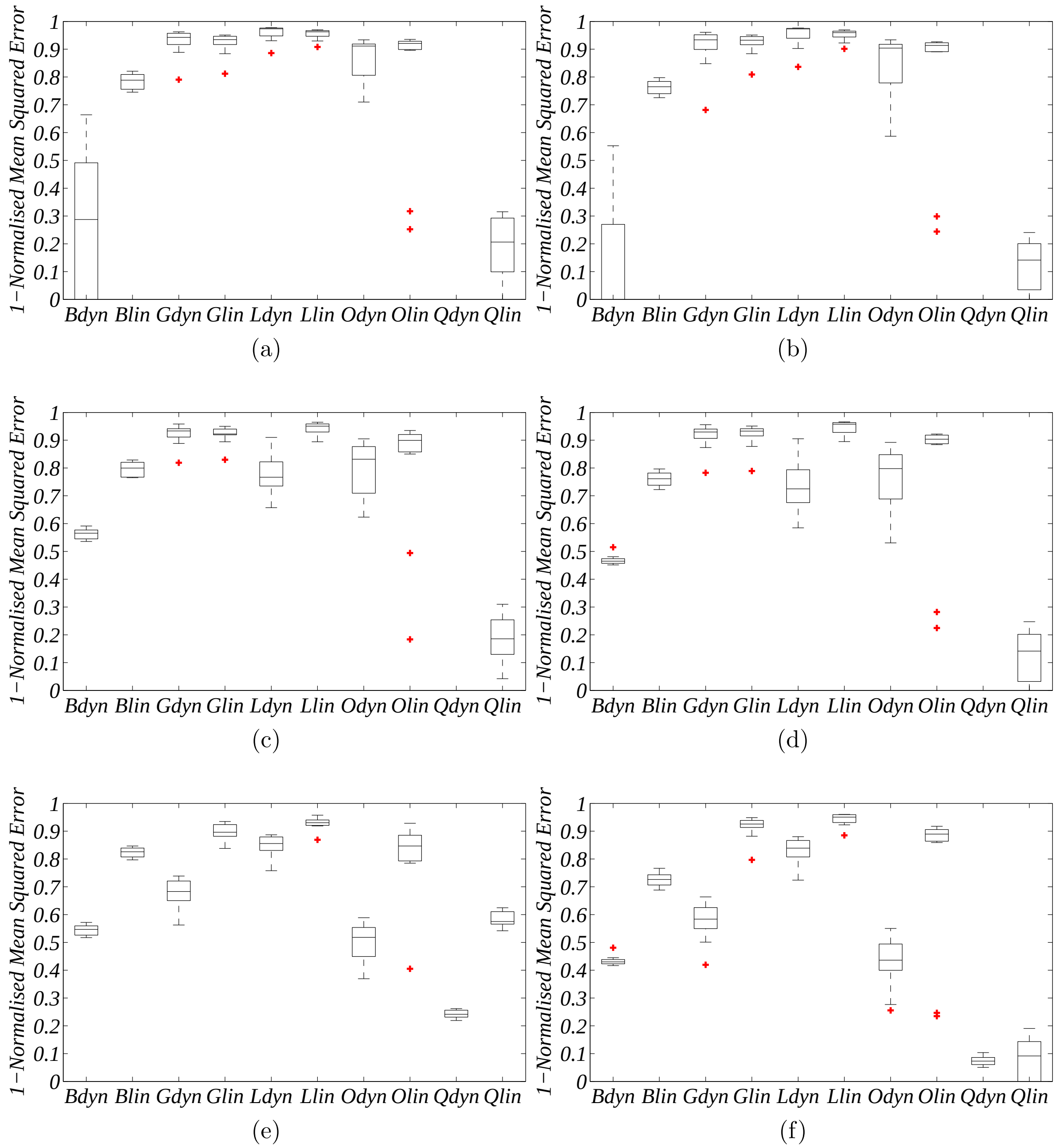

Figure B.3: *Estimation of load from capacitance data using linear (lin) and dynamic (dyn) methods using* ***gait data****. y axis: '1' is best, '0' is worst. Left column: prior to shifting back to correct absolute values, right column: post shifting back. (a,b): the results that were optimised per experiment.*
The lower two rows show results calculated with pooled results:
(c,d): estimated using the medians of the estimators of the gait experiments.
(e,f): estimated using the medians of the estimators of the step experiments.
The Linear estimation consistently delivers better results than the dynamic estimation method.

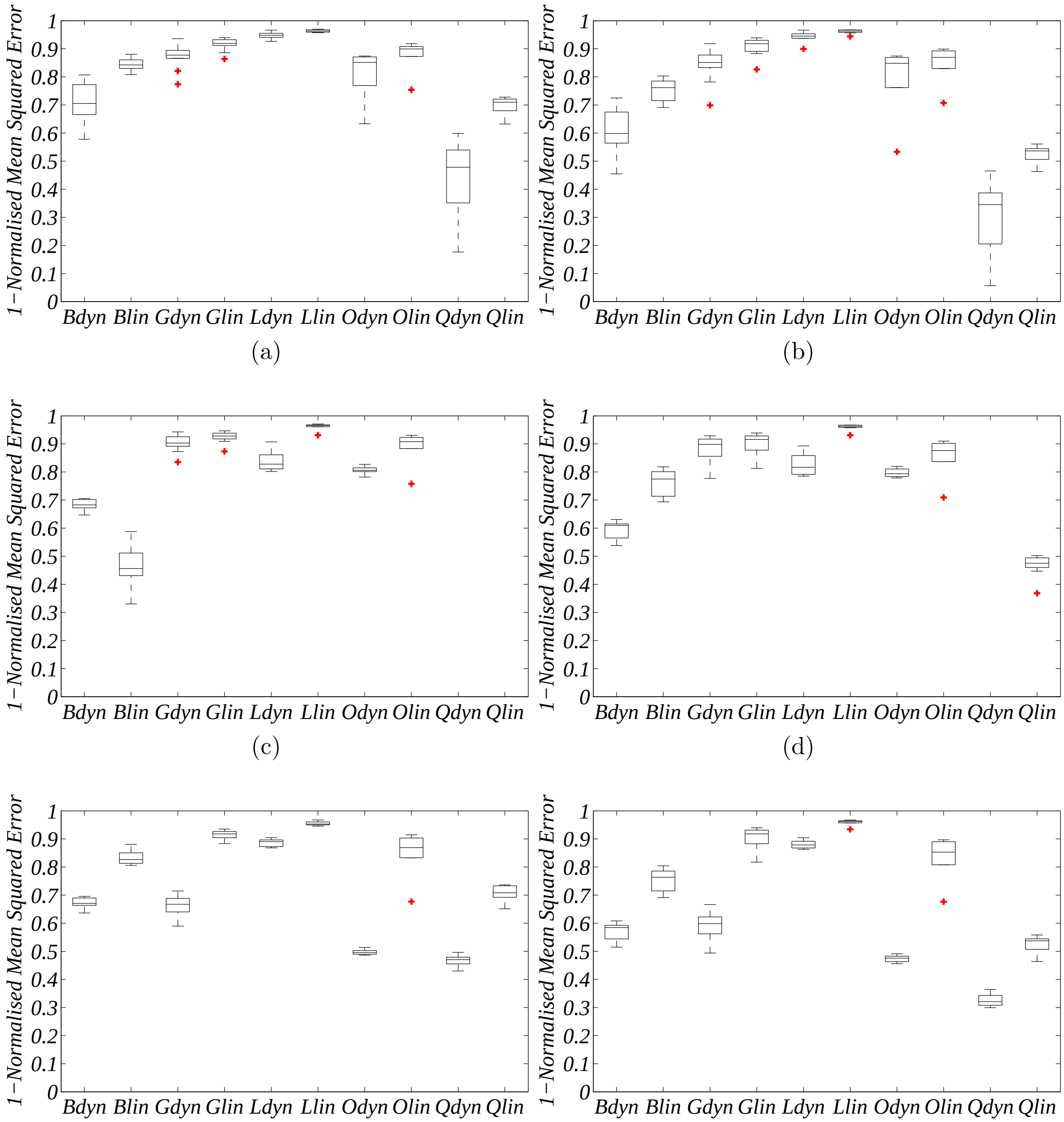

(a) (b)

(c) (d)

(e) (f)

Figure B.4: *Estimation of load from capacitance data using linear (lin) and dynamic (dyn) methods using* ***step data****. y axis: '1' is best, '0' is worst. Left column: prior to shifting back to correct absolute values, right column: post shifting back. (a,b): the results that were optimised per experiment.*
The lower two rows show results calculated with pooled results:
(c,d): estimated using the medians of the pooled estimators of the gait experiments.
(e,f): estimated using the medians of the pooled estimators of the step experiments.
The Linear estimation consistently delivers better results than the dynamic estimation method.

Sensor	Test	Covariance (cap,load)	Slope [fF/KN] ($\mu\pm$ SE)	Intercept [fF] ($\mu\pm$ SE)	Slope % of max
B	1	0.0000	0.000±0.000	0±0.000	0
	2	0.9585	1.976±0.054	15970±0.047	99
	3	0.9609	1.978±0.052	15978±0.046	99
	4	0.9575	1.996±0.054	15984±0.046	100
	5	0.9590	1.922±0.056	15990±0.049	96
	6	0.9569	1.914±0.056	15992±0.048	96
	7	0.9581	1.936±0.063	15996±0.055	97
	8	0.9562	1.969±0.063	15998±0.055	99
	9	0.9577	1.985±0.056	15999±0.048	99
	10	0.9617	1.971±0.065	16001±0.057	99
	11	0.9577	1.945±0.063	15999±0.055	97
G	1	0.9583	3.505±0.124	15492±0.110	68
	2	0.9635	3.917±0.135	15511±0.117	75
	3	0.9690	4.199±0.133	15514±0.115	81
	4	0.9705	4.442±0.138	15519±0.120	86
	5	0.9724	4.570±0.144	15521±0.125	88
	6	0.9736	4.629±0.138	15523±0.122	89
	7	0.9744	4.832±0.136	15526±0.120	93
	8	0.9800	4.999±0.115	15531±0.100	96
	9	0.9753	5.042±0.149	15526±0.129	97
	10	0.9751	5.065±0.145	15535±0.128	98
	11	0.9766	5.189±0.148	15535±0.128	100

Table B.2: *Results for bearing gait tests for sensor B and G*

where:

covariance(cap,load)	Covariance between capacitance and load data
slope	Slope of the first order relationship between capacitance and load
intercept	Intercept of the first order relationship between capacitance and load
Slope % of max	Slope, expressed in percentage of the maximum of the slope of that sensor

Sensor	Test	Covariance (cap,load)	Slope [fF/KN] ($\mu\pm$ SE)	Intercept [fF] ($\mu\pm$ SE)	Slope % of max
L	1	0.9813	7.184±0.215	15577±0.189	66
	2	0.0000	0.000±0.000	0±0.000	0
	3	0.0000	0.000±0.000	0±0.000	0
	4	0.9820	9.804±0.229	15594±0.198	89
	5	0.9801	9.818±0.262	15591±0.228	90
	6	0.9835	10.216±0.219	15595±0.191	93
	7	0.9816	10.512±0.246	15596±0.218	96
	8	0.9829	10.802±0.243	15625±0.214	99
	9	0.9817	10.908±0.255	15624±0.226	100
	10	0.9813	10.958±0.291	15596±0.251	100
	11	0.9825	10.893±0.268	15592±0.232	99
O	1	0.9593	2.327±0.084	15385±0.073	57
	2	0.9754	2.660±0.065	15390±0.056	65
	3	0.9681	3.016±0.092	15394±0.079	74
	4	0.9713	3.230±0.099	15401±0.085	79
	5	0.9747	3.390±0.089	15407±0.077	83
	6	0.9702	3.521±0.114	15411±0.102	86
	7	0.9721	3.640±0.102	15415±0.089	89
	8	0.9711	3.770±0.108	15418±0.094	92
	9	0.9743	3.900±0.107	15422±0.094	96
	10	0.9716	3.892±0.115	15423±0.102	95
	11	0.9742	4.083±0.116	15427±0.100	100

Table B.3: *Results for bearing gait tests for sensor L and O.*

where:

covariance(cap,load)	Covariance between capacitance and load data
slope	Slope of the first order relationship between capacitance and load
intercept	Intercept of the first order relationship between capacitance and load
Slope % of max	Slope, expressed in percentage of the maximum of the slope of that sensor

Sensor	Test	Covariance (cap,load)	Slope [fF/KN] ($\mu\pm$ SE)	Intercept [fF] ($\mu\pm$ SE)	Slope % of max
Q	1	0.9261	1.180±0.046	15269±0.039	100
	2	0.9309	1.128±0.052	15274±0.046	96
	3	0.9189	1.041±0.067	15304±0.058	88
	4	0.9162	1.056±0.053	15308±0.046	89
	5	0.9128	1.097±0.057	15311±0.049	93
	6	0.9314	1.167±0.058	15313±0.050	99
	7	0.9226	1.047±0.058	15316±0.051	89
	8	0.9313	1.120±0.057	15317±0.051	95
	9	0.9204	1.083±0.059	15319±0.051	92
	10	0.9347	1.178±0.058	15321±0.050	100
	11	0.9181	1.038±0.055	15322±0.048	88

Table B.4: *Results for bearing gait tests for sensor Q.*

where:

covariance(cap,load)	Covariance between capacitance and load data
slope	Slope of the first order relationship between capacitance and load
intercept	Intercept of the first order relationship between capacitance and load
Slope % of max	Slope, expressed in percentage of the maximum of the slope of that sensor

Sensor	Test	Cov (cap,load)	Slope [fF/KN] ($\mu\pm$ SE)	Intercept [fF] ($\mu\pm$ SE)	Slope % of max
B	1	0.9593	3.041±0.049	15970±0.033	100
	2	0.0000	0.000±0.000	0±0.000	0
	3	0.0000	0.000±0.000	0±0.000	0
	4	0.9556	2.861±0.052	15983±0.036	94
	5	0.9554	2.765±0.052	15990±0.036	91
	6	0.9569	2.747±0.050	15992±0.034	90
	7	0.9608	2.721±0.049	15996±0.034	89
	8	0.9582	2.826±0.048	15998±0.033	93
	9	0.9598	2.687±0.047	15999±0.033	88
	10	0.9577	2.773±0.047	16000±0.032	91
	11	0.0000	0.000±0.000	0±0.000	0
G	1	0.9744	3.730±0.041	15492±0.028	75
	2	0.9701	3.829±0.051	15510±0.035	77
	3	0.9755	4.115±0.052	15514±0.036	83
	4	0.9725	4.116±0.057	15519±0.038	83
	5	0.9764	4.419±0.056	15521±0.037	89
	6	0.9765	4.538±0.058	15523±0.040	91
	7	0.9760	4.509±0.055	15526±0.037	90
	8	0.9770	4.668±0.059	15531±0.040	94
	9	0.0000	0.000±0.000	0±0.000	0
	10	0.9771	4.792±0.058	15534±0.040	96
	11	0.9788	4.988±0.060	15535±0.041	100

Table B.5: *Results for bearing step up/down tests for sensor B and G.*

where:

cov(cap,load)	Covariance between capacitance and load data
slope	Slope of the first order relationship between capacitance and load
intercept	Intercept of the first order relationship between capacitance and load
Slope % of max	Slope, expressed in percentage of the maximum of the slope of that sensor

Sensor	Test	Cov (cap,load)	Slope [fF/KN] ($\mu\pm$ SE)	Intercept [fF] ($\mu\pm$ SE)	Slope % of max
L	1	0.9895	8.123±0.076	15577±0.052	77
	2	0.0000	0.000±0.000	0±0.000	0
	3	0.0000	0.000±0.000	0±0.000	0
	4	0.9866	9.686±0.093	15594±0.063	92
	5	0.9885	9.556±0.083	15591±0.058	91
	6	0.9862	9.876±0.099	15595±0.067	94
	7	0.9867	10.201±0.099	15596±0.068	97
	8	0.9872	10.211±0.103	15625±0.070	97
	9	0.9856	10.350±0.103	15624±0.071	99
	10	0.9879	10.497±0.092	15596±0.062	100
	11	0.9863	10.402±0.108	15592±0.074	99
O	1	0.0000	0.000±0.000	0±0.000	0
	2	0.0000	0.000±0.000	0±0.000	0
	3	0.0000	0.000±0.000	0±0.000	0
	4	0.0000	0.000±0.000	0±0.000	0
	5	0.0000	0.000±0.000	0±0.000	0
	6	0.9686	3.220±0.046	15411±0.032	90
	7	0.9692	3.261±0.049	15415±0.034	91
	8	0.9663	3.363±0.055	15419±0.038	94
	9	0.9659	3.443±0.056	15422±0.038	96
	10	0.9692	3.508±0.051	15424±0.034	98
	11	0.9686	3.576±0.053	15427±0.037	100

Table B.6: *Results for bearing step up/down tests for sensor L and O.*

where:

cov(cap,load)	Covariance between capacitance and load data
slope	Slope of the first order relationship between capacitance and load
intercept	Intercept of the first order relationship between capacitance and load
Slope % of max	Slope, expressed in percentage of the maximum of the slope of that sensor

Sensor	Test	Cov (cap,load)	Slope [fF/KN] ($\mu\pm$ SE)	Intercept [fF] ($\mu\pm$ SE)	Slope % of max
Q	1	0.9279	2.001±0.047	15269±0.032	100
	2	0.9209	1.878±0.047	15274±0.033	94
	3	0.9273	1.892±0.042	15303±0.029	95
	4	0.9209	1.862±0.045	15308±0.031	93
	5	0.9255	1.903±0.050	15311±0.034	95
	6	0.9283	1.862±0.048	15313±0.033	93
	7	0.9270	1.850±0.041	15315±0.028	92
	8	0.9271	1.919±0.047	15317±0.032	96
	9	0.9283	1.785±0.044	15319±0.031	89
	10	0.9278	1.839±0.045	15320±0.032	92
	11	0.0000	0.000±0.000	0±0.000	0

Table B.7: *Results for bearing step up/down tests for sensor Q.*

where:

cov(cap,load)	Covariance between capacitance and load data
slope	Slope of the first order relationship between capacitance and load
intercept	Intercept of the first order relationship between capacitance and load
Slope % of max	Slope, expressed in percentage of the maximum of the slope of that sensor

C Appendix: Dielectric Constants of Human Tissue

Table C.1 shows the various relative dielectric constant (ϵ_r) and loss factor (δ). Both factors have an influence on field strength in a particular material; when the electric field is present in two materials, the material with an ϵ_r that is twice as large will result in a field strength that also is twice the magnitude. Materials with a high ϵ_r will produce a virtual parasitic capacitance, that influences capacitive measurements that are not properly contained within a certain area. Using a parallel plate capacitance is an example where the field is contained, because most of the field is between the two parallel plates. A capacitance that is constructed using two adjacent plates is an example of an electric field that is not properly contained, and which might be influenced by external factors, such as ϵ_r of the tissue that is in the near vicinity. The loss tangent δ is a measure of decay of the electric field, depending on the frequency [Hz] of the field.

Figure C.1 shows the effect of increasing the effect of in-axis distance and off-axis misalignment of two coils with a diameter of 30 mm on the coupling factor k. What becomes clear is that increasing the in-axis distance of the coils reduces the

Material	ϵ_r	**Loss tangent (tan δ)**
air	1.00	depends on humidity
Blood	6.1	0.27
Cartilage from septum of nose(1)	200	
Cortical skull bone(1)	25-50	
Cancellous skull bone(1)	30-80	
fat	5.5	0.21
Muscle	49	0.33
Skin$^{(1)}$	100-150	
Tendon, depending on hydratation$^{(2)}$	100	
Water, distilled	77	0.157

Table C.1: *Resistive materials and their permittivity and loss tangent. (1): at 10Mhz [186] (2): at 10 MHz [187]*

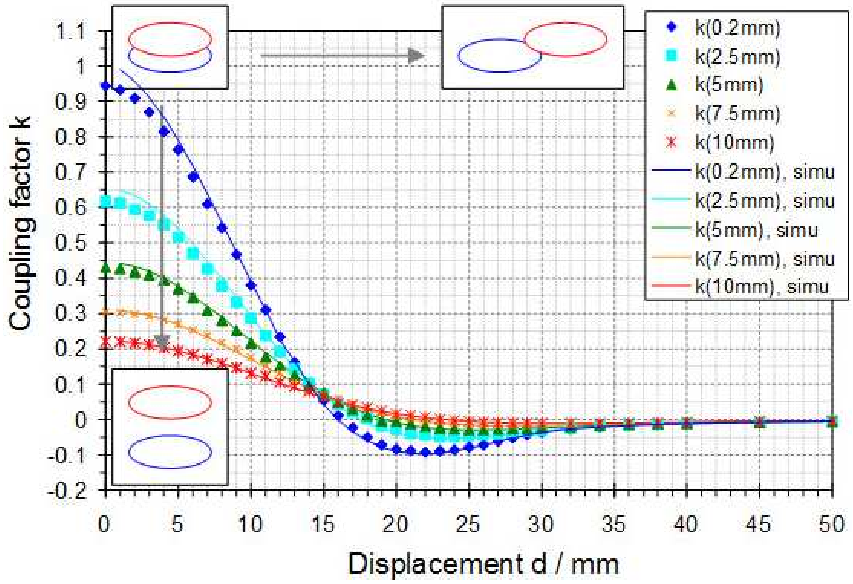

Figure C.1: *Measured (points) and simulated (lines) coupling factors for two planar coils with 30mm diameter [85]*

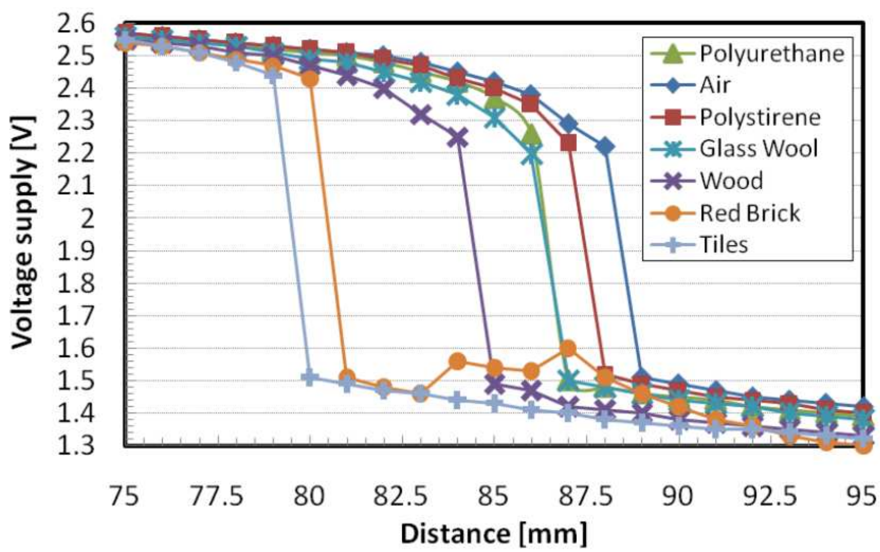

Figure C.2: *Transponder voltage supply for different distances and materials [87]*

coupling factor, and off-axis displacement reduces and even inverses the amplitude of the coupling factor.

Figure C.2 shows the influence of non-conducting materials between two parallel planar coils, separated by said materials. The type of material, as well as the distance between the two coils is of major importance.

D Appendices for Chapter 6

D.1 Appendix: Dielectric Constants of Human Tissue

The Maxwell Equations describe the relationship between electric and magnetic field strength:

$$\nabla \bullet \mathbf{E} = \frac{1}{\epsilon}\rho \tag{D.1}$$

$$\nabla \bullet \mathbf{B} = 0 \tag{D.2}$$

$$\nabla \times \mathbf{E} = -\frac{\partial \mathbf{B}}{\partial t} \tag{D.3}$$

$$\nabla \times \mathbf{B} = \mu\mathbf{J} + \mu\epsilon\frac{\partial \mathbf{E}}{\partial t} \tag{D.4}$$

where:

E electric field, in V/m

ϵ dielectric permittivity of vacuum [in F /m], e.g., 8.85E 12

ρ free charge density in C/m^3

B magnetic field in A/m

μ dielectric permeability in H/m

J free current density in A/m^2

According to Ohm's law, the current density in a lossy medium is:

$$\mathbf{J} = \sigma\mathbf{E} \tag{D.5}$$

where:

σ conductivity in S/m

Since the free charge density is only relevant in transient behaviour, while in this application attenuation is the main focus, ρ is assumed to be 0 [188]. The Maxwell

Equations become:

$$\nabla \bullet \mathbf{E} = 0 \tag{D.6}$$

$$\nabla \bullet \mathbf{B} = 0 \tag{D.7}$$

$$\nabla \times \mathbf{E} = -\frac{\partial \mathbf{B}}{\partial t} \tag{D.8}$$

$$\nabla \times \mathbf{B} = \mu\sigma\mathbf{E} + \mu\epsilon\frac{\partial \mathbf{E}}{\partial t} \tag{D.9}$$

The wave equations can then be found by rewriting the Maxwell Equations:

$$\nabla^2\mathbf{E} = \mu\epsilon\frac{\partial^2 \mathbf{E}}{\partial t^2} + \mu\sigma\frac{\partial \mathbf{E}}{\partial t} \tag{D.10}$$

$$\nabla^2\mathbf{B} = \mu\epsilon\frac{\partial^2 \mathbf{B}}{\partial t^2} + \mu\sigma\frac{\partial \mathbf{B}}{\partial t} \tag{D.11}$$

If a plane wave is considered travelling in the positive z direction, with polarisation in the x direction, then the plane wave solutions are [188]:

$$E_x = Ak^2e^{-jkz} = E_0e^{-jkz} \tag{D.12}$$

$$B_y = A(\omega\epsilon - j\sigma)k^2e^{-jkz} = B_0e^{-jkz} \tag{D.13}$$

$$E_y = E_z = B_x = B_z = 0 \tag{D.14}$$

$$k = \sqrt{\omega^2\mu\epsilon - j\omega\mu\sigma} \tag{D.15}$$

where:

A initial amplitude of the wave

k propagation constant in m^{-1}

z propagation distance in m

ω angular frequency is rad/s

The propagation constant is complex and therefore the electric and magnetic fields propagating through a lossy medium are attenuated. The complex propagation constant can be rewritten to:

$$
\begin{aligned}
k &= \alpha + j\beta && \text{(D.16)}\\
\alpha &\equiv \omega\sqrt{\frac{\epsilon\mu}{2}}\left[\sqrt{1+\left(\frac{\sigma}{\epsilon\omega}\right)^2}+1\right]^{\frac{1}{2}} && \text{(D.17)}\\
\beta &\equiv \omega\sqrt{\frac{\epsilon\mu}{2}}\left[\sqrt{1+\left(\frac{\sigma}{\epsilon\omega}\right)^2}-1\right]^{\frac{1}{2}} && \text{(D.18)}
\end{aligned}
$$

The imaginary part of the propagation constant results in an attenuation of the wave with:

$$e^{-\beta d} \tag{D.19}$$

Where d is the propagation distance of the wave through the lossy medium. The wave impedance is obtained as follows [188]:

$$Z_0 = \frac{E_x}{B_y} = \frac{E_0}{B_0} = \sqrt{\frac{\omega\mu}{\omega\epsilon - j\sigma}} \tag{D.20}$$

The wave impedance is complex in a lossy medium, which means that in addition to an attenuation of the wave a phase difference between the electric and magnetic component occurs.

D.2 Antenna Radiation Patterns

D.3 RSSI Calibration

D.3.1 Introduction

The base station can measure RSSI using a 5-bit ($2^5 = 32$ signal levels) internal ADC ('RSSIint') or 12-bit ($2^{12} = 4096$ signal levels) external ADC ('RSSIext'), whereas

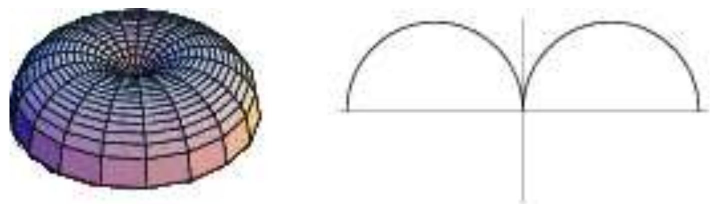

(a)

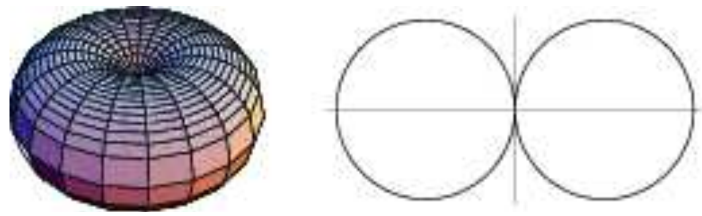

(b)

Figure D.1: *(a) Normal mode radiation pattern of a helix antenna over a ground plane, with the antenna aligned with the vertical axis and (b) normal mode radiation pattern of a square loop antenna, with the antenna aligned with the horizontal axis. The antenna receives and transmits most efficiently at a maximum of the curve [150].*

RSSI_{int}	V_{ant}	$\mathrm{P}_d Bm$
0	5 μV	-108
31	4 mV	-50

Table D.1: *The relationship between internally measured received signal strength ($RSSI_{int}$), measured antenna voltage (V_{ant}), and antenna power (P_{dBm}) [144]*

the implant module can only measure RSSIint. RSSI is dimensionless, whereas the universally accepted method method of reporting signal attenuation is by expressing power in decibels per milliwatt (dBm).

The signal levels for RSSI_{int} are shown in Table D.1. The received power in dBm was calculated by using Equation D.21 and Equation D.22. Per step of RSSI_{int}, the signal power increases by (108-50)/(32-1) = 1.87 dB. P_{dBm} can be calculated directly by using Equation D.23.

$$P_W = \frac{{V_{ant}}^2}{R_{eff}} \tag{D.21}$$

where:

P_W Received power [W]

V_{ant} RMS Voltage measured at the antenna terminal

R_{eff} Effective input impedance of the ZL70102, equal to 1620 Ω.

$$P_{dBm} = 10 \times log_{10}\frac{P_W}{P_{ref}} \tag{D.22}$$

where:

P_{dBm} Received power [dBm]

P_W Received power [W]

P_{ref} Reference power of 1 mW or 0.001 W

$$P_{dBm} = \frac{58}{31} \times RSSI_{int} - 108 - P_{corr} \tag{D.23}$$

where:

P_W Received power [W]

V_{ant} RMS Voltage measured at the antenna terminal

R_{eff} Effective input impedance of the ZL70102, equal to 1620 Ω.

P_{corr} Correction factor to obtain a calibrated RSSI

Because during the measurements, all RSSI$_{int}$ were at the maximum magnitude of 31, and additionally, to increase the resolution of the measured signal, all RSSI signals were measured using RSSI$_{ext}$. To determine the signal level in dBm for RSSI$_{ext}$, the relationship to calculate RSSIint from RSSIext was determined, by measuring both at identical power levels, and fitting a linear relationship to the data. For a correctly calibrated RSSI$_{int}$, the relationship between received signal strength and RSSI can be calculated using Equation D.23. Calibration occurs within the ZL70102 with a special register.

Calibration Protocol

To calibrate RSSI, the voltage at the antenna connector was simultaneously measured with the ZL70321, which is the ZL70102 packaged together with antenna filters, and the Tektronix DPO5204 oscilloscope (Tektronix, Inc., Beaverton, OR, USA) in conjunction with the TAP1500 active 1.5 GHz probe (Tektronix). The default settings were used for the oscilloscope, and the probe was connected to the circuit with a 5 mm wire. The input schematic may be represented by Figure D.2. The ZL70321 has an input impedance of 1620 Ω. The TAP1500 has an input resistance of 1 MΩ parallel to a capacitance of 1 pF, which at 400 MHz equals an impedance of $Z_{osc} = 397.89\Omega$ (using Equation D.24). Placing Z_{osc} and Z_{in} in parallel decreases the effective impedance R_{eff} of Equation D.21 to 256 Ω during calibration. Decreasing R_{eff} changes the antenna voltage, but since the voltage is measured by the oscilloscope and the ZL70321 simultaneously, this is irrelevant. The carrier wave frequency was set to 402.15 MHz. All measurement data were processed in MATLAB. Because the measured antenna voltage is filtered inside the ZL70321 with a 450 kHz low pass filter, the data that was measured with the oscilloscope was filtered with a 10th order band pass filter with corner frequencies 402.15 and 402.6 MHz (450 kHz wide). As a compromise between the oscilloscope minimum sensitivity and the ZL70321 maximum input magnitude, an RSSI signal of 3802 (slightly below the maximum RSSI of the ZL70321) was generated by adjusting the distance between the base station and the implant module.

$$Z_c = \frac{1}{2 \times \pi \times f \times C} \tag{D.24}$$

where:

Z_c Capacitor impedance

f frequency [Hz]

C capacitance

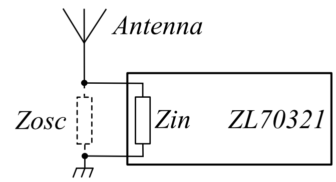

Figure D.2: *Schematic representation of input impedance, which is loading the antenna during calibration measurements. Zin = the input impedance of the ZL70102 and antenna matching filters (1620 Ω), Zosc = the impedance of the oscilloscope probe (398 Ω).*

D.3.2 Results

The relation between measured internal RSSI and antenna voltage was determined first by measuring the external voltage and the external RSSI, then measuring the relation between RSSI measured with the internal low accuracy and external higher accuracy ADC.

The measured voltage has a median value of 52.7 μV and the calculated received power expressed in dBm for an input impedance of 256 Ω is -81.2 dBm, with 25^{th} and 75^{th} percentiles at -86.1 and -77.9 dBm respectively (Figure D.3).

The relationship between internal and external RSSI is shown in Equation D.25, and can also be seen in Figure D.4.

$$RSSI_{int} = 0.0123 \times RSSI_{ext} - 10.56 \tag{D.25}$$

where:

$RSSI_{int}$ RSSI measured using the internal DAC

$RSSI_{ext}$ RSSI measured using the external ADC

According to the calibration measurement, an RSSIext of 3802 equals -79.7 dBm. An external RSSI value of 3802 equals an internal RSSI of 36.02, using Equation D.25, which equals a received power of -40.27 dBm, using Equation D.23. Therefore, in order to calibrate the ZL70321 properly, the measured received power calculated from RSSI needs an adjustment of -81.2+40.27 = -40.93 dB.

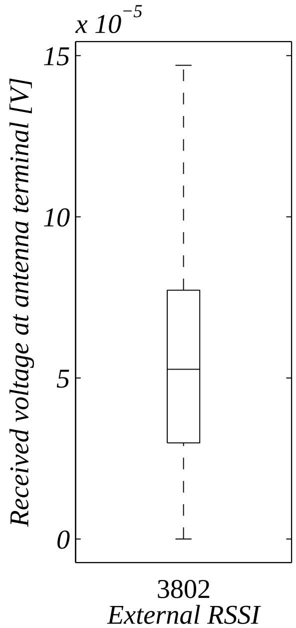

(a)

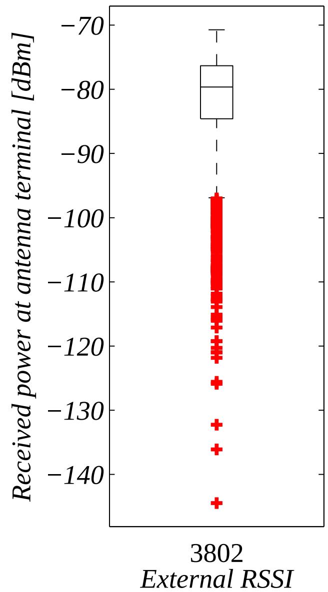

(b)

Figure D.3: *The measured voltage (a) and calculated signal power (b) at the antenna terminal for an input impedance of 366 Ω during calibration. The median of the antenna voltage is 52.7 μV, and the 25^{th} and 75^{th} percentiles are 29.9 μV and 77.2 μV. The median of the antenna power is -79.7 dBm, and the 25^{th} and 75^{th} percentiles are -84.6 and -76.3 dBm respectively. An external RSSI of 3802 equals an internal RSSI of 36.2, using equation D.25.*

D.3.3 RSSI Calibration

Given that communication with 4FSK did work but resulted in too many unrecoverable errors, and that 4FSK works with a minimal signal level of -84 dBm (see Section 6.3.6), and the measured signal powers ranged from -88 to -80 dBm (Figure 6.8), the calibration is likely to be within $\pm$4dB of the true value.

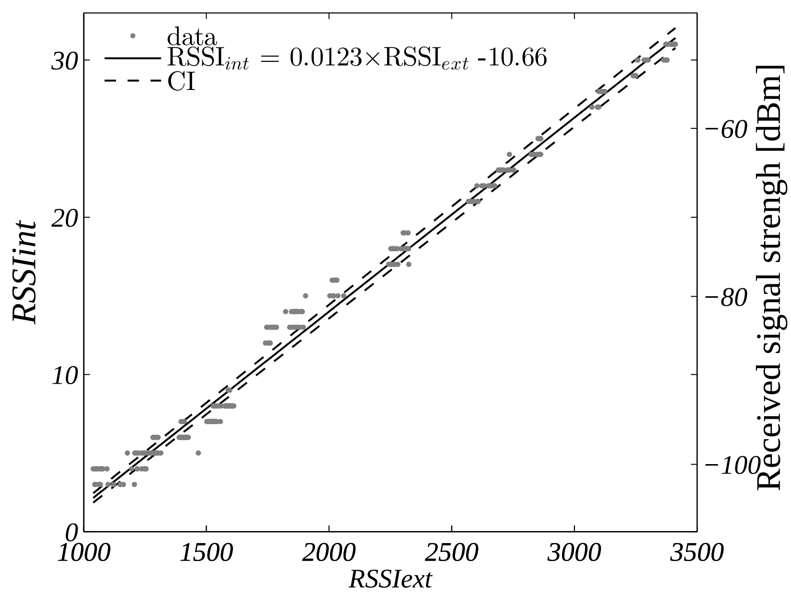

Figure D.4: *The relationship between the received antenna signal strength (RSSI) measured using the internal (RSSI$_{int}$) and external (RSSI$_{ext}$) ADC of the ZL70102 base station, and the linear relation between the two, with the confidence interval (CI). On the right axis the corresponding signal strength is shown in dBm.*

D.4 Appendix: Wireless Measurement Data

	Distance between antennas [m]						
	0.02	**0.05**	**0.1**	**0.15**	**0.2**	**1**	**2**
air:	27.3±20.4	27.3±11.6	30.2±19.6	29.3±15.7	24.0±16.1	51.7±22.5	-
skin:	49.3±10.2	44.5±21.7	36.7±13.4	34.7±15.4	33.9±9.3	70.7±28.1	74.8±21.6
fat:	30.7±11.8	30.6±14.2	38.1±12.4	64.5±25.9	550±807	62.7±36.7	397±258
NaCl:	22.0±8.4	24.3±15.4	27.4±13.2	24.8±16.0	26.9±9.6	27.6±11.4	376±134
Metal:	24.7±11.4	25.2±16.3	26.6±13.1	24.3±10.2	37.9±14.7	-	-

(a)

	Distance between antennas [m]						
	0.02	**0.05**	**0.1**	**0.15**	**0.2**	**1**	**2**
air:	0.1±0.6	0.1±0.6	0.0±0.0	0.0±0.0	0.1±0.6	0.0±0.0	0.2±0.8
skin:	0.0±0.0	0.0±0.0	0.1±0.6	0.0±0.0	0.0±0.0	0.1±0.6	0.1±0.6
fat:	0.2±0.8	0.0±0.0	0.0±0.0	0.0±0.0	0.1±0.6	0.4±1.9	0.0±0.0
NaCl:	0.0±0.0	0.0±0.0	0.0±0.0	0.0±0.0	0.0±0.0	0.0±0.0	0.3±1.1
Metal:	0.0±0.0	0.0±0.0	0.1±0.6	0.0±0.0	0.0±0.0	-	-

(b)

Table D.2: *Number of recovered packets (mean± CI) from the base station to the implant module with the (a)* ***2FSK*** *and (b)* ***2FSK HS*** *modulation scheme per 10,000 packets sent; using the* ***square loop antenna*** *for several antenna separation distances and surrounding tissues. " - " measurements that were not performed.*

	Distance between antennas [m]						
	0.02	**0.05**	**0.1**	**0.15**	**0.2**	**1**	**2**
air:	0.9±0.6	1.0±0.0	1.0±0.0	0.9±0.6	1.1±0.6	1.2±1.2	-
skin:	0.9±0.6	1.0±0.0	1.0±0.0	1.0±0.0	1.0±0.0	0.9±0.6	1.0±0.0
fat:	1.1±0.6	1.0±0.0	1.1±0.6	1.0±0.0	1.1±0.6	0.8±1.2	1.0±0.0
NaCl:	1.1±1.1	1.0±0.0	1.1±0.6	1.1±0.6	1.0±0.0	1.0±0.9	1.0±0.9
metal:	1.0±0.0	1.0±0.0	1.0±0.0	1.0±0.0	1.0±0.0	-	-

(a)

	Distance between antennas [m]						
	0.02	**0.05**	**0.1**	**0.15**	**0.2**	**1**	**2**
air:	0.0±0.0	0.1±0.6	0.3±0.9	0.3±0.9	0.3±0.9	0.5±1.0	0.4±1.0
skin:	0.4±1.0	0.5±1.0	0.4±1.0	0.1±0.6	0.3±0.9	0.3±0.9	0.8±0.8
fat:	0.1±0.6	0.3±0.9	0.4±1.0	0.2±0.8	0.2±0.8	0.5±1.9	0.2±0.8
NaCl:	0.7±1.1	0.3±1.1	0.3±1.1	0.0±0.0	0.0±0.0	0.0±0.0	0.3±1.1
Metal:	0.1±0.6	0.2±0.8	0.1±0.6	0.3±0.9	0.1±0.6	-	-

(b)

Table D.3: *Number of unrecoverable packets (mean±CI), sent from the implant module to the base station with (a) the **2FSK** modulation scheme and (b) the **2FSK HS** modulation scheme per 10,000 packets sent, using the **square loop antenna** for several antenna separation distances and surrounding tissues. " - " indicates measurements that were not performed.*

	ECC	**CRC**
air:	0.0±0.0	0.1±0.6
skin:	0.0±0.0	0.0±0.0
fat:	0.0±0.0	0.5±1.4

Table D.4: *Number of recoverable packets (ECC) and unrecoverable packets (CRC) (mean±CI), sent from the base station to the implant module with the 2FSK HS modulation scheme per 10,000 packets sent, using the **custom foil antenna** for an antenna separation distances of 1 m and surrounding tissues.*

	Distance between antennas [m]						
	0.02	**0.05**	**0.1**	**0.15**	**0.2**	**1**	**2**
air:	0.3±0.9	0.2±0.8	0.0±0.0	0.0±0.0	0.0±0.0	0.3±0.9	-
skin:	0.1±0.6	0.2±0.8	0.0±0.0	0.0±0.0	0.4±1.0	35.0±47.6	0.1±0.6
fat:	0.3±0.9	0.2±0.8	0.1±0.6	0.2±0.8	122±291	12.3±48.3	1.6±4.0
NaCl:	0.3±0.9	0.3±0.9	0.2±0.8	0.4±1.0	0.1±0.6	0.1±0.6	0.1±0.6
Metal:	0.2±0.8	0.3±0.9	0.2±0.8	0.0±0.0	0.2±0.8	-	-

(a)

	Distance between antennas [m]						
	0.02	**0.05**	**0.1**	**0.15**	**0.2**	**1**	**2**
air:	0.0±0.0	0.0±0.0	0.0±0.0	0.1±0.6	0.0±0.0	0.0±0.0	0.4±2.5
skin:	0.0±0.0	0.0±0.0	0.0±0.0	0.1±0.6	0.0±0.0	0.2±0.8	0.1±0.6
fat:	0.0±0.0	0.1±0.6	0.0±0.0	0.0±0.0	0.0±0.0	0.6±2.6	0.0±0.0
NaCl:	0.0±0.0	0.0±0.0	0.0±0.0	0.0±0.0	0.0±0.0	0.0±0.0	0.0±0.0
Metal:	0.0±0.0	0.0±0.0	0.1±0.6	0.2±0.8	0.0±0.0	-	-

(b)

Table D.5: *Number of recovered packets (mean± CI) from the base station to the implant module with the (a)* ***2FSK*** *and (b)* ***2FSK HS*** *modulation scheme per 10000 packets sent. " - " means missing measurements*

	Distance between antennas [m]						
	0.02	**0.05**	**0.1**	**0.15**	**0.2**	**1**	**2**
air:	0.0±0.0	0.0±0.0	0.0±0.0	0.0±0.0	0.0±0.0	0.1±0.6	-
skin:	0.0±0.0	0.0±0.0	0.1±0.6	0.0±0.0	0.0±0.0	0.0±0.0	0.0±0.0
fat:	0.0±0.0	0.0±0.0	0.0±0.0	0.0±0.0	0.3±1.3	0.0±0.0	0.0±0.0
NaCl:	0.2±1.2	0.1±0.6	0.0±0.0	0.0±0.0	0.0±0.0	0.1±0.6	0.0±0.0
Metal:	0.0±0.0	0.0±0.0	0.0±0.0	0.0±0.0	0.0±0.0	-	-

(a)

	Distance between antennas [m]						
	0.02	**0.05**	**0.1**	**0.15**	**0.2**	**1**	**2**
air:	0.0±0.0	0.0±0.0	0.0±0.0	0.0±0.0	0.0±0.0	0.0±0.0	0.0±0.0
skin:	0.0±0.0	0.0±0.0	0.0±0.0	0.0±0.0	0.1±0.6	0.0±0.0	0.0±0.0
fat:	0.0±0.0	0.0±0.0	0.0±0.0	0.1±0.6	0.0±0.0	0.3±1.9	0.0±0.0
NaCl:	0.0±0.0	0.0±0.0	0.0±0.0	0.0±0.0	0.0±0.0	0.0±0.0	0.0±0.0
Metal:	0.0±0.0	0.0±0.0	0.0±0.0	0.0±0.0	0.0±0.0	-	-

(b)

Table D.6: *Number unrecoverable packets (mean± CI) from the implant module to the base station with the (a)* ***2FSK HS*** *and (b)* ***2FSK*** *modulation scheme per 10000 packets sent. " - " means omitted measurements*

E Appendices for Chapter 7

E.1 DC-DC Converter Measurement

E.1.1 Introduction

DC-DC converters are used to convert a direct current on the input side to a different direct current on the output side. They use a switching method to create a stable output voltage. In the case of a boost converter, this voltage may be higher than the voltage at the input, a buck converter reduces the voltage, and a buck/boost converter can do both. In this experiment, a buck/boost converter was tested, to create a stable output voltage to power the implant.

E.1.2 Method

To determine the typical efficiency of a suitable buck/boost converter, the TPS61200 [189] (Texas Instruments Inc, Dallas, Texas USA), an experiment was performed. The output voltage was set to 2.85 Vdc, and a current sink was used to create a secondary load of 0.025 mW. On the input of the converter, an increasing voltage was applied, and both voltage and input current was measured using a PM2521 digital benchtop multimeter (Philips Electronics UK Ltd, Guildford, UK). Efficiency was determined by dividing output power by input power.

E.1.3 Results

The voltage measurements are shown in Table E.1. The highest efficiency of this converter is 50%, and it drops to 25% if the input voltage is lower than the output voltage.

E.1.4 Discussion

A DC-DC converter is not very efficient for low current conversions.

$\mathbf{V}_{in}$ [$\mathbf{V}_{rms}$]	$\mathbf{I}_{in}$ [mA]	$\mathbf{V}_{out}$ [$\mathbf{V}_{rms}$]	$\mathbf{I}_{out}$ [mA]	$\mathbf{P}_{in}$ [mW]	$\mathbf{P}_{out}$ [mW]	η [%]
0.777	129	2.85	8.6	100	25	24
0.91	106	2.85	8.9	96	25	26
1.04	90	2.85	8.5	94	25	26
1.11	86	2.85	8.7	95	25	26
1.51	62	2.85	8.9	94	25	27
2.05	36	2.85	8.7	74	25	34
2.53	24	2.85	8.7	61	25	41
3.04	16	2.85	8.7	49	25	51
3.51	14	2.85	8.7	49	25	50
4.01	13	2.85	8.8	52	25	48

Table E.1: *Voltages (V), currents (I), power (P) and efficiency (η) for the TPS61200, for several input voltages with one fixed output voltage . Efficiency ranges from 24-51 %. The TPS61200 is powered from the input voltage.*

E.2 Cost Calculation

	Cost per 1000 [£]	N pins
AD7746 C2D	3.09	16
1x 100 nF capacitor	0.005	2
3x 2.2 uF capacitor	0.042	6
TMP05/06 temperature sensor	0.59	5
1x 100 nF capacitor	0.005	2
KMX61G[a] accelerometer	5?	24
1x 100 nF capacitor	0.005	2
2x 2.2 uF capacitor	0.028	4
ZL70321[a] transceiver	30	43
2x 100 nF capacitor	0.005	4
2x RF capacitor	0.117	4
2x RF inductor	0.018	4
2x resistor	0.004	4
MSP430FR5738 processor	1.54	24
1x 1 uF capacitor	0.043	2
1x 100 nF capacitor	0.005	2
TLV717285P regulator	0.09	5
2x 1 uF capacitor	0.086	4
BZT52C5V6T-7[b] zener diode	0.048	2
BC847BT[b] transistor	0.014	3
1x resistor[b]	0.002	2
1x 100 nF capacitor[b]	0.005	2
1x 2.2 uF capacitor[b]	0.014	2
diode[c]	0.022	2
BC847AT[c]	0.094	3
diode[d]	0.022	2
1x capacitor[d]	0.005	2
subtotal	40.624	177
assembly	10[e]	
pcb	2[e]	
coil[f]	0.013	
total	52.63	

Table E.2: *Cost and amount of pins of the electronic components. The prices are obtained from a large UK supplier.* [a] *estimated.* [b] *components for the linear regulator (Figure 7.3f) .* [c] *components for the inductive communications (Figure 7.3c) .* [d] *components for the rectifier (Figure 7.3d) .* [e] *estimated for a UK manufacturer.* [f] *for a 10 meter length of 50 μm diameter copper wire.*

References

[1] P S Walker, Y Heller, D J Cleary, and G Yildirim. Preclinical evaluation method for total knees designed to restore normal knee mechanics. *Journal of Arthroplasty*, 26:152–160, April 2011.

[2] T Wehner, L Claes, and U Simon. Internal loads in the human tibia during gait. *Clin Biomech (Bristol, Avon)*, 24(3):299–302, March 2009.

[3] A J Meyer, D D D'Lima, T F Besier, D G LLoyd, C W Colwell, and B. J. Fregly. Are external knee load and emg measures accurate indicators of internal knee contact forces during gait? *Journal of Orthopaedic Research*, 31:921–9, 2013.

[4] T W Lu, J J O'Connor, S J Taylor, and P S Walker. Validation of a lower limb model with in vivo femoral forces telemetered from two subjects. *Journal of Biomechanics*, 31(1):63–9, January 1998.

[5] D D D'Lima, N Steklov, B J Fregly, S A Banks, and C W Colwell. In vivo contact stresses during activities of daily living after knee arthroplasty. *Journal of Orthopaedic Research*, 26(12):1549–55, December 2008.

[6] B Kirking, J Krevolin, C Townsend, C W Colwell, and D D D'Lima. A multiaxial force-sensing implantable tibial prosthesis. *Journal of Biomechanics*, 39(9):1744–51, 2006.

[7] D D D'Lima, S Patil, N Steklov, S Chien, and C W Colwell. In vivo knee moments and shear after total knee arthroplasty. *Journa of Biomechanics*, 40 Suppl 1:S11–7, 2007.

[8] K M Varadarajan, A L Moynihan, D D'Lima, C W Colwell, and G Li. In vivo contact kinematics and contact forces of the knee after total knee arthroplasty

during dynamic weight-bearing activities. *Journa of Biomechanics*, 41(10):2159–68, July 2008.

[9] B Heinlein, F Graichen, A Bender, A Rohlmann, and G Bergmann. Design, calibration and pre-clinical testing of an instrumented tibial tray. *Journal of Biomechanics*, 40 Suppl 1:S4–10, 2007.

[10] B Heinlein, I Kutzner, F Graichen, A Bender, A Rohlmann, A M Halder, A Beier, and G Bergmann. ESB Clinical Biomechanics Award 2008: Complete data of total knee replacement loading for level walking and stair climbing measured in vivo with a follow-up of 6-10 months. *Clinical Biomechanics*, 24(4):315–26, May 2009.

[11] D D D'Lima, S Patil, N Steklov, and C W Colwell. The 2011 ABJS Nicolas Andry Award: 'Lab'-in-a-knee: in vivo knee forces, kinematics, and contact analysis. *Clinical Orthopaedics and Related Research*, 469(10):2953–70, October 2011.

[12] D W Murray, J W Goodfellow, and J J O'Connor. The oxford medial unicompartmental arthroplasty - a ten year survival study. *The Journal of Bone & Joint Surgery*, 80-B:983–989, 1998.

[13] G W Keys, Z Ul-abiddin, and E M Toh. Analysis of first forty oxford medial unicompartmental knee replacement from a small district hospital in uk. *Knee*, 11:375–377, 2004.

[14] U C G Svard and A J Price. Oxford medial unicompartmental knee arthroplasty - a survival analysis of an independent series. *Journal of Bone & Joint Surgery (Br)*, 83-B:191–4, 2001.

[15] R Verdonk, D Cottenie, K F Almqvist, and P Vorlat. The oxford unicompartmental knee prosthesis: a 2-14 year follow-up. *Knee Surg Sports Traumatol Arthosc*, 13:163–166, 2005.

[16] J Newman, R V Pydisetty, and C Ackroyd. Unicompartmental or total knee replacement - the 15-year results of a prospective randomised controlled trial. *Journal of Bone & Joint Surgery (Br)*, 91-B:52–7, 2009.

[17] J et al Holmes. Schematic view of the knee, April 2011. `https://upload.wikimedia.org/wikipedia/commons/thumb/0/09/Knee_diagram.svg/658px-Knee_diagram.svg.png`.

[18] H Gray, 1918. URL `http://www.bartleby.com/107/illus349.html`.

[19] R K Miller, J W Goodfellow, D W Murray, and J J O'Connor. In vitro measurement of patellofemoral force after three types of knee replacement. *Journal of Bone & Joint Surgery (Br)*, 80:900–906, 1998.

[20] K Rajendran. Mechanism of locking at the knee joint. *Journal of Anatomy*, 143: 189–194, 1985.

[21] R Shenoy, P S Pastides, and D Nathwani. Biomechanics of the knee and tkr. *Orthopaedics and trauma*, 27:6:364–371, 2013.

[22] P G Bullough and A Jagannath. The morphology of the calcification front in articular cartilage. Its significance in joint function. *Journal of Bone and Joint Surgery*, 65(1):72–8, January 1983.

[23] P Sarzi-Puttini, M A Cimmino, R Scarpa, R Caporali, F Parazzini, A Zaninelli, F Atzeni, and B Canesi. Osteoarthritis: an overview of the disease and its treatment strategies. *Seminars in Arthritis and Rheumatism*, 35((1) Suppl 1): 1–10, August 2005.

[24] S Patil, C W Colwell, K A Ezzet, and D D D'Lima. Can normal knee kinematics be restored with unicompartmental knee replacement? *Journal of Bone and Joint Surgery*, 87(2):332–8, February 2005.

[25] A J Price, J L Rees, D J Beard, H S Gill, C A Dodd, and D M Murray. Sagittal plane kinematics of a mobile-bearing unicompartmental knee arthroplasty at 10 years: a comparative in vivo fluoroscopic analysis. *Journal of Arthroplasty*, 19 (5):590–7, August 2004.

[26] D D D'Lima, Steklov N Patil, S, J E Slamin, and C W Colwell. Tibial forces measured in vivo after total knee arthroplasty. *Journal of Arthroplasty*, 21(2): 255–62, February 2006.

[27] A J Price. *Medial meniscal bearing unicompartmental arthroplasty - wear, mechanics and clinical outcome*. DPhil thesis, Oxford University, 2003.

[28] H Pandit, B H Van Duren, J A Gallagher, D J Beard, C A F Dodd, H S Gill, and D W Murray. Combined anterior cruciate reconstruction and Oxford unicompartmental knee arthroplasty: in vivo kinematics. *Knee*, 15(2):101–6, March 2008.

[29] D Hollinghurst, J Stoney, T Ward, H S Gill, J H Newman, D W Murray, and D J Beard. No deterioration of kinematics and cruciate function 10 years after medial unicompartmental arthroplasty. *Knee*, 13(6):440–4, December 2006.

[30] A J Price, P T Oppold, D W Murray, and A B Zavatsky. Simultaneous in vitro measurement of patellofemoral kinematics and forces following oxford medial unicompartmental knee replacement. *Journal of Bone and Joint Surgery*, 88 (12):1591–5, December 2006.

[31] J Y Jenny, Y Lefebvre, M Vernizeau, F Lavaste, and W Skalli. In vitro analysis of the continuous active patellofemoral kinematics of the normal and prosthetic knee. *Revue de Chirurgie Orthopedique et traumatologique*, 88(8):797–802, December 2002.

[32] B J Robinson, J L Rees, A J Price, D J Beard, and D M Murray. A kinematic study of lateral unicompartmental arthroplasty. *The Knee*, 9(3):237–240, 2002.

[33] L E O A Whiteside and D S McCarthy. Laboratory evaluation of alignment and kinematics in a unicompartmental knee arthroplasty inserted with intramedullary instrumentation. *Clinical orthopaedics and related research*, 274:238–47, 1992.

[34] A J Price, A Short, C Kellett, D Beard, H S Gill, H Pandit, C A F Dodd, and D W Murray. Ten-year in vivo wear measurement of a fully congruent mobile bearing unicompartmental knee arthroplasty. *Journal of Bone & Joint Surgery*, 87-B, 11:1493–97, 2005.

[35] C F Kellett, A Short, A J Price, H S Gill, and D W Murray. In vivo measurment of total knee replacement wear. *Knee*, 11:183–187, 2004.

[36] H S Gill, J C Waite, Short A, C F Kellett, A J Price, and D W Murray. In vivo measurement of volumetric wear of a total knee replacement. *Knee*, 13:312–317, 2006.

[37] H Pandit, C Jenkins, K Barker, C A F Dodd, and D W Murray. The oxford medial unicompartmental knee replacement using a minimally-invasive approach. *Journal of Bone & Joint Surgery*, 88-B:54–60, 2006.

[38] M C Edmondson, D Isaac, M Wijeratna, S Brink, P Gibb, and P Skinner. Oxford unicompartmental knee arthroplasty, medial pain and functional outcome in the medium term. *Journal of Orthopadic Research*, 6:52:1–7, 2011.

[39] NJR 9th annual report 2011, 2011. URL `http://www.njrcentre.org.uk/njrcentre/Reports,PublicationsandMinutes/Annualreports/Archivedannnualreports/tabid/87/Default.aspx`. Accessed on Jan 9 2014.

[40] NHS health survey for England - 2011 trend tables, 2011. URL `http://www.hscic.gov.uk/catalogue/PUB09302`. Accessed on Jan 9 2014.

[41] T J Harris, C G Owen, C R Victor, R Adams, and D G Cook. What factors are associated with physical activity in older people, assessed objectively by accelerometry? *British Journal of Sports Medicine*, 43(6):442–50, June 2009.

[42] www.orthoload.com, accessed 27th june 2012, file name: ”k1 110108 1 80p gait.akf”.

[43] I Kutzner, B Heinlin, F Griachen, A Bender, A Rohlmann, A Halder, A Beier, and G Bergmann. Loading of the knee joint during activities of daily living measured in vivo in five subjects. *Journal of Biomechanics*, 43, issue 11:2164–2173, 2010.

[44] F Johnson, S Leitl, and W. Waugh. Distribution of load across the knee. *Journal of Bone and Joint Surgery*, 62-B(3):346–349, August 1980.

[45] G Bergmann, F Graichen, and A Rohlmann. Hip joint loading during walking and running, measured in two patients. *Journal of Biomechanics*, 26(8):969–90, August 1993.

[46] D D D'Lima, Patil S, Steklov N, Slamin J E, and Colwell C W Jr. Chitranjan ranawat award in vivo knee forces after total knee arthroplasty. In *Presentation*, 2005.

[47] D Crescini, E Sardini, and M Serpelloni. An Autonomous Sensor for Force Measurements in Human Knee Implants. *Procedia Chemistry*, 1(1):718–721, September 2009.

[48] D Crescini, E Sardini, and M Serpelloni. Design and test of an autonomous sensor for force measurements in human knee implants. *Sensors and Actuators A*, 166, issue 1:1–8, 2011.

[49] E Pegg, H Pandit, H S Gill, G W Keys, U G C Svard, J J O'Connor, and D W Murray. Examination of ten fractured oxford unicompartmental knee bearings. *Journal of Bone & Joint Surgery*, 93:1610–16, 2011.

[50] E C Pegg, D W Murray, H G Pandit, J J O'Connor, and H S Gill. Fracture of mobile unicompartmental knee bearings: A parametric finite element study. *Journal of Engineering in Medicine*, 227(11):1213–23, 2013.

[51] D Beebe, D D Denton, R G Radwin, and J G Webster. A silicon-based tactile sensor for finger-mounted applications. *IEEE transactions on biomedical engineering*, 45(2):151–59, 1998.

[52] S Almouahed, M Gouriou, Ch Hamitouche, E Stindel, and C Roux. Design and evaluation of instrumented smart knee implant. *IEEE Transactions on biomechanical engineering*, 58:971–82, 2011.

[53] C Lahuec, S Almouahed, M Arzel, D Gupta, C Hamitouche, M Jezequel, E Stindel, and C Roux. A self-powered telemetry system to estimate the postoperative instability of a knee implant. *IEEE transactions on biomedical engineering*, 58: 822–5, 2011.

[54] E Romero and A Rincon. Piezoelectric load measurement model in knee implants. In *34th Annual International Conference of the IEEE EMBS*, San Diego, CA, USA, August 2012.

[55] S Karki, J Lekkala, H Kuokkanen, and J Halttunen. Development of a piezoelectric polymer film sensor for plantar normal and shear stress measurements. *Sensors and Actuators A: Physical*, 154:57–64, 2009.

[56] Maeder Crottet, D, D T, Fritschy, H Bleuler, L P Nolte, and I P Pappas. Development of a force amplitude- and location-sensing device designed to improve

the ligament balancing procedure in tka. *IEEE Transactions on Biomedical Engineering*, 52:1609–11, 2005.

[57] S Matsuda, S E White, V G II Williams, D S McCarthy, and L A Whiteside. Contact stress analysis in meniscal bearing total knee arthroplasty. *Journal of Arthroplasty*, 13:699–706, 1998.

[58] G I Hay, D J Southee, P S A Evans, D J Harrison, G Simpson, and B J Ramsey. Examination of silvergraphite lithographically printed resistive strain sensors. *Sensors and Actuators A*, 135:534–46, 2007.

[59] D C Wilson, C A Niosi, Q A Zhu, T R Oxland, and D R Wilson. Accuracy and repeatability of a new method for measuring facet loads in the lumbar spine. *Journal of Biomechanics*, 39:348–53, 2006.

[60] J M Brimacombe, D R Wilson, A J Hodgson, K C T Ho, and C Anglin. Effect of calibration method on tekscan sensor accuracy. *Journal of Biomechanical Engineering*, 131:1–4, 2009.

[61] J K Otto, T D Brown, and J J Callaghan. Static and dynamic response of a multiplexed-array piezoresistive contact sensor. *Experimental mechanics*, 39, No 4:317–323, 1999.

[62] L Martinelli, C Hurschler, and D Rosenbaum. Comparison of capacitive versus resistive joing contact stress sensors. *Clinical orthopaedics and related research*, 447:214–20, 2006.

[63] R A Jr Pax, J G Webster, and E Radin. A conductive polymer sensor for the mesurement of palmar pressures. In *IEEE Engineering in Medicine & Biology Society 11th annual international conference*, Seattle, November 1989.

[64] N Maalej, S Bhat, H Zhu, J G Webster, W J Tompkins, J J Wertsch, and P Bach-y Rita. a conductive polymer pressure sensor. *IEEE engineering in medicine & biology society 10th annual international conference*, 88:770–1, New Orleans, November 1988.

[65] Vishay. Tn-505-4 technical report, document number: 11055, Nov 2010. URL `www.micro-measurements.com`. Accessed Jan 9 2014.

[66] E S Hwang, J H Seo, and Y J Kim. A polymer-based flexible tactile sensor for both normal and shear load detections and its application for robotics. *Journal of Microelectromechanical Systems*, 16:556–63, 2007.

[67] A Arami, M Simoncini, O Atasoy, W Hasenkamp, S Ali, A Bertsch, E Meurville, S Tanner, H Dejnabadi, V Leclercq, P Renaud, C Dehollain, P A Farine, B M Jolles, K Aminian, and Peter Ryser. Instrumented prosthesis for knee implants monitoring. In *IEEE International Conference on Automation Science and Engineering*, Trieste, Italy, August 2011.

[68] W Hasenkamp, N Thevenaz, J Villard, A Bertsch, A Arami, K Aminian, A Terrier, and P Renaud. Design and test of a mems strain-sensing device for monitoring artificial knee implants. *Biomedical Microdevices*, 15:831–39, 2013.

[69] Stoeckel and Yu. Superelastic ni-ti wire. *Wire Journal International*, pages 45–50, March 1991.

[70] A R Pelton, X Gong, and T Duerig. Fatigue testing of diamond-shaped specimens. *SMST-2003: Proceedings of the International Conference on Shape Memory and Superelastic Technologies*, pages 293–302, 2003. A. Pelton and T. Duerig, Ed. (Pacific Grove, CA).

[71] N B Morgan, J Painter, and A Moffat. Mean strain effects and microstructural observations during in-vitro fatigue testing of niti. *Proceedings of the Interna-*

tional Conference on Shape Memory and Superelastic Technologies, pages 303–310, 2003. A.R. Pelton and T.W. Duerig, Ed (Pacific Grove, CA),.

[72] J Holmberg, L Alexander, R Rajamani, and J E Bechtold. Battery-less wireless instrumented knee implant. *Journal of Medical Devices*, 7:011006–1:011006–11, 2013.

[73] J A Dobrzynska and M A M Gijs. Capacitive flexible force sensor. *Procedia Eurosensors XXIV*, 5:404–7, 2010.

[74] J A Dobrzynska and M A M Gijs. Flexible polyimide-based force sensor. *Sensors and Actuators A*, 173:127–35, 2012.

[75] J A Dobrzynska and M A M Gijs. Polymer-based flexible capacitive sensor for three-axial force measurements. *Journal of Biomechanics, Microengineering*, 23: 1–11, 2013.

[76] H K Lee, S I Chang, and E Yoon. A flexible polymer tactile sensor: Fabrication and modular expandability for large area deployment. *Journal of microelectromechanical systems*, 15:1681–86, 2006.

[77] R Surapaneni, K Park, M A Suster, D J Young, and C H Mastrangelo. A highly sensitive flexible pressure and shear sensor array for measurement of ground reactions in pedestrian navigation. *IEEE*, Transducers 2011, Beijng, China, June 11.

[78] M Y Cheng, X H Huan, C W Ma, and Y J Yang. A flexible capacitive tactile sensing array with floating electrodes. *Journal of Biomechanics, Microengineering*, 19:1–10, 2009.

[79] H K Lee, J Chung, S I Chang, and E Yoon. Polymer tactile sensing array with a unit cell of multiple capacitors for three-axis contact force image construction.

Micro Electro Mechanical Systems, pages 623–26, February 2007. MEMS, Kobe, Japan.

[80] B Rubehn and T Stieglitz. In vitro evaluation of the long-term stability of polyimide as a material for neural implants. *Journal of Biomaterials*, 31:3449–58, 2010.

[81] S M Kurtz. *UHMWPE biomaterials handbook, second edition.* Elsevier, Burlington, MA, USA, 2009.

[82] M Y Cheng, C L Lin, Y T Lai, and Y J Yang. A polymer-based capacitive sensing array for normal and shear force measurement. *Sensors (Basel)*, 10(11): 10211–25, 2010.

[83] M Y Cheng, C L Lin, and Y J Yang. Tactile and shear stress sensing array using capacitive mechanisms with floating electrodes. In *23rd IEEE International Conference on Micro Electro Mechanical Systems*, Hong Kong, June 2010.

[84] T Salpavaara, J Verho, P Kumpulainen, and J Lekkala. Wireless interrogation techniques for sensors utilizing inductively coupled resonance circuits. *Procedia Engineering*, 5:216–219, 2010.

[85] Wireless Power Consortium. Qi Coupling Factor (www.wirelesspowerconsortium.com/technology/coupling-factor.html). URL `http://www.wirelesspowerconsortium.com/technology/coupling-factor.html`. Accessed on Jan 9 2014.

[86] D Marioli, E Sardini, M Serpelloni, and A Taroni. A new measurement method for capacitance transducers in a distance compensated telemetric sensor system. *Measurement Science and Technology*, 16:1593, 2005.

[87] E Sardini and M Serpelloni. Passive and self-powered autonomous sensors for remote measurements. *Sensors*, 9(2):943–960, 2009.

[88] D Marioli, E Sardini, M Serpelloni, and A Taroni. Contactless Transmission of Measurement Information Between Sensor And Conditioning Electronics. In *Instrumentation and Measurement Technology Conference, 2005. IMTC 2005. Proceedings of the IEEE*, volume 1, pages 395–99. IEEE, 2005.

[89] P J Chen, S Saati, R Varma, M S Humayun, and Y C Tai. Wireless Intraocular Pressure Sensing Using Microfabricated Minimally Invasive Flexible-Coiled LC Sensor Implant. *Journal of Microelectromechanical Systems*, 19(4):721–34, 2010.

[90] K Takahata and Y B Gianchandani. A micromachined capacitive pressure sensor using a cavity-less structure with bulk-metal/elastomer layers and its wireless telemetry application. *Sensors*, 8(4):2317–30, 2008.

[91] S M Kurtz, M L Villarraga, M P Herr, J S Bergstrm, C M Rimnac, and A A Edidin. Thermomechanical behavior of virgin and highly crosslinked ultra-high molecular weight polyethylene used in total joint replacements. *Biomaterials*, 23 (17):3681–97, Sep 2002.

[92] M Niinomi, Enjitsu T Wang, L, and K Fukunaga. Fatigue characteristics of ultra high molecular weight polyethylene with different molecular weight for implant material. *Journal of Materials Science: Materials in Medicine*, 12:267–72, 2001.

[93] RW Meyer and LA Pruitt. The effect of cyclic true strain on the morphology, structure, and relaxation behavior of ultra high molecular weight polyethylene. *Polymer*, 42(12):5293–5306, 2001.

[94] I Urries, F J Medel, R Ros, E Gomez-Barrena, and J A Puertolas. Comparative cyclic stressstrain and fatigue resistance behavior of electronbeam- and gamma-

irradiated ultrahigh molecular weight polyethylene. *Journal of Biomedical Materials Research B Applied Biomaterials*, 70:152–60, 2004.

[95] J S Bergstrom, S M Kurtz, C M Rimnac, and A A Edidin. Constitutive modeling of ultra-high molecular weight polyethylene under large-deformation and cyclic loading conditions. *Biomaterials*, 23(11):2329–43, June 2002.

[96] M Kitagawa and T Matsutani. Effect of time and temperature on nonlinear constitutive equation in polypropylene. *Journal of materials science*, 23:4085–90, 1988.

[97] D L Bartel, V L Bicknell, and T M Whright. The effect of conformity, thickness, and material on stresses in ultra-high molecular weight components for total joint replacement. *J Bone Joint Surg Am*, 68:1041–51, 1986.

[98] A. Avanzini. Mechanical characterization and finite element modelling of cyclic stress-strain behaviour of ultra high molecular weight polyethylene. *Materials & Design*, 29(2):330–43, 2008.

[99] WN Findley, J S Lai, and K Onaran. *Creep and relaxation of nonlinea viscoelastic materials*. Elsevier, Amsterdam, 2012.

[100] D J Krzypow and C M Rimnac. Cyclic steady state stress-strain behavior of UHMW polyethylene. *Biomaterials*, 21(20):2081, October 2000.

[101] S M Kurtz, D Mazzucco, C Rimnac, and D Schroeder. Anisotropy and oxidative resistance of highly crosslinked uhmwpe after deformation processing by solid-state ram extrusion. *Journal of Biomaterials*, 27:23–34, 2006.

[102] F Abraham, T Alshuth, and S Jerrams. The effect of minimum stress and stress amplitude on the fatigue life of non strain crystallising elastomers. *Materials and Design*, 26:239–45, 2005.

[103] P T Ton That, K E Tanner, and W Bonfield. Fatigue characterization of a hydroxyapatite-reinforced polyethylene composite. ii. biaxial fatigue. *Journal of Biomedical Materials Research*, 3:461–8, 2000.

[104] A Avanzini. Effect of cyclic strain on the mechanical behavior of virgin ultra-high molecular weight polyethylene. *Journal of Meche Behavior of Biomedical Materials*, 4(7):1242–56, October 2011.

[105] S T Gomaa and S Leisinger. Testing and modeling the nonlinear behavior of uhmwpe used in orthopaedic implants. In *Conference Proceedings of the Annual Meeting of the American Soc;*, Providence, RI, 2010.

[106] F Khan, C Yeakle, and S Gomaa. Characterization of the mechanical properties of a new grade of ultra high molecular weight polyethylene and modeling with the viscoplasticity based on overstress. *Journal of the mechanical behaviour of biomedical materials*, 6:174–80, 2012.

[107] S M Kurtz, L Pruitt, C W Jewett, R P Crawford, D J Crane, and A A Edidin. The yielding, plastic flow, and fracture behavior of ultra-high molecular weight polyethylene used in total joint replacements. *Biomaterials*, 19(21):1989–2003, November 1998.

[108] S D Waldman and J T Bryant. Compressive stress relaxation behavior of irradiated ultrahigh molecular weight polyethylene at 37 degrees c. *Journal of Applied Biomaterials*, 5:333–38, 1994.

[109] M Deng and K E Uhrich. Viscoelastic behaviors of ultrahigh molecular weight polyethylene under three-point bending and indentation loading. *J Biomater Appl*, 24(8):713–32, May 2010.

[110] R Hales, S R Holdsworth, M P O'Donnell, J J Perrin, and Skelton R P. A code

of practice for the determination of cyclic stress-strain data. *Materials at High Temperatures*, 19(4):165–85, 2002.

[111] James W Pritchett. Heat generated by knee prostheses. *Clinical Orthopaedics and Related Research*, 442:195–8, January 2006.

[112] G Bergmann, F Graichen, A Rohlmann, N Verdonschot, and G H van Lenthe. Frictional heating of total hip implants. Part 2: finite element study. *Journal of Biomechanics*, 34(4):429–35, April 2001.

[113] G Bergmann, F Graichen, A Rohlmann, N Verdonschot, and G H van Lenthe. Frictional heating of total hip implants. Part 1: measurements in patients. *Journal of Biomechanics*, 34(4):421–8, April 2001.

[114] J A Davidson, G Schwartz, G Lynch, and S Gir. Wear, creep, and frictional heating of femoral implant articulating surfaces and the effect on long-term performance–Part II, Friction, heating, and torque. *Journal of Biomedical Material Research*, 22(A1 Suppl):69–91, April 1988.

[115] J A Davidson, S Gir, and J P Paul. Heat transfer analysis of frictional heat dissipation during articulation of femoral implants. *Journal of Biomedical Material Research*, 22(3 Suppl):281–309, December 1988.

[116] C. Becher, J. Springer, S. Feil, G. Cerulli, and H. Paessler. Intra-articular temperatures of the knee in sports–An in-vivo study of jogging and alpine skiing. *BMC Musculoskeletal Disorders*, 9(1):46, 2008.

[117] A Tanavalee, S Honsawek, T Rojpornpradit, M Sakdinakiattikoon, and S Ngarmukos. Inflammation related to synovectomy during total knee replacement in patients with primary osteoarthritis: a prospective, randomised study. *Journal of Bone & Joint Surgery*, 93(8):1065–70, August 2011.

[118] S Honsawek, B Deepaisarnsakul, A Tanavalee, M Sakdinakiattikoon, S Ngarmukos, K Preativatanyou, and P Bumrungpanichthaworn. Relationship of serum IL-6, C-reactive protein, erythrocyte sedimentation rate, and knee skin temperature after total knee arthroplasty: a prospective study. *Annals of Clinical & Laboratory Science*, 35(1):31–5, January 2011.

[119] C L Romano, D Romano, F Dell'Oro, N Logoluso, and L Drago. Healing of surgical site after total hip and knee replacements show similar telethermographic patterns. *Journal of Orthopaedics and Traumology*, 12(2):81–6, June 2011.

[120] J S Bergstrom, C M Rimnac, and S M Kurtz. Prediction of multiaxial mechanical behavior for conventional and highly crosslinked uhmwpe using a hybrid constitutive model. *Journal of Biomaterials*, 24:1365–80, 2003.

[121] S M Kurtz, C M Rimnac, T J Santer, and D L Bartel. Exponential model for the tensile true stress-strain behavior of as-irradiated and oxidatively degraded ultra high molecular weight polyethylene. *Journal of Orthopadic Research*, 14: 755–61, 1996.

[122] S J Mellon, Y M Kwon, S Glyn-Jones, D W Murray, and H S Gill. The effect of motion patterns on edge-loading of metal-on-metal hip resurfacing. *Medical Engineering & Physics*, 33:1212–20, 2011.

[123] E C Pegg, J Walter, S J Mellon, H G Pandit, D W Murray, D'Lima D D, B J Fregly, and H S Gill. Evaluation of factors affecting tibial bone strain after unicompartmental knee replacement. *Journal of Orthopadic Research*, 31(5): 821–8, 2013.

[124] F E Kennedy, J H Currier, S Plumet, J L Duda, D P Gestwick, J P Collier, B H Currier, and M C Dubourg. Contact fatigue failure of ultra-high molecular

weight polyethylene bearing components of knee prostheses. *ASME*, 122:332–9, 2000.

[125] N Chang, A Bellare, R E Cohen, and M Spector. Wear behavior of bulk oriented and fiber reinforced uhmwpe. *Wear*, 241:109–17, 2000.

[126] S T Kuo, M C Yip, and K N Chiang. Time and temperature dependent mechanical characterization of polyimide materials in electronic packaging application. In *Proceedings of 4th Electronics Packaging Technology Conference*, Singapore, Dec 2002.

[127] M Pecht and X Wu. Characterization of polyimides used in high density interconnects. *Components, Packaging, and Manufacturing Technology, Part B: Advanced Packaging, IEEE Transactions on*, 17:632–9, 1994.

[128] S G Pereira, R Osorio, M Toledano, and T G Nunes. Evaluation of two bis-gma analogues as potential monomer diluents to improve the mechanical properties of light-cured composite resins. *Elsevier Dental Materials*, 21:823–30, 2005.

[129] M Helvatjoglu-Antoniades, Y Papadogiannis, R S Lakes, P Dionysopoulos, and D Papadogiannis. Dynamic and static elastic moduli of packable and flowable composite resins and their development after initial photo curing. *Elsevier Dental Materials*, 22:450–9, 2006.

[130] R Khazaka, M L Locatelli, S Diaham, and P Bidan. Effects of mechanical stress, thickness and atmosphere on ageing of polyimide thin films at high temperature. *Polymer Degradation and Stability*, 98:361–7, 2013.

[131] C Hassler, T Boretius, and T Stieglitz. Polymers for neural implants. *Journal of Polymer Science*, 49:18–33, 2011.

[132] F Graichen, R Arnold, A Rohlmann, and G Bergmann. Implantable 9-channel telemetry system for in vivo load measurements with orthopedic implants. ieee transactions on bio-medical engineering. *IEEE transactions on biomedical engineering*, 54:253–61, 2007.

[133] T Just, D Laqua, and P Husar. In-vivo signal transmission using an intra-corporal rf transmitter. *33rd Annual International Conference of the IEEE EMBS*, pages 7662–5, September 2011. Boston, Massachusetts, MA.

[134] E Y Chow, A L Chlebowski, S Chakraborty, W J Chappell, and P P Irazoqui. Fully wireless implantable cardiovascular pressure monitor integrated with a medical stent. *IEEE transactions on Bio-medical Engineering*, 57:1487–96, 2010.

[135] Analog Devices. Adf7023 datasheet, revision c, July 2012. URL `http://www.analog.com/static/imported-files/data_sheets/ADF7023.pdf`. accessed October 2013.

[136] Atmel. At86rf233 complete datasheet, revision 8351d, August 2013. URL `http://www.atmel.com/Images/Atmel-8351-MCU_Wireless-AT86RF233_Datasheet.pdf`. accessed Oct 2013.

[137] Texas Instruments. Cc2500 low-cost low-power 2.4 ghz rf transceiver (rev. c), May 2009. URL `http://www.ti.com/lit/gpn/cc2500`. Accessed Oct 2013.

[138] Maxim. Max7030 datasheet, version rev 4, June 2012. URL `http://datasheets.maximintegrated.com/en/ds/MAX7030.pdf`. Accessed Oct 2013.

[139] Freescale Semiconductor. Mc13201, technical data document number mc13201, April 2008. URL `https://www.google.co.uk/url?sa=t&rct=j&q=&esrc=s&source=web&cd=2&cad=rja&ved=0CDYQFjAB&url=http%3A%2F%2Fwww.freescale.com%2Ffiles%2Frf_if%`

2Fdoc%2Fdata_sheet%2FMC13201.pdf&ei=oTBxUpKBHKes0QXJ9IG4CA&usg=AFQjCNGKW8P14e-hUedrVAK07HdfrENJ0Q&sig2=PbGY3IF6a8ZuVUtH68yFng. accessed Oct 2013.

[140] Microchip. Mrf49xa data sheet, November 2011. URL http://ww1.microchip.com/downloads/en/DeviceDoc/70590C.pdf. accessed Oct 2013.

[141] Nordic Semiconductor. nrf24l01p-ps product specificationversion 1.0, 9 2008. URL http://www.nordicsemi.com/eng/nordic/download_resource/8765/2/59847448. accessed Oct 2013.

[142] Silicon Labs. Si4438 high-performance, low-current transceiver, version 0.1, 6 2012. URL http://www.silabs.com/Support%20Documents/TechnicalDocs/Si4438.pdf. accessed 30 Oct 2013.

[143] Semtech. Sx1211 datasheet, version rev 8, February 2013. URL http://www.semtech.com/apps/filedown/down.php?file=sx1211.pdf. accessed Oct 2013.

[144] Microsemi. Zl70102 medical implantable rf transceiver mics rf telemetry data sheet, 1st edition, June 2010. URL http://www.microsemi.com/index.php?option=com_docman&task=doc_download&gid=125431. Accessed Nov 2013.

[145] S Mathur. Small scale fading in radio propegation. *Wireless communication technologies*, 16:332–546, Piscataway, NJ 2005.

[146] Mistretta F Bottigioli D Dahel K Goujon C Nicolas J F Hennino A Laurent P E Laurent, A. Echographic measurement of skin thickness in adults by high frequency ultrasound to assess the appropriate microneedle length for intradermal delivery of vaccines. *Vaccine*, 29:8438–42, 2011.

[147] S H Lee, J Lee, Y J Yoon, S Park, C Cheon, K Kim, and S Nam. A wideband spiral antenna for ingestible capsule endoscope systems: Experimental results in

a human phantom and a pig. *IEEE Transactions on Biomedical Engineering*, 58: 1734–41, 2011.

[148] U Kim and J Choi. An implantable antenna for wireless body area network application. *Journal of the Korean institue of electromagnetic engineering and science*, 10, no 4:206–11, 2010.

[149] A Peyman, S Holden, and C Gabriel. Dielectric properties of tissues at microwave frequencies. pages 1–50, 2005.

[150] *Vita, de, P, AN4190 Application Note - Antenna selection guidelines - Doc ID 023812 - November 2012.* Accessed on January 9 2014.

[151] C A Balanis. *Antenna theory, analysis and design, third edition.* Wiley & Sons, Inc, Hoboken, New Jersey, 2005.

[152] S Hao, J Gorjon, and S J Taylor. Scimitar: Subject-carried implant monitoring inductive telemetric ambulatory reader for remote data acquisition from implanted orthopaedic prostheses. *Medical Engineering & Physics*, xxx:in press, 2013.

[153] Z Cui, H Wang, Z Chen, and W Yang. Image reconstruction for field-focusing capacitance imaging. *Measurement Science and Technology*, 22:1–9, 2011.

[154] M Carminati, G Ferrari, F Guagliardo, and M Sampietro. Zeptofarad capacitance detection with a miniaturized cmos current front-end for nanoscale sensors. *Sensors and Actuators A*, 172:117–123, 2011.

[155] H M Prasser, A Bottger, and Zschau. A new electrode-mesh tomograph for gasliquid flows. *Flow measurement and instrumentation*, 9:111–119, 1998.

[156] W Q Yang. Further developments in an ac-based capacitance tomography system. *Review of scientific instruments*, 72:3902–7, 2001.

[157] M J Silva, Da, E Schleicher, and U Hampel. Capacitance wire-mesh sensor for fast measurement of phase fraction distributions. *Measurement Science and Technology*, 18(7):2245–51, 2007.

[158] K Arshak, D Morris, A Arshak, O Korostynksa, and K Kaneswaran. Development of oxide thick film capacitors for a real time pressure monitoring system. *Materials Science and Engineering C*, 27:1406–10, 2007.

[159] Analog Devices. Ad7745/ad7746, 24-bit capacitance-to-digital converter with temperature sensor, rev 0, 2005. URL `www.analog.com/static/imported-files/data_sheets/AD7745_7746.pdf`. Accessed on Nov 12th 2013.

[160] Philips Semiconductors. The i2c specification version 2.1, January 2000. URL `www.cs.unc.edu/Research/stc/FAQs/Interfaces/I2C-BusSpec-V2.1.pdf`. Accessed on Jan 7 2014.

[161] Maxim semiconductors. Max6666/6667 high-accuracy pwm output temperature sensors, rev 3, Aug 2009. URL `http://datasheets.maximintegrated.com/en/ds/MAX6666-MAX6667.pdf`. Accessed on Dec 23 2013.

[162] Texas Instruments. Lm73 2.7v, sot, 11-to-14 bit digital temperature sensor with 2-wire interface datasheet - snis141d, May 2009. URL `http://www.ti.com/general/docs/lit/getliterature.tsp?literatureNumber=snis141d`. Accessed on Dec 23 2013.

[163] Analog Devices. Tmp05/06 0.5c accurate pwm temperature sensor in 5-lead sc-70 datasheet rev c, May 2009. URL `http://www.analog.com/static/imported-files/data_sheets/TMP05_06.pdf`. Accessed on Dec 23 2013.

[164] Texas Instruments. High-accuracy, low-power, digital temperature sensor with smbustm/two-wire serial interface in sot563 datasheet rev b, June 2009. URL `http://www.ti.com/lit/gpn/tmp112`. Accessed on Dec 23 2013.

[165] H S Gill and J J O'Connor. Heelstrike and the pathomechanics of osteoarthrosis: a pilot gait study. *J Biomech*, 36(11):1625–31, November 2003.

[166] D L Benoit, D K Ramsey, M Lamontagne, L Xu, P Wretenberg, and P Renstrom. Effect of skin movement artifact on knee kinematics during gait and cutting motions measured in vivo. *Elsevier Gait and Posture*, 24:152–64, 2006.

[167] I Sudhoff, Van S Driessche, S Laporte, de J A Guise, and W Skalli. Comparing three attachment systems used to determine knee kinematics during gait. *Elsevier Gait and Posture*, 25:533–43, 2007.

[168] K B Mansour, N Rezzoug, and P Gorce. Accelerometric signal during gait: cut-off frequency as a function of movement speed and sensor location. *Computer methods in biomechanics and biomedical engineering*, 16:68–69, 2013.

[169] ST Microelectronics. Lis3mdl datasheet - digital output magnetic sensor: ultra low power, high performance 3-axis magnetometer, rev 2, April 2013. URL `http://www.st.com/st-web-ui/static/active/en/resource/technical/document/datasheet/DM00075867.pdf`. Accessed on Nov 7th 2013.

[170] R E Mayagoitia, A V Neneb, and P H Veltink. Accelerometer and rate gyroscope measurement of kinematics: an inexpensive alternative to optical motion analysis systems. *Journal of Biomechanics*, 35:537–42, 2002.

[171] J R Davids. *Metals Handbook*. ASM International, 1998.

[172] Texas Instruments. Msp430fr573x/msp430fr572x family mixed signal microcontroller datasheet, slas639h, 2013 Sept. URL `http://www.ti.com/paramsearch/docs/parametricsearch.tsp?familyId=1751&sectionId=95&tabId=2475&family=mcu`. Accessed on November 12th 2013.

[173] R Sayyah, T C Macload, and F D Ho. Radiation-hardened electronics and ferroelectric memory for space flight systems. *ferroelectrics*, 413:170–5, 2011.

[174] S dos Santos. Intrumented hip implants, electric supply systems. *Journal of Biomechanics*, 46:256171, 2013.

[175] S M Kurtz, O K Muratoglu, M Evans, and A A Edidin. Advances in the processing, sterilization, and crosslinking of ultra-high molecular weight polyethylene for total joint arthroplasty. *Elsevier Biomaterials*, 20:1659–88, 1999.

[176] A A El-Daly and A E Hammad. Enhancement of creep resistance and thermal behavior of eutectic sncu lead-free solder alloy by ag and in-additions. *Materials and Design*, 40:292–8, 2012.

[177] O Krammer and B Sinkovics. Improved method for determining the shear strength of chip component solder joints. *Elsevier microelectronics reliability*, 50:235–41, 2010.

[178] J Keller, D Baither, U Wilke, and G Schmitz. Mechanical properties of pb-free snag solder joints. *Elsevier Acta Materialia*, 59:2731–41, 2011.

[179] A Kantarcioglu and Y E Kalay. Effects of al and fe additions on microstructure and mechanical properties of snagcu eutectic lead-free solders. *Materials Science and Engineering A*, 2013.

[180] J C S Moraes, M M D S Sostena, and C R Grandini. *The Glass Transition Temperature in Dental Composites, Metal, Ceramic and Polymeric Composites for Various Uses*. Intech, 2011. doi: 10.5772/21289. URL `http://www.intechopen.com/books/metal-ceramic-and-polymeric-composites-for-various-uses/the-glass-transition-temperature-in-dental-composites`.

[181] C A Willis-Owen, K Brust, H Alsop, M Miraldo, and J P Cobb. Unicondylar knee arthroplasty in the uk national health service: An analysis of candidacy, outcome and cost efficacy. *Knee*, 16:473–8, 2009.

[182] D D D'Lima, Patil S, Steklov N, Slamin J E, and Colwell C W Jr. The chitranjan ranawat award: in vivo knee forces after total knee arthroplasty. *Clinical Orthopaedics and Related Research*, 440:440:45–9, 2005.

[183] D D D'Lima, N Steklov, S Patil, and C W Colwell. The Mark Coventry Award: in vivo knee forces during recreation and exercise after knee arthroplasty. *Clinical Orthopaedics and Related Research*, 466(11):2605–11, November 2008.

[184] A Mündermann, C O Dyrby, D D D'Lima, C W Colwell, and T P Andriacchi. In vivo knee loading characteristics during activities of daily living as measured by an instrumented total knee replacement. *J Orthop Res*, 26(9):1167–72, September 2008.

[185] D Zhao, B J Fregly, S A Banks, D D D'Lima, and C W Jr Colwell. In vivo medial and lateral tibial loads during gait, stair, kneel, and lunge activities. In *52nd annual meeting of the orthopaedic research society*, 2006.

[186] C Gabriel. Compilation of the dielectric properties of body tissues at rf and microwave frequencies. Technical report, Kings College London and Occupational and Environmental Helth Directorate, Brooks Airforce Base, Texas, 1996.

[187] M Gulino, P Bellia, F Falciglia, F. Musumeci, A Pappalardo, A Scordino, and A. Triglia. Role of water content in dielectric properties and delayed luminescence of bovine Achilles' tendon. *FEBS letters*, 579(27):6101–6104, 2005.

[188] D J Griffiths. *Introduction to Electrodynamics*. Benjamin-Cummings Publishing Company, 3rd edition, 2008. ISBN-13: 9780138053260.

[189] Texas Instruments. Datasheet: Tps61200, tps61201,tps61202, low input voltage synchronous boost converter with 1.3-a switches, March 2013. URL www.ti.com/lit/pdf/SLVS577. Accessed on January 9th 2014.

.